

1976

Effects of negative pulsed voltage on the characteristics of an electrode system with clean and contaminated anode

Luong Chon Thanh
University of Wollongong

Follow this and additional works at: <https://ro.uow.edu.au/theses>

University of Wollongong

Copyright Warning

You may print or download ONE copy of this document for the purpose of your own research or study. The University does not authorise you to copy, communicate or otherwise make available electronically to any other person any copyright material contained on this site.

You are reminded of the following: This work is copyright. Apart from any use permitted under the Copyright Act 1968, no part of this work may be reproduced by any process, nor may any other exclusive right be exercised, without the permission of the author. Copyright owners are entitled to take legal action against persons who infringe their copyright. A reproduction of material that is protected by copyright may be a copyright infringement. A court may impose penalties and award damages in relation to offences and infringements relating to copyright material.

Higher penalties may apply, and higher damages may be awarded, for offences and infringements involving the conversion of material into digital or electronic form.

Unless otherwise indicated, the views expressed in this thesis are those of the author and do not necessarily represent the views of the University of Wollongong.

Recommended Citation

Thanh, Luong Chon, Effects of negative pulsed voltage on the characteristics of an electrode system with clean and contaminated anode, Doctor of Philosophy thesis, Department of Electrical Engineering, University of Wollongong, 1976. <https://ro.uow.edu.au/theses/4473>

EFFECTS OF NEGATIVE PULSED VOLTAGE ON THE
CHARACTERISTICS OF AN ELECTRODE SYSTEM
WITH CLEAN AND CONTAMINATED ANODE.

Thesis for the Degree of
DOCTOR OF PHILOSOPHY

Submitted by

Luong Chon THANH, B.E., M.ENG.SC.(N.S.W.), S.I.E.E.E.

Department of Electrical Engineering
(The University of Wollongong-[formerly
Wollongong University College])
The University of New South Wales.

November, 1976.

<u>CONTENTS</u>	<u>Page</u>
Abstract	(i)
Acknowledgements	(iv)
CHAPTER 1. INTRODUCTION	1
1.1-Industrial Background	1
1.2-Literature Survey	4
1.3-Formulation of the Problem	10
CHAPTER 2. REVIEW OF BACKGROUND THEORY OF GAS DISCHARGE	16
2.1-Introduction	16
2.2-The Townsend Theory of Breakdown	16
2.3-The Streamer Theory of Breakdown	21
CHAPTER 3. THEORETICAL STUDY OF CORONA DISCHARGE	26
3.1-Introduction	26
3.2-Calculation of Field for a Point-to-Plane System	27
3.2.1-Introduction	27
3.2.2-Charge Simulation Technique	29
3.2.3-Results	32
3.3-Corona Onset Voltage	37
3.3.1-Introduction	37
3.3.2-Theoretical Analysis	39
(a) The Photoelectric Emission of Secondary Electrons	42
(b) The Secondary Emission by Positive Ion Bombardment	43
(c) The Onset Condition	44
3.3.3-Data used in Numerical Calculations	45
3.3.4-Justification of the Theoretical Model	46
3.3.5-Discussion	51
3.4-Corona Current Waveshape	55
3.4.1-Introduction	55
3.4.2-Calculation Method	57
3.4.3-Comparison of Calculated and Experimental Results	60
CHAPTER 4. INSTRUMENTS	64
4.1-Introduction	64
4.2-Electrode Systems	66

4.2.1-Wire-to-Plane Parallel System	66
4.2.2-Point-to-Plane System	68
4.2.3-Contamination Materials	71
4.3-Measuring Equipments	72
4.3.1-The Photomultiplier	72
4.3.2-Corona Wind Velocity Measuring Device	83
4.3.3-Pulsed Power Supplies	85
CHAPTER 5. CHARACTERISTICS OF CORONA SYSTEM -	
CLEAN COLLECTING ELECTRODE	92
5.1-Introduction	92
5.2-Nature of the Discharge in the Vicinity of the Wire Electrode	93
5.2.1-Introduction	93
5.2.2-The Discharge Pattern in the Vicinity of the Cathode	94
5.2.2.1-Measurement of the Discharge Pattern	95
5.2.2.2-Results and Discussion	98
(a) Results	98
(b) Relationship between Photomultiplier Current and Corona Current	103
(c) Comparison between D.C. and Pulsed Voltage	112
5.2.3-The Corona Current Waveshape	114
5.2.3.1-Measurement of the Corona Current Pulse	114
5.2.3.2-Results and Discussion	117
(a) Results	117
(b) Instantaneous Characteristics of Current Pulse	120
(i) Low Voltage Level	120
(ii) High Voltage Level - Effects of Space Charges	128
(c) Average Characteristics of Current Pulse	130
5.3-Associated Phenomena in the Low Field Region	131
5.3.1-Introduction	131
5.3.2-Current-Voltage Characteristics	132

5.3.2.1-Experimental Technique	132
5.3.2.2-Results and Interpretation	134
5.3.3-Mathematical Model of a Corona System	138
5.3.3.1-Introduction	138
5.3.3.2-Equivalent Circuit of a Corona System	142
5.3.3.3-Analysis of First Order Non-Linear Circuit	143
5.3.3.4-Comparison between Calculated and Measured Results	145
5.3.4-The Corona Wind	151
5.3.4.1-Introduction	151
5.3.4.2-Theory of the Corona Wind	152
5.3.4.3-Measurement Technique	154
5.3.4.4-Results	156
5.3.4.5-Discussion	158
(a) Variation of Corona Wind with respect to Gap Length	158
(b) Effective Area of Collector	159
(c) Relationship between Corona Wind Velocity and Voltage	162
5.4-Sparkover of Clean Electrode System	172
5.4.1-Introduction	172
5.4.2-Measurement of Sparkover Voltage	173
5.4.3-Results	173
5.4.4-Discussion	175
5.4.4.1-Effects of Streamer Branching on Sparkover Voltage	176
5.4.4.2-Dependence of Corona Current on the Condition of Cathode	178
5.4.4.3-Sparkover Voltage versus Gap Length	179
5.4.5-Sparkover Voltage with Pulsed Energis- ation	181
5.5-Summary	182
CHAPTER 6. CHARACTERISTICS OF CORONA SYSTEM-CONTAMINATED COLLECTING ELECTRODE	190
6.1-Introduction	190
6.2-A Survey on the Subject	192
6.3-Voltage Distribution across the Contaminant Layer	194

6.3.1-Introduction	194
6.3.2-Measurement of Surface Potential	194
6.3.3-Results and Discussion	197
6.4-Conduction of Current in the Contaminant	204
6.4.1-Introduction	204
6.4.2-Measurement of Conduction Current	205
6.4.3-Results and Discussion	206
6.4.3.1-Volume Conduction Current	209
6.4.3.2-Surface Conduction Current	212
6.4.3.3-Current due to Schottky Emission	214
6.5-Electrical Breakdown in Contaminant	216
6.5.1-Introduction	216
6.5.2-Contaminant in Plane Parallel Electrodes	217
6.5.2.1-Calculation of Field between Adjacent Particles	217
6.5.2.2-Limitation of the Model	222
6.5.3-Contaminant on the Collecting Plane	223
6.5.3.1-Formation of Back Corona Channels	223
6.5.3.2-Effects of Back Corona on Potential across the Contaminant	227
6.5.4-The Critical Resistivity	228
6.6-Distribution of Surface Potential when Back Corona is present	234
6.6.1-Introduction	234
6.6.2-Analytical Study of Surface Potential Distribution	235
6.6.3-Comparison between Estimated and Measured Potentials	243
6.7-A Proposed Mechanism of the Formation of Back Corona	246
6.7.1-The Build up of Voltage across the Contaminant	246
6.7.2-The Perforation of Contaminant Layer	251
6.7.3-The Formation of Stable Discharge	252
6.8-Sparkover of the Contaminated Corona System	253
6.8.1-Introduction	253
6.8.2-Effects of Contaminant on Sparkover Voltage	254

6.8.2.1-Negative D.C. Energisation	254
6.8.2.2-Negative Pulsed Energisation	258
6.8.3-Dependence of Sparkover Voltage on Contaminant Thickness	260
6.9-Summary	266
References	268
Appendices	278

ABSTRACT

The electrostatic precipitator has been widely used for many years in the electricity supply industry to remove particles from a gas stream.

The collection of particles in an electrostatic precipitator is adversely affected if the resistivity of the particles is high. Attempts to overcome this problem have been made by: flue gas conditioning, operating at high and low temperatures, modifying the shape of the applied voltage. This project is limited to the investigation of the last method.

Effects of negative pulsed voltage on the characteristics of corona discharge in clean atmosphere are investigated when the laboratory scale electrode system is clean with collector electrode in clean and contaminated conditions respectively.

Fundamental characteristics of clean electrode system are investigated to check whether there is any difference in the discharge mechanism under negative pulsed and negative D.C. voltages. From the measurement of the light intensity emitted from the discharge electrode, the ionisation activities in the high field strength region are interpreted both in the forms of average corona current and the temporal development and movement of ions and electrons. Linear relationship is found to exist between the average photon current and the average corona current under both negative D.C. and pulsed voltages. When the average photon current is the same, the discharge patterns are similar for both kinds of voltage. The collisions of highly energised ions with

neutral gas molecules give rise to the phenomenon which is known as Electrical Wind is studied. Experimental evidence of these characteristics coupled with a theoretical study of corona discharge indicate that within the frequency range of 13 Hz -150 Hz the discharge mechanism is the same for both voltages, and the instantaneous properties of the corona current pulse are affected by the accumulation of negative and positive space charges in the neighbourhood of the discharge electrode. Sparking mode is studied with a multiple-point electrode and the results are compared with that obtained with a single point electrode to check the role of negative streamers in forming the complete breakdown. Sparkover voltage is measured when the electrode system is energised by negative D.C. voltage and is compared with that which is obtained with pulsed voltage.

The characteristics of the electrode system are changed when the anode plane is covered with a layer of high-resistivity, porous material which is used to simulate the contamination condition. The sparkover voltage of the system is drastically reduced by the local gas discharge which takes place in the contaminant. In order to explain the change of sparkover voltage with pulsed energisation, some important properties of the discharge are studied, such as: the distribution of surface charge which accumulates on the layer, the conduction of current and the electrical breakdown in the contaminant, the effect of surface potential gradient on the formation of a stable back discharge. These features are summarised in a proposed mechanism of the formation of back corona discharge. This is extended to

explain an increase in sparkover voltage when the system is energised with pulsed voltage in comparison to that with negative D.C. voltage.

ACKNOWLEDGEMENTS

The author wishes to thank the University of Wollongong for granting a scholarship to do this research; the Electricity Commission of New South Wales for their support of this project; the Chairman of the Department of Electrical Engineering, Professor B.H. Smith and its members of staff for permitting him to use the available technical facilities; Professor P. Cooperman of Fairleigh-Dickinson University for his stimulating discussion on some aspects of this work during his visit and Mrs M. Inglis for her keen interest in typing this thesis.

Last but not least, the author is much obliged to his supervisor, Dr. K.J. McLean for his interest, patience and fruitful guidance throughout this work.

CHAPTER 1: INTRODUCTION

1.1 Industrial Background

The electrostatic precipitator has been widely used for many years in the electricity supply industry to remove charged particles from a gas stream. It is essentially an asymmetrical corona discharge device in which suspended particles are first charged by ions generated in the high field strength region and subsequently removed from the gas by electrostatic forces. Details of their construction and the basic theory describing their operation is conveniently summarised in books by White [1], Rose and Wood [2] and Robinson [3].

In practice, the operating condition of an electrostatic precipitator is determined by the complex interaction of a wide range of parameters including: gas properties, temperature, electrode shape, electrode spacing, method of energisation, inlet dust density (i.e. space charge effects), particle size distribution, resistivity of the deposited layer of particles.

One of the most important parameters affecting the electrostatic precipitator performance is the resistivity of the collected particles. A layer of high-resistivity particles on the collecting electrode reduces the sparkover voltage for negative corona discharge. Attempts to overcome this deleterious effect have been made by

- (a) flue gas conditioning
- (b) operating at high temperatures
- (c) operating at low temperatures.

One other possible method of improving the performance of an electrostatic precipitator, which has not yet been tried in practice, is to modify the shape of the applied voltage.

In a modern electrostatic precipitator, the conventional power supply comprises of a single phase bridge rectifier with either a full-wave or half-wave output. The shape of the output voltage is fixed by the frequency of the A.C. supply and parameters of the precipitator, and little can be done to the waveshape to optimise the precipitator operation except to alter the value of the peak voltage.

A number of methods of modifying the voltage have been suggested and tested in the laboratory. These include the use of pulsed voltages - White [4], Thomas and Williams [5], Koschany [6], A.C. voltage - Lau [7], a bidirectional low frequency pulsed voltage - Herceg and Huey [8], a pulse-charging system in combination with a third electrode, Lüthi, Masuda [29],[30], and energisation with positive instead of the usual negative voltage - Cooperman [9],[10]. Of these proposals, the use of pulsed voltages with variable frequency and pulse duration has been the method most extensively investigated and has resulted in the construction and testing of a commercial prototype. Because of hardwave problems the method was not developed commercially at the time of these tests, however due to modern advances in switching of high voltages, interest has again been revived [11].

The advantages claimed for the pulsed power supply are [10]

- (a) Higher operating peak voltage and average current.
- (b) Uniform, diffuse corona discharge in contrast to spotty, localised corona with conventional systems with high resistivity ash on collecting plates.
- (c) Optimum duty cycle and waveform adjustable.
- (d) Lower rate of sparking increase with peak voltage.
- (e) Greater precipitator sectionalisation possible.

Multiple channel pulsers energising 4 to 6 individual precipitator sections are possible to reduce cost - either by using a high voltage distributor switch or by using separate pulse circuits fed from a common D.C. supply and charging choke.

- (f) High stability under sparking conditions; no transient disturbances fed back into the power line circuit.
- (g) Low intensity sparks reduces dust loss and wire burning.
- (h) Three-phase balanced line input - high overall electric efficiency.

Some attempts are being made by the U.S. Environmental Protection Agency to check the feasibility of using pulsed power supply but to date no test results have been published.

Since the use of pulsed power supply is one of the few areas in which significant change in the technology of electrostatic precipitators is possible, it has been decided to initiate a program to investigate their characteristics using laboratory scale electrodes. The object of

this thesis is to investigate the physics of the corona discharge and sparking of an electrode system with clean and contaminated collecting plate and energised by a negative pulsed voltage. This will then be compared with the discharge resulting from energisation by steady voltage. Once the physics of the corona and sparking mechanism is better understood, it will then be possible to extend the work to commercial size electrode systems at some future date.

1.2 Literature Survey

A comprehensive survey of literature on gas discharge up to 1963 has been presented by Loeb [12], and since that time there has been a steady flow of papers appearing in the journals. His work covers research in the basic mechanisms of corona discharge in clean gas and clean electrode system.

At the time of publication of Loeb's book, White completed his study of corona phenomena in connection with electrical precipitation [1], his work together with that by Rose and Wood [2] published three years later are considered as the first two complete monographs on electrostatic precipitation.

The earliest investigation of the characteristics of corona in air produced by pulsed voltage at atmospheric pressure was made by Hall [13]. Positive and negative pulses up to 60 KV and of duration one to two microseconds were used at repetition rates of 250 to 2000 pulses per second,

to energise electrode systems which comprised wires in cylindrical and parallel plane electrodes. He observed a diffuse glow extending along the discharge electrode for negative impulse corona at voltages well below the sparking point. However, he did not attempt to explain the nature of the discharge pattern on the wire electrode under such condition.

A few years later Moore and English using a square wave pulse generator to energise a point-to-plane system, reported the negative impulse corona which has a streamer type of discharge superimposed on the regular Trichel pulse corona [14]. Voltage pulses had one and two micro-second duration and repetition rates of 50 to 2000 pulses per second. By using the nonelectron-attaching gases such as hydrogen and nitrogen, they were able to show that the streamers were due to the negative ion space charge formed by the Trichel pulse in the gap. At the end of one applied voltage pulse, the intense field developed between this negative space charge and the positive ion space charge at the point electrode was sufficient to cause a streamer to propagate. This hypothesis was based mainly on their visual observation of the discharge pattern at the point tip by means of telemicroscope and camera. They were not entirely successful in resolving the corona pulses completely from the high voltage pulse on which they were superimposed. As a result, they were unable to detect electrically the existence of the streamer discharge.

Following the above works, Thomas and Williams initiated an investigation of the current-voltage relationships of negative impulse corona for a wide range of pulse lengths and repetition rates [15],[16]. A cylindrical electrode system was used in conjunction with a load capacitance which tended to smooth out the applied voltage pulses. Their results indicated that the peak value of the sparkover voltage was higher than that of D.C. voltage and the product of sparkover voltage and average corona current which was defined as corona loss, was of the same order as for the D.C. case. However, they did not attempt to explain their results or to analyse them with the help of a mathematical model. Two years later they published their continuing study on the same subject [5], by using the same set of equipment and a differential amplifier, they were successful in resolving the corona current pulses from the displacement currents which occurred at the leading and trailing edges of the applied voltage pulses. For pulse length varying from one to fifty microseconds and pulse frequency from 1,000 to 91,000 pulses per second, they normalised the average corona current with respect to the pulse duty ratio and plotted this quantity against the peak applied voltage. By making a comparison between the characteristic for impulse negative corona and that for D.C. corona, and with the help of the oscilloscopic recording, they suggested the existence of pre-corona discharge pulses which were attributed to the current flow which precedes and accompanies space charge formation during the negative

corona transient. However, because of the condition that prevails in the wire-to-cylinder system, several discharge sites can exist simultaneously and no attempt was made to observe the discharge pattern along the wire electrode. The effects of negative impulse voltage on the corona discharge and its basic mechanism still remain unresolved.

The method of using negative pulse voltage to energise an electrostatic precipitator which can be considered as an electrode system with contaminated gas and electrodes, was introduced by White [4]. Except for a very good description of the pulse generator, little information on the current-voltage relationship, the nature of the discharge and the increase in sparkover voltage under pulse energisation was found in his work.

Following White's method, Koschany used a D.C. power supply in connection with a circuit breaker and a pulse transformer to generate voltage pulses of 15 to 1,120 microsecond duration and repetition rates of 7 to 400 pulses per second [6]. A comparison between the current-voltage relationship for impulse voltage and that for D.C. case was presented together with collection efficiency of the precipitator under both methods of energisation. She concluded that a considerable increase in efficiency can be attained in collecting dust of high resistivity of approximately 10^{11} ohm-m by using impulse voltage excitation.

Recently, a group of investigators at the Southern Research Institute conducted a theoretical study of pulse energisation [17]. They utilised a charging subroutine

program to run a comparison between pulse energisation using pulses of 100 microsecond duration and half-wave rectification at the same frequency (60 pulses per second) for electrostatic precipitator. The analytical results indicated the difference in pulse energisation and half-wave rectification is rather small.

More recently, Masuda has applied the method of pulse charging in combination with a third electrode [30], to a pilot precipitator. His results indicated an increase of collection efficiency from 63% to 93% for dust having very high resistivity of approximately 10^{11} ohm-m. This method of using pulsed excitation was initially introduced by Lüthi [29], in which the current density can be adjusted entirely independent of the main field strength by changing the height or repetition frequency of the pulsed voltage. A uniform current density on the collecting plates is obtainable with this technique [30].

Table 1.1 is used to summarise the details of output voltage waveforms, experimental conditions and geometry of electrode system discussed above.

Source	Pulse Duration (microseconds)	Pulse Rate (C/s)	Electrode Geometry	Electrode Condition
Hall	1-2	250-2000	Wire-cylinder	Clean
Moore and English	1-2	50-2000	Point-to-Plane	Clean
Thomas and Williams	1-50	1000-91,000	Wire-cylinder	Clean
White	100-150	240-480	Wire-parallel plates	Contaminated electro- des and gas
Koschany	15-1120	7-400	Wire-parallel plates	Contaminated electro- des and gas
Masuda	1-2000	20-1000	Wire-parallel plates with third biased electrode	Contaminated electro- des and gas

TABLE 1.1 DETAILS OF VOLTAGE WAVEFORMS, EXPERIMENTAL
CONDITIONS AND GEOMETRY OF ELECTRODE SYSTEM
USED BY VARIOUS WORKERS.

1.3 Formulation of the Problem

An investigation of all the factors affecting the performance of an actual electrostatic precipitator when energised by a pulsed power supply would be very complex and beyond the scope of a single thesis. In order to limit the scope of the investigation, it is proposed to investigate the characteristics of corona discharge in a clean atmosphere using a laboratory scale electrode system with:

- (a) Clean collecting electrode
- (b) Contaminated collecting electrode

using a negative pulsed voltage and then comparing the results with those obtained with a D.C. voltage. In particular, the following features will be investigated.

A - Characteristics of clean electrode system

- (i) One special feature of the discharge which has been visually observed, is an apparent change in the appearance of the discharge along the wire electrode. With a negative pulsed voltage, the evenly spaced bright discharge points, which are the characteristic of a smooth negative D.C. voltage, are less intense and the discharge is more uniform (Hall [13]). Since the ionisation of the gas molecules in the high field strength region gives rise to the transport of negative ions into the low field strength section, it is expected that the external current flow is proportional to the ionisation. Consequently, any change in the appearance of the discharge along the wire cathode would be associated with a change in the current distribution along the anode surface. The problem

is to find out if the visual difference is due to significant difference in the discharge mechanism. Experimental results obtained by means of optical technique will be used to find the dependence of discharge intensity on the repetition rate and amplitude of the pulsed voltage. Electrical method will be used to resolve the corona current pulse from the displacement current due to pulsed voltage. These characteristics will be compared with those obtained for a steady voltage. The basic mechanism of corona discharge will be studied by means of a phenomenological model. Criteria for corona onset voltage and corona current waveshape are solved with the use of a digital computer. The calculated results will be compared with the experimental results to check the validity of the model.

- (ii) Average corona current will be plotted against peak and average pulsed voltage for different frequencies, and compared with those obtained under negative D.C. voltage. A mathematical model which simulates asymmetrical electrode system is proposed, and will be used to interpret the dependence of corona current-voltage characteristics on frequency, duration and duty cycle of the pulsed voltage.
- (iii) Another phenomenon associated with the ionisation process is the electrical wind. This is caused by collisions between ions created in the high field region and gas molecules. The transfer of momentum from the ions to the molecules creates a pressure

difference in any section of the gas and causes a stream of gas to move. The movement of gas across a section of the discharge system per second is defined as electrical wind velocity, which therefore is proportional to the ionisation. Because in an electrostatic precipitator, the charged particles are driven toward the collector by the resultant effect of the applied electric field and the turbulence caused by the electric wind, it is of interest to study this phenomenon under pulsed excitation. An experimental technique is designed to measure the corona wind velocity for both pulsed and D.C. voltages. The dependence of this quantity on gap length, amplitude and repetition rate of pulsed voltage will be investigated.

- (iv) Since one of the significant advantages of using pulsed voltage to energise an electrostatic precipitator is the possible increase in the maximum operating voltage, it is necessary to investigate the sparkover of clean electrode system. The results will be compared with those obtained when the collecting plane anode is covered with a layer of high-resistivity material. The role of highly-stressed cathode in the spark discharge is investigated by means of a multiple-point electrode, in which separation distance between discharge electrodes is adjustable.

B - Characteristics of contaminated electrode system.

The characteristics of the discharge system is changed if the electrodes are contaminated. Since in a negative corona system, the contamination of the plane anode results in drastic effects on the electrical characteristics, it is desirable to limit the investigation to the situation in which the collecting plane is covered with high-resistivity materials. In order to explain the change of sparkover voltage with pulsed energisation, it is necessary to describe in much greater detail, than has been done in the past, the formation of back corona. Due to the complexity of the phenomenon, it is convenient to describe each step of its formation which can be summed up as follows:

- (i) The accumulation of negative charge carriers on the surface of the contaminant gives rise to a voltage distribution which resembles a Normal Distribution curve because of the injection of charge carriers into the contaminant, the repulsion between carriers of the same polarity and the non-linear equivalent resistance of the contaminant.
- (ii) The conduction of current through the contaminant will be investigated and interpreted by means of a theoretical model. Attention will be given to the conduction through thin surface layer of particles and the high electric field induced in the air voids due to the constriction of current flow through the contact areas between adjacent particles. This induced field causes electrons to jump across the air gap and results in an increase of the effective

contact area.

- (iii) The electrical breakdown in the contaminant will be studied by calculating the electric field in the air voids and comparing this value with the breakdown field strength of air. The local gas discharge that takes place inside the contaminant is so vigorous that it triggers a complete breakdown across the contaminant and causes the layer to be perforated. With the occurrence of back corona discharge in the perforations, the potential build up across the contaminant is redistributed in such a way that the field line distribution in the air gap directs more negative ions toward the channels.
- (iv) The redistribution of potential build up across the contaminant is analysed to substantiate the significant role of the surface potential gradient in maintaining a stable back corona discharge in the channel. A mechanism of the formation of back corona is proposed, it includes all the important features discussed previously. These features will be condensed into a qualitative explanation of the phenomenon.
- (v) Effects of back corona discharge on sparkover of the contaminated electrode system will be investigated and the dependence of sparkover voltage on the thickness of contaminant will be expressed in a semi-empirical formula. The increase of sparkover voltage with pulsed energisation over that with negative

D.C. excitation will be explained by extending the proposed mechanism for back corona formation and comparing the results with those obtained by other workers.

CHAPTER 2: REVIEW OF BACKGROUND THEORY

ON GAS DISCHARGE

2.1 Introduction

Over the years, considerable effort has been directed towards investigating of the partial and complete breakdown in air of an asymmetrical electrode system at normal temperature and pressure and a wide range of literature is available. It seems appropriate at this stage of the thesis to present a brief outline of the generally accepted theories used to model these discharges so that easy reference can be made to them in the latter part of the thesis.

2.2 The Townsend Theory of Breakdown

A gas such as air is normally an almost perfect insulator but because of cosmic radiation some electrons and ions will always be present. Under the influence of a strong electric field at least one free electron in the gas will be accelerated toward the anode. This electron collides with the gas molecules and may excite or ionise them. By this process a new electron-ion pair is formed. It is a cumulative process and the number of electrons and positive ions grows rapidly. The number of electrons produced through ionisation by collision per unit is described by "Townsend's first ionisation coefficient", α . The value of α was determined experimentally by many researchers for a variety of gases at different pressures and field strengths [18],[19]. The general relationship between α , the external field and the pressure can be expressed by :

$$\frac{\alpha}{p} = A \cdot \exp(-B \cdot p/E)$$

where:

p = gas pressure

E = external electric field

A, B = constants determined experimentally,
which have different values for
different ranges of E/p .

The positive ions are also accelerated in the field but it is unlikely that they can ionise the gas molecules because of their much larger mass. They lose a major portion of their kinetic energy in each inelastic collision and as a result they gain considerably less energy than the electrons. It was observed that ions must have at least 400 eV in order to ionise in molecular gases and lower energies in atomic gases [19].

However, positive ions can produce new electrons by bombardment of the surface of the cathode. If n_0 electrons start at the cathode, they will form an electron avalanche on arriving at the anode and the number of electrons can be expressed as:

$$n = n_0 \cdot \exp(\alpha d) \quad (2.1)$$

where:

d is the distance between electrodes

n : number of electron in the avalanche.

The positive ions which are left behind by the avalanche will arrive at the cathode and get neutralised. In addition to the electrons required for neutralisation, secondary electrons are emitted at the cathode. The

probability for this kind of secondary emission is denoted by γ_i . The new electrons will form a larger electron avalanche and again the electrons will be collected by the anode and the ions will move toward the cathode. The whole process can be expressed by:

$$n = n_0 \cdot \frac{\exp(\alpha d)}{1 - \gamma_i (\exp(\alpha d) - 1)} \quad (2.2)$$

The mechanism of secondary emission through positive ions bombardment is not always possible because of the very short transition times involved. It was observed that the transition from a Townsend non self-sustaining discharge to a self-sustaining discharge can take place in less than 10^{-6} second. The transit time of positive ions between electrodes is usually of the order of 10^{-6} second. It is likely that the other secondary processes are more important and responsible for the short transition time.

The photoelectric emission from the cathode caused by photons produced by inelastic collisions in the gas. The excitation energy of the gas atom or molecules should be greater than the work function of the cathode material for this mechanism to take place. By taking into account the number of excited states formed in the collision process, the absorption of photons by the gas and the geometrical factor which specifies the fraction of the photons that arrives at the cathode, it can be shown that [19]

$$n = n_0 \cdot \frac{\exp(\alpha d)}{1 - \frac{\Delta g \theta}{\alpha - \mu} (\exp(\alpha - \mu) d - 1)} \quad (2.3)$$

where: Δ : probability of photoelectric emission due to radiation from the gas.

g : geometrical factor dependent on the dimension of electrodes and location.

θ : number of excited states due to electron collision per unit length.

μ : coefficient of photon absorption of the gas.

The quantity $\Delta g\theta/(\alpha-\mu)$ can be regarded as the coefficient of photoemission, γ_p . Expression (2.3), therefore is identical to (2.2) except for γ_p .

Secondary emission can also take place with the action of metastable particles. They succeed in attracting electrons from the cathode when their energy is greater than the work function of the cathode material. The transit time of metastables is even longer than that of ions because they are neutral atoms and reach the cathode through thermal diffusion. This process is naturally much slower than ionic motion under the field-to-pressure ratio normally used.

The photoionisation of a gas is considered as the second major source of secondary electrons. The process is caused by the absorption of photons by a gas whose absorbing molecules or atoms can be excited or ionised by the absorbed photons. The produced photoelectrons will be accelerated by the external electric field and will form electron avalanches similarly to the primary electrons. The number of secondary electrons can be expressed in the following equation, a complete derivation can be found in literature [19]

$$n = n_o \cdot \frac{\exp(\alpha d)}{1 - \epsilon g f \frac{\mu}{\alpha - \mu} (\exp(\alpha - \mu) d - 1)} \quad (2.4)$$

where ϵ : ratio of ionising photons to total number of absorbed photons also known as photo-ionisation efficiency coefficient.

The remaining terms are the same as above.

A generalised form for expressions (2.2), (2.3) and (2.4) can be expressed as

$$n = n_o \cdot \frac{\exp(\alpha d)}{1 - \gamma (\exp(\alpha - \mu) d - 1)} \quad (2.5)$$

where γ is commonly known as the second Townsend coefficient of ionisation.

A transition from non self-sustaining discharge to self-sustaining discharge or breakdown of a uniform field gap takes place when the denominator of equation (2.5) equals zero i.e.

$$\gamma (\exp(\alpha - \mu) d - 1) = 1 \quad (2.6)$$

The condition set by equation (2.6) is known as Townsend's criterion of breakdown. It requires the formation of several electron avalanches in order to attain a breakdown. This criterion has been used by many researchers to calculate the breakdown field strength of uniform gaps. The discrepancies between the calculated and experimental results are caused by the difficulty in obtaining the correct value for γ as it is very sensitive to electrode conditions and gas impurities. Schumann [20] has proposed an expression which has terms determined experimentally for

the Townsend's breakdown criterion

$$\int_0^d \alpha dx = k \quad \text{where } k \text{ is empirically chosen as } 20.$$

Another form of Townsend mechanism has been suggested by Hutton [21], Ver Planck [22] who replaced k with a function of gas pressure and field strength of cathode.

The Townsend theory of breakdown cannot explain an extremely short transition time of the order of 10^{-8} second which has been recorded for short uniform gaps. It does not give any information about the temporal growth of the processes leading to breakdown, in particular the effect of the space charge left over by earlier electron avalanches, this could give a resultant α larger than that expected for space charge free case. This weakness led to the concept of the streamer type of breakdown.

2.3 The Streamer Theory of Breakdown

The Streamer Theory was proposed by Meek [23] and independently by Raether [24]. It has been elaborated by Loeb, Meek and Raether [25-28]. The theory is based on considerations of individual electron avalanches, the transition from an avalanche to a streamer and the mechanism of propagation of streamers.

The criteria for the transition from an avalanche into a streamer obtained by Meek and Raether are useful in engineering application to calculate the breakdown field of uniform gaps. However, they did not explicitly include the absorption of photons in the photoionisation process although it was stated such ionisation had to be adequate [25], [26].

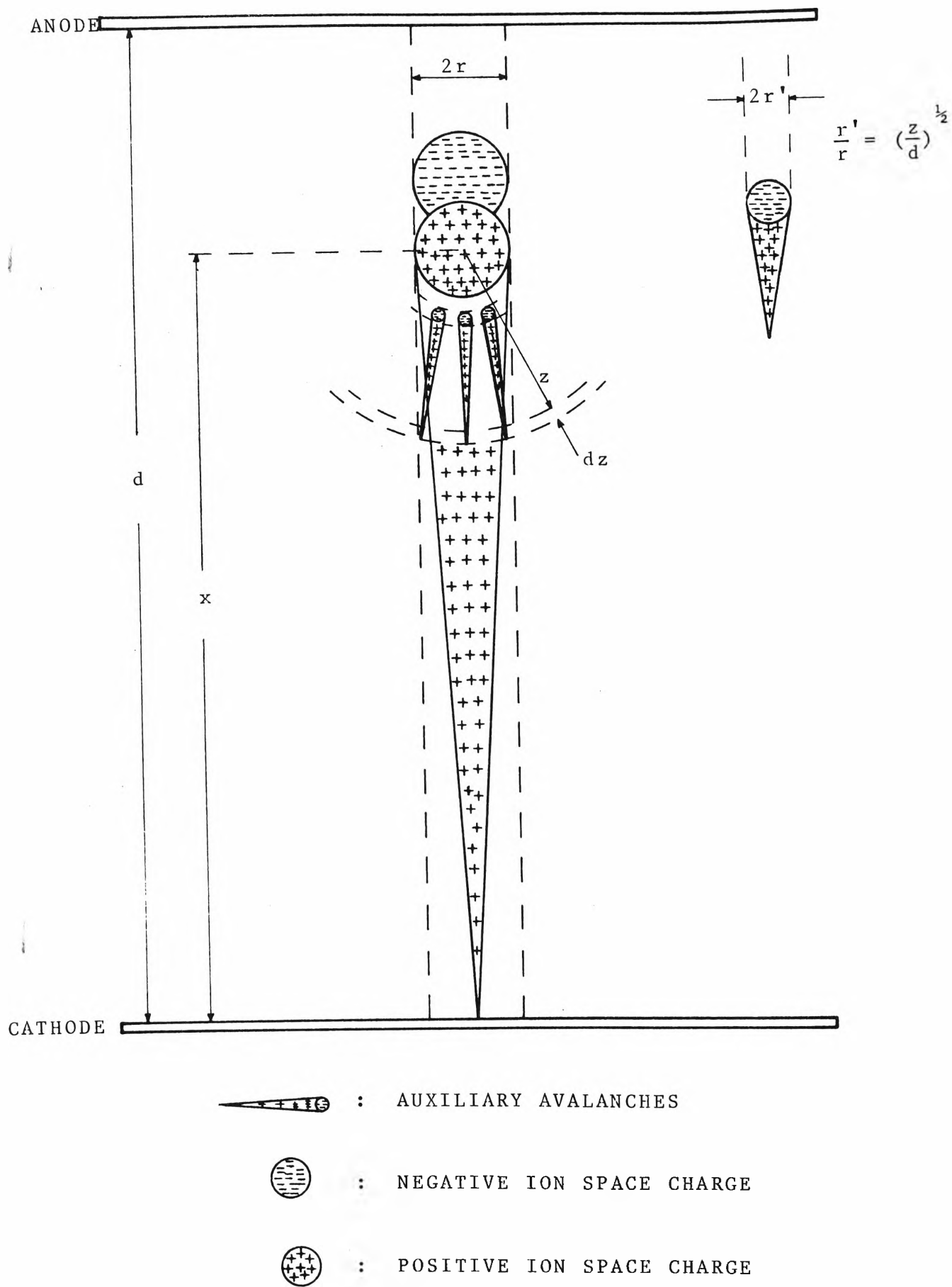


FIG. 2.1 ILLUSTRATION OF THE FORMATION OF A SELF-PROPAGATING STREAMER IN UNIFORM FIELD GAP.

A more elaborated model was formulated by Loeb to find the relation for the threshold of the burst pulse corona taking into account the absorption of photons [32]. An extension of this model including the photo-ionisation in the gas was later developed by Loeb and Wijsman to determine the threshold for a cathode-directed positive streamer in uniform fields [27]. The derivation of the self-propagating streamer criterion is discussed with the illustration shown in Fig. 2.1. The following assumptions are made:

- (i) Only photons absorbed by the gas that is confined in a cylindrical volume which has the same radius as the space charge of the primary avalanche contributes to the advance of streamer toward the cathode.
- (ii) The drift velocity and diffusion of electrons of the primary and auxiliary avalanches are the same.

The number of photoelectrons produced in a spherical shell of thickness dz is

$$n_1 = \epsilon f n \frac{r^2}{4z^2} e^{-\mu z} \mu dz \quad (2.7)$$

where:

ϵ = coefficient of photo-ionisation

f = ratio of excited states to ionised
states per electron

n = number of ions in the primary avalanche

r = radius of the sphere containing ions
of the primary avalanche

μ = coefficient of absorption

z = location of the tip of the primary avalanche.

Each photoelectron will create one auxiliary avalanche in the same manner as the primary avalanche with one exception that the first Townsend's coefficient α is now a function of location z . The total number of positive ions produced by one auxiliary avalanche is

$$n_p = \frac{4}{3}r \left(\frac{z}{d}\right)^{\frac{1}{2}} \alpha(z) e^{\int_r^z \alpha(z) dz} \quad (2.8)$$

The number of positive ions produced by n_1 photoelectrons is: $n_1 n_p$ and the total number of positive ions produced by all the photoelectrons existing ahead of the primary avalanche tip is:

$$\int_r^d n_1(z) n_p(z) dz \quad (2.9)$$

The condition for streamer propagation is satisfied when this number of secondary positive ions is greater than or equal to the number of positive ions in the primary avalanche tip i.e.

$$\int_r^d n_1(z) n_p(z) dz \geq n$$

which can be written as:

$$\frac{1}{3} \epsilon_f r^3 \mu d^{-\frac{1}{2}} \int_r^d \alpha(z) z^{-\frac{3}{2}} e^{-\mu z} e^{\int_r^z \alpha(z) dz} dz \geq 1 \quad (2.10)$$

The breakdown field strength is determined implicitly from equation (2.10) by using the semi-empirical relation between α , E and p . The model for streamer propagation is also valid for non-uniform fields where the mathematical expression is similar to Eq. (2.10). By using the same approach, Nasser [19] obtained the criterion for the

propagation of cathode directed positive streamer in a positive point-to-plane corona system. Heiszler [34] used this model to compute the corona onset voltage and the streamer length of a point-to-plane system.

CHAPTER 3: THEORETICAL STUDY OF CORONA

DISCHARGE

3.1 Introduction

In this chapter, a theoretical study of corona discharge is presented. It is important as it will be referred to in the later part of the thesis as one of the main claims of this thesis that the basic physics of corona discharge is the same for both pulsed and negative D.C. voltages. The similarity will be substantiated by experimental results obtained by means of photo-electric and electrical methods.

This analysis will show that the time taken to form each discrete group of avalanche is so short that any change in the applied voltage of the pulse will be insignificant. The main effect of the increasing voltage is to change the rate of clearance of the negative ion space charge from the ionisation region.

In order to compute the corona current waveshape, it is necessary to find the field intensity distribution of the electrode system and to obtain the criterion for the onset of negative corona.

The onset of corona is defined as the transition from a non-self-sustained discharge to a self-sustained one and it takes place when the cathode field reaches a critical value. The expression used to calculate this critical field is based on the Townsend's theory of breakdown (Section 2.2).

Although this method has been used by other workers [68] in their attempts to correlate the corona current waveshape to its interference on the transmission of signals at Radio Frequency, the following analysis adopts the same technique

and takes into account a number of factors which, according to the author, reflect more closely the physics of negative corona discharge.

3.2 Calculation of Field for a Point-to-Plane System

3.2.1 Introduction

There are a variety of methods of calculating the electric field strength, but they are all based on the solution of Laplace's or Poisson's equation with boundary condition satisfied. This can be solved either by analytical or numerical methods. Because of the complex configurations of most physical electrode systems, the numerical method, with the availability of the high speed digital computer, has been commonly used. Numerical methods are broadly based on the finite difference technique, the successive image technique and the integral form of Poisson's and Laplace's equations, the last one is also known as the charge simulation technique.

The Finite Difference method has been attempted by many workers to find the field distributions of many systems which have complex boundary shapes [69],[70],[71]. A complete survey on this subject is beyond the scope of this section.

Briefly, the finite-difference method consists of the calculations of values at discrete points spaced in an ordered way over the whole field region of the function which describes the field. These values are obtained by replacing the one partial differential equation of the field by many simple finite difference equations which take the form of linear equations connecting the potential at each

point with the potential at other points close to it [72]. The solution of the field is reduced to solution of a set of simple simultaneous algebraic equations for the potential values.

The method of successive image charges is well known in solving electrostatic and electromagnetic problems [73]. It is based on the concept of imaginary point or line charges not located within the region of field calculation, but so selected that the field of the image charges within this region is identical with that of the induced charges on the boundaries of the region. This method has been extended to a system of parallel cylindrical conductors by replacing the actual charge distribution on the conductor surfaces by a series of image line charges [74].

The charge simulation technique arises from the integrals of Poisson's and Laplace's equations, and has been widely used over the past ten years. It has been claimed that the method is more successful than the finite difference method when the solution for a three-dimensional field without axial symmetry is required [75].

In this method, the highly stressed electrode is simulated by a number of line charges and/or point charges. The magnitude of these charges are calculated so that their total effect on the electrode system satisfies the boundary conditions at a chosen number of points on the boundary. As the potentials due to these charges satisfy Laplace's or Poisson's equation inside the space under consideration, the solution is unique in that space.

This method is used by Abou-Seada and Nasser [76],[77]

and is considered suitable for the work in this thesis, since it is reasonably simple and gives good accuracy. The calculation obtained in this work can be conveniently compared with their results for a similar type of electrode system [76].

3.2.1 Charge Simulation Technique

The electrode system used in this analysis comprises a hemispherically capped point electrode and a plane electrode. By using the image of the point electrode with the plane acting as a mirror, Abou-Seada and Nasser, in their work [76], substituted the point-to-plane system with a point-to-point system. They assumed the permittivity of the medium is constant and the potential difference between the electrodes is unity. The co-ordinates of any point in a cylindrical co-ordinate system can be described by r and z because of symmetry with respect to the z axis, as shown in Fig. 3.1.

The point electrode is represented by a point charge located at the centre of the hemispherical portion of the electrode and a set of semi-infinite line charges along the axis of the cylindrical portion. The potential V at any point (r,z) is:

$$V(r,z) = Q_p \cdot P(r,z) + \sum_{j=1}^n Q_j \cdot R(r,z ; A_j) \quad (3.1)$$

where

Q_p : total point charge

Q_j : charge per unit length of any line charge
of the n line charges.

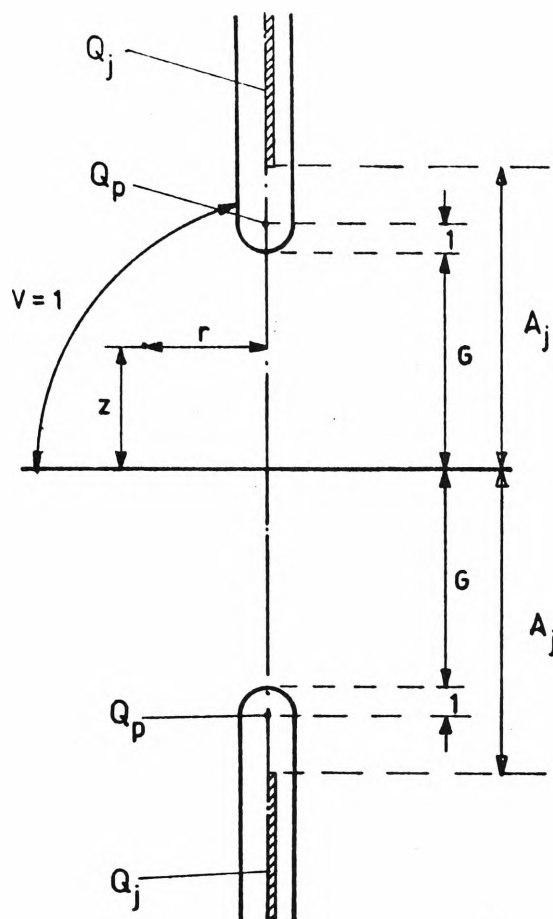


FIG. 3.1.a. DIAGRAM OF HEMISPHERICALLY CAPPED CYLINDER-TO-PLANE ELECTRODE SYSTEM WITH IMAGE OF CYLINDRICAL ELECTRODE

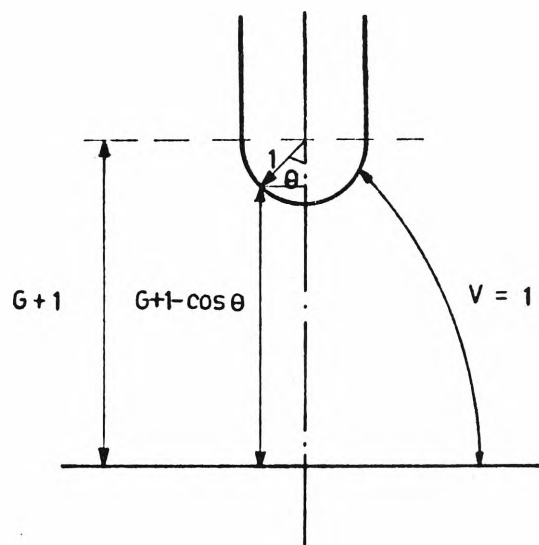


FIG. 3.1.b. COORDINATES AS FUNCTIONS OF ANGLE θ

$$P(r, z) = \frac{1}{\sqrt{r^2 + (G+1-z)^2}} - \frac{1}{\sqrt{r^2 + (G+1+z)^2}}$$

and

$$R(r, z ; A_j) = \ln \left(\frac{A_j + z + \sqrt{r^2 + (A_j + z)^2}}{A_j - z + \sqrt{r^2 + (A_j - z)^2}} \right)$$

where

G : ratio of gap length to point radius; d/R ,

this is also referred to as Gap Ratio.

The electric field at any point can be obtained from

$$E(r, z) = -\text{grad}.V(r, z)$$

$$= - \left[\frac{\partial}{\partial r} V(r, z) \cdot \hat{r} + \frac{\partial}{\partial z} V(r, z) \cdot \hat{z} \right]$$

where

\hat{r} , \hat{z} are the unit vector in the radial and axial directions respectively.

By using equation (3.1), this can be written

$$\begin{aligned} E(r, z) = & - \left\{ \left[Q_p \cdot \frac{\partial}{\partial r} P(r, z) + \sum_{j=1}^n Q_j \cdot \frac{\partial}{\partial r} R(r, z; A_j) \right] \cdot \hat{r} \right. \\ & \left. + \left[Q_p \cdot \frac{\partial}{\partial z} P(r, z) + \sum_{j=1}^n Q_j \cdot \frac{\partial}{\partial z} R(r, z; A_j) \right] \cdot \hat{z} \right\} \end{aligned} \quad (3.2)$$

Boundary Conditions

The boundaries of the point electrode are the cylindrical shaft and the hemispherical tip. The plane surface of the second electrode is the third boundary.

The potential of any point on the cylindrical portion of the boundary is assumed equal to the unit point potential. This is done by selecting several points along the surface of the point electrode and substituting them in (3.1), thus:

$$V(1, z_i) = 1 \quad \text{for} \quad z_i \geq G+1$$

The potential along the hemispherical portion of the boundary is also assumed equal unity by setting the potential at point $(r = 0, z = G)$ equal to unity. In order to ensure a unit equipotential surface coinciding with the hemispherical part of the electrode, the first and even derivatives of the potential $V(0, G)$ with respect to the angle θ , are set equal to zero.

The potential of any point on the plane is equal to zero. This condition is automatically satisfied by image charges.

From the calculations obtained with different sets of values of z_i and A_j , they selected the values summarised in Table 3.1, with which they claimed to obtain an error of less than 2% in comparison with the measurement utilizing an electrolytic tank.

z_i	(G+1)	(G+2)	(G+15)	(G+40)	(G+140)	(G+440)			
A_j	(G+1)	(G+1.1)	(G+1.2)	(G+1.5)	(G+2)	(G+10)	(G+25)	(G+90)	(G+240)

TABLE 3.1 VALUES OF z_i AND A_j SELECTED FOR THE CALCULATION OF FIELD STRENGTH [76].

3.2.3 Results

The above technique is applied in this work to calculate the field strength of point-to-plane gap for gap ratio varying from 50 to 800.

The validity of the charge simulation technique was tested by modifying some of the values of z_i and A_j . The results indicate a close agreement between the calculated and actual potential on the boundary as long as A_j is selected

in increasing values and within the range of z_i . In order to illustrate this point, a sample of the computation of field strength for a gap length of 3 cm and point electrode radius of .03 cm is tabulated in Table 3.2 in which the values of A_j and z_i are varied. It can be seen that the calculated value of the potential at the boundary point is very close to unity for the first four variations and the change of potential at points further away from the main axis is consistent. When $A(2)$ is set equal to $(G+1)$, its value is the same as $A(1)$, the boundary condition is not satisfied and the potential at other points changes in a sporadic manner. For this reason, in the following calculations, the values of $A_{(j)}$ and $Z_{(i)}$ are selected according to Table 3.1.

The calculated potential along the surface of the cylindrical portion of the cylinder is summarised in Table 3.3 for normalised distance measured from the plane electrode varying from 101 to 130. It indicates a consistent agreement with the boundary condition required for this part of the point electrode.

The cathode field intensity per unit potential is calculated for three different point radii and gap length of 1-11 cm, the results are plotted in Fig. 3.2. It is of interest to note that the cathode field intensity depends insignificantly on the gap length or the point radius, but is a function of their ratio only. This can be seen in Fig. 3.3 which is a plot of cathode field strength per unit potential against the gap ratio, the results are obtained by comparing results of the same gap ratio in Fig. 3.2.

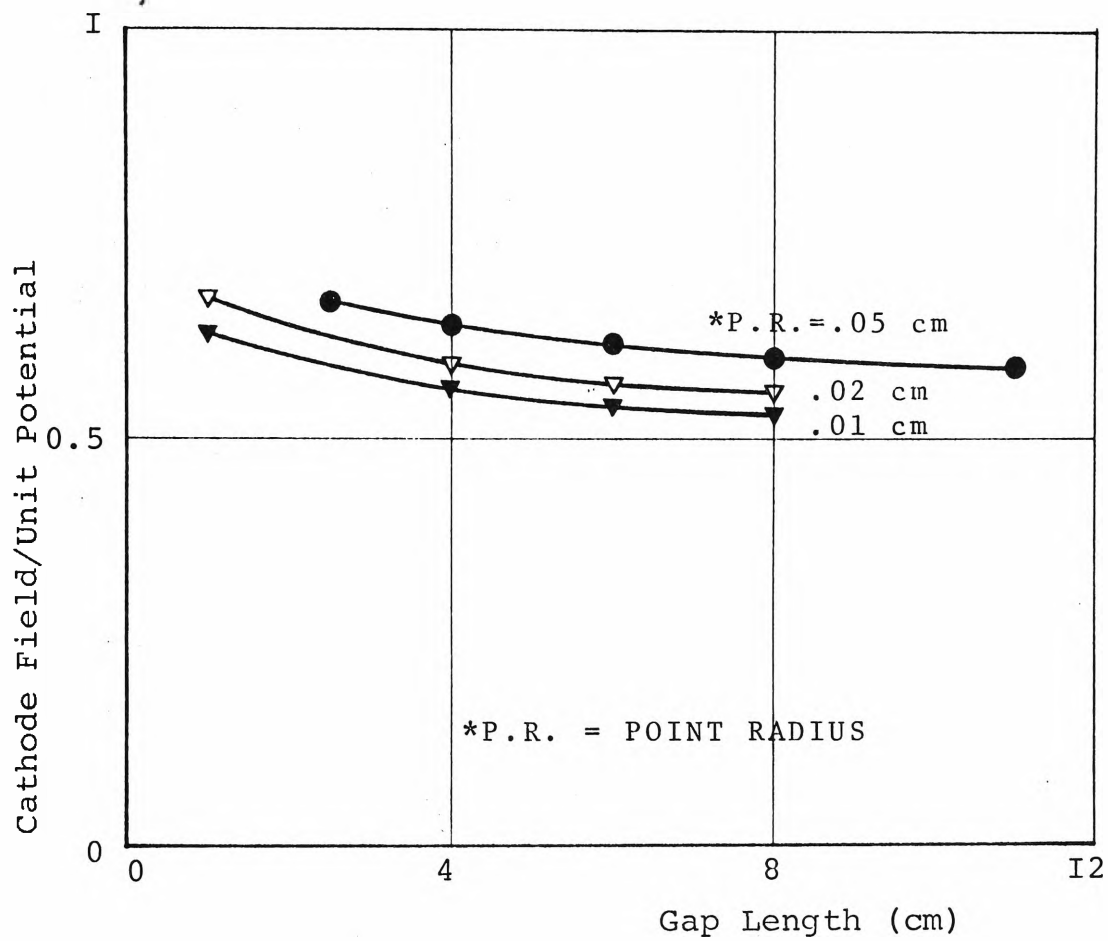


FIG. 3.2

CATHODE FIELD INTENSITY per UNIT
POTENTIAL VERSUS GAP LENGTH.

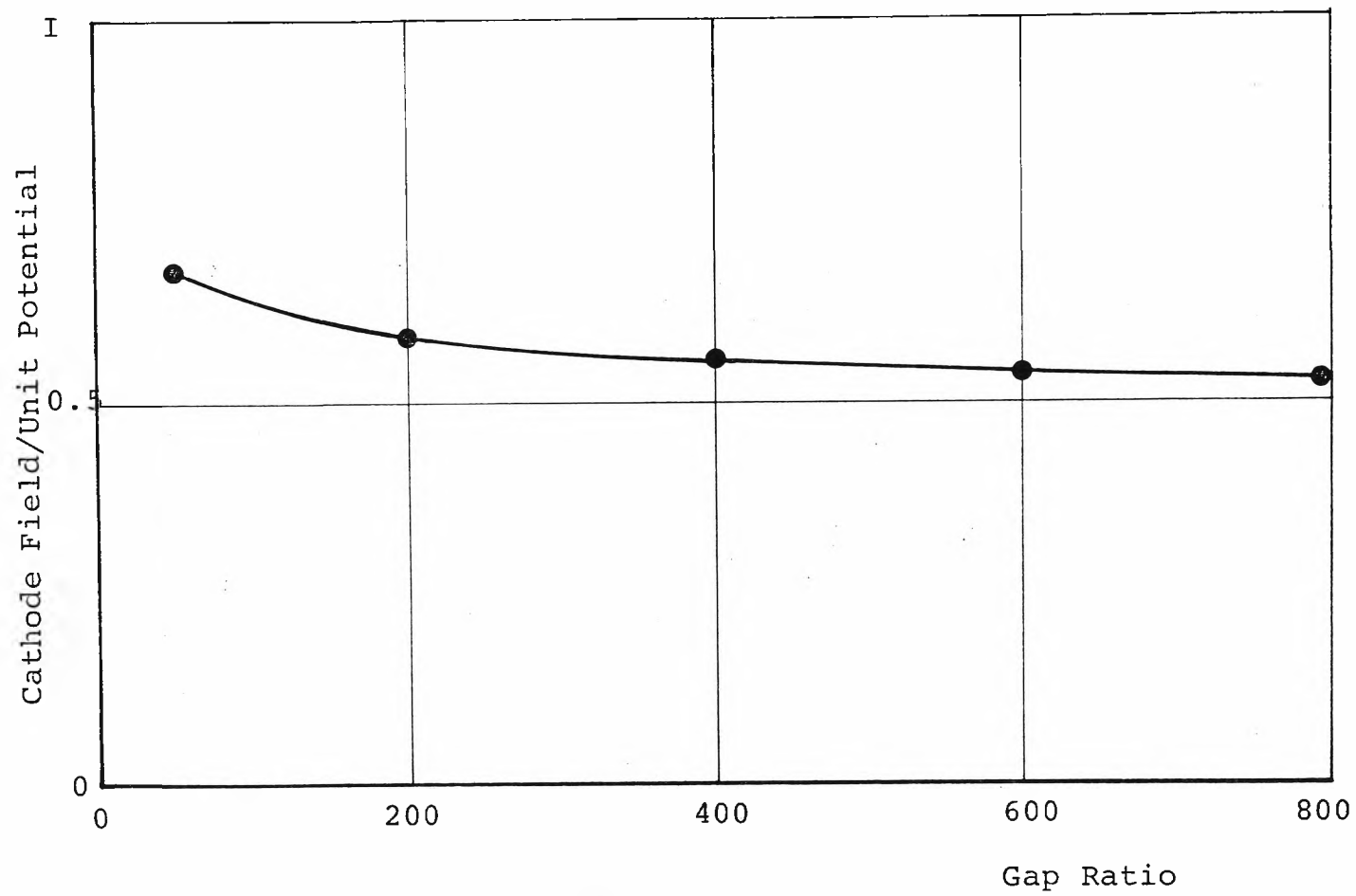


FIG.3.3 CATHODE FIELD INTENSITY per UNIT POTENTIAL VERSUS GAP RATIO.

	Normalised Radial Distance	Axial Field	Radial Field	Potential
A(6) = G+10	0	.626279	0	1.00008
	.2	.588966	-.117456	.987939
	.4	.497379	-.196498	.955731
A(6) = G+15	0	.629273	0	1.0001
	.2	.591794	-.11802	.987911
	.4	.499771	-.197455	.955454
A(9) = G+139	0	.629035	0	1.00009
	.2	.591567	-.117975	.987929
	.4	.499588	-.197377	.955558
Z(7) = G+339	0	.651179	0	1.00006
	.2	.612405	-.122131	.987468
	.4	.517197	-.20435	.953888
A(8) = G+1	0	.632654	0	.958734
	.2	.601501	-.119805	.695491
	.4	.512158	-.19977	.78496

Table 3.2 DEPENDENCE OF CALCULATED RESULTS ON THE
SELECTION OF A(_j) and Z(_i). NORMALISED
DISTANCE MEASURED FROM PLANE, G = 100

Value of G	Potential
101	1.00007
102	1.00011
103	1.00448
104	.997334
105	1.00014
106	1.00601
107	1.01079
108	1.01493
109	1.01325
110	1.00703
115	1.00009
120	1.00551
125	.997321
130	.990475
Gap Length = 3 cm Gap Ratio = 100 Point Radius = .03 cm	

Table 3.3 CALCULATED UNIT POTENTIAL ALONG THE
BOUNDARY OF POINT ELECTRODE.

The actual cathode field strength under space charge free condition can thus be estimated at any applied voltage

$$E = E_n \cdot \frac{V}{R} \quad (3.3)$$

where E = cathode field strength at voltage V
 E_n = calculated cathode field strength at unit potential
 R = point electrode radius

If $V = V_o$; the corona onset voltage then the onset cathode field strength can be found by using the above expression and the curve in Fig. 3.3.

3.3 Corona Onset Voltage

3.3.1 Introduction

There has been many attempts to determine the critical field strength at the surface of the highly stressed conductor at the onset of corona. The expressions obtained mostly from experimental investigation and on a smaller proportion from theoretical studies.

The well-known empirical formula originally derived by Peek [78] and similar expressions proposed by other workers [79], [80], have the general form

$$\frac{E_o}{\delta} = K1 + \frac{K2}{\sqrt{\delta r}}$$

where δ is the relative air density, r is the radius of conductor and $K1$, $K2$ are experimentally determined constants.

This equation has recently been extended to cover various electrode configurations [81] and modified to arrive

at a more accurate onset field strength [82].

Theoretical studies are based mainly on the application of the Townsend breakdown theory to derive the condition for onset. Loeb established the criterion for the onset of positive burst pulse corona, his derivation is based on the streamer theory of breakdown [12]. Alexandrov made a detailed analysis of negative D.C. corona onset [83]. An approximate theoretical study of the electric field within the D.C. corona layer has been made by Kapsow [84], the negative ion space charge was roughly estimated since no data on electron attachment was available. Sarma and Janischewskyj analysed the distribution of the electric-field in the ionisation layer of a D.C. corona discharge under equivalent steady state conditions. The criterion for corona onset is analysed on the basis of the Townsend theory. Their results indicate the theoretical corona onset field strengths are comparatively insensitive to changes in the value of the appropriate secondary-ionisation coefficient [85].

Recently, Khalifa et al. have calculated the theoretical onset field strength at the cathode surface for single conductor-to-plane and coaxial cylinder systems [86]. The criterion of the corona onset is based mainly on the Townsend theory with modification made to suit the condition of corona onset in non-uniform field. The transition from a non self-sustained discharge into a self-sustained one is determined by the availability of secondary electron emitted from the cathode. This is somewhat different from the condition in uniform field where the Townsend's criterion is attained when the conduction current increases rapidly to

infinity. This method is considered as more suitable for the case of negative corona, since the steady state assumed in Sarma et al 's method is only valid for pulseless corona discharge in which the continuity equation is assumed for an average condition in the corona layer. The following criterion is arrived at following a similar approach used by Khalifa's et al, with appropriate assumptions being suggested to represent the discharge process closer to physical observations.

3.3.2. Theoretical Analysis

It has been known that the negative corona discharge is initiated by electrons that are sufficiently accelerated in the vicinity of the cathode to produce avalanches. The electron avalanches extend away from the cathode to the low field region where electrons attach to neutral gas molecules and form negative ions. Positive ions left behind in the avalanche are attracted to the cathode and neutralised on arrival. Excited molecules created by the ionising collisions give up their excess energy in the form of photons which are partly absorbed by the gas. This absorption leads to the photo-ionisation of gas molecules. Photons that reach the cathode and positive ions produce the secondary electrons which maintain the discharge. This process is in contrast to the positive corona discharge in which the self-sustained discharge is maintained by secondary electrons produced by photoionisation of the gas molecules. It is, therefore, reasonable to apply the Townsend theory of breakdown in uniform gap to the derivation of the criterion for the onset of corona in non-uniform field in this case.

The following assumptions are made:

- (i) The photoionisation of gas molecules makes the major contribution to the growth of the avalanches.
- (ii) The photoionisation coefficient is constant
- (iii) The effect of negative ion space charge is negligible at the onset of corona.

Consider a hemispherically-capped cylinder-to-plane system in a cartesian co-ordinate system as shown in Fig. 3.4, for convenience sake the terminology introduced by Herceg [40] is used here to identify the regions between the electrodes. They are defined as:

- (a) The ionisation region extending from the cathode to the boundary where the coefficient of ionisation by collision is equal to the attachment coefficient.
- (b) The buffer region extending from the end of the ionisation region to the place where 99.9% of the electrons get attached to neutral molecules.
- (c) The transport region occupying the rest of the air gap.

The numbers of electrons created by ionising collisions, photoionisation of gas molecules and lost by attachment when the avalanche advances over a distance dx are

$$dn_i = n\alpha dx$$

$$dp = n\zeta dx$$

$$dn_a = -n\beta dx$$

where α, ζ, β are the coefficient of ionisation by collision, the coefficient of photoionisation and the attachment coefficient respectively.

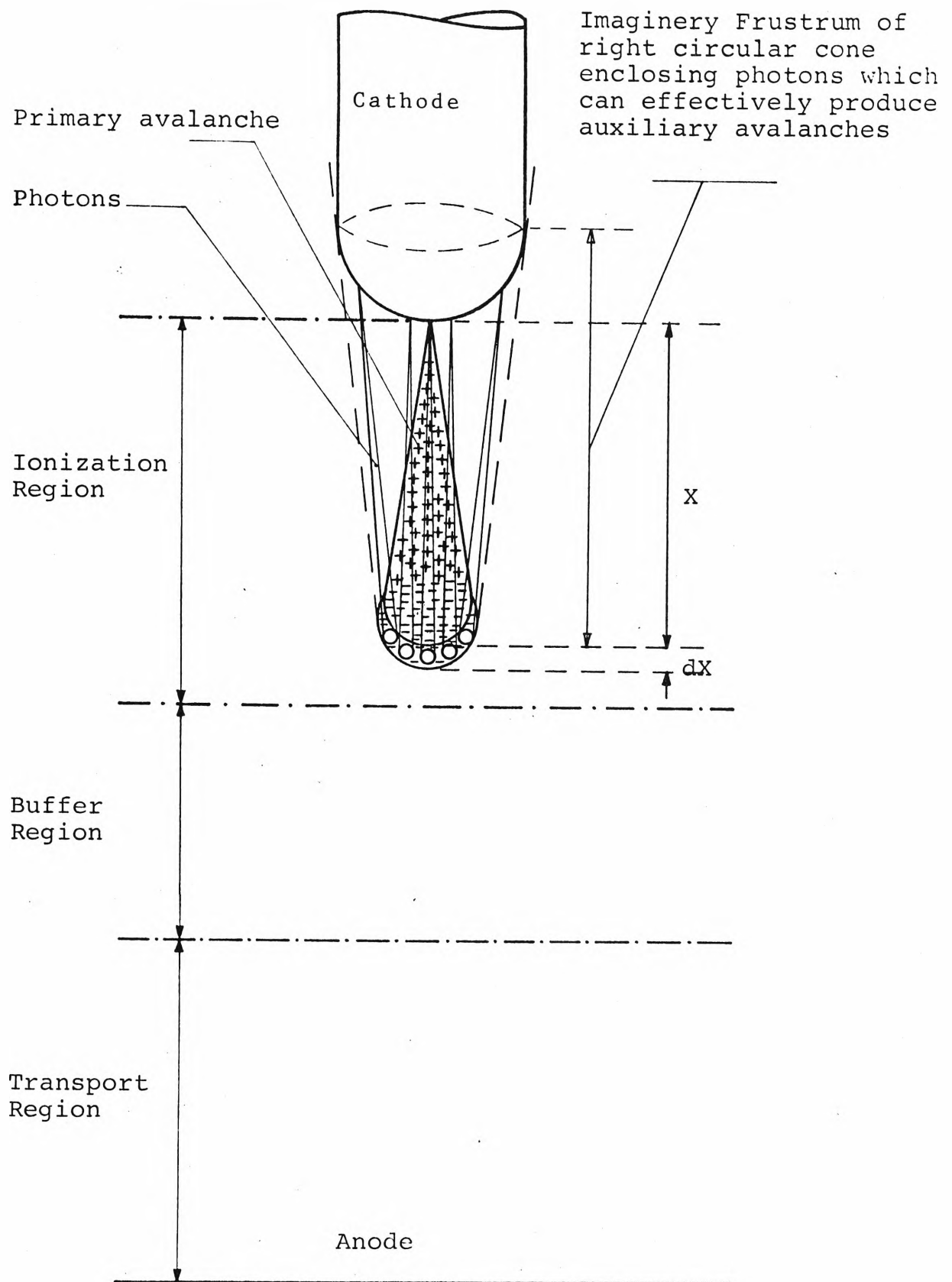


FIG. 3.4 SCHEMATIC DIAGRAM OF THE REGIONS AND THE PROGRESS OF AVALANCHE IN NEGATIVE CORONA DISCHARGE

The total number of electrons created is thus equal to

$$dn(x) = n(\alpha - \beta + \zeta) dx \quad (3.4)$$

(a) The photoelectric emission of secondary electrons

Integrate (3.4) and assume that the number of electrons starting from the cathode is n_0 , then

$$n(x) = n_0 \cdot \exp\left(\int_0^x (\alpha - \beta + \zeta) dx\right)$$

The $n(x)$ number of electrons can be considered to enter a unit area of a cylindrical slab per second, located at distance x from the cathode, having a thickness dx . The number of excited states produced by collisions within the slab is

$$\begin{aligned} dn'(x) &= n(x) \cdot \theta \cdot dx \\ &= n_0 \theta \exp\left(\int_0^x (\alpha - \beta + \zeta) dx\right) \end{aligned}$$

Each excited state will emit at least one photon when it returns to the ground state. The number of photons emitted in slab of thickness dx is thus:

$$dn'_p(x) = dn'(x)$$

Part of these photons is absorbed by the surrounding gas, the number of photons surviving the absorption process is:

$$e^{-\mu x} \cdot dn'_p(x) = e^{-\mu x} \cdot n_0 \theta \exp\left(\int_0^x (\alpha - \beta + \zeta) dx\right)$$

where μ is the coefficient of absorption.

These surviving photons scatter in all directions and only those which arrive at the cathode will contribute to the production of the secondary electrons. Thus the number of

electrons created by the photoelectric emission at the cathode is:

$$\begin{aligned} dn_p(x) &= g(x) \cdot \gamma \cdot e^{-\mu x} dn'_p(x) \\ &= g(x) \cdot \gamma \cdot e^{-\mu x} n_o \theta \exp\left(\int_0^x (\alpha - \beta + \zeta) dx\right) \end{aligned}$$

where $g(x)$ is the geometry factor, γ is the probability of photoelectric emission at the cathode.

The total number of secondary electrons emitted by photoelectric effect as the avalanche traverses the ionisation zone is

$$\begin{aligned} n_p &= \int_0^{x_o} dn_p \cdot dx \\ \text{or } n_p &= \int_0^{x_o} g(x) \cdot \gamma \cdot e^{-\mu x} n_o \theta \cdot \exp\left(\int_0^x (\alpha - \beta + \zeta) dx\right) dx \end{aligned} \quad (3.5)$$

by replacing θ by $f\alpha(x)$ and then $f\gamma$ by γ_p the coefficient of photoelectric emission, equation (3.5) can be written:

$$n_p = n_o \gamma_p \int_0^{x_o} g(x) \cdot e^{-\mu x} \alpha(x) \exp\left(\int_0^x (\alpha - \beta + \zeta) dx\right) dx \quad (3.6)$$

(b) The secondary emission by positive ion bombardment

The number of electrons and positive ions produced in the gas by ionising collisions is equal to $(n - n_o)$. The positive ion distribution is most dense along the axis of symmetry, they arrive at the cathode and produce the secondary electrons by bombarding the cathode. The number of electrons created by this process is

$$n_i = \gamma_i (n - n_o)$$

which can be written as:

$$n_i = \gamma_i n_o \left[\exp \int_0^{x_o} (\alpha - \beta + \zeta) dx - 1 \right] \quad (3.7)$$

where γ_i is the coefficient of secondary emission by impact.

(c) The onset condition

The total number of secondary electrons is obtained by summing (3.6) and (3.7):

$$n_s = n_p + n_i$$

or

$$n_s = n_o \left[\gamma_p \int_0^{x_o} g(x) e^{-\mu x} \alpha(x) \exp\left(\int_0^x (\alpha - \beta + \zeta) dx\right) dx + \gamma_i \left(\exp\left(\int_0^{x_o} (\alpha - \beta + \zeta) dx\right) - 1\right) \right] \quad (3.8)$$

The discharge becomes self-sustained if this number of electrons equals that emitted from the cathode at the beginning

$$n_s \geq n_o$$

This condition is equivalent to:

$$\gamma_p \int_0^{x_o} g(x) \cdot e^{-\mu x} \alpha(x) \cdot \exp\left(\int_0^x (\alpha - \beta + \zeta) dx\right) dx + \gamma_i \left(\exp\left(\int_0^{x_o} (\alpha - \beta + \zeta) dx\right) - 1\right) \geq 1 \quad (3.9)$$

It can be seen that the derivation is based on the application of the Townsend's theory into a non-uniform field but the criterion is arrived at by an approach similar to that which is used in the Streamer theory of breakdown (c.f. Section 2.3). The approach which has been commonly used in Townsend's criterion of breakdown for uniform gap cannot be applied in non-uniform gap since it leads to different expressions which do not represent truly the physics of negative corona discharge. This can be explained as follows.

It can be shown that the following two expressions may be obtained by direct application of the Townsend's Theory [19]

$$n_p = n_o \frac{\exp\left(\int_0^{x_o} (\alpha - \beta + \zeta) dx\right)}{1 - \gamma_p \int_0^{x_o} e^{-\mu x} g(x) \alpha(x) \exp\left(\int_0^x (\alpha - \beta + \zeta) dx\right) dx} \quad (3.10)$$

for the number of secondary electrons emitted by the photo-electric effect, and

$$n_i = n_o \frac{\exp\left(\int_0^{x_o} (\alpha - \beta + \zeta) dx\right)}{1 - \gamma_i \left(\exp\int_0^{x_o} (\alpha - \beta + \zeta) dx - 1\right)} \quad (3.11)$$

for secondary emission by positive ion impact.

The denominators of equations (3.10) and (3.11) resemble equations (3.6) and (3.7). However an expression similar to (3.9) cannot be obtained since the current in this case does not increase to infinity.

3.3.3 Data used in numerical calculations

The coefficient of ionisation by collision can be expressed as a function of applied electric field strength and pressure, it is of the form

$$\frac{\alpha}{p} = A \cdot \exp(-Bp/E) \quad (3.12)$$

A and B are constants determined experimentally. Comparison made between α in non-uniform geometry to α in uniform field shows that their ratio is between 0.8 and 1.1 for air at atmospheric pressure [87]. It is considered satisfactory to use data measured for uniform field in this calculation. The results obtained by Harrison and Geballe [88] are used for $E/p \leq 60$ V/cm.Torr. and those obtained by Masch [89] and Sanders [90] are used in the

range $60 < E/p \leq 240$ V/cm.Torr. In the calculation, the values of A and B are found to fit curves shown in Fig. 3.5 and 3.6, in six ranges of value. The data on electron attachment is approximated by the quadratic equation

$$\frac{\beta}{p} = a + b(E/p) + c(E/p)^2$$

where a,b,c are constants determined by curve fitting.

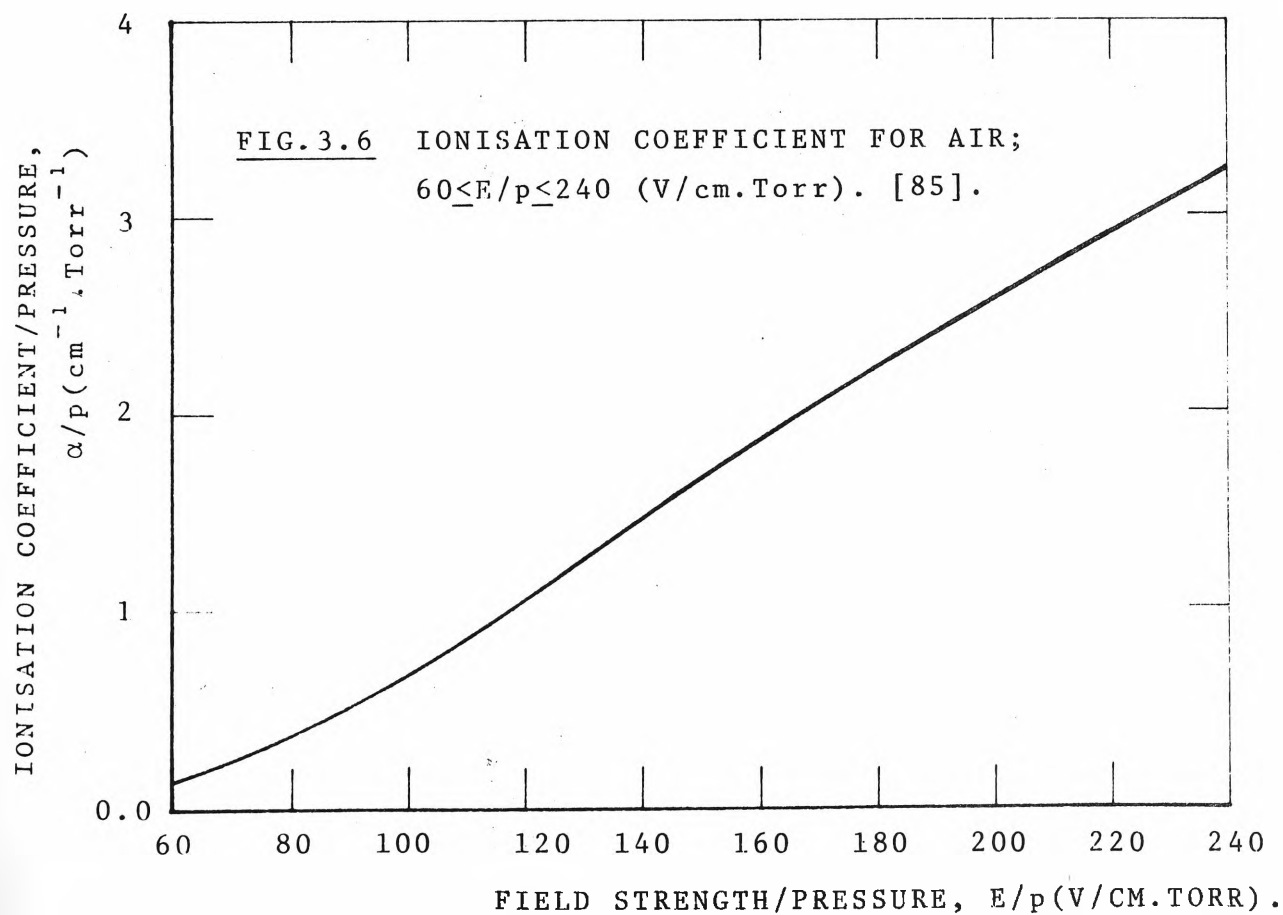
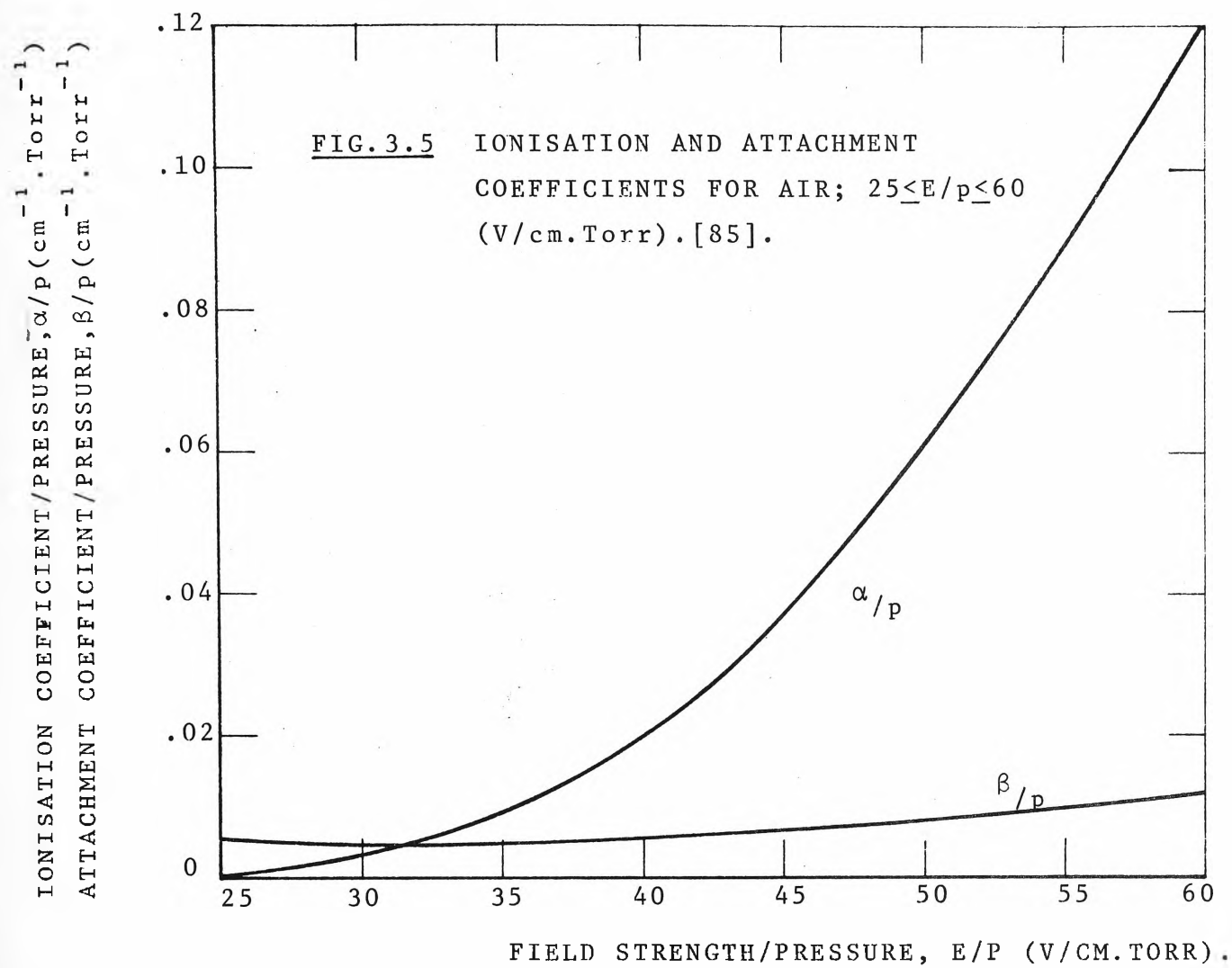
The absorption coefficient μ for photon in air may have a large range of values, it has been measured in air at atmospheric pressure $\mu \approx 6\text{cm}^{-1}$ [91]. In this calculation 5cm^{-1} is selected for μ and the coefficient of photoionisation ζ .

The coefficients of secondary emission depend on a number of factors, such as the conductor material, surface condition, composition of the gas surrounding the conductor etc. Measurements of γ under laboratory conditions show that it does not vary significantly for a small variation in the value of E/p [91]. It is plausible to assume that γ is constant in the calculation of corona onset field strength for various gap ratios. The values of the coefficients of secondary emission by photon γ_p and by positive ion impact γ_i are selected equal to 5×10^{-4} and 10^{-3} respectively [12].

3.3.4 Justification of the theoretical model

The above analysis is used to calculate the critical field strength at the cathode of a point-to-plane system. The relationship between α and E as expressed in equation (3.12) means that when equation (3.9) is satisfied, the onset field strength can be found.

Assuming the avalanche advances along the axis of the electrode system and the axial field component is dominant



in creating a self-sustained discharge. The calculation is started by selecting an arbitrary value of the applied voltage from which the field strength is determined. The left hand side of equation (3.9) is then calculated by using available data and compared with unity. The integration is carried out by using trepezoidal rule with a step size of $1/\alpha$ in the ionisation region and $1/\beta$ in the buffer region. This selection of step-sizes is reasonable since they are the ionisation-free and attachment-free path lengths in the two regions, as the avalanche proceeds from the cathode to the low field strength area.

The calculated results are obtained for three point radii .01, .02 and .05 cm, and gap length varying from as short as 1 cm to 10 cm. The onset voltage depends little on the gap length as it is shown in Fig. 3.7, the dependence becomes less as the electrode radius decreases. The cathode field strength at onset is virtually independent of gap length and is a function of the electrode radius only, this is shown in Fig. 3.8. The relationship between onset voltage and the electrode diameter is plotted in Fig. 3.9. The results are compared with those measured by English [12] using a hemispherically capped cylinder-to-plane electrode system which has a ratio of gap length to electrode radius of 160. The validity of the theoretical model is proved by close agreement between the two results. As a further check, the calculated field strength at onset of negative corona is compared with that obtained by Bandel for a gap ratio of 160. From Bandel's results for a point radius of .019 cm and gap length of 3.1 cm [12], the measured onset voltage was 5 kV,

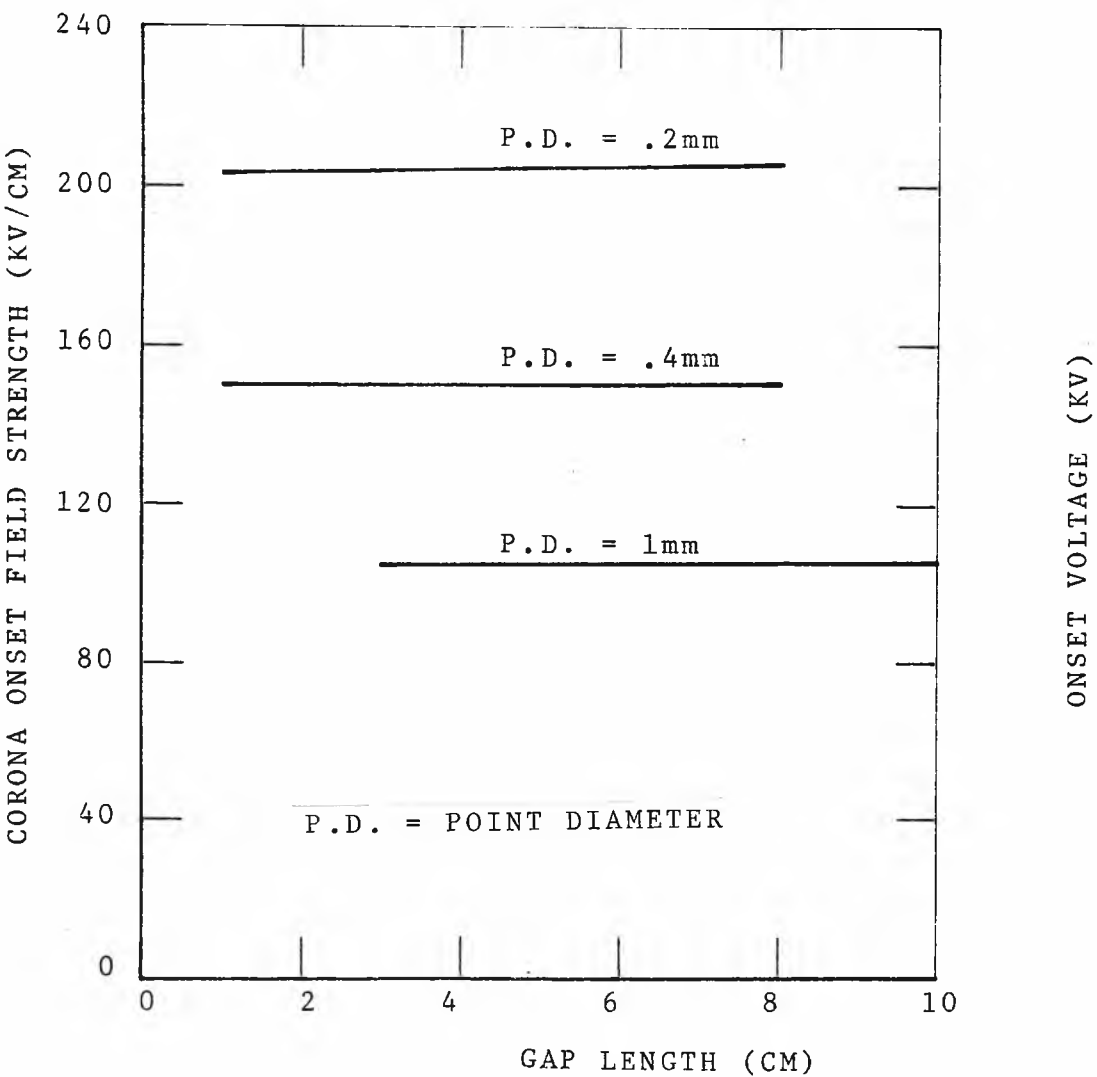


FIG. 3.8 CORONA ONSET FIELD STRENGTH
VERSUS GAP LENGTH.

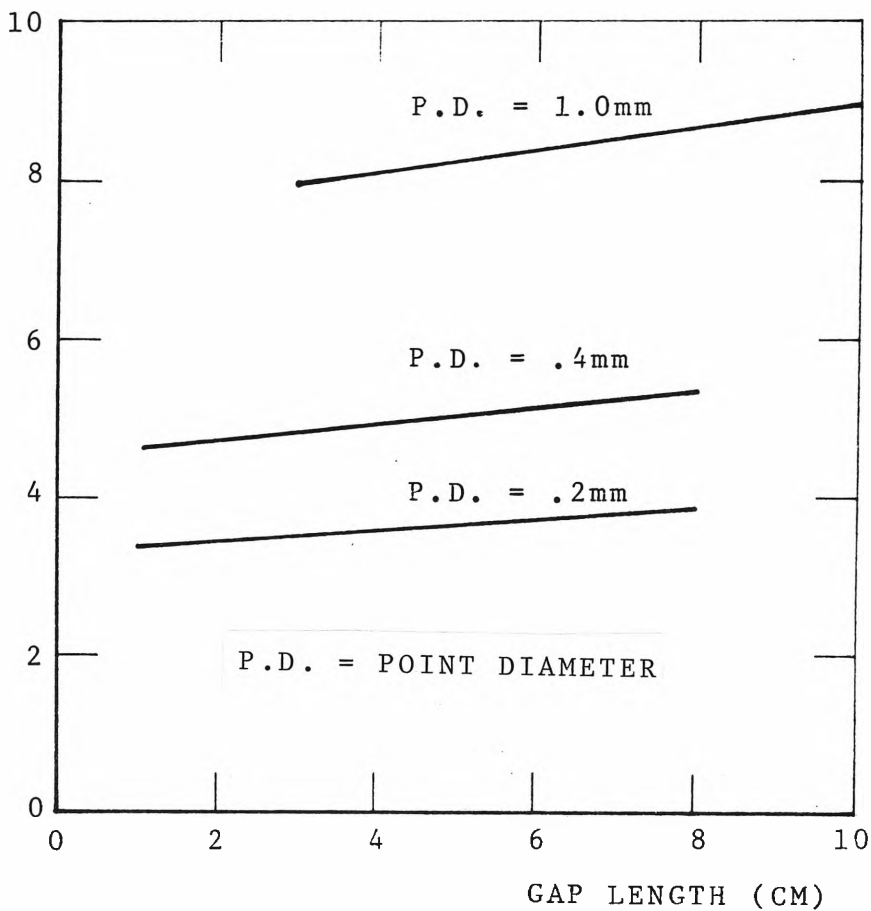


FIG.3.7 NEGATIVE CORONA ONSET VOLTAGE
 VERSUS GAP LENGTH.

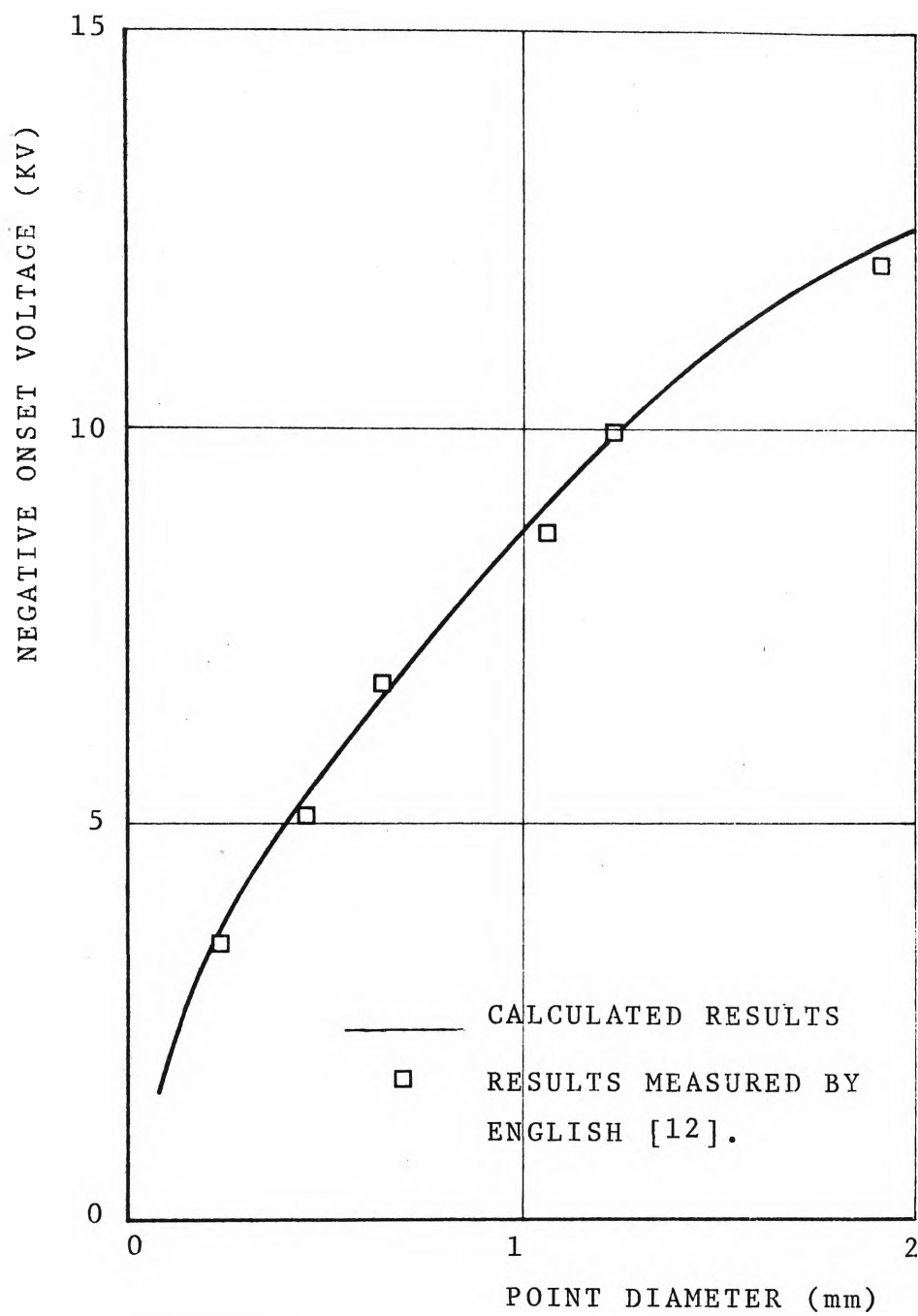


FIG.3.9 NEGATIVE CORONA ONSET VOLTAGE VERSUS POINT DIAMETER.

by using equation (3.3) the onset field strength is found to be 157 kV/cm, whereas the onset voltage and field strength as calculated by equations (3.9) and (3.3) are 5 kV and 153 kV/cm respectively, the difference between the two values of field strength is less than 3%.

3.3.5 Discussion

The onset field strength is plotted against the electrode diameter in Fig. 3.10. The shape of the curve indicates that as the discharge electrode gets smaller the critical field strength used to maintain a self-sustained discharge becomes larger. The independence of onset field strength on the gap length is not only restricted to the cathode surface but also extends to the ionisation and buffer regions as well. The ionisation region is defined as the space limited by the cathode surface and the location where the ionisation coefficient equals the attachment coefficient. The buffer region is limited by the boundary of ionisation region and the position where 99.9% of the generated electrons attach to neutral gas molecules. These regions are illustrated in Fig. 3.4. The distribution of field strength in the air space is shown in Fig. 3.11 for point radii of .01 cm , -.05 cm and gap length from 3 cm to 10 cm. For one electrode radius, all the points which correspond to the field strength at different locations for various gap lengths form one single curve which decreases exponentially with the distance from the cathode to the boundary of the buffer region. The width of ionisation and buffer regions is plotted against gap length in Fig. 3.12 and 3.13. It can be seen that the width of these regions is dependent on the electrode radius

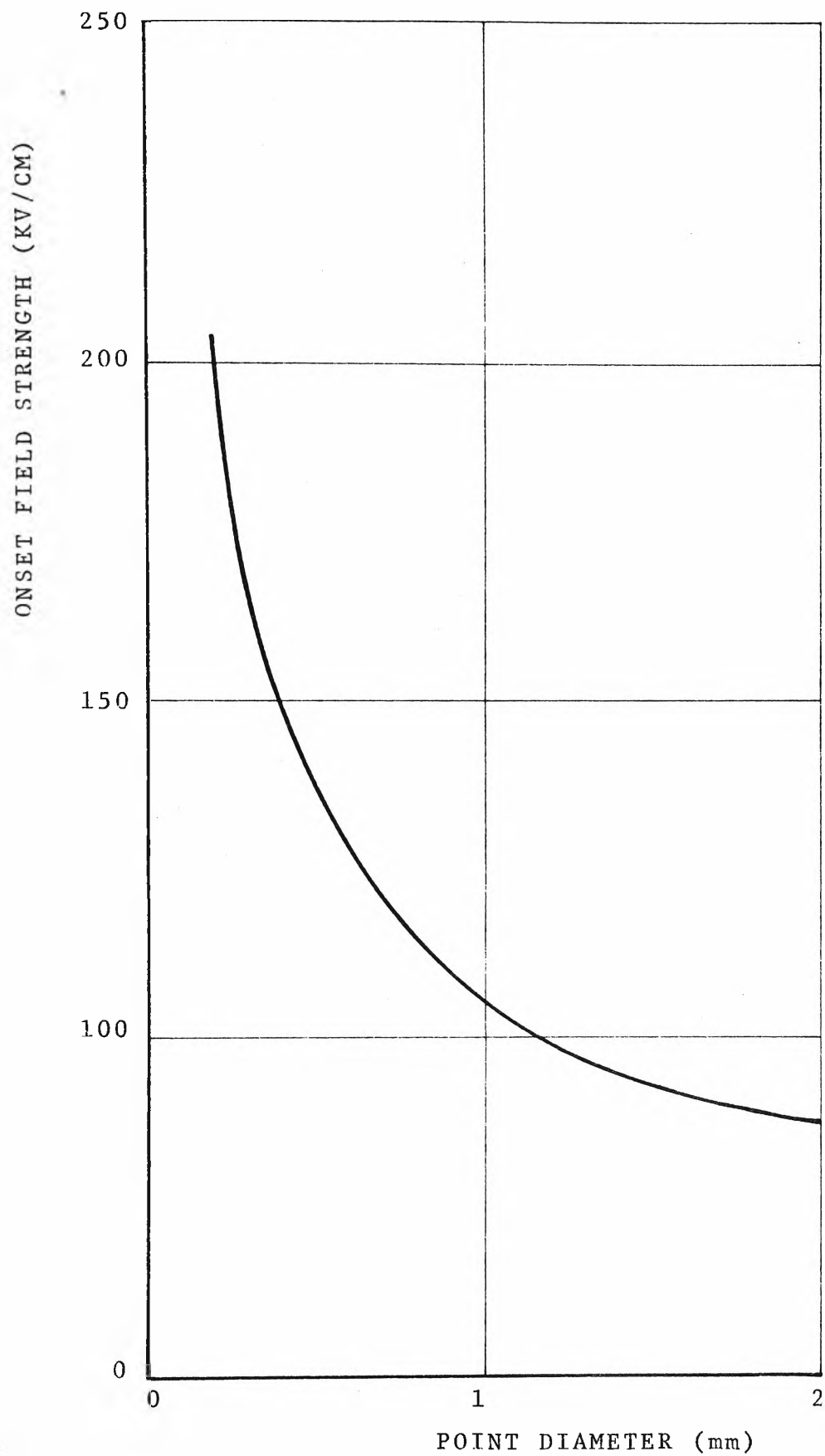


FIG. 3.10 NEGATIVE CORONA ONSET FIELD
STRENGTH VERSUS POINT DIAMETER.

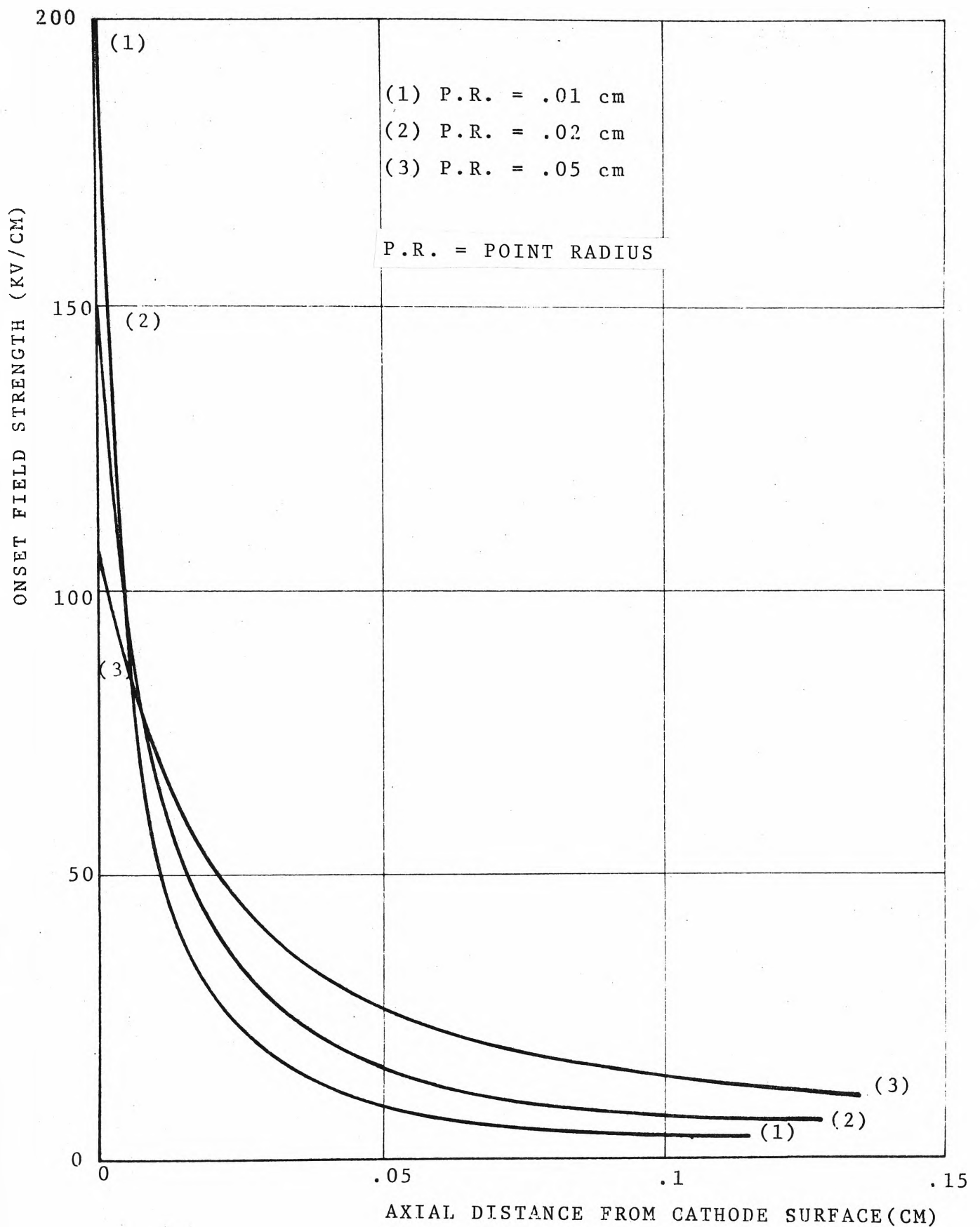


FIG. 3.11 DISTRIBUTION OF FIELD STRENGTH AT ONSET OF CORONA.

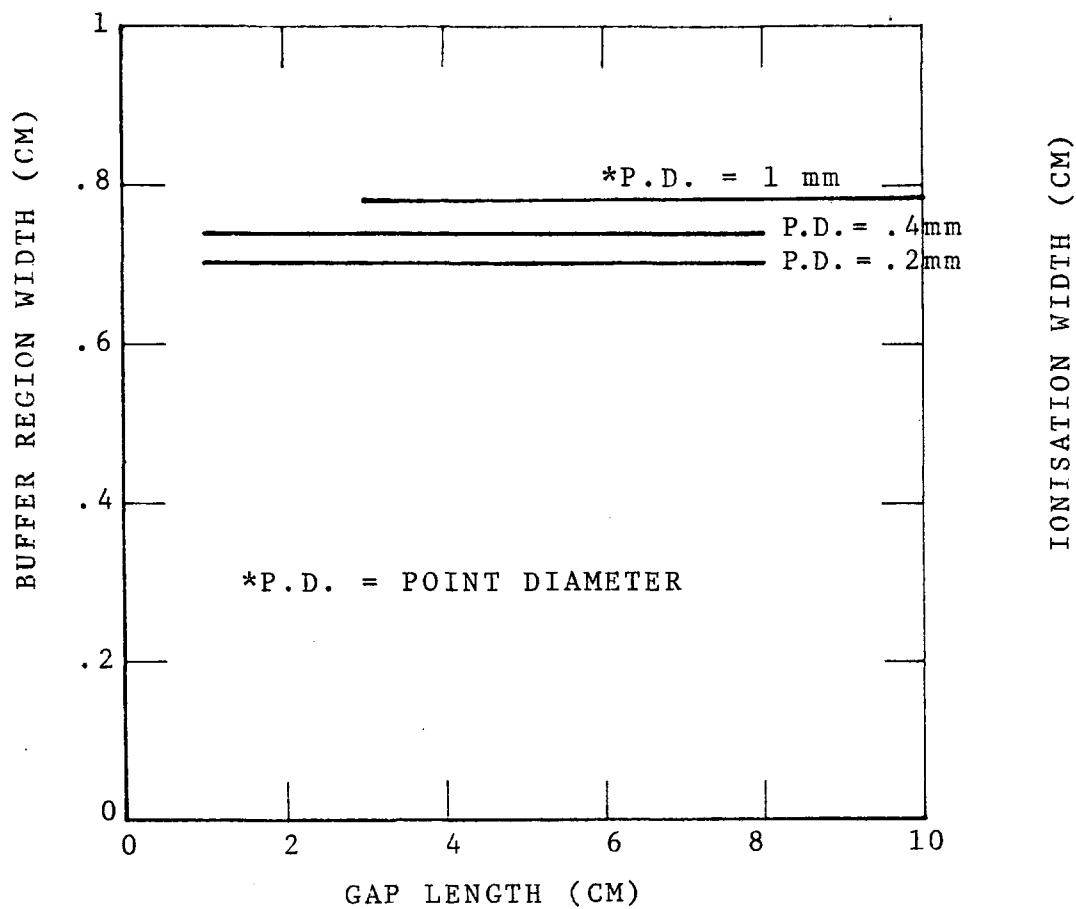


FIG. 3.13 BUFFER REGION WIDTH VERSUS
GAP LENGTH.

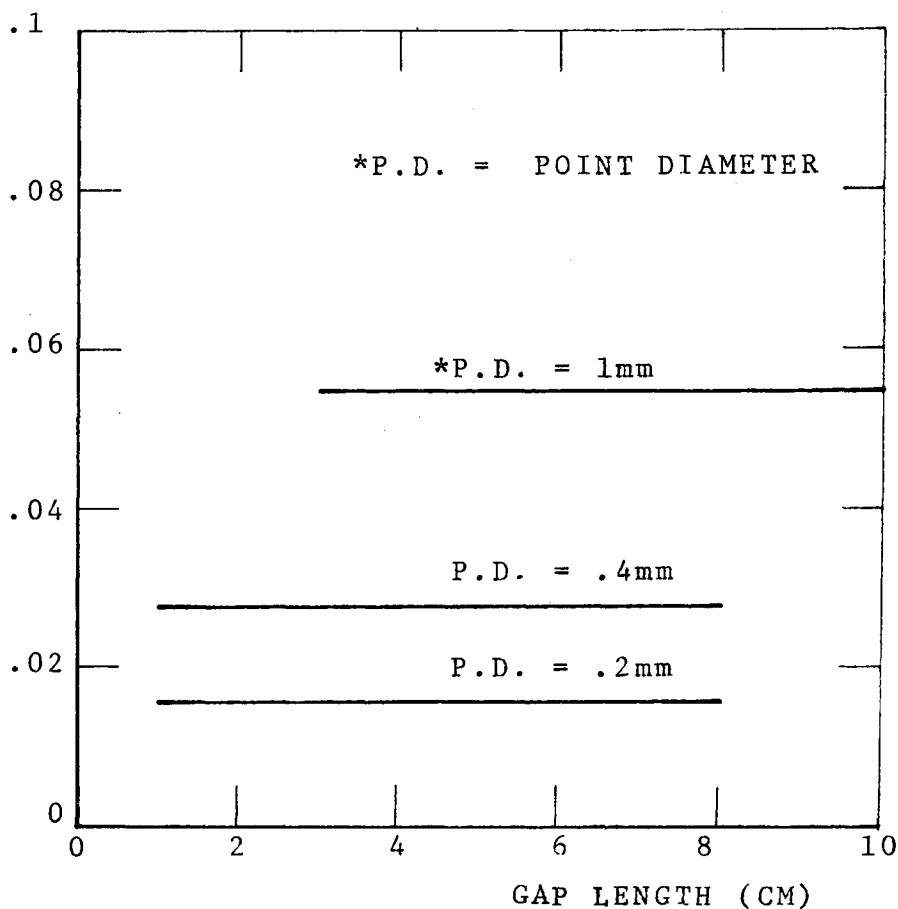


FIG. 3.12 IONISATION WIDTH VERSUS
GAP LENGTH.

only. The distribution of field strength in the vicinity of cathode (Fig.3.11) indicates the high field region is restricted to approximately one radius distance from the cathode surface. The smaller the point radius, the faster the field strength decreases. Fig. 3.14 is a plot of the width of ionisation and buffer regions which is normalised with respect to the point radius versus the electrode diameter. The curves indicate that while the ionisation process takes place over a region, the dimension of which is approximately independent of the size of the discharge electrode, the attachment of electrons to gas molecules requires a wider area which depends markedly on the electrode radius.

3.4 Corona Current Waveshape

3.4.1 Introduction

The corona current pulse has been observed by many workers, but only a few have attempted to obtain an analytical expression describing its waveshape.

Fletcher investigated the formative time lag of spark breakdown over a very short range from .05 to 50 nanoseconds. In his analysis, he applied the continuity equation in the high field region surrounding the highly stressed electrode to determine the critical avalanche size [92]. Heintz used these space charge equations to obtain a complete expression for a negative corona current pulse [93] neglecting the diffusion effects. Recently, Herceg used the same approach but assuming that the ionisation process can be described by a continuity equation for negative carriers in the buffer region, he arrived at the same expression [40].

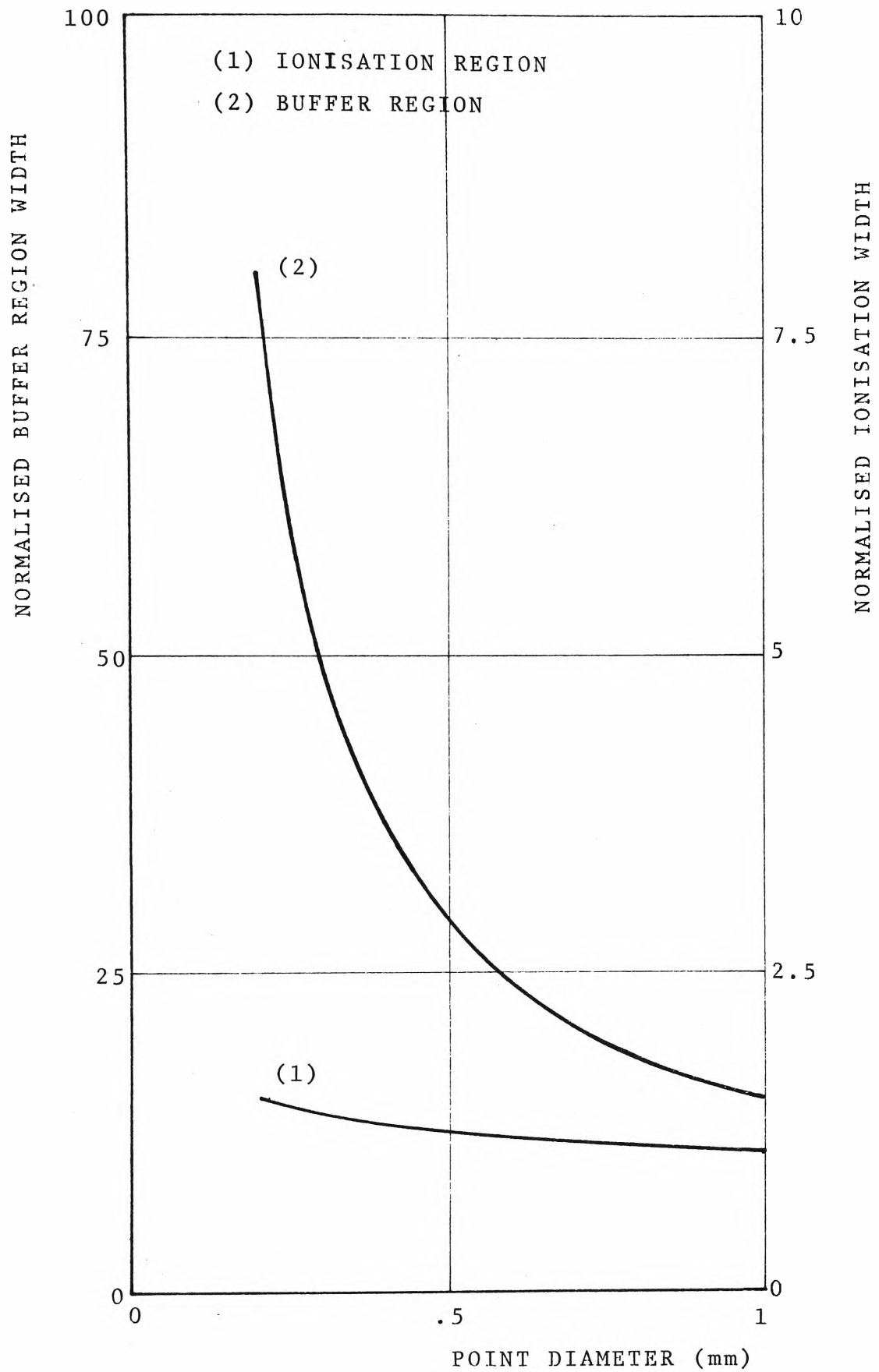


FIG. 3.14 NORMALISED BUFFER REGION WIDTH AND IONISATION WIDTH VERSUS POINT DIAMETER.

3.4.2 Calculation method

The numerical solution obtained in this part is based on the results obtained from the calculations of field strength distribution and the corona onset voltage as has been discussed. It is of interest to note that in the calculation of the corona onset voltage, when equation (3.9) is satisfied the number of negative ions formed in the buffer region is much too small to distort the cathode field strength, yet it marks the beginning of the self-sustained discharge. The negative corona current which was observed and studied by Trichel [67] is caused by the quenching effects of the negative ion space charge on the ionisation process. This indicates there must be a voltage difference between the two regions. Loeb and English discussed the relative starting potential of positive and negative coronas in their work [94]. They observed that a voltage difference exists between the onset of self-sustained discharge and the appearance of the first Trichel pulse. This value may range from 50 to 250 volts depending on circuitry, point diameter, triggering and so on. This point is checked in the theoretical study and the value which gives a convergent result is selected to provide a waveform which resembles the measured one. This selection does not impair the validity of the calculating method since it is chosen only as a priori condition.

The condition set by equation (3.9) implies that there must be at least one photoelectron to maintain the discharge at the end of one generation of avalanche at the onset of corona. At a few hundred volts above the threshold, the ionisation process will probably start in a similar fashion

for the first generation of avalanche, however equation (3.9) is satisfied while the first avalanche is still proceeding. This means there will be a second generation of avalanche and possibly some higher order generation of avalanche existing along the path of the first avalanche, the time delays are determined by the drift velocity of electrons moving from cathode to the position at which equation (3.9) is satisfied. The second and higher order generations of avalanche may in turn give rise to further ionising avalanches and the whole process is similar to the branching of a tree. A computation which covers the whole process would therefore be very complex and impossible. The calculation can be simplified without obscuring the true process to a great extent because of the following reasons:

- (i) The time required for equation (3.9) to be satisfied is less than one nanosecond and the time delays between generations of avalanche, therefore, can be safely assumed to be negligible.
- (ii) Due to the quenching effect of the negative ion space charge formed by the first generation of avalanche, the avalanches belong to higher order generation which may be diminishing rapidly and hence contribute little to the whole process of forming a complete corona current pulse.

In the following part, only the first generation of avalanche is considered as dominant in forming the corona current pulse and is called the primary avalanche. The subsequent avalanches created by the primary avalanche are called the secondary, third and so on avalanches. The

computation is carried out with the following assumptions:

- (i) One electron starts the primary avalanche at the cathode.
- (ii) All the photoelectrons created when the primary avalanche reaches the end of the ionisation zone are considered as if they are emitted from cathode simultaneously for the next avalanche.
- (iii) 99.9% of all electrons generated in one avalanche get attached to neutral molecules in the buffer zone.
- (iv) The recombination between electrons of one avalanche and the positive ions of the previous avalanches is negligible.
- (v) The axial components of the applied field, the fields of positive ion space charge, the electron space charge and the negative ion space charge are dominant in creating the ionising processes.

The integration of the left hand side of equation (3.9) is carried out in the same way as before. In the primary avalanche the effect of the space charge on the ionisation process is negligible. At the end of one avalanche, the results are stored in matrices that will be used to plot the current pulse. In the subsequent avalanches, the ionising collisions take place under the effects of positive and negative ion space charges. The distribution of positive ions and negative ions in the ionisation and the buffer regions are found. The computation process is ended when the netcathode field strength is less than the corona onset field intensity. The transit time of positive ions when

they move from the ionisation region to the cathode is determined. The time required for negative ion space charge to move sufficiently from the buffer region so that the cathode field strength is restored to its onset value is found and it is approximately equal to the Trichel pulse period. The instantaneous value of the corona current pulse is the sums of the instantaneous current components contributed by each avalanche and it can be expressed as

$$i(t) = \sum_{k=1}^N e \cdot n_k(x) \cdot \frac{v(x)}{d} \quad (3.13)$$

where e = the electronic charge

$n_k(x)$ = the number of electrons generated at position x for k th avalanche

$v(x)$ = the drift velocity of electron

d = the distance travelled by the avalanche.

Substitute $v(x) = K \cdot E(x)$ into equation (3.13) and one can obtain

$$i(t) = \sum_{k=1}^N e \cdot n_k(x) \cdot K \cdot \frac{E(x)}{d}$$

where K is the electron mobility, equal to $500 \text{ cm}^2/\text{Vsec}$ since in general, it is in the order of 200 or more times higher than those for ions [12].

3.4.3 Comparison of calculated and experimental results

The flow chart is attached in Appendix A. The program is computed by the UNIVAC 1106 computer with double precision format. From the graph plotted by the printer, the result is reproduced and compared with the experimental one as shown in Fig. 3.15. The calculated corona current pulse for a point radius of .05 cm, gap length of 4 cm, at voltage of

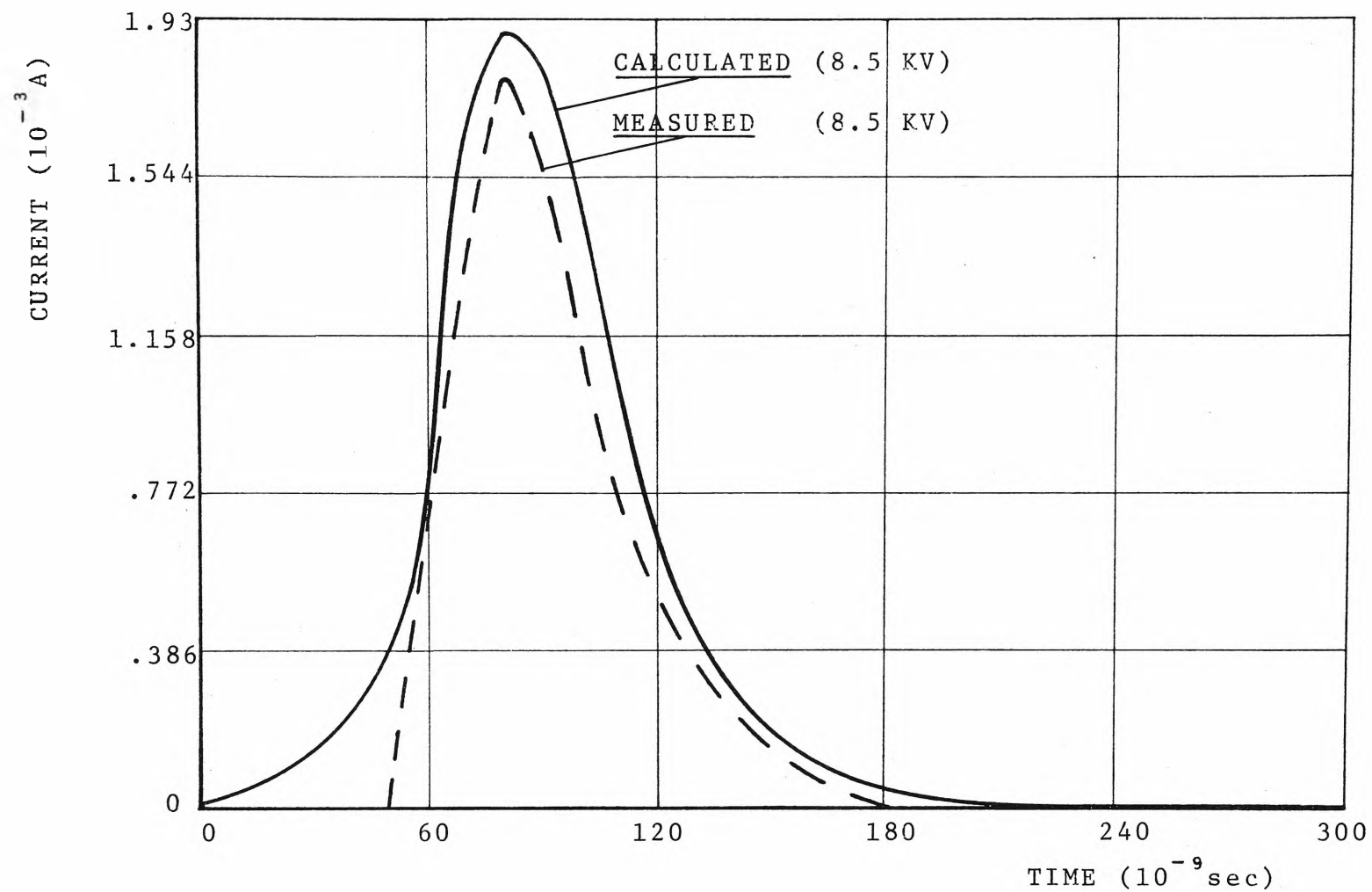


FIG.3.15 COMPARISON BETWEEN CALCULATED AND MEASURED
CORONA CURRENT PULSE.

8.5 kV is in close agreement with the measured pulse. The amplitude of the computed pulse is bigger than that of the experimental pulse by approximately 15%. The discrepancy is due to the limitation imposed by the response time of the oscilloscope, the selection of empirical data used in the calculation, the upset of the field strength distribution in the air gap caused by the measuring circuitry and the round off error of computation.

It can be seen that the model which is based on the Townsend's theory of breakdown produces reasonably good results. Other parameters obtained from the computation confirm some observations which were made by other workers, these are:

- 1) The potential difference between the threshold of self-sustained discharge and the onset of regular Trichel pulses is 300 volts [94] .
- 2) The number of electrons in the primary avalanche is in the order of 10^4 [12].
- 3) The number of electrons forming a Trichel pulse is in the order of 10^9 [12].
- 4) The number of negative ion forming a space charge that is sufficiently strong to quench the discharge at the cathode is in the order of 10^9 [12].
- 5) The time required for adequate removal of negative ion space charge from the buffer region is in the order of a hundred microseconds [12] and the location of the centre of the space charge is just inside the transport region.
- 6) The transit time of positive ion from the boundary of

the ionisation region to the cathode is in the order of a microsecond [12].

- 7) The charge content in one Trichel pulse is in the order of hundred picocoulombs [40].

CHAPTER 4: INSTRUMENTS

4.1 Introduction

One of the difficulties in understanding the basic electrical characteristics of a commercial electrostatic precipitator is caused by many interdisciplinary parameters which, in certain circumstances, tend to obscure the electrical mechanism. The main task in designing a laboratory model, is to circumvent that difficulty by providing a suitable condition, in which unwanted parameters can be isolated from more interesting processes without changing the electrical characteristics of a precipitator. A simulating model is considered to be an adequate method for the investigation of the basic mechanisms.

In an electrostatic precipitator, the charged airborne dust particles deposited on the highly stressed cathode may affect the ionisation process in its vicinity and alter the field distribution in the high field strength region. This effect may be overcome by an extensive distortion of the field strength characterised by the accumulation of negative ion space charge which already existed in the low field strength region, under D.C. energisation. However, the effect may become more pronounced when the cathode is energised with a pulsed voltage. The ionisation process that takes place over a short duration of the voltage pulse produces on the average a smaller number of negative ions. The space charge formed by these ions is more diffuse, less concentrated and its field strength is diminutive. The discharge in the immediate neighbourhood of the cathode becomes less localised and tends to spread over a larger

area of the cathode. This phenomenon enhanced by the alteration of the field distribution due to the deposited dust particles may result in a diffuse glow rather than a tuftlike discharge that has been observed spreading along the cathode wire of an industrial precipitator.

It is, therefore, appropriate to investigate the effects of pulsed voltage on the discharge pattern on the cathode by using a wire-to-plane parallel electrode system in which the conditions on the surface of the wire can be conveniently checked and the discharge pattern can be measured.

Similarly, the discharge pattern and the field distribution at a particular discharging spot on the line electrode can be simulated by using a point-to-plane electrode system. The effects of the discharge process at a point on those which occur at its neighbouring points can also be studied by replacing a single point electrode with a multiple point electrode, the interelectrode distance of which can be adjusted at will.

Layers of dust particles deposit on the anode surface of a real electrostatic precipitator are generally non-uniform, with the tendency of forming thicker layer over areas right in the projection of discharging points on the cathode. Thinner layers are observed to form on the anode areas pertaining to non-discharging regions between discharging points on the cathode. In addition to the non-uniformity, the structure of the dust particle layers can be disrupted at the onset of back corona, with the re-entrainment of dust particles. These factors make the contamination geometry and the contamination-to-gas boundary very difficult to be

determined. Consequently, measurements taken in such conditions would not reveal any evidence leading to the understanding of the basic mechanisms of back corona formation. It is, alternatively, anticipated that simulating materials which are porous, have amorphous structure and similar characteristics like those of dust particles, can be used.

4.2 Electrode Systems

4.2.1 Wire-to-plane parallel system

The dimension of the wire-to-plane parallel system was chosen so as to be compatible with the instrumentations available in the laboratory. The whole electrode system can be placed into a completely light-tight box to provide suitable background for discharge pattern observation.

The electrode system, illustrated in Fig. 4.1, consists of a supporting frame, two adjustable collecting plates and one removable high tension wire.

The frame comprises base 1 with vertical and horizontal stand rods 2 and 3, providing supports for collecting plates and discharge electrode respectively.

The collecting plates which are made of brass are mounted on four insulator rods, sliding fit and secured to the supporting rods by screws. Additional support is provided by insulator spacers which can be inserted between plate-to-plate and plate-to-base spaces.

The discharge electrode which is made of steel is connected between two vertical posts, its two ends are covered with insulating rods which have been tapered to reduce the edge-effect. The mechanical tension on the discharge electrode can be adjusted by tightening a retaining

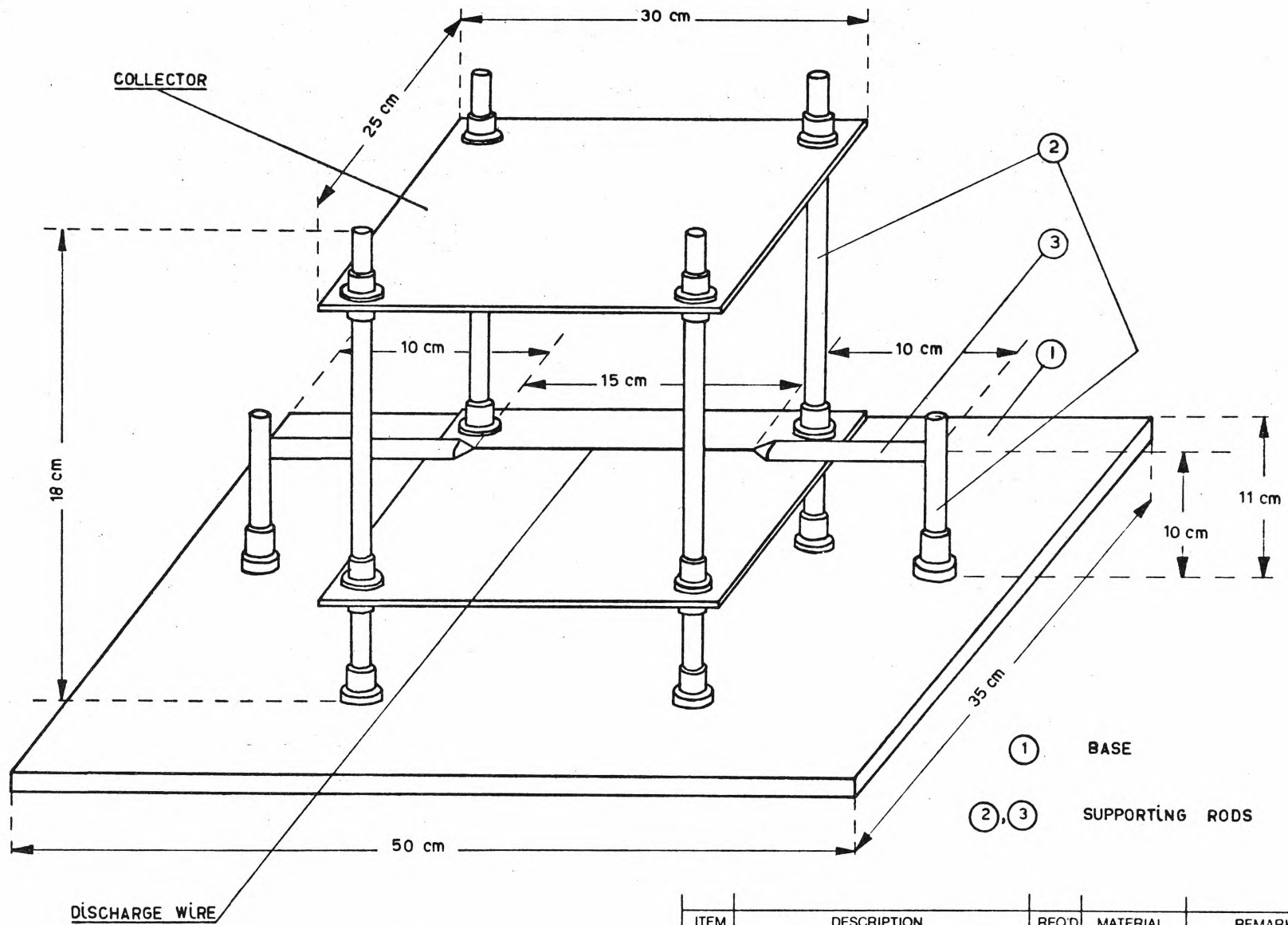


FIG. 4.1 SCHEMATIC DIAGRAM OF WIRE-TO-PLANE PARALLEL ELECTRODE SYSTEM.

ITEM	DESCRIPTION	REQ'D	MATERIAL	REMARKS	
		SCALE		PASSED	DATE
		DRAWN		DRAWING NUMBER	
		TRACED			
		CHECKED			

screw. The wire-to-plane distance can be accurately set at different values by varying the position of the collecting plates.

4.2.2 Point-to-plane system

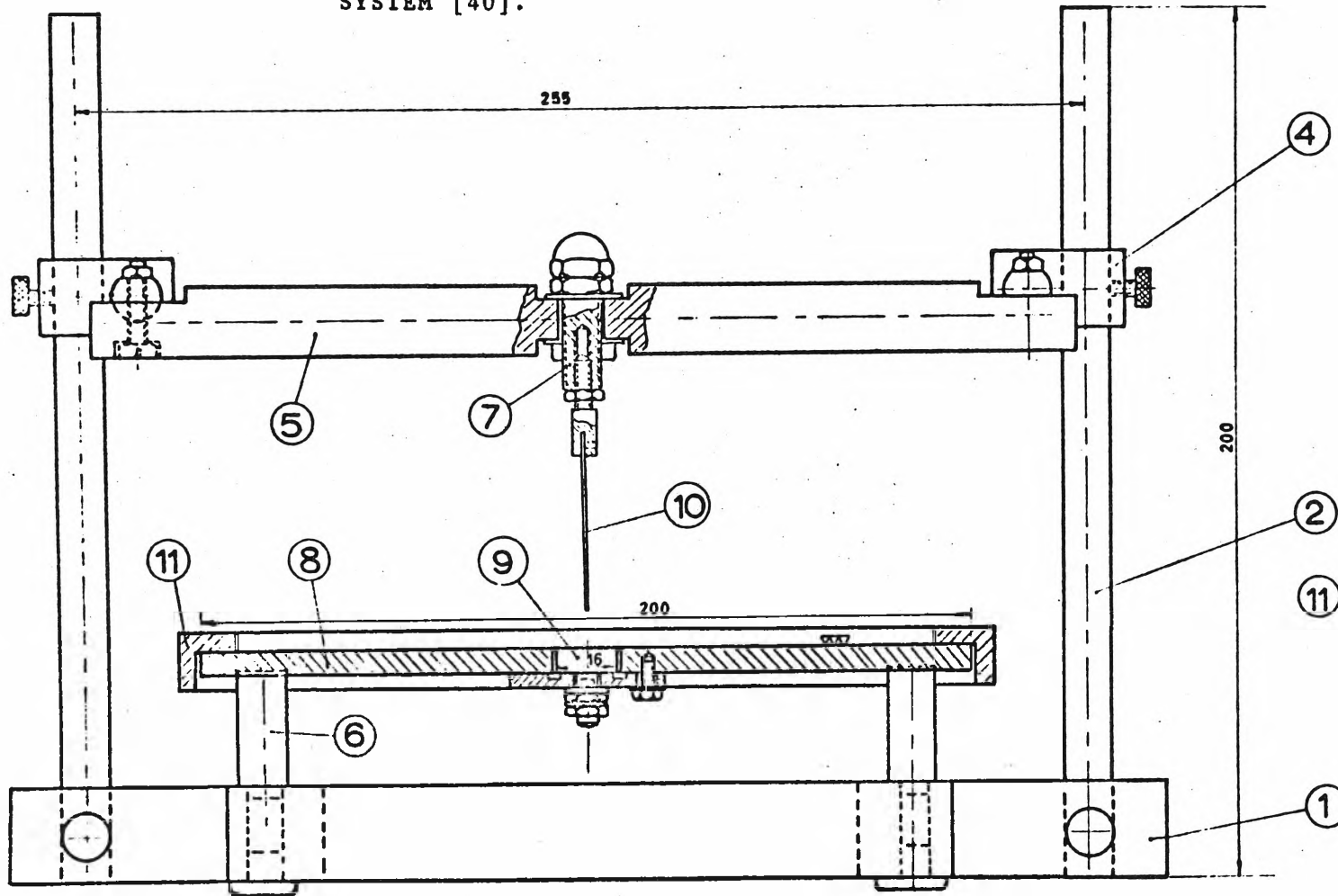
The point-to-plane electrode system which was originally designed by Herceg [40], is shown in Fig. 4.2.

It consists essentially of a supporting frame and interchangeable corona-system electrodes. The frame comprises base 1, vertical and horizontal supporting rods 2 and 3.

The plate electrode 8 is mounted on four Teflon stand-off insulators. Being insulated from the ground, it enables current measurements with grounded instruments. The central part of the plate is a 2 cm^2 disc insulated from the plate and designed for the current-density measurement in the central region. It can also be connected to the plate when the total current versus voltage characteristics are plotted. Under contaminated condition, the central disc is used as a current probe which provides a reasonable sample to determine the average characteristics for the whole contamination layer.

The point electrode is a hemispherically capped platinum wire which can be replaced by conically capped steel needles. The hemispherical point-to-plane configuration is found more suitable in theoretical computation, permitting accurate calculation of the field distribution throughout the gap space by using a charge simulation technique. The method was attempted initially by Dodd [41], who used charge representation with hand solution of several simultaneous equations. Abou-Seada and Nasser [42] applied this technique to find the field distribution of a rod-plane gap using digital

FIG.4.2 SCHEMATIC DIAGRAM OF POINT-TO-PLANE ELECTRODE SYSTEM [40].



- ① Base
- ② Vertical stand rods
- ③ Horizontal stand rods
- ④ Bossheads
- ⑤ H.T. Support rod , teflon
- ⑥ Stand-off insulator , teflon
- ⑦ H.T. Electrode
- ⑧ Plate electrode } stainless steel
- ⑨ Central disc }
- ⑩ Point electrode, platinum
- ⑪ Frame, teflon

Scale : 1:1 approx.
All measures in mm

CORONA JIG

computer. The same technique is adopted in this thesis to find the field strength in the gap space for various gap length to point radius ratios. To ensure an adequate non-uniformity so that the ionisation process in the neighbourhood of the point electrode is isolated from the secondary action at the plane, a gap ratio of 40 is selected as the minimum value. This ratio requires that for a gap length of 1 cm, a point electrode of radius .025 cm should be used. A platinum wire of this radius was found too soft to withstand mechanical vibration induced by the electric wind, and as the result, the point electrode moved around to give a ring-like corona discharge at its tip. To be certain that the phenomenon was not caused by simultaneous discharging points at the electrode as it has been observed by Guck [43], who used much larger spherical electrodes; the discharge was carefully observed by using a telemicroscope and a magnifying lens separately. It was found to move around faster as the applied voltage was increased and became stationary at the onset of corona. The phenomenon disappeared when a steel electrode was used and the discharge at the electrode tip was stable and stationary throughout the voltage range. Steel electrodes, therefore, will be used in most parts of this work, particularly in short gap length measurements. Sputtering effect was also observed at the surface of the point cathode, it is caused by the removal of metal from the cathode under positive ion bombardment. The effect, however, did not alter the corona characteristics significantly, because of reasonably low voltage and current involved in small gap length.

4.2.3 Contamination materials

To investigate the characteristics of a contaminated electrode system under D.C. and pulsed energisations, it would be highly appropriate to use dust particles from an electrostatic precipitator because of its technical pertinence. However, the difficulties in depositing electrostatically layers of dust particles of uniform compactness and thickness, and in defining contamination-to-gas boundary under back corona conditions make the measurements with dust rather confusing and irreproducible.

For systematic comparison of the experimental results for D.C. and pulsed voltages, different materials were selected. They satisfy some of the following requirements [40]:

- (i) resistivity high enough for back corona conditions.
- (ii) resistivity varying with temperature, humidity and applied electric field in a similar manner as the resistivity of fly-ash.
- (iii) coherent form, preferably sheets of uniform thickness and density.
- (iv) well defined porosity of similar magnitude as the average porosity of compacted dust layers.

In this work, Teflon filtering papers having precisely defined porosity ($10 \pm 2\mu\text{m}$ diameter pore) and uniform thickness ($125 \pm 15\mu\text{m}$) was used as contamination in the studies of overall current voltage characteristics, surface potential distribution and effect of contaminant thickness on the sparkover voltage of the contaminated system.

For the simulation of back corona channel, materials which have high-resistivity and non porous structure such as mica was used.

The thickness of the contamination can be varied by stacking several sheets of the material on top of one another.

4.3 Measuring Equipments

4.3.1 The photomultiplier

The photomultiplier is a very sensitive electron device which has a photoelectric cathode and a dynode system capable of electron multiplication by means of secondary emission. The tube selected for this work is an RCA 931 A which has a spectral response in the wavelength range 3000 \AA^0 - 6500 \AA^0 , suitable for the visible spectrum of the discharge.

Fig. 4.3 is a reproduction of the typical spectral response characteristics of the tube. The dynode structure is of circular cage, electrostatic focus type with nine stages. The cathode is opaque and made of Cesium-Antimony.

The principle of operation of the tube is illustrated in Fig. 4.4. A photon striking the photosensitive cathode C may cause an electron to be emitted from the opposite side of the cathode. The probability of this happening is dependent on the work function of the cathode material and on the wavelength of the incident photon. It is known as the Quantum Efficiency χ . Thus for n photons striking the cathode there will be $n\chi$ electrons emitted. These electrons are attracted to the first dynode due to its positive potential with respect to the cathode. Upon collision with dynode D1, $n\chi m_1$ secondary electrons are liberated. These, in turn, travel to dynode D2, where more secondary electrons are

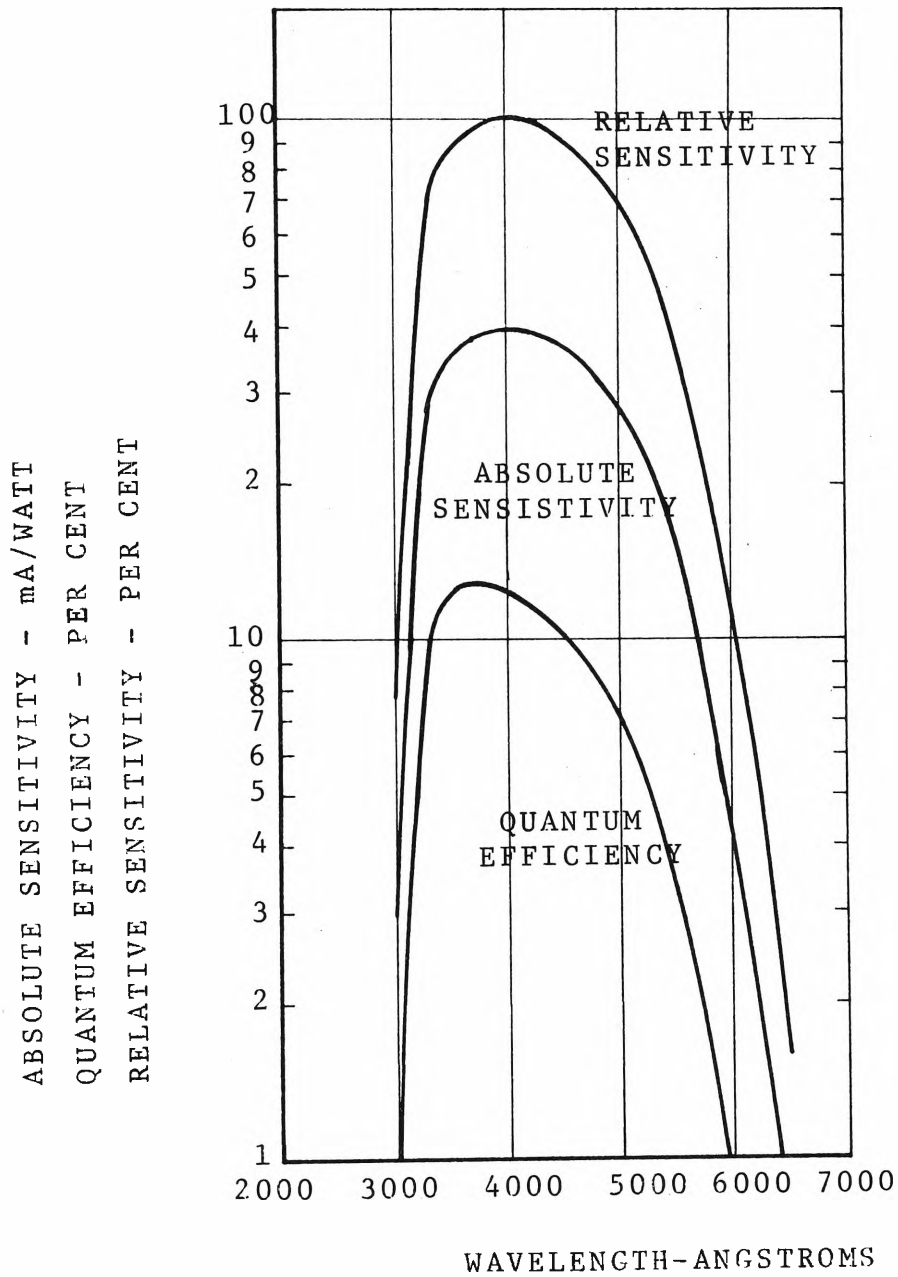


FIG.4.3 TYPICAL SPECTRAL RESPONSE CHARACTERISTICS OF PHOTOMULTIPLIER TUBE [31].

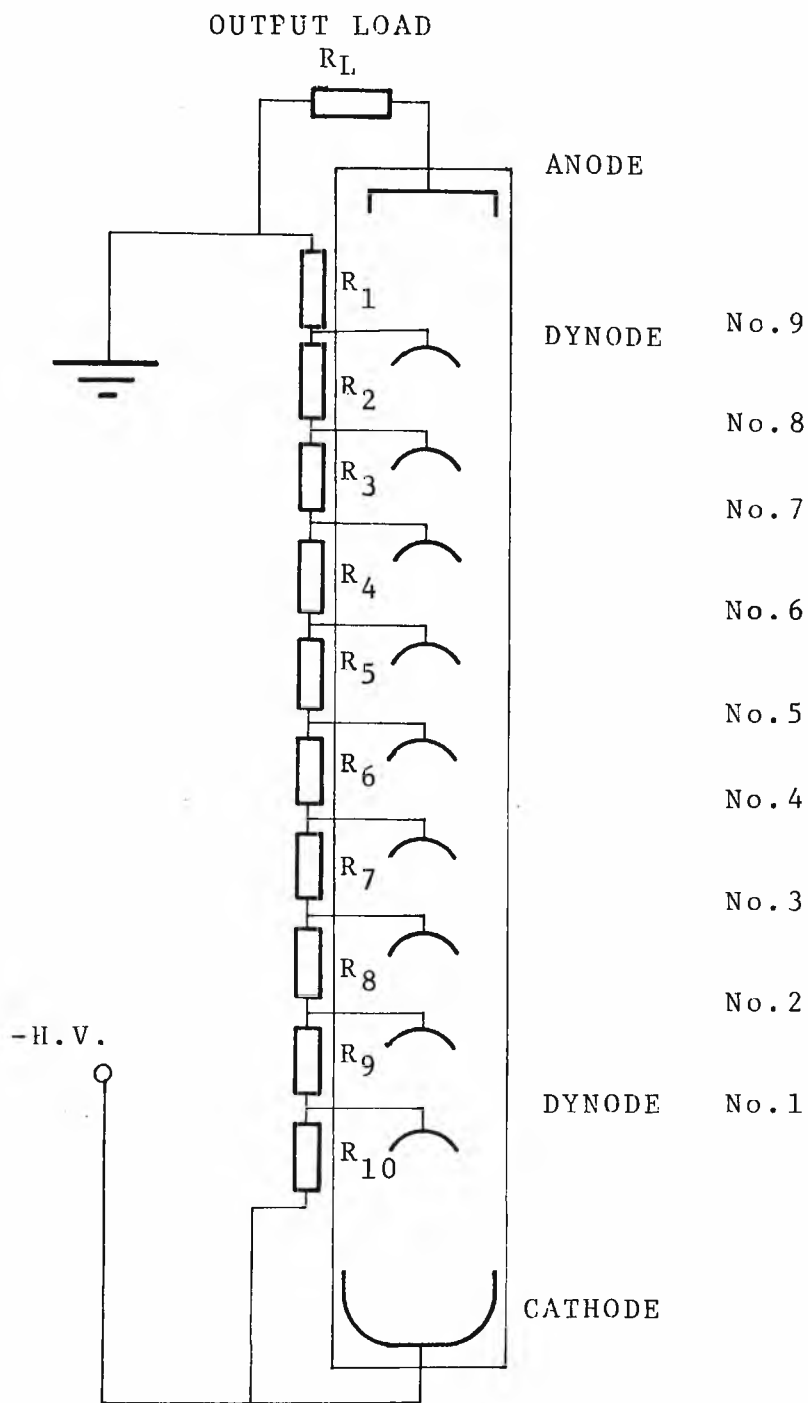


FIG. 4.4 SCHEMATIC DIAGRAM OF A PHOTOMULTIPLIER

released, the number of electrons emitted is $n \times m_1 m_2$.

The secondary emissions at the following plates will repeat in the same fashion and the electrons from the last dynode are finally collected by the anode. The tube gain is defined as the ratio of output electrons to input ones.

$$G = m_1 \cdot m_2 \cdot m_3 \cdots m_{n-1} \cdot m_n$$

The values of m_1, m_2, m_3 etc. and therefore of G are not constant but are statistical in nature. In practice, it is desirable that the dynode gain distributions be Poissonian in nature rather than exponential and that the first dynode gain m_1 be as large as possible. This will minimise the fluctuations of the tube gain G and consequently the output pulse amplitude. Replacing all the dynode gains by their average value \bar{m} , the tube gain can be written as

$$G = \bar{m}^n \quad \text{where } n \text{ is the number of dynode}$$

and the output current:

$$I_o = G \cdot I_i$$

where I_i is the input or cathode current.

Current Amplification; also defined as the photomultiplier tube gain G , which is a function of dynode gain m_n . The dynode gain in each stage of the photomultiplier tube is of the same value if the interstage voltage V_n is constant. It has been specified as for the RCA 931 A tube, $m_n = 5$ for $V_n = 100$ volts. This gives a total amplification of 2×10^6 for a nine staged tube. Since the dynode gain is linearly dependent on the interstage voltage, it can be shown that the fluctuation of the tube gain can be minimised

by using a power supply which has a very good stability factor.

For an n-staged tube, the total voltage across the tube is:

$$V_s = (n+1)V_n$$

The interstage voltage V_n can be written as (\bar{m}/K) and the gain becomes:

$$G = \left(K \frac{V_s}{n+1}\right)^n$$

Taking the derivative of both sides with respect to V_s ,

$$\frac{dG}{dV_s} = n \left(\frac{K}{n+1}\right)^n (V_s)^{n-1}$$

The fluctuation of gain can be expressed as:

$$\frac{\Delta G}{G} = n \cdot \frac{\Delta V_s}{V_s} \quad (4.1)$$

From Equation (4.1), it can be seen that a very well stabilised power supply must be used to minimise the tube gain variation. For instance, if a gain variation of 0.5 per cent is required, a supply which has a stability factor of 0.6 per cent should be used. The Fluke 412 B is used to bias the photomultiplier tube used in this work. It has a stability factor which is better than .02 per cent.

Dark Current; is regarded as the small current measured when the photomultiplier tube is energised in complete darkness. This current is mainly caused by the thermionic emission from the photocathode. This emission depends strongly on the temperature of the metallic surface. Electrons are also emitted from surface of dynodes with a large portion liberated from the first dynode. Dark current may also be

created by the ionisation of residual gas in the tube and the scintillation effect due to electrons hitting the walls. These two factors can be ignored at low operating voltages, but become more significant at higher voltage level. Ion bombardments on the surface of dynodes may also create secondary electrons if the voltage is sufficiently high. This will cause further increase in dark current.

Due to its thermal nature, the dark current of a photomultiplier tube can be reduced by utilising refrigerant, such as dry ice or liquid air. However, cooling needs special equipment such as photomultiplier tube housings, attachment for preventing condensation. Cooling was not used for measurements in this work, since the dark current of the tube at normal room temperature was found sufficiently low (5×10^{-9} ampere) and the light levels from the discharge are intensive enough to bring the signal current well above this value.

Noise; In addition to dark current, there also is one important source of noise in a photomultiplier tube caused by statistical fluctuations in electron emission when the cathode is illuminated by a constant source of light. A detailed discussion on this parameter can be found in literature [44,45], for the measurements obtained in this work, it is reasonable to say that in order to minimise the noise in a photomultiplier tube the average dynode gain \bar{m} should be increased by operating the tube at higher voltage. The limit is the increase in dark current which can happen due to the non-thermal effects discussed previously.

Optical System; The photomultiplier is used as a detector in a complete optical system to study the discharge pattern on the wire electrode. In order to monitor the spatial distribution of the discharge, additional elements should be used to restrict the viewing area of the photomultiplier tube. There are many ways to achieve this such as; installing slots in front of the tube [46],[47], lenses [48],[49] or fiber optics [50],[51]. Each method has its own merit as well as disadvantages, depending on the experimental conditions. Since the main interest of this work is on the steady state of the discharge under both D.C. and pulsed voltages, or in other words the average luminous flux emitted at the discharge sites under such conditions, the optical system was designed to suit this objective. The system is described with the illustration given in Fig. 4.7. In Fig. 4.6 , the discharge site is the object radiating luminous flux which is detected by the photomultiplier tube. If the tube is located at the image plane of the first lens, the output current from the tube represents the time resolution of the ionisation process at the discharge site. As the optical system scans along the electrode, the amplitude of the output current pulse will fluctuate because of the non-uniform distribution of light at the discharge site. The fluctuation in the number of photons striking the photocathode, enhanced by the statistical nature of the secondary emission at the cathode, and the variation in the sensitivity of the cathode response area, may result in spurious signals at the output of the tube. Additional electronic equipment such as pulse discriminator and amplifier may be required to filter

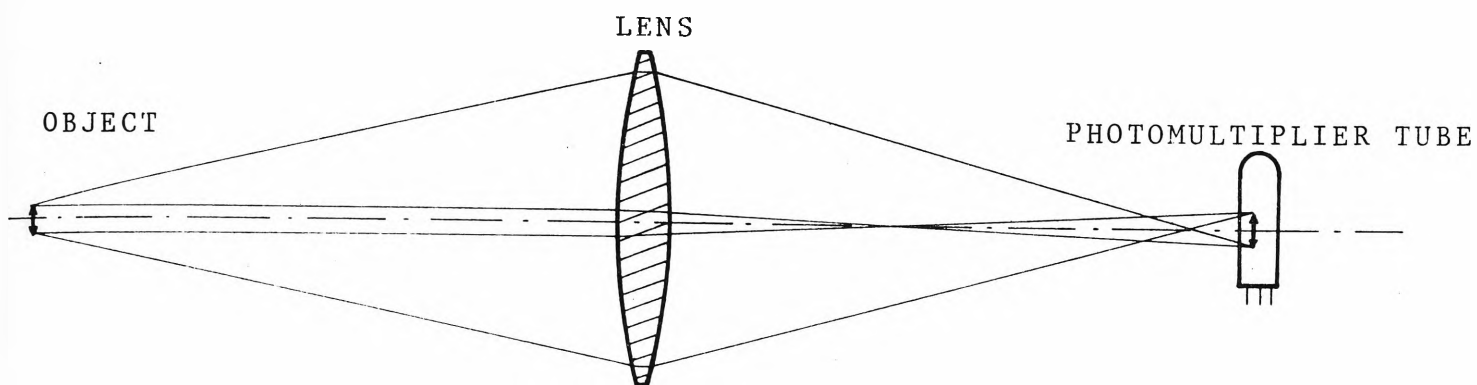


FIG.4.6 METHOD FOR MEASURING OF LIGHT INTENSITY
EMITTED FROM AN OBJECT.

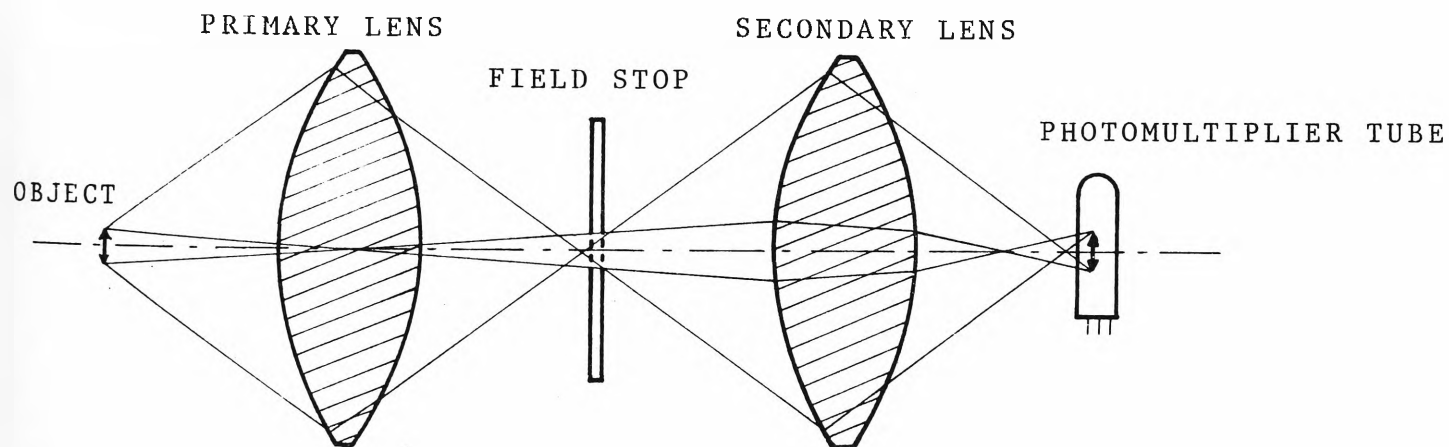


FIG.4.7 SCHEMATIC ARRANGEMENT OF THE OPTICAL SYSTEM.

the wanted signal current pulse out of the total output pulses. The wanted signal then can be averaged by using D.C. measuring equipment or displayed on an oscilloscope.

In order to minimise the errors without the need of expensive equipment, a field stop can be utilised. It can be a physical aperture such as rectangular slits or a portion of an optical modulator. In this work, it is made of a piece of ground glass having an adjustable optical window. All of the radiant flux from the object collected by the first lens passes through the window of the ground glass. Since the photocathode of the photomultiplier tube is placed inside a glass window, the tube must be placed a short distance back of the field stop. As the tube is moved back from the field stop, its photocathode must be made larger in order to accept all of the radiant flux. Since the most sensitive area of the photocathode of a photomultiplier tube is small and cannot be altered, this problem can be solved by means of a secondary lens. The radiant flux incident on the field stop refracts through the ground glass and becomes a uniform light source. The secondary lens forms an image of the diffuse window of the field stop, collects all of the radiant flux passing through the field stop, and directs it through this image.

There are two ways of describing the amount of radiant flux collected by an optical system:

- (a) Focal length/Number of the Optics or ($f/N.O.$), which is equivalent to (f/D) where f is the equivalent focal length and D is the diameter of the aperture stop. It is an inverse term; the smaller the

($f/N.O.$) the greater the radiant flux collected.

This is evident, as the collecting crosssectional area is directly proportional to the square of its diameter.

(b) Numerical Aperture or (NA) is defined as:

$$NA = n \cdot \sin \beta$$

where n = refraction index of the medium between the final optical plane and the second focal point.

β = half the angle of the cone of rays converging at the focal point [52].

All the above terms are illustrated in Fig. 4.8.

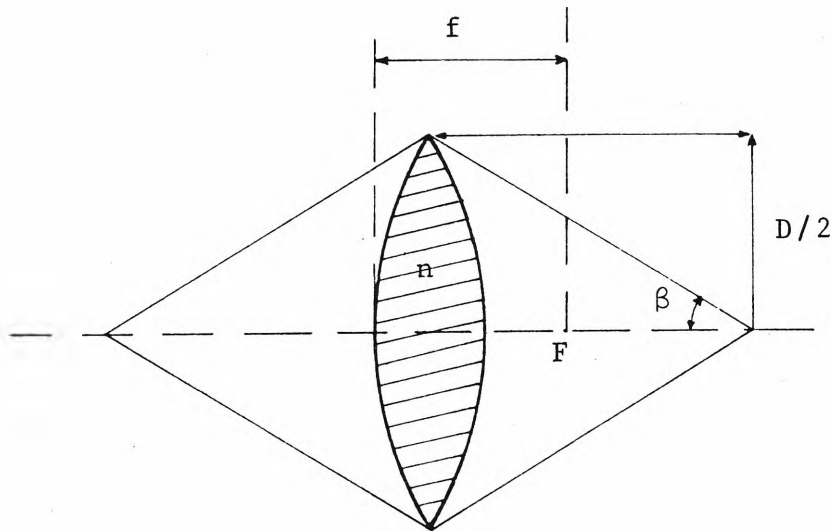


FIG.4.8 PARAMETERS OF A CONVERGING LENS.

It can be shown that:

$$NA = \frac{1}{2(f/NO)} = \frac{1}{2(f/D)} \quad (4.4)$$

From equation 4.4, it is obvious that the subtended area of the photocathode in an optical system depicted in Fig. 4.7 will become:

$$A' = A. \left(\frac{NA_p}{NA_s} \right)^2 \quad (4.5)$$

where: A' = subtended area of the photocathode with the secondary lens.

A = subtended area of the photocathode without the secondary lens.

NA_s = numerical aperture of the secondary lens.

NA_p = numerical aperture of the primary lens.

The area A' can be greatly reduced by means of secondary lens which has larger numerical aperture. However, this also introduces the problem of combining several elements together and enhances the transmission losses in the secondary lens. The selection of the secondary lens is a compromise between the obtainable sensitive area of the photomultiplier cathode and those two factors. In this work, a secondary lens having the same parameters as the primary one was utilised for the above reason, moreover the wavelength spectrum of the discharge requires only a small area which is provided adequately by the cathode of the photomultiplier tube. The lenses used are equiconvex and have focal length of 50 mm and aperture diameter of 50 mm.

4.3.2 Corona wind velocity measuring device

The corona wind is a special feature of the discharge in a highly non-uniform field. This phenomenon refers to the movement of gas induced by repulsion of ions from the neighbourhood of a highly-stressed electrode. It has been known since the earliest electrostatic studies in the late 1600's [12]. There are several methods of measuring the corona wind speed. One of the methods used earlier involves the measurement of pressure differences experienced across a distance by means of an oil manometer [53]. Later Ratner [54] used a negative point and a gauze plane to measure the pressure, induced by the movement of gas, with a moving vane suspended from a calibration torsion head [12]. In 1961, Robinson described a system consisting of a negative point, the tip of which is concentric with a wire screen serving as the collecting electrode [55]. He used this system to generate air draft, but did not mention the technique used to measure the wind speed. Most recently, Le Ny et al [56] detected the corona wind speed in a positive corona discharge system, by means of a Pitot tube located behind a grid-like electrode. Most of the above methods require some modifications to the asymmetrical electrode system in such a way that the measuring device can be accommodated in the same confined cylindrical chamber. This may make the values of corona wind speed, measured in such conditions, become impertinent to the real condition prevailing in a usual electrode system. In order to circumvent that problem, the technique of using thermistors to measure the temperature difference was used in this work.

Thermistors, or thermally sensitive resistors, are devices made of solid semiconducting materials whose resistance varies rapidly with temperature. In the design of the corona wind speed measuring device, the following factors were considered:

(i) Mechanical dimensions of the thermistor including those of the supports.

(ii) The dissipation constant and power sensitivity.

The dissipation constant is the watts that are dissipated in the thermistor divided by its temperature rise in centigrade degrees above its surroundings. The power sensitivity is the watts dissipated to reduce the resistance by one per cent. These constants are determined by the area and nature of the surface, the surrounding medium and the thermal conductivity of the supports [57].

Both the dissipation constant and power sensitivity increase with the gas velocity. The dependence of the dissipation constant on the gas velocity is the basis of the application of thermistors as flowmeters. In this application, the undesired response of the thermistor to the ambient temperature of the medium can be eliminated by utilizing a second thermistor of similar characteristics in the measuring circuit. The compensating thermistor is exposed to the same ambient temperature, but is isolated from the effect being measured such as gas flow. The two thermistors can be connected into adjacent arms of a Wheatstone bridge which is balanced when the test effect is removed and becomes unbalanced when the effective thermal conductivity of the medium

is increased.

The measuring circuit used in this work is described in Fig. 4.9. The sensitive element of the thermistor flowmeter is a small bead 0.5 mm in diameter enclosed in a glass probe, suspended by two fine wires in a tubular bulb. Resistors R_1 and R_2 connected to a variable resistor form two arms of the Wheatstone bridge, while the other two are occupied by two thermistors having a dissipation constant of 0.85 milliwatt/ $^{\circ}\text{C}$. The reference thermistor R , R_1 and R_2 are placed inside a thermal flask to isolate them from any fluctuation in the ambient temperature and possible movement of room air. The measuring thermistor is given extra support by means of a glass pipe for attachment to the chamber whose air velocity is to be measured. The circuit components are selected in such a manner that the operating point is in the portion of the volt-ampere characteristics which has a negative slope, and the heating effect in the thermistors is minimised. The minimum measurable velocity is limited by the convection currents produced by the heated thermistor, the meter sensitivity and the ability to maintain the zero setting for reasonable periods of time in the presence of the variations of supply voltage and ambient temperature.

4.3.3 Pulsed power supplies

In order to investigate the characteristics of an electrostatic precipitator in its operating conditions, a laboratory scale electrode system has been developed and various methods of energising the model are now discussed.

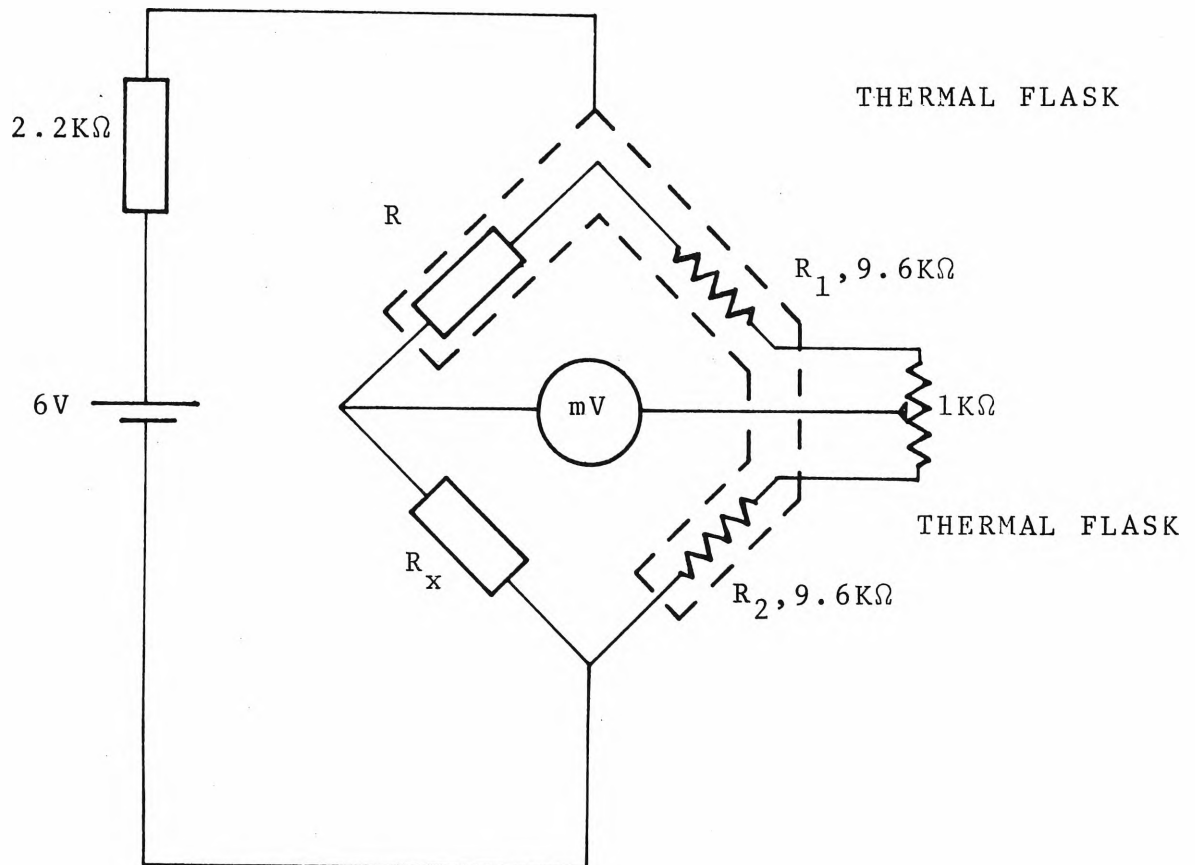


FIG. 4.9 SCHEMATIC ARRANGEMENT OF ELECTRICAL WIND
VELOCITY MEASURING DEVICE.

Since the technology of the precipitators can be significantly changed with the use of pulsed energisation technique, a pulsed power supply should satisfy the need of improving the performance of the electrostatic precipitator without invoking excessive costs.

The conventional power supply used in the precipitator industry consists of a single phase bridge rectifier with either a half-wave or full-wave output. One possible method of converting this kind of power supply into a pulsed power supply is to filter the ripple output voltage by means of a filtering capacitor, the output then used to trigger a spark gap to generate pulsed waveforms. The schematic diagram of this type of pulsed power supply is illustrated in Fig.4.10. C_s is the filtering capacitor which has high voltage rating. C_1 represents the stray capacitance of the circuit and used to store energy transferred from the supply across the spark gap. Resistor R_1 and C_1 form a network that affects the rise time of the pulsed waveform. The high voltage probe can be represented by an equivalent capacitor C_p and resistor R_p which forms a discharging path across C_1 . The energy stored in C_1 is discharged through an equivalent resistance comprising R_2 , R_p and the non linear resistance of the electrode system. The operation of the circuit can be briefly described as follows.

The high voltage supply charges the input capacitor up to its peak value and gives rise to a field distribution in the gap space between the sphere electrodes. When the electric field intensity reaches the breakdown field strength of air, a sparkover is initiated in the gap and forms a

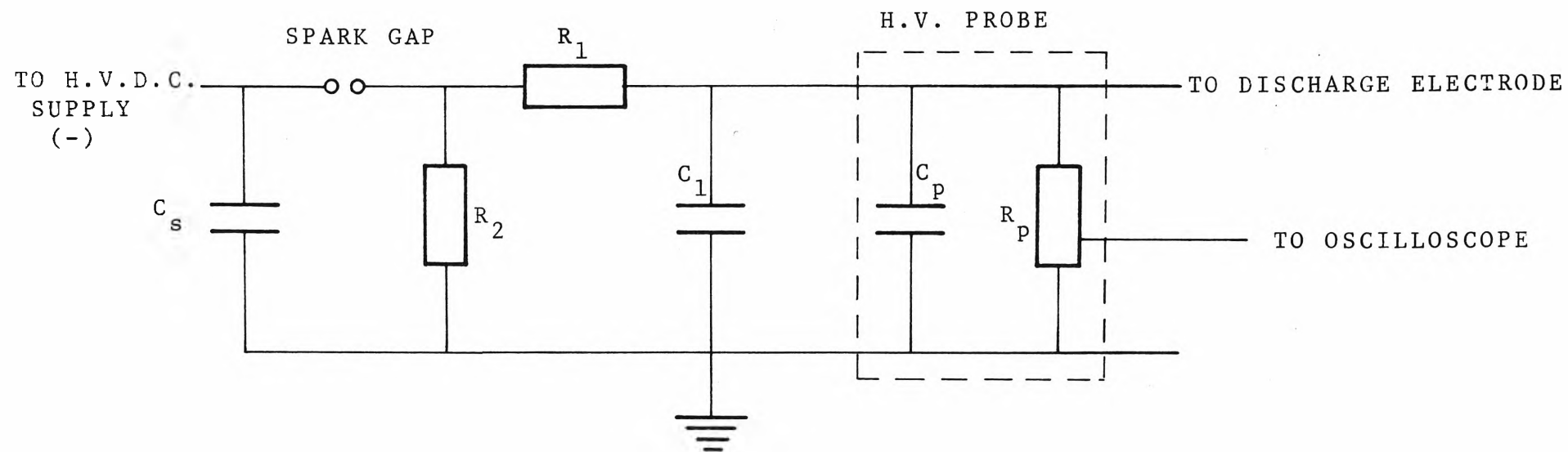


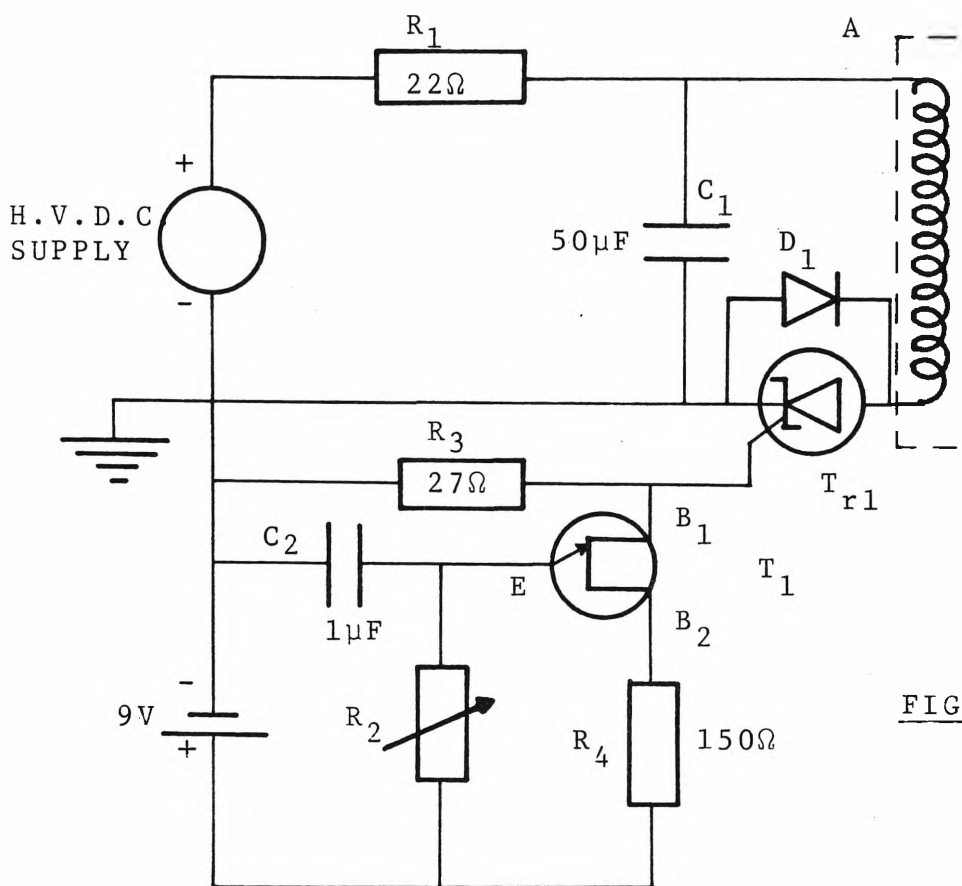
FIG. 4.10 SCHEMATIC DIAGRAM OF PULSED POWER SUPPLY
USING SPARK GAP.

highly conducting channel bridging the sphere electrodes. A small amount of the energy stored in C_s is dissipated by the ionisation process in the spark gap, the remaining energy is transferred across the gap to charge up C_1 through resistor R_1 . The voltage across capacitor C_1 is rapidly increased and the ionisation process ceases when the potential difference between the sphere electrodes drop below its breakdown value. The charge of capacitor C_1 is leaking through R_2 , the probe resistance R_p and the equivalent resistance of the corona system with the spark gap acting as a reverse biased rectifying diode. The voltage across C_1 is decaying as an exponential function of time and when this value is sufficiently low, the potential difference across the sphere electrodes will attain the sparkover voltage. The ionisation process is once more initiated and repeated periodically. The period of the output pulses depends mainly on the voltage output from the D.C. supply and the formation time lag of the breakdown process in the sphere gap. However, at high voltage level the sphere gap becomes highly-overvolted, the fluctuation of the time lag due to the statistical nature of the ionisation process is negligible and the period of the pulses is consistently a function of the voltage. Since only the steady state characteristics of the electrode system under pulsed energisation is investigated in this work, the pulse rise and fall times do not play important roles in such conditions as they do in transient conditions [58-62], this kind of power supply is considered adequate. In order to study the effects of pulse duration and pulse duty ratio upon the corona system characteristics, a more sophisticated

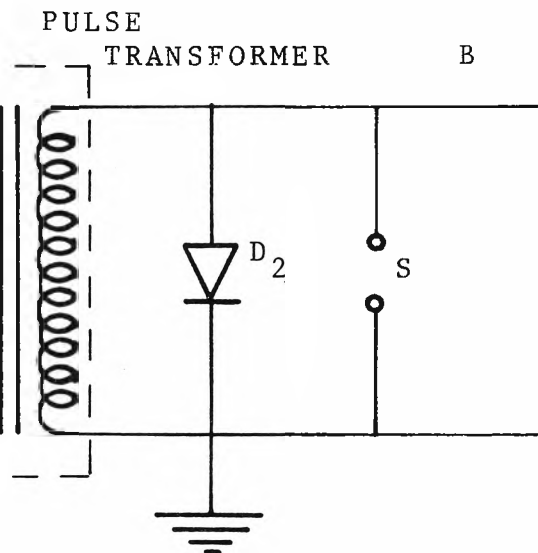
pulsed power supply was used, its schematic diagram is illustrated in Fig. 4.11.

The circuit utilizes an oscillator to trigger the discharge across a capacitor whose output pulses are coupled to the primary of a pulse transformer. The output pulses from the secondary winding is rectified by a high voltage silicon diode.

When the SCR diode T_{r1} is in OFF state, the storage capacitor C_1 is charged by the high voltage D.C. supply through resistor R_1 which affects the rise time of the input pulses. T_{r1} is switched ON by triggering pulses generated by a relaxation oscillator circuit comprising a unijunction transistor T_1 , R_2 , C_2 , R_3 and R_4 . The frequency of oscillation is controlled by C_2 and R_2 . Capacitor C_1 discharges through the resistance of the primary winding and equivalent resistance of T_{r1} . The input pulses are amplified by 400 times through a pulse transformer whose secondary winding is protected by a spark gap S. The pulsed power supply can generate pulses of frequency as low as a few cycles per second to a hundred cycles per second, 20 kilovolts in maximum amplitude, and 150/150 microseconds wave shape. A description of the pulse shape and frequency of the power supply is attached in Appendix B.



FIG



.4.11 SCHEMATIC DIAGRAM OF PULSED POWER SUPPLY USING PULSE TRANSFORMER.

CHAPTER 5: CHARACTERISTICS OF CORONA SYSTEM-CLEAN COLLECTING ELECTRODE

5.1 Introduction

It has been recognised that complex processes take place in a commercial electrostatic precipitator and that sensitive inter-relationships exist between gas composition, gas density, particle properties, electrical energisation etc... make the discharge mechanism under pulsed voltage a complicated phenomenon. So as to limit the scope of this thesis to first essentials, the electrical characteristics of a laboratory scale electrode system will be investigated when excited with both negative D.C. and pulsed voltages.

In this chapter only clean electrode system will be investigated, the steady state of the discharge pattern in the vicinity of the highly-stressed wire cathode is observed by means of an optical system, the output of which is measured with an electrometer and a chart recorder. These results are then compared with the bulk electrical characteristics of the ionisation process as measured by the average corona current-voltage relationship. The dependence of the characteristics on the pulse repetition rate is simulated by a mathematical model. The similarity in the discharge process under pulsed and D.C. voltages revealed from these results is further substantiated by measurement of corona current pulses. The collisions between the highly-energised ions, created in the proximity of the cathode, and the gas molecules give rise to the electrical wind, the characteristics of which are measured. One of the significant advantages of pulsed energisation over D.C. one is the higher sparkover voltage obtained. The sparking phenomena is

investigated and particular attention is given to the effects of negative streamers on the sparkover value. The results will be used to interpret the characteristics of the electrode system under contaminated conditions.

5.2 Nature of the Discharge in the Vicinity of the Wire

Electrode

5.2.1 Introduction

The ionisation process in gas can be detected and measured by a number of experimental methods. These can basically be divided into two types of measuring techniques.

- (i) The optical method which detects the emission of quanta of light from gas molecules excited by electrons in the ionisation process. This technique can only detect the effect of ionising electrons if their energy is sufficient to excite molecules in the inelastic collisions.
- (ii) The electrical method which measures the movement of electrons and ions in the high field region. This enables the study of the temporal development of the ionisation process and the instantaneous value of the current at any moment.

At this part of the thesis, the ionisation process taking place in the vicinity of the discharge wire electrode is observed by means of an optical system. The results are complemented by the electrical measurement of the corona current pulses generated by a point electrode.

5.2.2 The Discharge Pattern in the Vicinity of the Cathode

One of the important characteristics of a clean corona discharge system when energised with a negative pulsed voltage is the appearance of the discharge on the active cathode. On a wire electrode, it is more uniform and diffuse than the evenly spaced bright discharge points of a D.C. negative corona (Hall [13]). On a point electrode, it resembles a "Roman candle" with streamer discharge superimposed on the regular Trichel pulse corona (Moore and English [14]).

Because of the complex processes taking place in the high field strength region and the nature of the interaction of one discharge point with the other, the discharge mechanism under pulsed energisation is a complicated phenomenon. Many observations have been reported, but no complete investigation has been made. The main interest in this has been in the electrical breakdown of non-uniform field gap under the application of a single impulse and more recently in the formation of leaders in a spark channel under positive impulse voltage.

In this section, the steady state of the discharge pattern on the highly-stressed wire cathode is observed by means of an optical system. The results are compared with those obtained under D.C. voltage. The dependence of discharge intensity on the repetition rate and amplitude of the pulsed voltage is determined.

5.2.2.1 Measurement of the discharge pattern

The arrangement used to observe the discharge pattern on the wire electrode is illustrated in Fig. 5.1. The electrode system comprises two parallel brass plates spaced at 6 cms and a single discharge wire electrode, 15 cms long and 0.035 cm diameter placed midway between the two plates. Since the contamination on both electrodes may affect the appearance of the discharge, the condition of the electrodes is checked after each hour of operation and if necessary the discharge wire is cleaned with methylated spirit and the plates polished to remove any contamination. To ensure that the apparent difference in the discharge pattern under D.C. and pulsed energisation is caused by the ionisation process, and by neither the alteration of the surface condition of the highly-stressed electrode, nor the change in environmental conditions such as temperature, pressure and humidity, the measurements are taken under similar, if not identical, conditions. The new wire electrode made of high-carbon steel has been conditioned by means of D.C. energisation. This process is necessary for reproducible results to be obtained.

The electrode system is placed inside a light-tight box containing the optical system and a fan is used to circulate the air. The optical system is mounted on a platform, the position of which can be adjusted in a three-dimensional co-ordinate system by means of a gear drive mechanism. The two systems are properly aligned in such a way that the proximity of the wire electrode is focused upon the photocathode of the photomultiplier. This set-up is required to minimise possible errors caused by light reflection on the

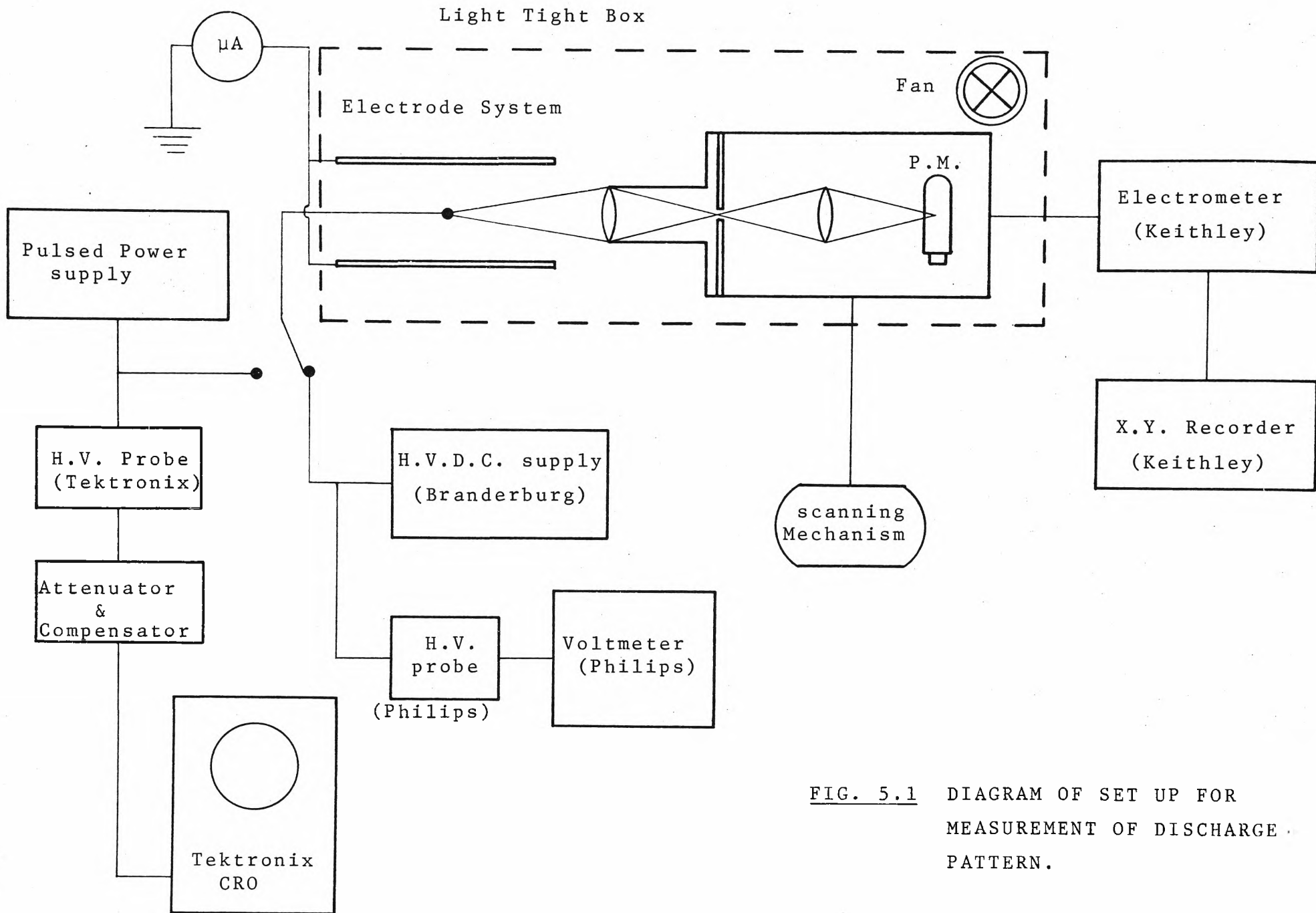


FIG. 5.1 DIAGRAM OF SET UP FOR MEASUREMENT OF DISCHARGE PATTERN.

surface of the discharge wire. The alignment procedure can be briefly discussed as follows.

- (i) The optical system is adjusted so that the field stop (or slit) is at the middle of the lenses and the distance between the slit and the lens is twice the focal length. The distance between the photocathode and the secondary lens is also twice the focal length. This has been illustrated in Fig. 4.7. This is done by using an aperture comprising a test slit and a light source and a piece of ground glass simulating the photocathode. The primary lens is adjusted until a good image of the light source is obtained on the field stop. The secondary lens then is focused to give a picture of the field stop on the ground glass.
- (ii) The test slit is now lined up against the wire electrode. The position of the optical system is adjusted until a picture of the test slit is observed on the ground glass.
- (iii) A telemicroscope is finally used to check the alignment. The photomultiplier tube is a very sensitive device, particularly at an accelerating voltage near maximum. The dark current is found comparatively high and spurious pulses observed when the tube is first turned on. It reduces from 10^{-8} A to 5×10^{-9} A after the photomultiplier tube has been operated for an hour. No significant drop from this typical value is observed after a few more hours.

A driving mechanism is used to scan the optical system over a distance of 4 cms along the wire electrode, at a rate of .017 cm/sec. It is driven by a D.C. motor which has a constant speed with an estimate error less than 3%. The average current from the photomultiplier tube is detected by means of an electrometer (Keithley-610B) and recorded on a chart recorder (Keithley-370). The chart speed is selected to give good spatial distribution of the light emitted from the highly-stressed wire electrode.

5.2.2.2. Results and Discussion

(a) Results

The set-up described in Fig. 5.1 is used to record the discharge pattern along the wire electrode. To check the consistency and reproducibility of the results, the new discharge electrode is conditioned by electrifying it with negative D.C. voltage for approximately one hour and the discharge intensity at one particular point is then recorded on the chart recorder for five to ten minutes. All the results are measured at room temperature and in atmospheric air.

The results are shown in Fig. 5.2 and 5.3 for pulsed voltage at rise time of 6 microseconds and D.C. voltage. The horizontal axis indicates the length of the discharge wire scanned by the optical system having an object-to-image ratio of 1. The ordinate is the average current from the photomultiplier, which has been calibrated on a logarithmic scale so that the relative shape of the curves over a wide range of voltages can be easily compared. The noise current of the photomultiplier tube is included in the output,

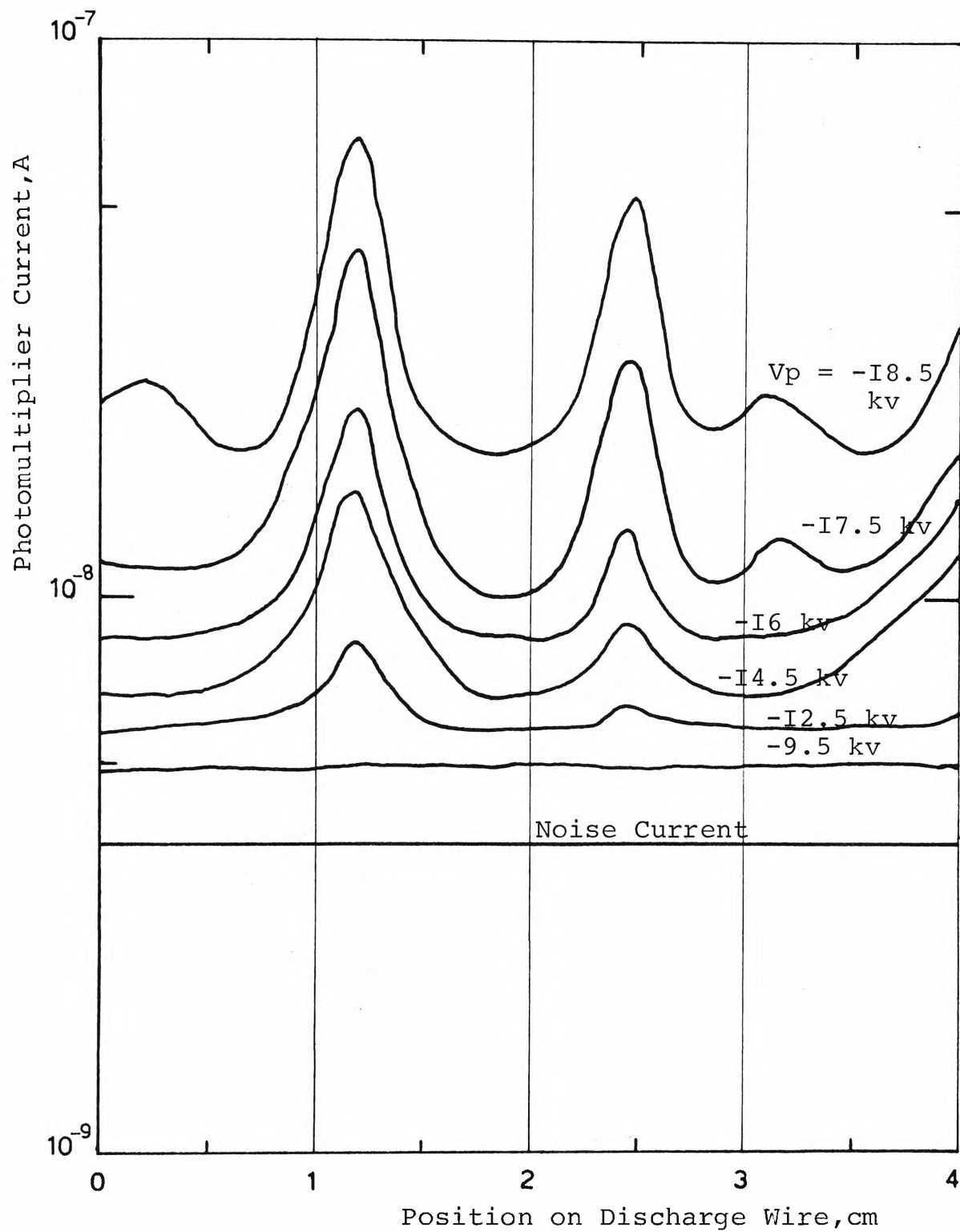


FIG.5.2 DISCHARGE PATTERN ALONG WIRE ELECTRODE
FOR PULSED VOLTAGE, RISE TIME = 6 micro-
seconds.

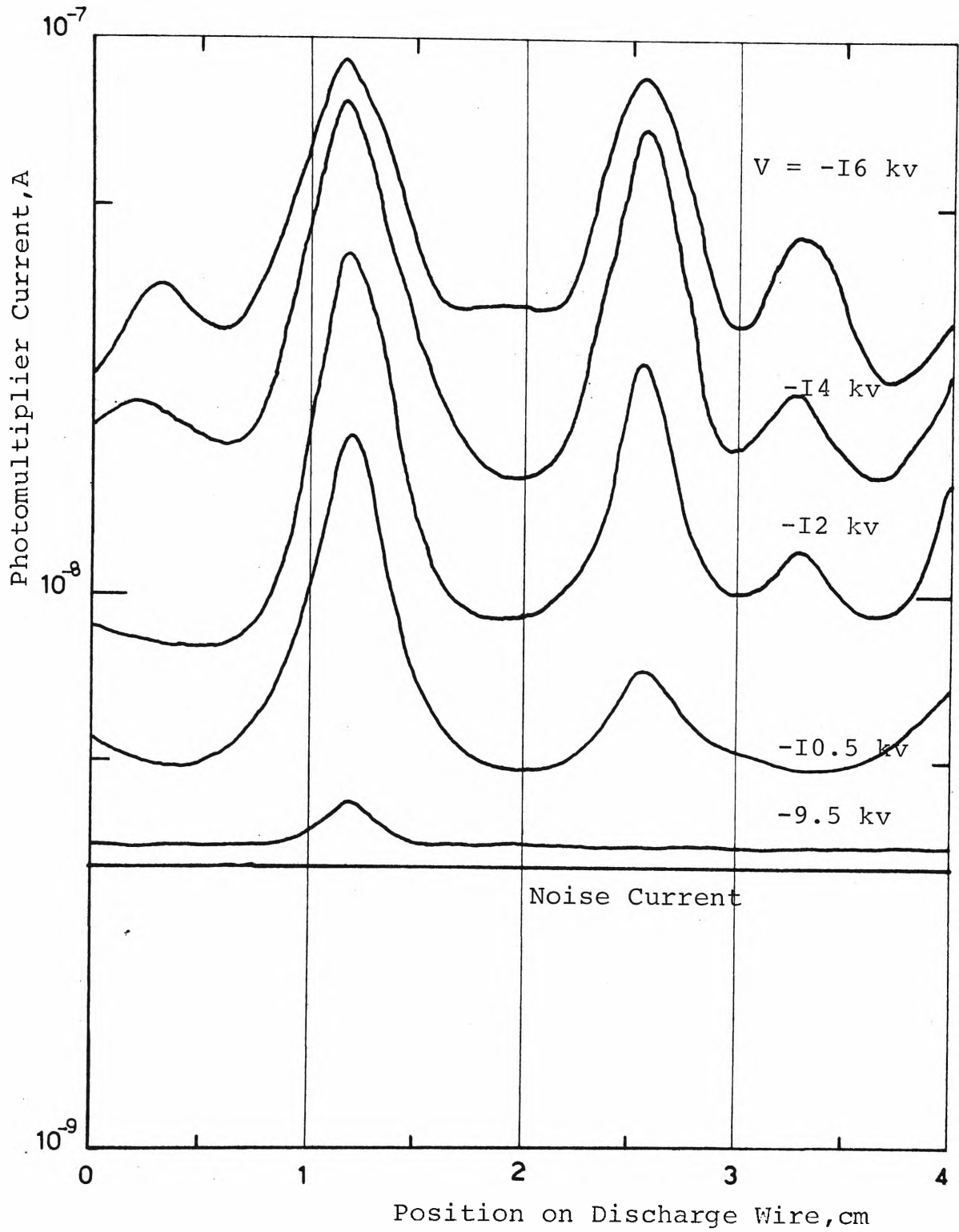


FIG. 5.3 DISCHARGE PATTERN ON WIRE ELECTRODE
FOR D.C. VOLTAGE

varying from 4×10^{-9} A to 3×10^{-9} A. The voltage value recorded in each figure is the peak value of the pulse.

It is seen that in Fig. 5.2, for lower values of peak voltage, the discharge along the wire appears as a constant glow and its intensity increases with the voltage. At higher voltages, distinct discharge points occur and the general shape of the intensity curve begins to follow that obtained with a smooth D.C. voltage (Fig. 5.3).

When the electrode is energised with a D.C. voltage the resultant output of the photomultiplier is shown in Fig. 5.3. In addition to a general glow along the length of the wire, a series of distinct bright discharge points are formed at approximately regular intervals along the wire. As the magnitude of the applied voltage is increased, the intensity of the glow increases together with the brightness of the individual points. At higher voltages, however, the brightness of the individual points do not appear to grow as rapidly as before but additional bright spots are formed in the valleys resulting in an overall increase in output per unit length of discharge wire.

By comparing Fig. 5.2 and 5.3, it can be seen that:

- (i) At high voltage levels, the general shape of the discharge intensity curves for pulsed voltages are similar to that obtained with D.C. voltage except the peak value of the voltage is considerably higher than that for D.C.
- (ii) Where the area of the photomultiplier output curve for the pulsed voltage is the same as that produced by the D.C. voltage (c.f. 12 kV D.C. with 17.5 kV

pulsed voltage), then the shapes of the curves are similar.

Since the number of photons created by ionising collisions is proportional to the number of electrons in the avalanche, it can be shown that the output current from the photomultiplier is proportional to the rate of generation of electrons [103]:

$$I_{pm} = \chi g D Q e G \frac{dn^-}{dt} \quad (5.1)$$

where χ is the quantum efficiency of the photomultiplier cathode (section 4.3.1), g is the geometry factor dependent on the relative position and distance between the photomultiplier and the discharge wire electrode, D is the transmission coefficient of the photomultiplier tube, Q is the photon efficiency per ionising collision and depends on the electron energy and the gas, e is the electronic charge and G is the amplification number of the tube.

The total corona current is the sum of the electron current edn^-/dt , the current components due to positive ion and negative ion space charges, and because the latter are proportional to the number of electrons generated, qualitatively expression (5.1) can be written:

$$I_{pm} = K.I \quad (5.2)$$

where I is the corona current measured electrically and K is the proportional constant and depends on Q , the photon efficiency.

This relationship between the photomultiplier current and the electrical current (or corona current) can be checked.

(b) Relationship between I_{pm} and I

(i) D.C. Voltage

Because of a difference in the discharge intensity from various discharge spots along the wire, it is appropriate to compare the spatial average of the discharge intensity instead of its peak magnitude with the average corona current. The spatial average of the photomultiplier current is found by integrating the discharge intensity (Fig. 5.3) over the scanned length of the discharge wire and dividing this quantity by its length. The results, together with the average corona current, are plotted against voltage as shown in Fig. 5.4. The linear relationship between the two currents can be seen in Fig. 5.6 and is consistent with expression (5.2). This indicates that the number of photons emitted in a discharge in air in the range of wavelengths from 3500 to 4000 \AA^0 is proportional to the number of ionising collisions. This observation is in agreement with Legler's works [104], who investigated the size of an avalanche by measuring its radiation in the range of wavelength from 3300 to 3600 \AA^0 . Because the upper limit of the photomultiplier response is in the visible range (4000-7000 \AA^0), it can be said that the linear relationship between the two currents holds from the corona onset level-when the secondary emission from the cathode is caused by photoelectric emission and the radiation emitted is mostly in the ultraviolet region - to voltage level much higher than the onset - when secondary electrons are mostly created by impact between positive ions and cathode, and the radiation gradually moves into the visible region.

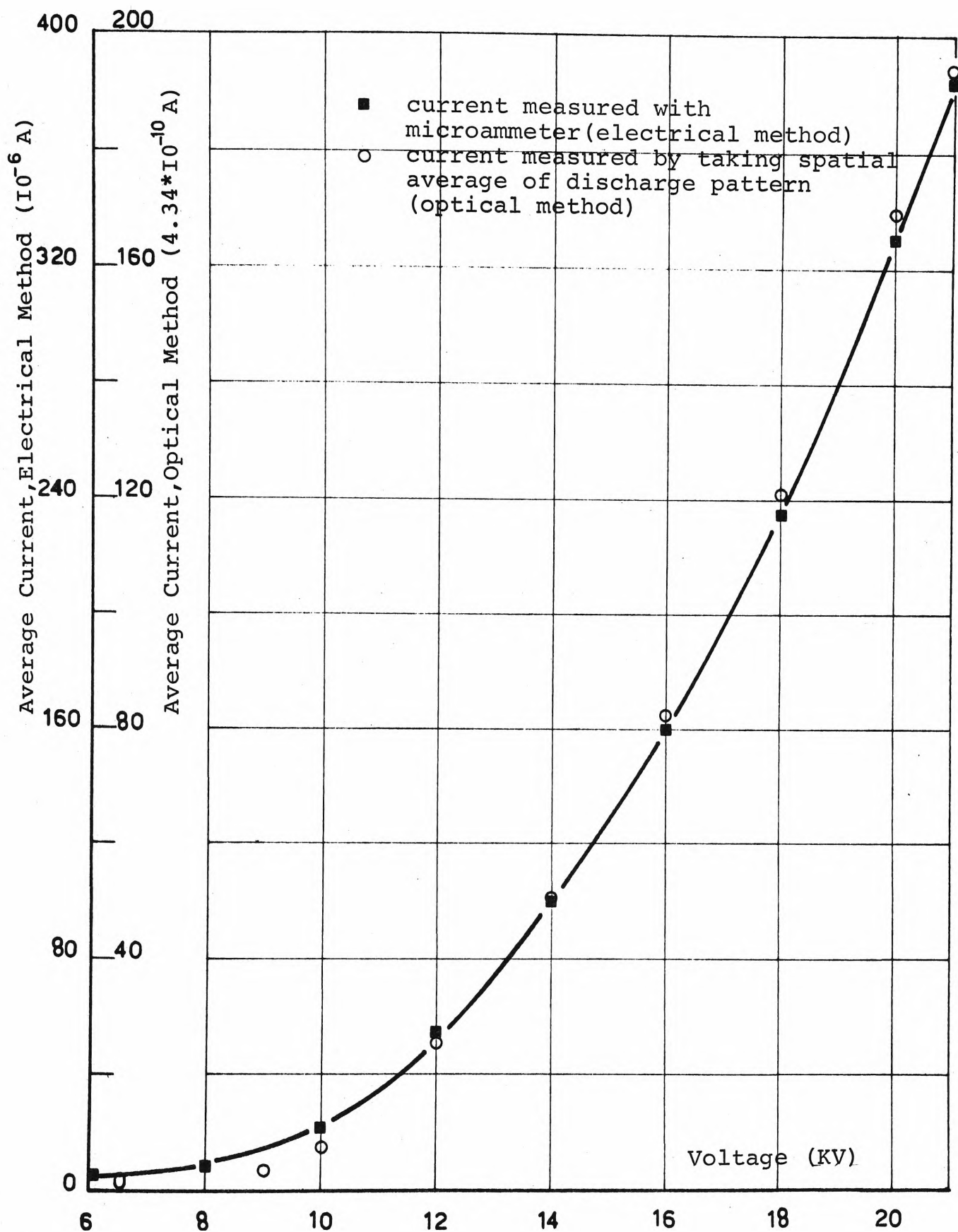


FIG. 5.4 AVERAGE CURRENT-VOLTAGE CHARACTERISTICS
FOR D.C. VOLTAGE

The linear relationship holds over the voltage range from 6 to 21 kV because the spatial average of the photomultiplier is used. If the peak current was used, the linear relationship would not hold over this range since at high voltage levels, the ionisation tends to spread over a larger area surrounding the discharge spots, this results in an increase of the background intensity and a less-rapidly increased maximum intensity. The increase of background intensity is also due to the increase of number of photons emitted from newly-created discharge spots. At voltage above 21 kV, the deviation from linearity may become severe since the generated photons are partly absorbed by ozone created in the neighbourhoods of the discharge spots. This is plausible because the absorption of ultraviolet light in ozone is higher than that in air, consequently the absorption of photons emitted from the avalanche in the air containing a considerable amount of ozone is also higher. From expressions (5.1) and (5.2), this means that K does not remain constant at high voltage. The decrease of Q , the photon efficiency and consequently of K means that at high electric field the number of electrons generated by ionising collisions increases more than the number of excited atoms or photons.

The value of K can be determined by plotting I versus I_{pm} as shown in Fig. 5.6. A qualitative discussion of the dependence of K on various parameters is presented. Assuming that the total corona current is twice the electron current, the value of K can be expressed as $0.5 (\chi g D G Q)$, where all the terms have been defined before. The quantum efficiency,

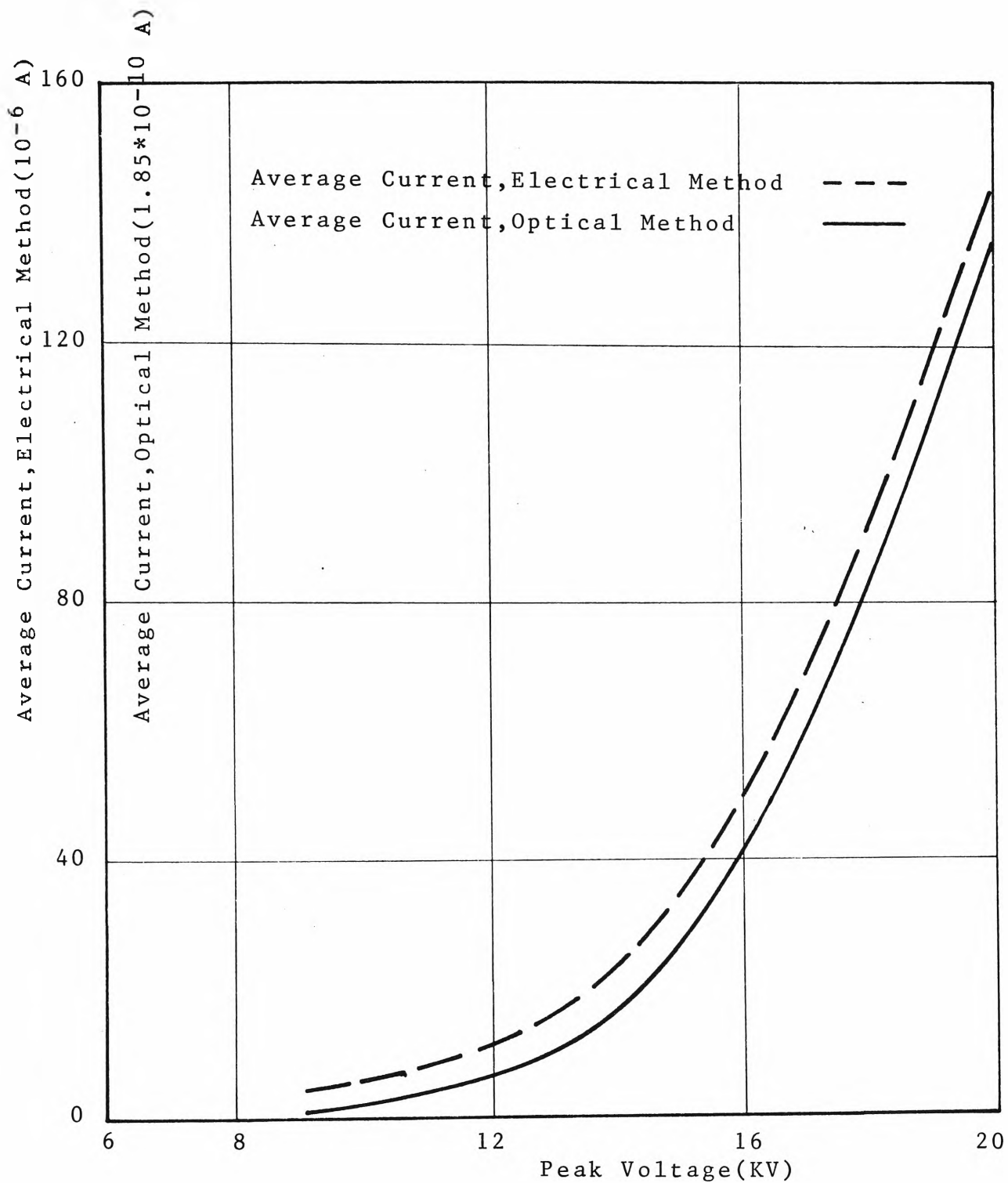


FIG. 5.5 AVERAGE CURRENT-PEAK VOLTAGE CHARACTERISTICS FOR PULSED VOLTAGE.

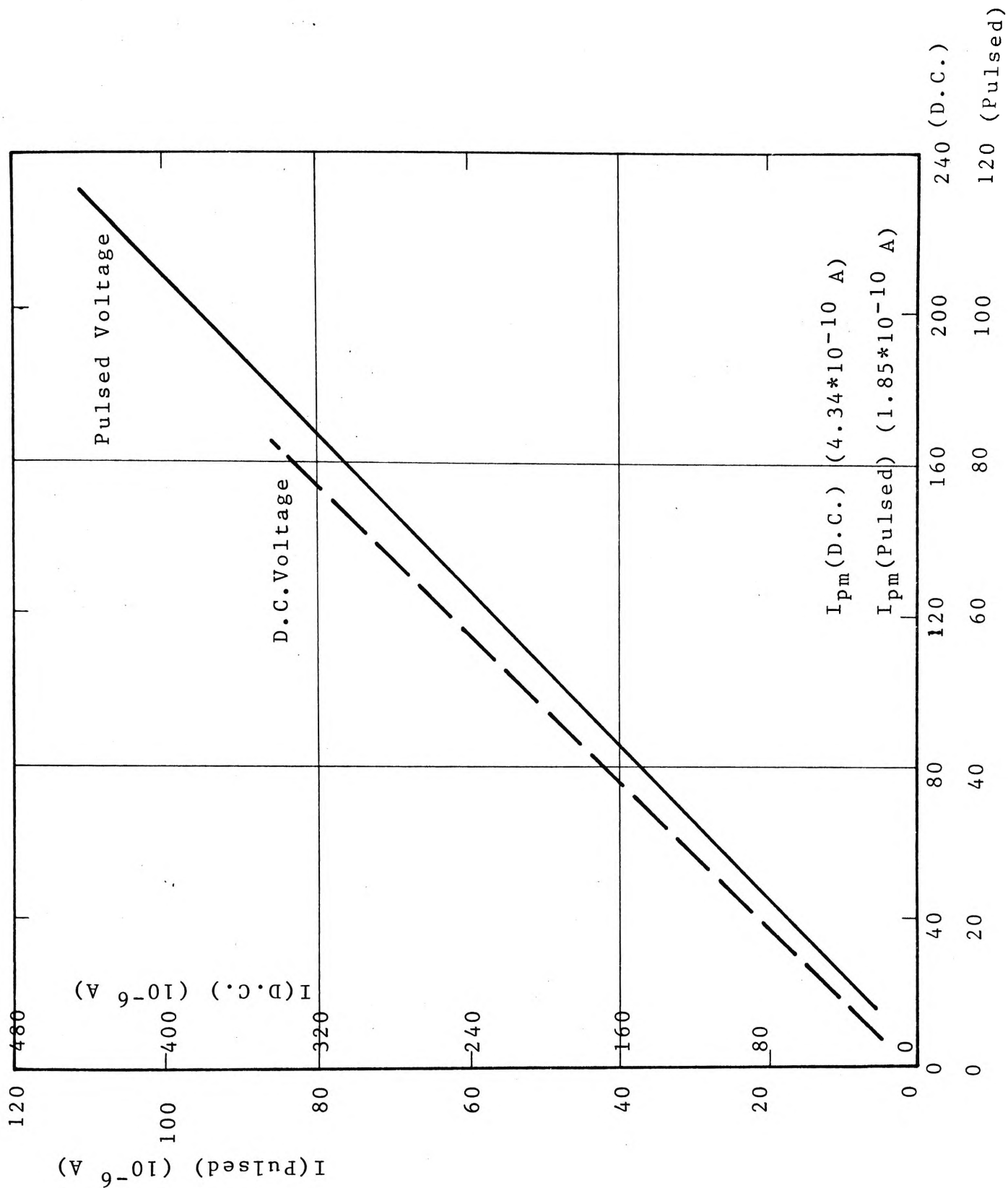


FIG.5.6 AVERAGE CORONA CURRENT - AVERAGE PHOTON CURRENT CHARACTERISTICS FOR D.C. AND PULSED VOLTAGES.

χ of the photomultiplier cathode is 0.1, the geometry factor, g can be estimated as the ratio of the length of the observed region and the distance between the discharge wire and the photomultiplier, it is 5×10^{-4} . The transmission coefficient, taking into account the transmission loss caused by the optical system can be estimated as equal to 10^{-1} . The amplification factor, G of the photomultiplier tube is 2×10^6 . The value of Q has been found to depend on the electric field-to-pressure ratio and the humidity of the gas. Under the experimental condition prevalent in this work, Q can be estimated by using the data obtained by Przybylski [12] for O_2 . Since the absorption of photons by O_2 is more predominant than that by N_2 , data obtained for O_2 can also be used for air without significant error. Q can be expressed as a function of pressure $1.5 \times 10^{-3} / (1 + P/P_0)$ where P_0 is the pressure at which half the excited atoms lose their excitation to radiationless collisions. Substituting $P_0 = 36$ mm Hg and $P = 760$ mm Hg into the above expression, Q is found equal to 6.78×10^{-5} , thus K is 3.4×10^{-4} . The inverse of the slope of the line in Fig. 5.6 gives K equal to 2×10^{-4} . The closeness of the two values of K does not necessarily mean the parameters should have the same values as selected, particularly the value of Q . However, this value seems to be reasonable since by assuming that the size of the avalanche, which is detectable to the optical system corresponds to the number of electrons at the onset of the self-sustaining discharge one can write:

$$g\chi DQ \exp\left(\int_0^{x_0} \alpha dx\right) = 1$$

where the exponential term denotes the amplification of the avalanche, the simplified form is used here for illustration (c.f. the complete expression in section 3.3.2) and the right hand side of the equation is the number of photo-electrons emitted from the cathode of the photomultiplier.

Substituting the values of all the parameters into the above expression, one gets:

$$\begin{aligned} \exp\left(\int_0^{x_0} \alpha dx\right) &= 1/g\chi DQ \\ &= 2.9 \times 10^9 \end{aligned}$$

This value is in the same order of magnitude with the number of electrons in one corona-current pulse at onset.

(ii) Pulsed Voltage

The relationship between the photomultiplier current I_{pm} and the average corona current, I is found by using the same approach as for D.C. voltage. The results are plotted against average and peak magnitudes of the pulsed voltage at rise time of 6 microseconds and shown in Fig. 5.5. It is seen that the linear relationship depicted by expression (5.1) also holds in this case.

From the recorded outputs of the pulsed power supply, the dependence of the average corona current and the average photomultiplier current on the pulse repetition rate can be found by extrapolation method, the details of which are shown in Appendix B. The results are summarised in Fig. 5.7 and 5.8 for frequency range of 70-150c/s. The relative position of the pulsed characteristics with respect to the D.C. characteristic indicates the filtering effect of the electrode system, the equivalent capacitance of which is

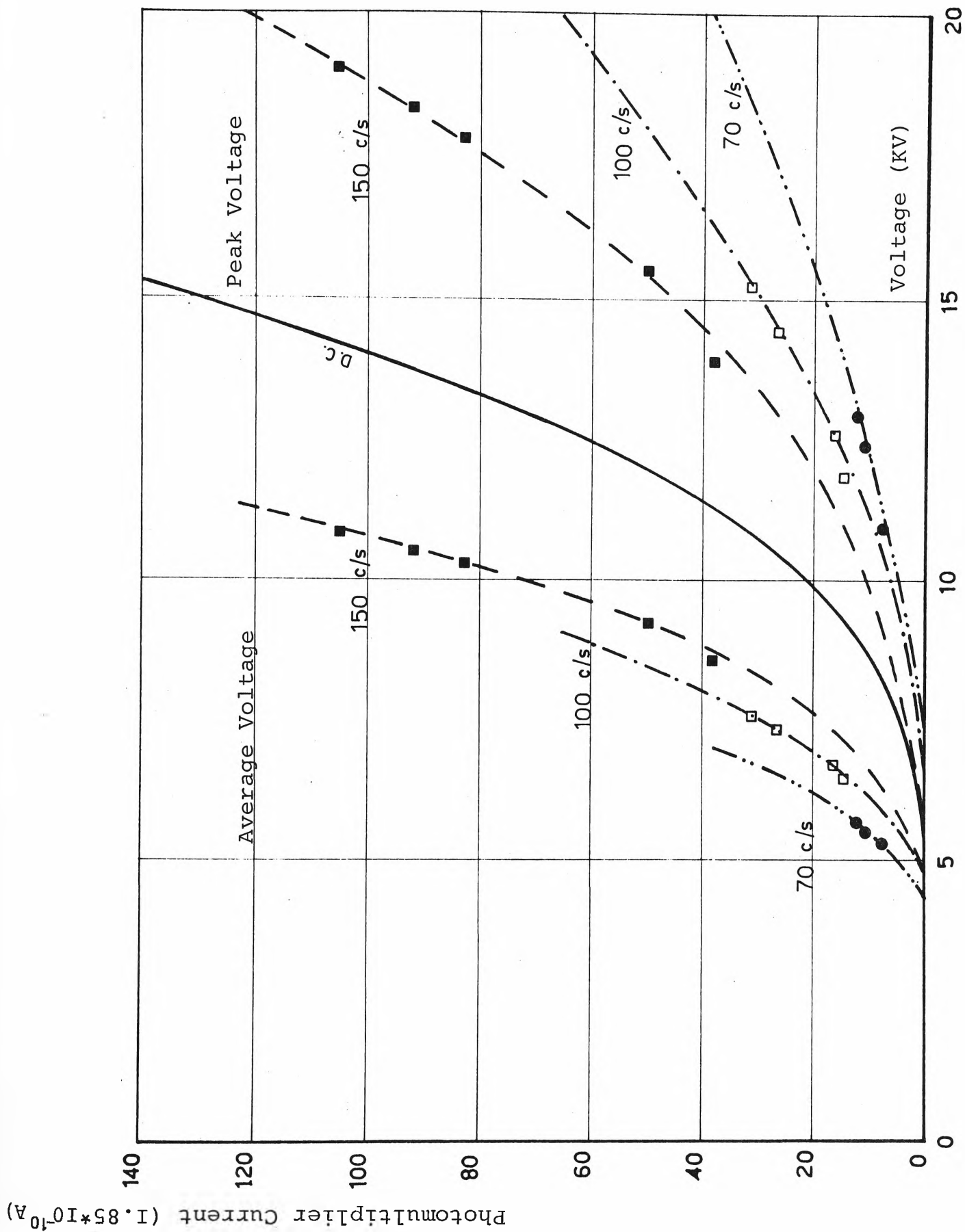


FIG. 5.7

AVERAGE PHOTOMULTIPLIER CURRENT-VOLTAGE CHARACTERISTICS FOR PULSED AT FREQUENCIES; 70, 100, 150 cycles/sec.

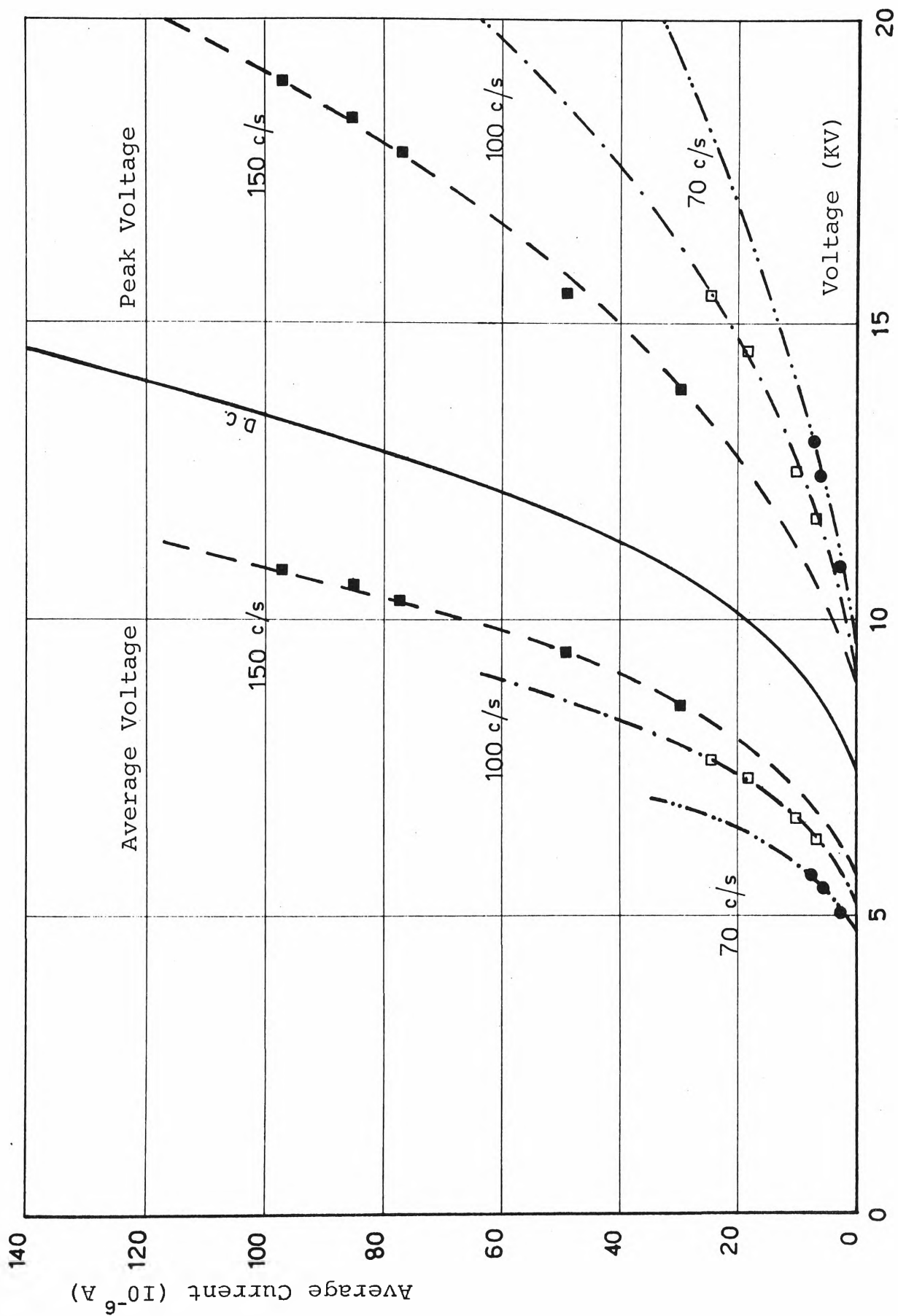


FIG. 5.8 AVERAGE CURRENT-VOLTAGE CHARACTERISTICS FOR PULSED VOLTAGE AT FREQUENCIES; 70, 100, 150 cycles/sec.

acting like a leaky condenser smoothing out the fluctuation of the applied pulsed voltage. At a given voltage level, the average value of the pulsed voltage is directly proportional to its repetition rate and under steady state condition this gives rise to more corona current. This dependence of the current-voltage characteristics on the pulse repetition rate will be discussed in full detail in section 5.3.2.

The linear relationship between I_{pm} and I is indicated in Fig. 5.6 for various frequencies, the inverse of the slope of the straight line gives the value of K equal to 1.85×10^{-4} which is fairly close to the value for D.C. voltage (2×10^{-4}).

(c) Comparison between D.C. and Pulsed Voltages

The appearance of the discharge along the wire cathode at onset level is observed to be somewhat different in the cases of D.C. and Pulsed voltage. The discharge appears as a glow existing along the wire under pulsed energisation, while it is spotty under D.C. energisation. Since the discharge wire had been conditioned by electrifying it with D.C. voltage for one hour under normal room air before measurements were taken, the difference in the appearance could be caused by the different modes of secondary emission. The following interpretation should be limited to the corona discharge on a wire cathode which has been already oxidised by previous discharges (the discharge wire has been subjected to chemical action by O_3 and NO_2).

When the electric field at the cathode is sufficient to cause the local ionisation at the cathode to become a self-sustaining discharge, the secondary emission is caused by the

photoelectric effect at the cathode surface. The corona discharge initially appears as a glow discharge at one point which has the highest value of γ_p , the photoelectric emission coefficient and spreads along the wire cathode as the applied voltage slightly increases. After some time the glow discharge contracts to several spots when the positive ion space charge in the vicinity of the cathode enhances the field so that positive ion impact is sufficiently strong to cause secondary emission (this corresponds to the pattern observed in Fig. 5.3 at 9.5 kV). This immediately alters the condition on the surface of the cathode and causes Trichel pulses to appear.

Under the application of pulsed voltage, because of its short duration, the self-sustaining discharge at the cathode is more likely caused by the photoelectric emission. The positive ion space charge, at just above the onset level, is too weak to enhance the cathode field sufficiently and positive ions require a considerable period of time to reach the cathode. As a result the discharge under pulsed energisation appears as a glow along the discharge cathode (i.e. at 9.5 kV in Fig. 5.2).

As the peak voltage is much higher than the onset level the accumulation of positive ions makes the condition of the space charge in the neighbourhood of the discharge wire become similar to that under D.C. voltage and the localised discharge sets in. Because of the slow decaying rate of the applied voltage pulse, at the end of one pulse, part of the positive ions will have reached the cathode and get neutralised and the rest stay near the cathode. In the meanwhile

the negative ion space charge moves away from the accumulation region, thus the possibility of a discharge between positive and negative ion space charges, as the cathode is grounded, is very small.

It is, therefore, plausible to hypothesise, that for the condition studied in this investigation, no essential difference has been shown to exist between the discharge pattern on the wire electrode when energised by a pulsed voltage from that produced by a smooth D.C. negative voltage. The peak value of the pulsed voltage, however, has to be considerably higher than that of the D.C. voltage before similar patterns are reproduced, and when the total average corona currents are the same, this also means that the space charge conditions in the air gap are the same, then the shapes of the radiation curves are similar [64].

5.2.3 The Corona Current Waveshape

5.2.3.1 Measurement of the Corona Current Pulse

Fig. 5.9 illustrates the set-up for measurement of corona current waveshape. Experimental results and theoretical studies have shown that the rise time of the current pulse is in the order of tens of nanoseconds. It is, therefore, desired that the time constant of the measuring RC network should not exceed 10^{-8} sec.[63]. The shunt capacitance is determined mainly by the vertical amplifier input capacitance of 47 pf and protective four-layer diodes of approximately 40 pf. The shunt resistance is selected as 50Ω to match the characteristic impedance of the coaxial cable terminated with a 50Ω resistor. Two kinds of display are obtained with the experimental set-up. One is used to

PULSED POWER
SUPPLY
(BRANDELBERG)

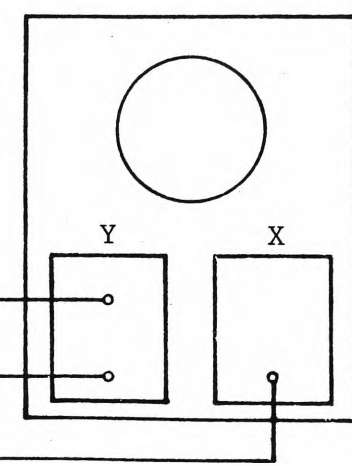
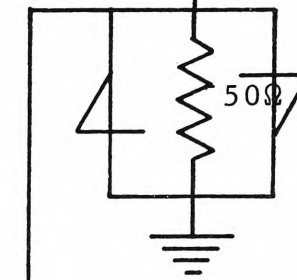
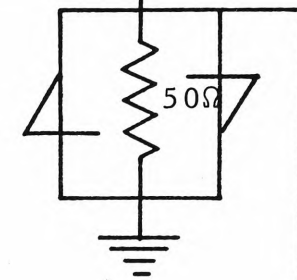
CATHODE

BALANCING
CAPACITOR

ANODE

H.V. PROBE
(P6015)

ATTENUATOR &
COMPENSATOR



	S1	S2	Y
LISSAJOUS FIGURE	1	1	3A9
SINGLE PULSE	2	2	3A6

FIG. 5.9 DIAGRAM OF SET UP FOR
MEASUREMENT OF CORONA
CURRENT PULSE.

locate the phase of corona current pulses with respect to the applied pulsed voltage by using Lissajous figure technique, and the other is used to observe the single pulse waveshape. The vertical differential-amplifier 3A9 is used to reject the common displacement components that exist in the electrode system and the balancing capacitor. The bandwidth of the plug-in 3A9 is 100Hz-300KHz, adequate for displaying the Lissajous figure. The corona current pulse is displayed by means of the 3A6 plug-in amplifier having a rise-time of 35 nsec and 10 MHz bandwidth. These factors and the maximum sweep rate of 100 nsec/cm of the time base unit limit the resolution of the current waveshape. However, limited accuracy and resolution of this measurement is not considered as a serious shortcoming for the intended comparison between the experimental results and calculated pulse shape, since semi-empirical values are selected for certain parameters used in the theoretical computations. The balancing capacitor is not required in this measurement, since the amplitude of the corona current pulse is much higher and its duration is much shorter (few hundred nanoseconds) than that of the displacement current. A proper adjustment of the triggering level and suitable choice of the sweep rate are sufficient to obtain a stable display. The electrode system consists of a hemispherically capped cylinder of platinum used as the discharge cathode and a stainless steel plane. The pulsed power supply which was described in Fig. 3.11 is used to energise this system. It produces pulses of constant rise time, and frequency in the range from 13-100c/s. The experiment was carried out at room

temperature and atmospheric air.

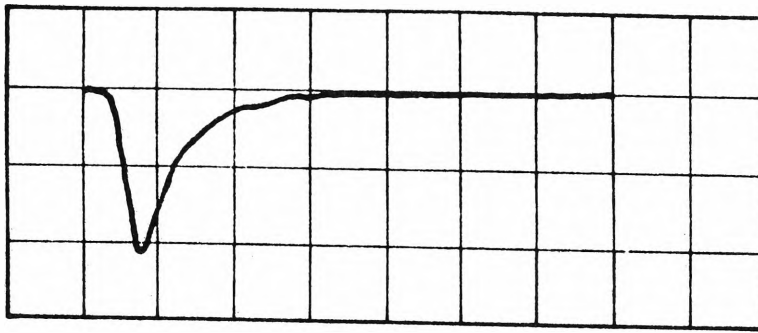
5.2.3.2 Results and Discussion

(a) Results

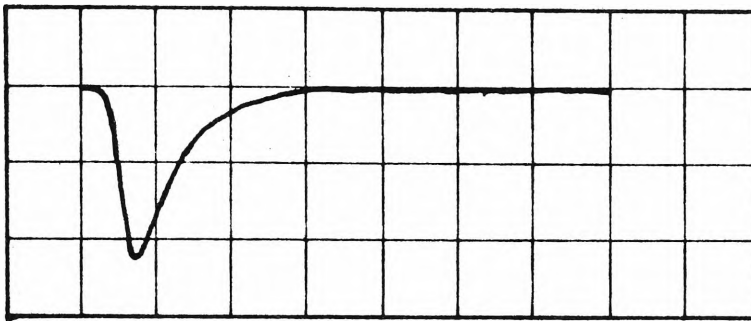
Photographic records of the experimental results are reproduced and shown in Fig. 5.10 and 5.11 for gap length of 2.5 cm, point radius of .045 cm for both pulsed and D.C. voltages. The results obtained with pulsed voltage do not show marked dependence on the pulse repetition rate and it is sufficient to present the results obtained at 30c/s. The current pulse rise time is limited by the response time of the oscilloscope which equals 30×10^{-9} seconds and its duration is roughly 300×10^{-9} seconds.

In order to observe the phase relationship between the corona current pulses and the applied voltage pulse, a slower sweep speed was used to obtain a complete picture of one voltage pulse. The results are reproduced from oscilloscopic records and shown in Fig. 5.12 which illustrates the composite picture of corona current pulses superimposing on the capacitor charging current. The number of current pulses created over one complete voltage pulse is proportional to its magnitude. The distribution of the current pulses is most dense around the region where the voltage pulse obtains its peak value. Because of the continuous changing of the voltage pulse magnitude, the dependence of the current pulse frequency and amplitude on the magnitude of the applied voltage is interpreted by means of the following method.

The voltage pulse is considered as consisting of several equal step increments, the step size is arbitrarily



a) $V_p = -8 \text{ kv}$



b) $V_p = -12 \text{ kv}$

FIG.5.10 CORONA
CURRENT PULSES FOR
PULSED VOLTAGE

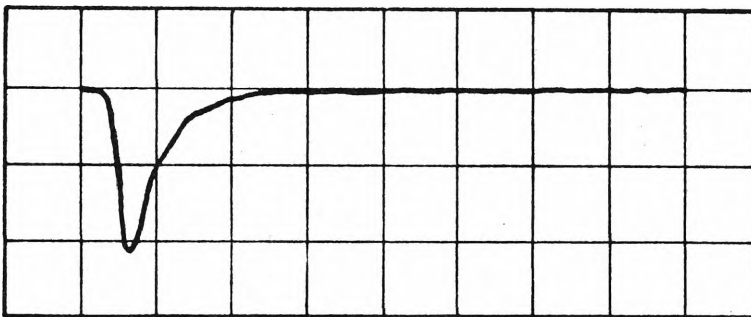
G.L.=2.5 cm

P.R.=.045 cm

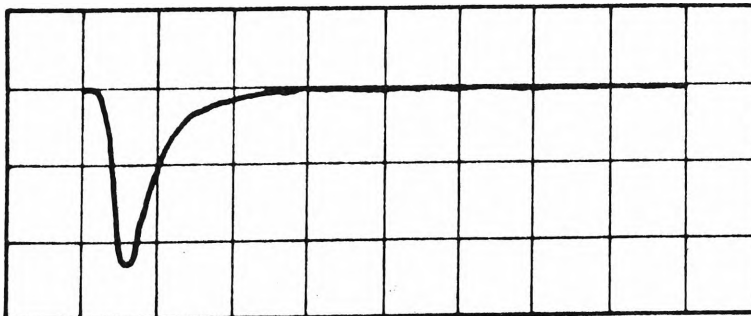
$F = 30 \text{ c/s}$

Vertical Axis=
I mA/div

Horizontal Axis=
.1 microsec/div



a) $V = -8 \text{ kv}$



b) $V = -12 \text{ kv}$

FIG.5.11 CORONA
CURRENT PULSES FOR
D.C. VOLTAGE

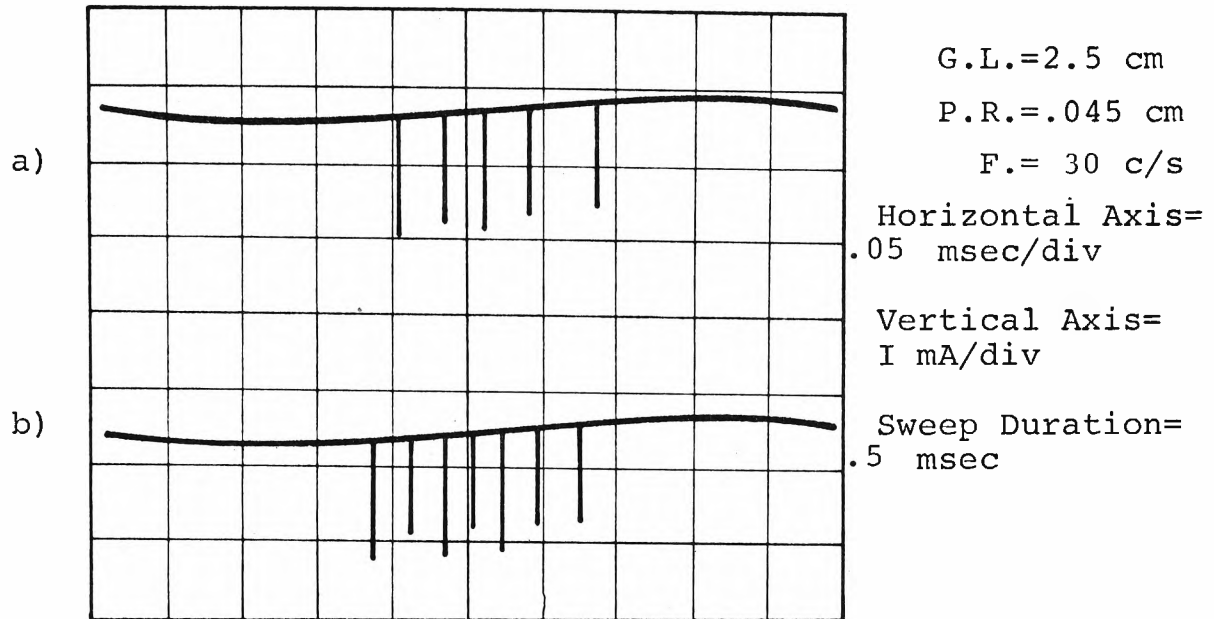
G.L. = 2.5 cm

P.R. = .045 cm

Vertical Axis=
I mA/div

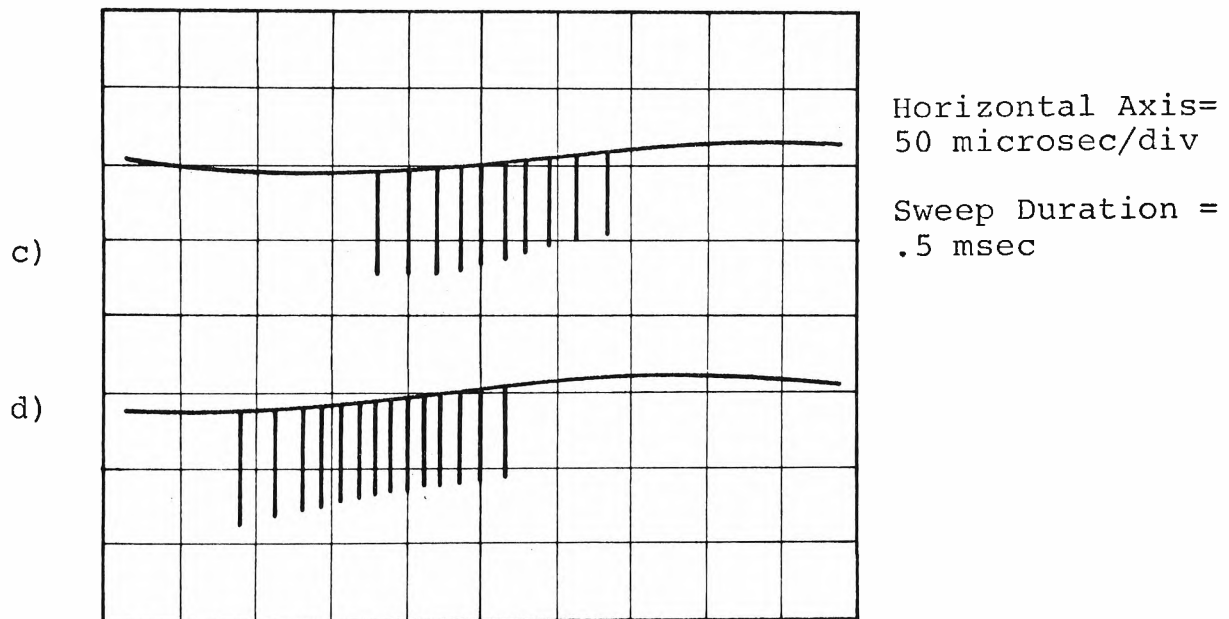
Horizontal Axis=
.1 microsec/div

FIG.5.12 DISTRIBUTION OF CORONA CURRENT PULSES
FOR A POINT-TO-PLANE SYSTEM



a) $V_p = -9$ kv

b) $V_p = -10$ kv



c) $V_p = -11$ kv

d) $V_p = -12$ kv

chosen to be 10%. The voltage pulse will, thus, obtain 10,20,...,90,100,90,...20,10% of its amplitude respectively over one complete cycle. By finding the number of current pulses existing in each voltage level, the distribution of current pulses in relation to the time interval between successive pulses and the current pulse amplitude can be found. The results are shown in Fig. 5.13 for various peak voltages and gap length of 2.5 cm. In the figure, the distribution of number of pulses versus time interval between pulses is plotted for 90,100,90% of peak voltage and for a complete pulse. Fig. 5.16 is the plot of number of current pulses versus their amplitudes for a complete applied voltage pulse at peak voltage of 14 and 16 kV. The dependence of number of pulses on the percentage level of pulsed voltage is found by dividing the number of current pulses which exist over various voltage levels by the duration of one complete sweep on the oscilloscope. The results are shown in Fig. 5.15. The mean amplitude of the current pulses is found and its relationship with the percentage of the applied voltage is plotted in Fig. 5.17.

(b) Instantaneous Characteristics of Current Pulse

(i) Low Voltage Level

The corona current pulses generated in a point-to-plane system have been investigated under D.C. and pulsed energisation. The presence of current pulses over the part of the applied voltage pulse above the corona onset level is predictable from the work on the discharge pattern presented in section 5.2.3.1. The pulses are obviously Trichel pulses and the measured rise and decay times are similar to those

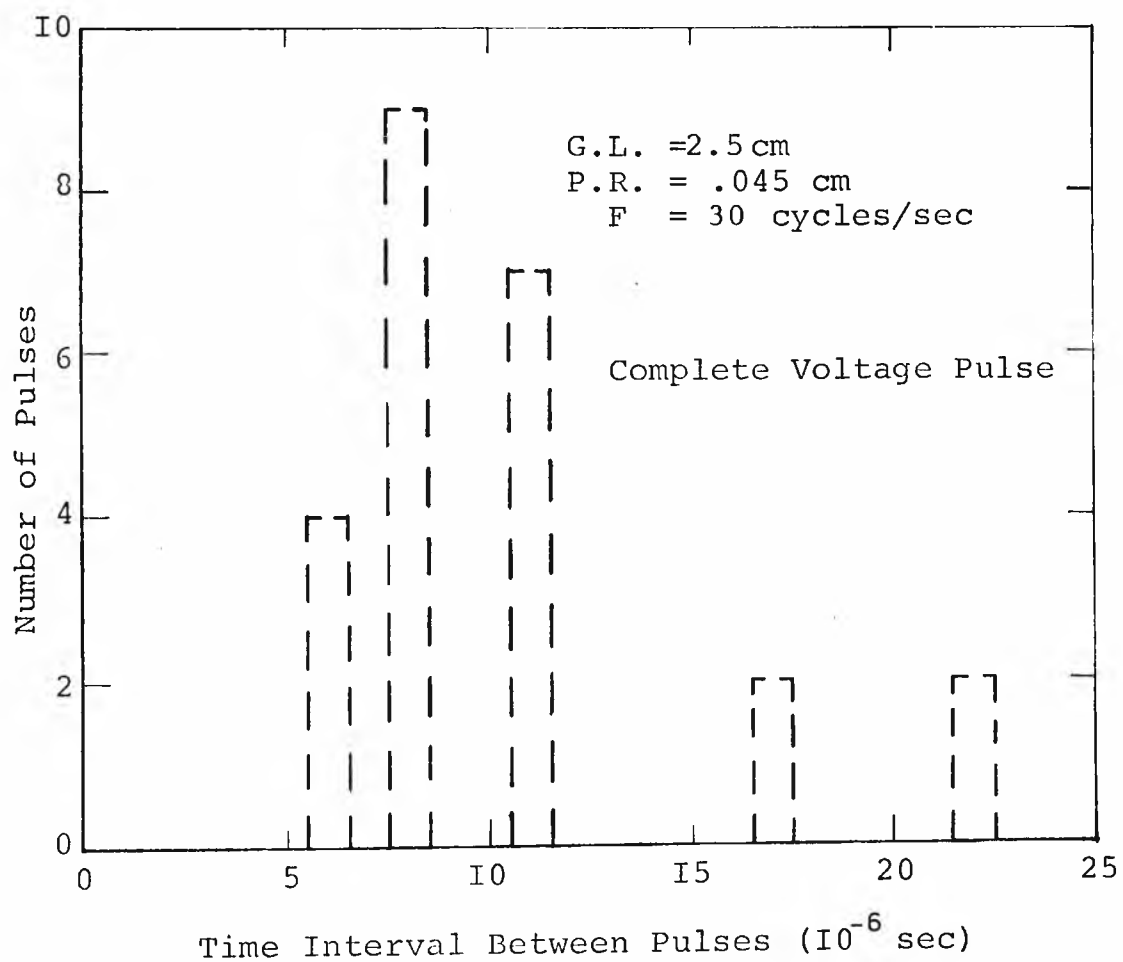
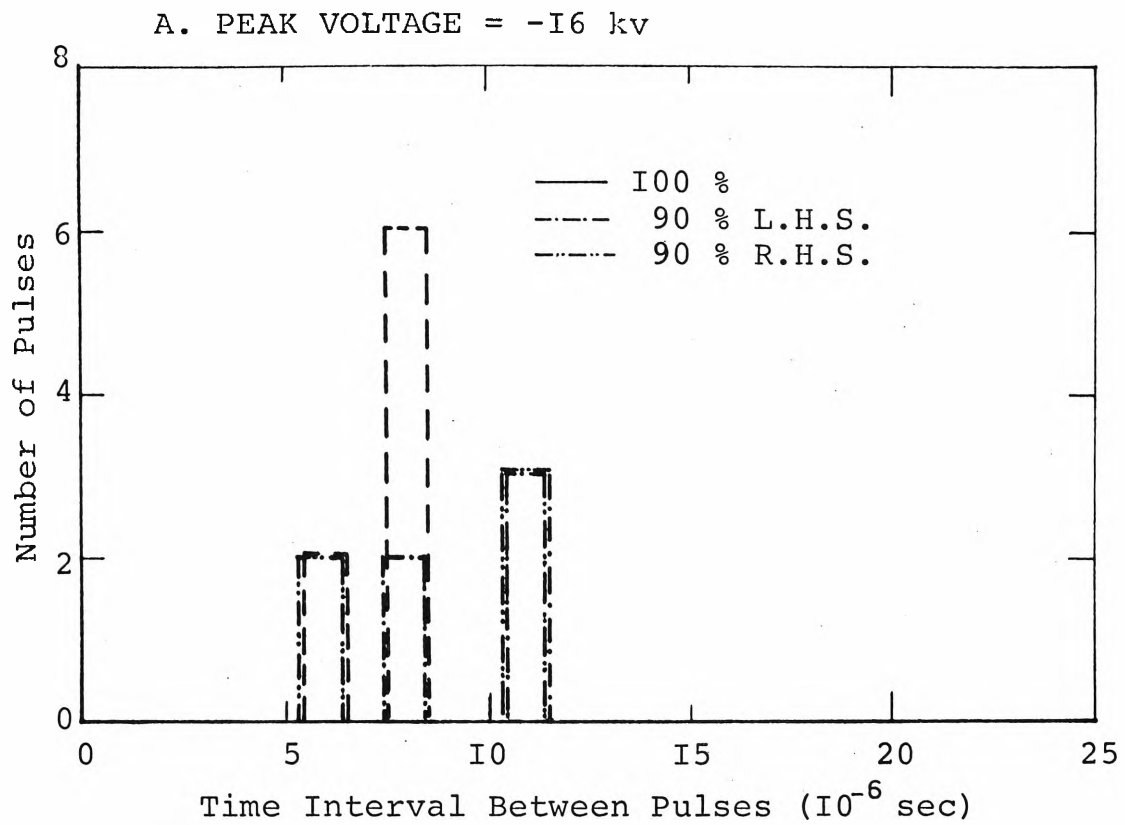


FIG.5.13 DISTRIBUTION OF NUMBER OF PULSES wrt TIME INTERVAL BETWEEN PULSES.

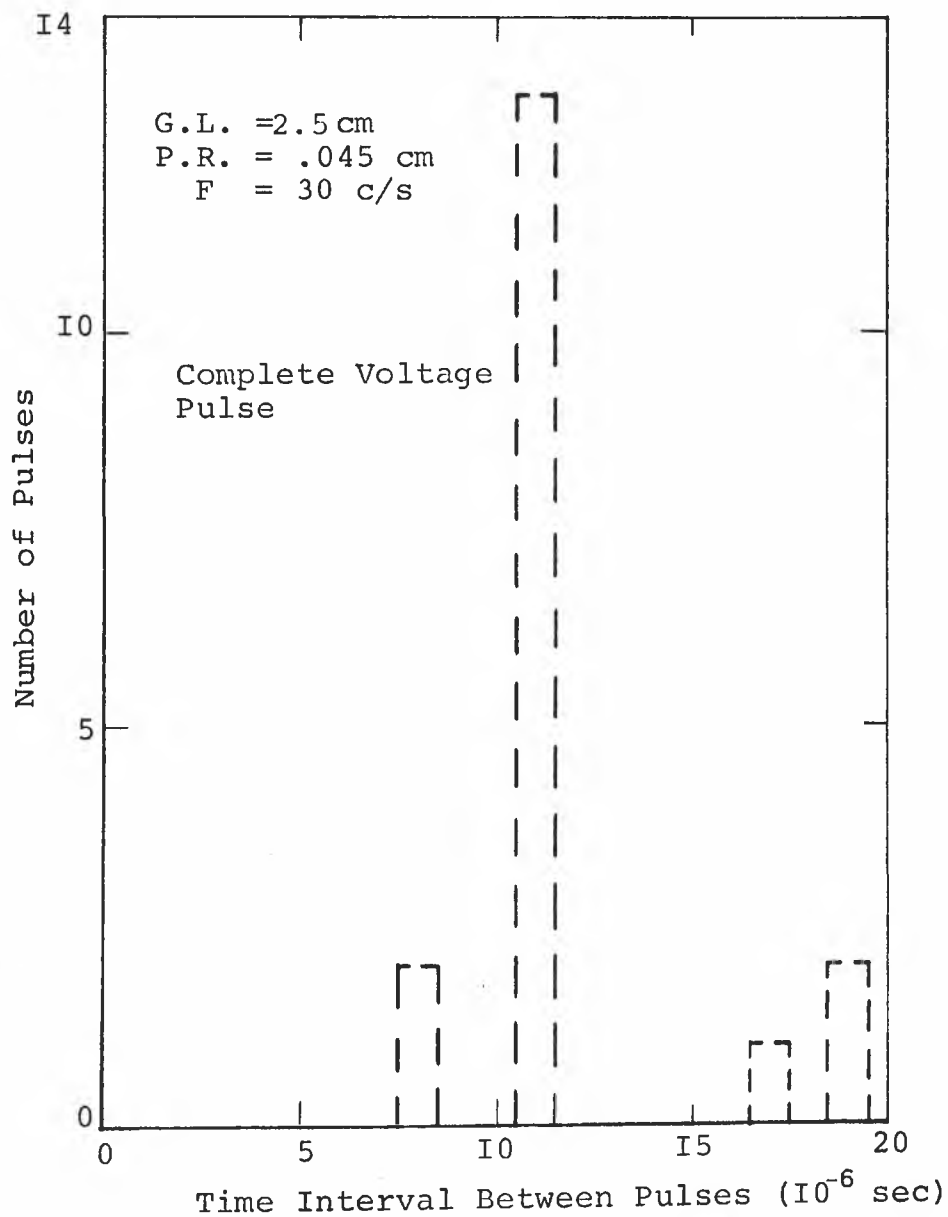
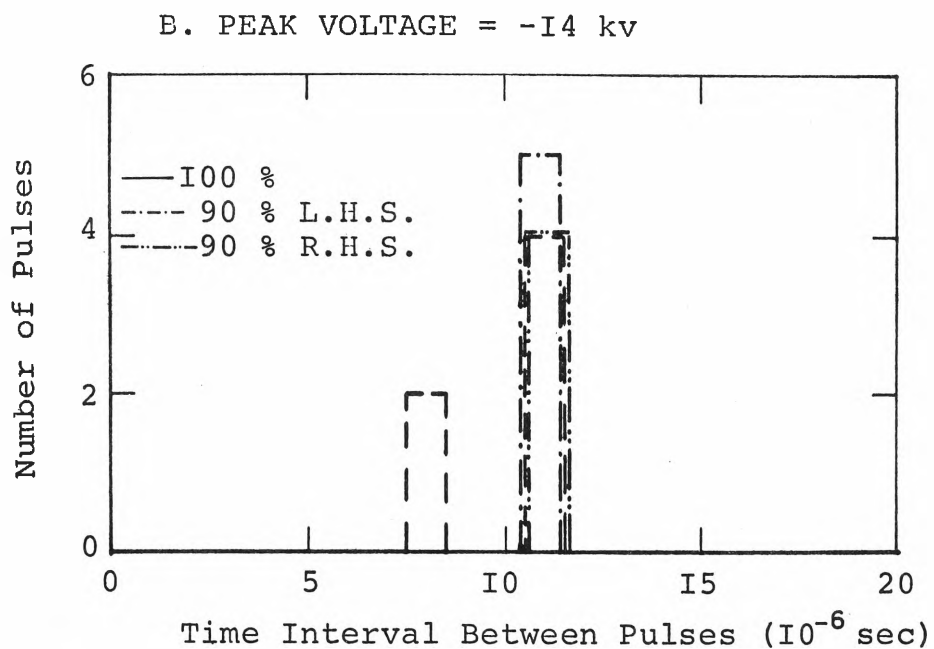


FIG.5.13

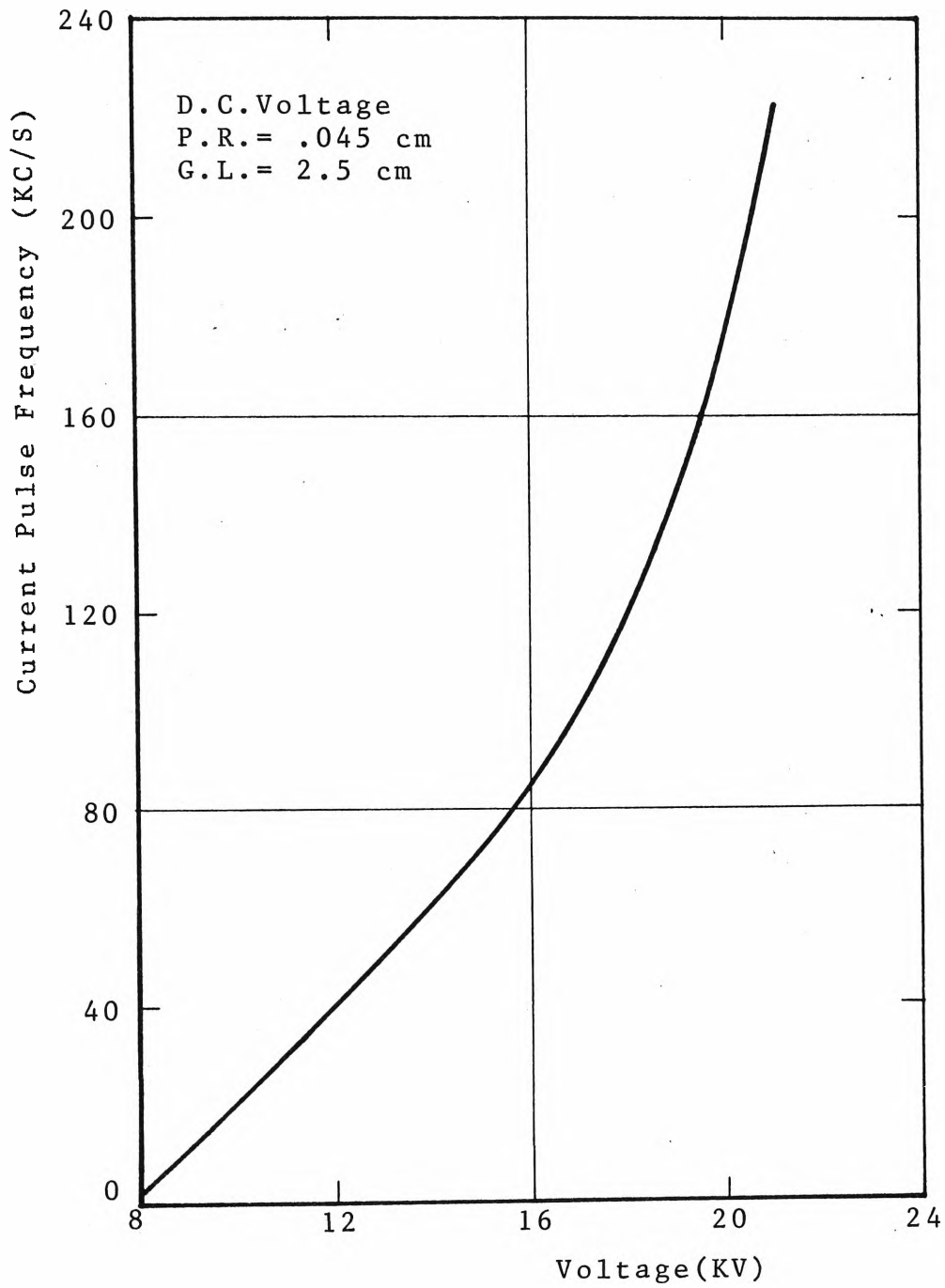


FIG. 5.14 FREQUENCY Vs VOLTAGE CURVE

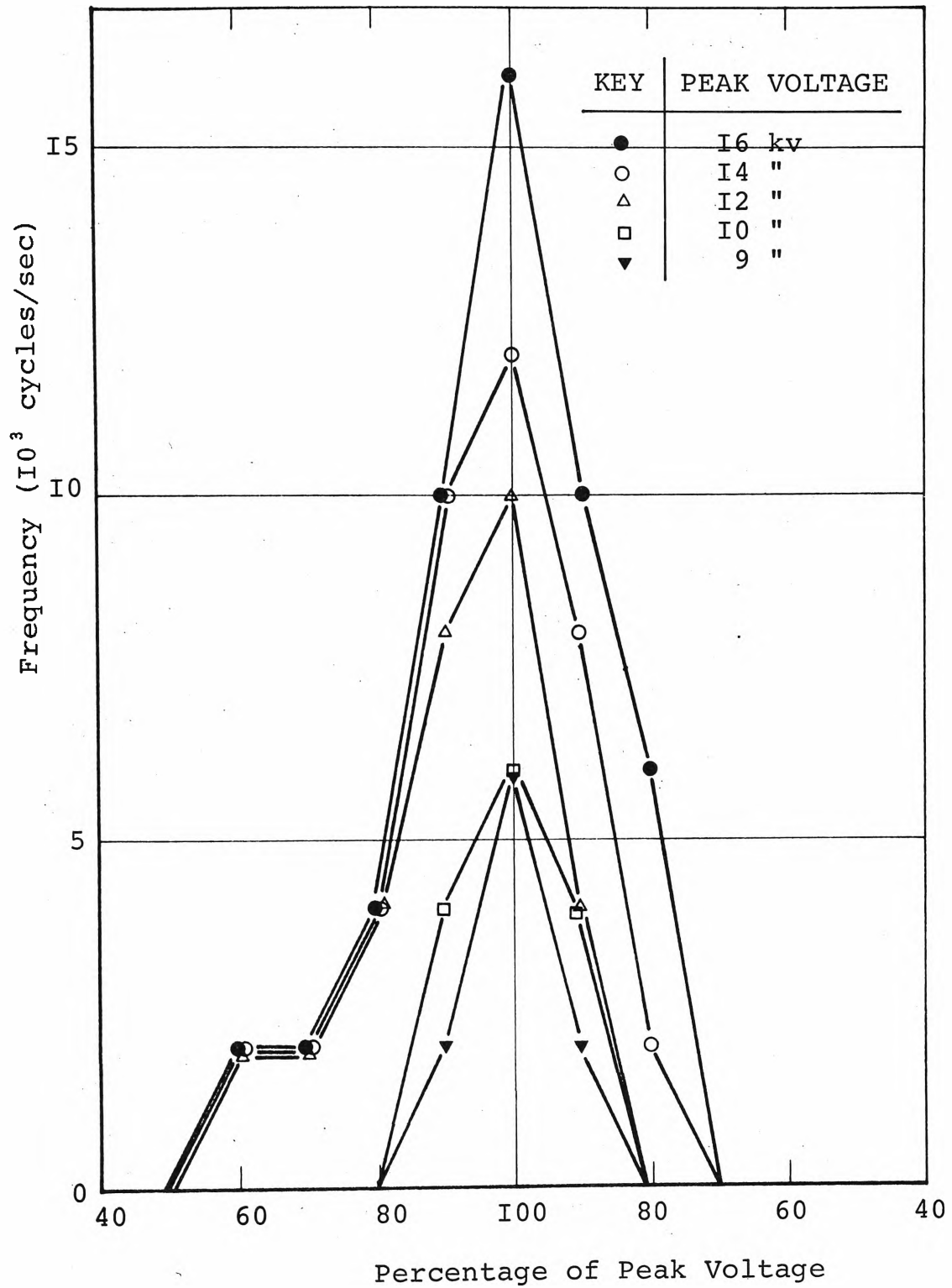


FIG.5.15 DISTRIBUTION OF FREQUENCY wrt PERCENTAGE LEVEL OF PULSED VOLTAGE.

G.L. = 2.5 cm

P.R. = .045 cm

F. = 30 cycles/sec.

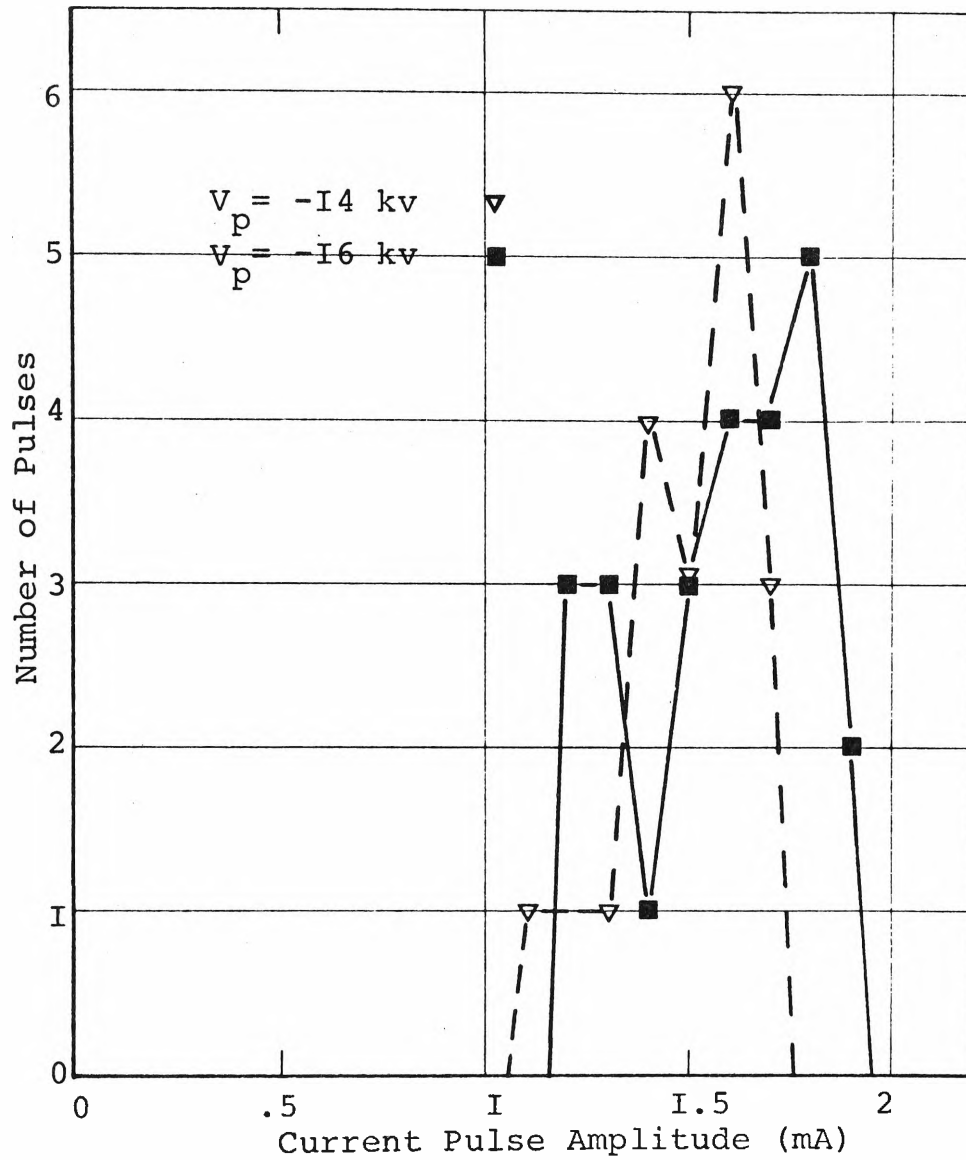


FIG.5.16 DISTRIBUTION OF NUMBER PULSES wrt
CURRENT PULSE AMPLITUDE

G.L. = 2.5 cm

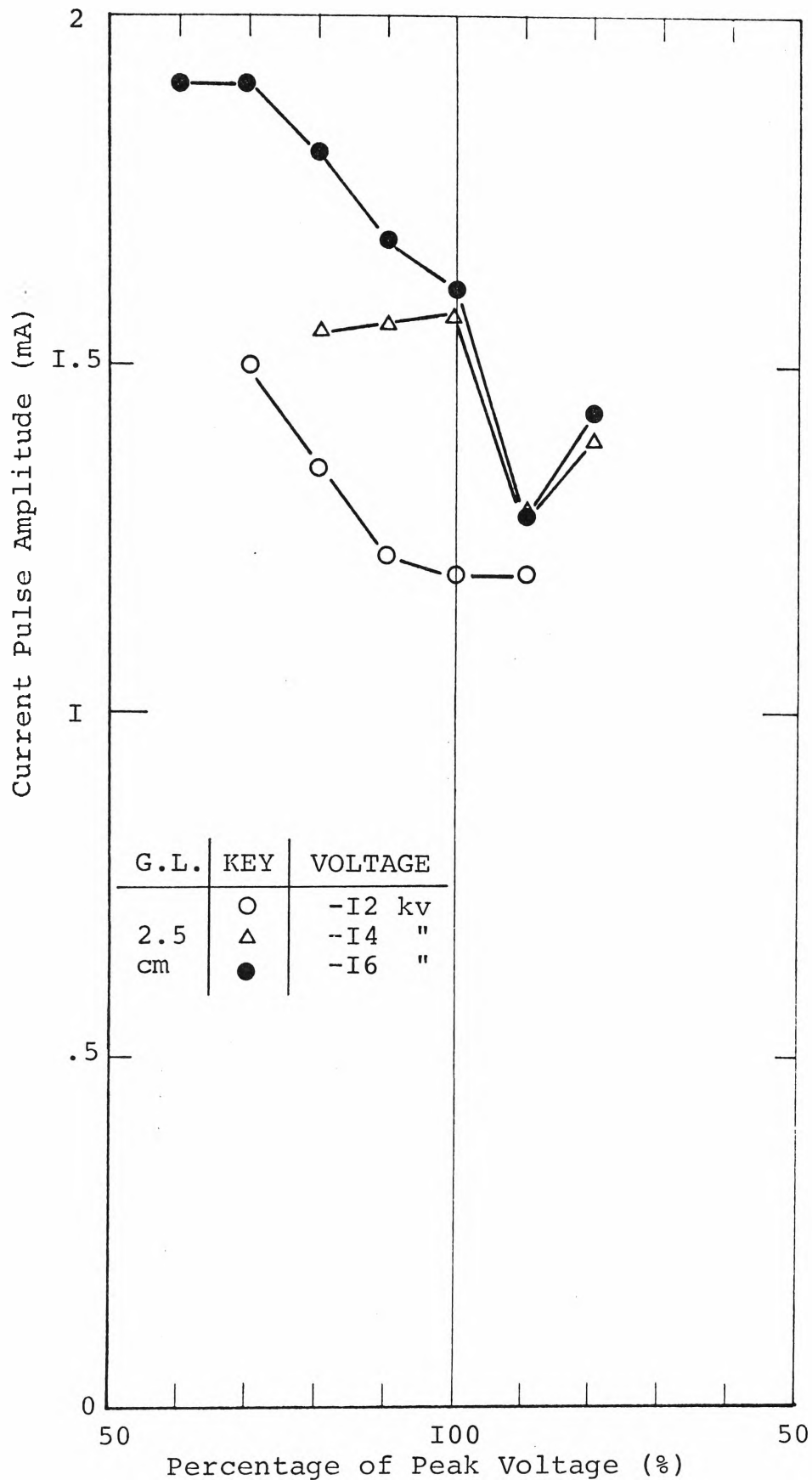


FIG.5.17 DISTRIBUTION OF CURRENT PULSE AMPLITUDE wrt PERCENTAGE OF VOLTAGE.

obtained with D.C. voltage. The Trichel pulse is formed by the ionising collisions taking place in the vicinity of the highly-stressed cathode. The created avalanches stop growing when the cathode field is reduced by negative ion space charge formed by electron attachments. The current pulses measured represent the currents induced in the external circuit by the fast movement of the electrons in the avalanches.

It has been well known that the shape and size of the negative corona current pulse, under D.C. energisation, do not change significantly with voltage level. This point is confirmed by the results obtained with D.C. voltage at voltage 8 and 12 kV (Fig.5.11). Somewhat similar results are observed by combining Fig. 5.10 and 5.12 for pulsed voltage. It can be seen that at just above the onset level (8 kV) the current pulse shapes for both cases are the same. The pulse detected at peak voltage of 12 kV is in fact the same as that at 8 kV since the oscilloscope was triggered by the first current pulse i.e. pulse at onset. However, the complete picture of one applied voltage pulse at 12 kV (Fig. 5.12 d) does indicate that the amplitude of the corona current pulses does not change very significantly with the voltage level. From the picture of the current pulse it can be estimated that the number of electrons forming one Trichel pulse is 1.4×10^9 .

The similarity between current pulses obtained with D.C. and pulsed voltages is further supported by the theoretical study of the Trichel pulse discussed in chapter 3. The formation time of the pulse is so short that the pulsed

nature of the applied voltage can have no significant effect on the basic processes. As the voltage pulse magnitude is increasing the applied cathode field also increases but the net field in the ionisation region remains approximately unchanged because of the diminishing effect of negative ion space charge on the cathode field. The effect of increase in applied potential is to increase the potential drop in the transport region, this results in the negative space charge with its increased density being removed from the ionisation region faster. At the end of one applied voltage pulse, because of the slow decay rate of the voltage, the positive ions which have been generated during the voltage pulse, are partly neutralised on arrival at the cathode and partly remain in the proximity of the cathode. The density of the positive space charge is so small that at the succeeding voltage pulse the ionisation processes are hardly affected by its presence. This is substantiated by the symmetrical distribution of the number of current pulses with respect to the percentage level of the applied voltage (Fig. 5.15 at 9 and 10 kV).

(ii) High Voltage Level - Effects of Space Charges

At voltage level much higher than the corona onset (≥ 12 kV), the effects of positive ion space charge on the ionisation activity in the proximity of the cathode can be observed. The positive space charge generated by corona discharge in one voltage pulse enhances the field strength at the cathode during the rising part of the following pulse until it is neutralised by electrons and negative ions which have been generated by ionisation processes in that succeed-

ing rising part of the voltage pulse. This means that in the rising part of the negative voltage pulse, the positive space charge from preceeding pulse increases the cathode field. Avalanches are formed by ionising collisions in the proximity of the cathode. The electrons in the avalanches form negative ions by attachment in the accumulation region (Fig. 3.4, Section 3.3.2). The negative space charge weakens the cathode field and the ionisation is quenched when the net cathode field is below the threshold field for avalanche formation. Ionisation processes cannot start again until the quenching negative space charge has been removed sufficiently from the ionisation zone. The removal of negative space charge depends on the total field at the cathode. The number of current pulses existing over each part of the applied voltage pulse should then be dependent on the total cathode field. The positive ion space charge also causes a concomitant effect on the size of the Trichel pulse. Fig. 5.15 indicates that there is a larger number of pulses in the rising part of the voltage pulse (at 12, 14, and 16 kV) than that in the decaying part. This is caused by the enhancement of the cathode field at the early part of the voltage pulse by the presence of positive ion space charge. The enhancing effect becomes less significant as the voltage ascends to its peak value because of the neutralisation by negative ion space charge. As the voltage pulse declines from its peak the mobility of the negative ion space charge becomes retarded by the diminishing effect of the negative space charge on the cathode field. Fig. 5.17

shows that the current pulse amplitude varies in the same manner as its frequency, this is because the residual positive space charge reduces the quenching effect of the negative space charge on the cathode field and thus facilitates the formation of bigger current pulses. On the contrary the copious accumulation of negative space charge which is formed as the voltage declines causes the ionisation processes to be quenched much sooner.

(c) Average Characteristics of Current Pulse

In spite of the effects of the space charges on the instantaneous characteristics of the corona current pulses, it is of interest to note that the average characteristics under pulsed energisation appear to follow the same pattern as with D.C. one. This is substantiated by the distribution of a number of current pulses with respect to the time intervals between pulses as shown in Fig. 5.13 for peak voltage of 16 and 14 kV respectively. The mean value of the distribution for one complete voltage pulse gives the mean frequency at that voltage. This value increases as the peak voltage increases (i.e. @ 14 kV, the mean frequency equals 80 Kc/s and @ 16 kV, it equals 96 Kc/s). The frequencies of the current pulses under D.C. energisation are 67 Kc/s and 86 Kc/s at 14 and 16 kV respectively, as they are shown in Fig. 5.14. The apparent peaks in Fig. 5.13A and 5.13B are only an indication that the continuous variation of the applied voltage pulse can only be approximated and for different step size the distribution diagram will show peaks at different time intervals. It is also interesting to note that when the instantaneous voltages are

the same the distribution diagrams have peaks at the same time interval i.e. the 90% of the peak voltage of 16 kV is 14.4 kV, the distributions of which have peaks at the time interval of 11 microseconds (Fig. 5.13A - Top Figure), this also is the time interval at which the distribution of 100% of the peak voltage of 14 kV has its maximum (Fig. 5.13B -Top Figure). This means that the frequency of the current pulses is the same at the same bulk space charge condition.

Figure 5.16 indicates that the distribution of number of pulses with respect to the pulse amplitude has the same mean value at different voltage levels, which is equal to 1.53 mA at 14 kV and 1.57 mA at 16 kV. The independence of the mean amplitude of the current with the voltage is concurrent with that observed with D.C. energisation.

5.3 Associated Phenomena in the Low Field Region

5.3.1 Introduction

In the previous sections two important features of the discharge characteristics have been investigated. These characteristics represent the ionisation process taking place in the neighbourhood of the highly-stressed cathode. The transport of negative ions from the buffer region to the plane anode results in an average current flow in the external measuring circuitry. This average current together with the average of the Trichel current pulse caused by the ionisation process and the quenching effect of negative ion space charge is commonly known as the average corona current. Because in an electrostatic precipitator the particles are charged mostly in the low field strength region (the buffer zone) and driven toward the collecting plane by the resultant

effect of the applied electric field and the turbulence caused by the electrical wind, it is of interest to investigate the bulk characteristics of the ionisation process and the electrical wind when the electrode system is clean.

5.3.2 Current-Voltage Characteristics

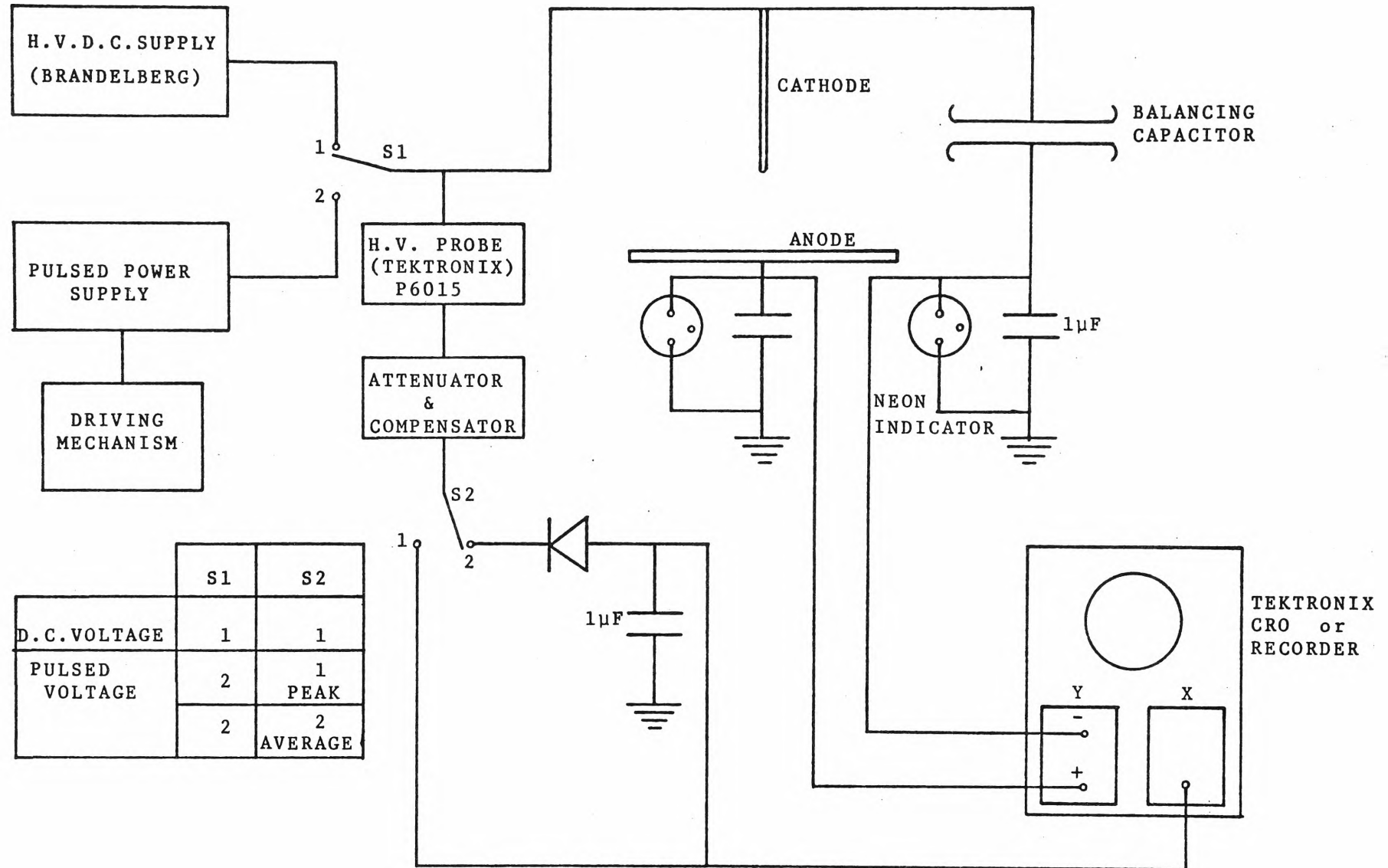
5.3.2.1 Experimental Technique

The set up used to plot the average corona current against peak and average pulsed voltage simultaneously is shown in Fig.5.18. The pulsed power supply has been described in section 4.3.3, Fig.4.11. The method of plotting the current-voltage characteristics with moderate accuracy is adequate to detect significant changes in the characteristics under different conditions of electrode, D.C. and pulsed voltages. Experience shows that the response time at each voltage setting is usually less than 10 seconds for a step increase of 1 kV. A voltage sweep rate of 10kV/minute was chosen.

The inconsistency of the results obtained under similar conditions by means of this measuring technique is less than 5% which is considered satisfactory. The sweep is controlled manually on the D.C. high voltage supply and automatically by utilising a D.C. motor to drive the output level knob on the pulsed power supply. The sweep speed is adjusted by varying the field voltage of the driving motor.

The external current measured from the collecting plane consists of two components, the displacement current and the corona current. The displacement is caused by the charging of the equivalent capacitor of the electrode system.

FIG. 5.18 DIAGRAM OF SET UP FOR MEASUREMENT OF CURRENT-VOLTAGE CHARACTERISTICS



Assuming the electrode capacitance is constant with respect to the applied voltage, the displacement current can be balanced out by using a balancing capacitor of the same value as the equivalent capacitance. The output currents are averaged by means of RC network forming by $1\mu\text{f}$ capacitor and the input impedance of the Tektronix oscilloscope of 1 M Ohms , whose product of 1 sec is adequate to give a smooth trace on the oscilloscope. These outputs are connected to a plug-in differential amplifier (3A9) that rejects the common component and displays the average corona current. The inputs of the amplifier are protected from sparkover voltage by means of small neon indicators. The pulsed voltage is measured by the use of a high voltage probe (Tektronix P6015) in conjunction with a compensator box (Tektronix) whose output is connected to the horizontal amplifier of the oscilloscope. To obtain the average pulsed voltage, a network comprising a rectifier diode, a capacitor and the input impedance of the oscilloscope is used. The time constant is approximately 1 second , sufficient to produce the average of voltage pulse of $150/150\text{ microseconds}$ waveshape.

The experiments are carried out under normal laboratory conditions at atmospheric pressure and no correction is made for the air humidity. Results are taken under similar conditions for both D.C. and pulsed voltages for comparison.

5.3.2.2 Results and Interpretation

From the oscillographic photographs and chart recorder output, the current-voltage characteristics of two gap lengths are replotted on the same graph for comparison. The

results are shown in Fig.5.19 and 5.20 for D.C. and pulsed voltages at various frequencies. The average current is plotted against the average and the peak magnitude of the applied voltage pulse. The dependence of the characteristics on frequency is clearly shown in those figures, as the frequency of the applied voltage is increased the average value of the corona current increases with respect to the peak voltage and the characteristics approach the D.C. curve in the counter clockwise direction, whereas the corona current decreases with respect to the average voltage and the characteristics approach the D.C. curve in the clockwise direction. This trend is consistent with that depicted in Fig.5.8 for a wire-to-plane parallel electrode system. The difference in the relative position of the D.C. characteristic with respect to the pulsed characteristics is due to the filtering effect of the equivalent capacitance. The load capacitance of the circuit set up for wire to parallel plane system is much bigger than that for the point-to-plane system.

In an electrostatic precipitator, it has been recognised that the collection efficiency is proportional to the product of the peak and the average field intensity which in turn is proportional to the peak and the average value of the applied voltage [1]. It is obvious that if the maximum voltage is limited to a given value, then the average current density will always be less with pulsed voltage, than with a D.C. voltage. The only way the average value of the corona current can be equal to the D.C. value is for the peak voltage during the pulse period to be above the D.C. value.

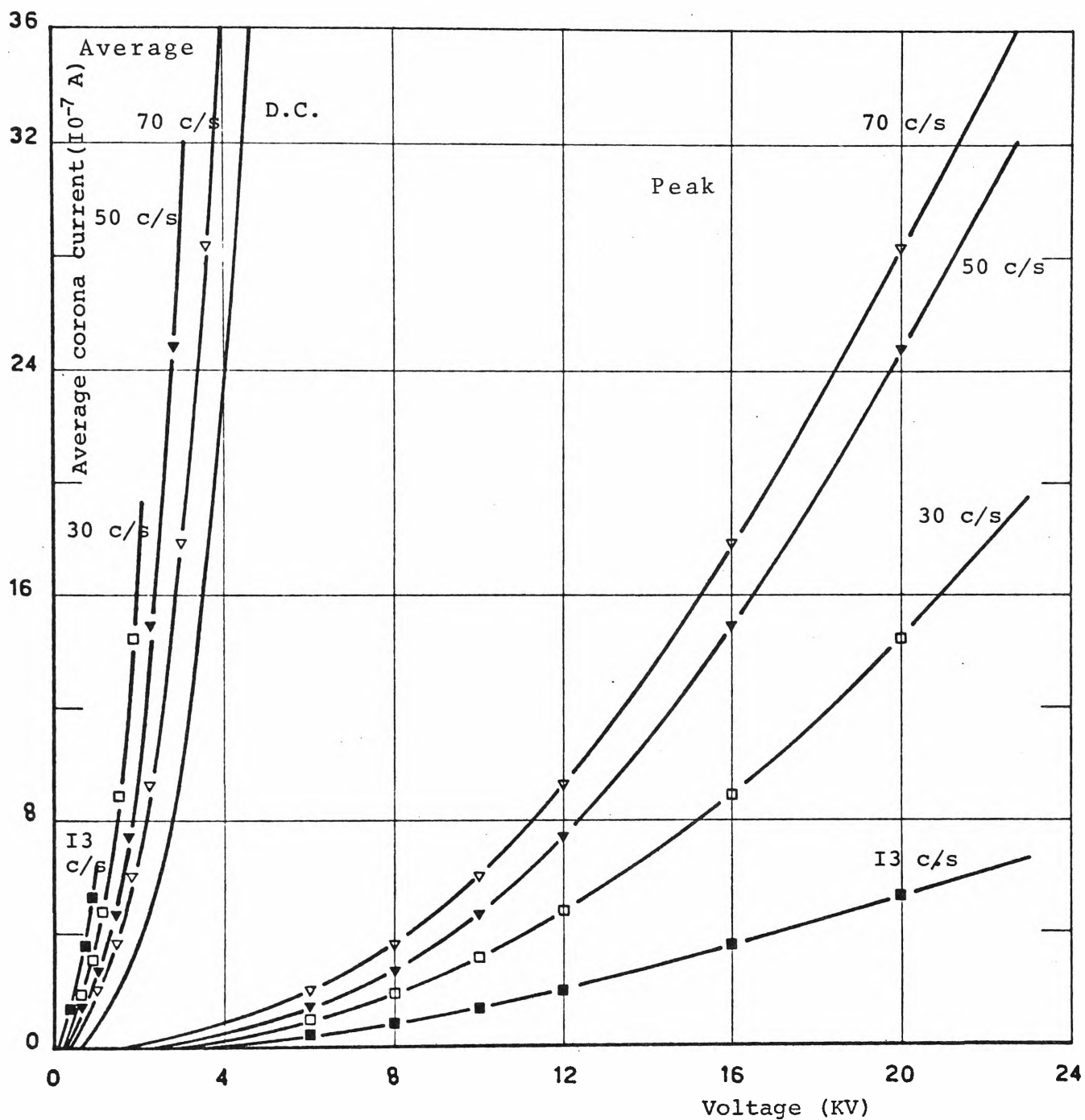


FIG.5.19 CURRENT-VOLTAGE CHARACTERISTICS OF POINT-TO-PLANE
SYSTEM.G.L.=1 cm;P.R.=.045 cm

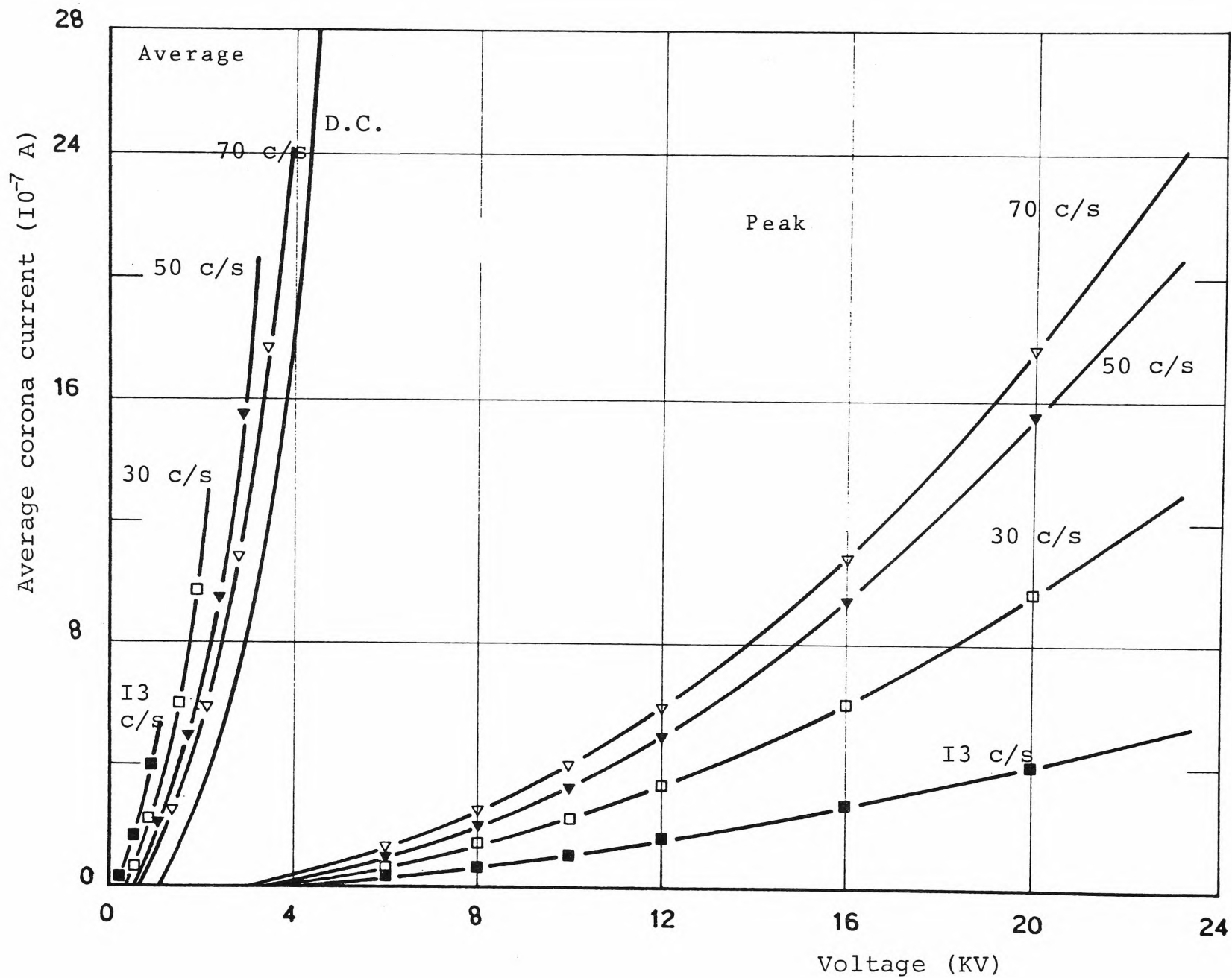


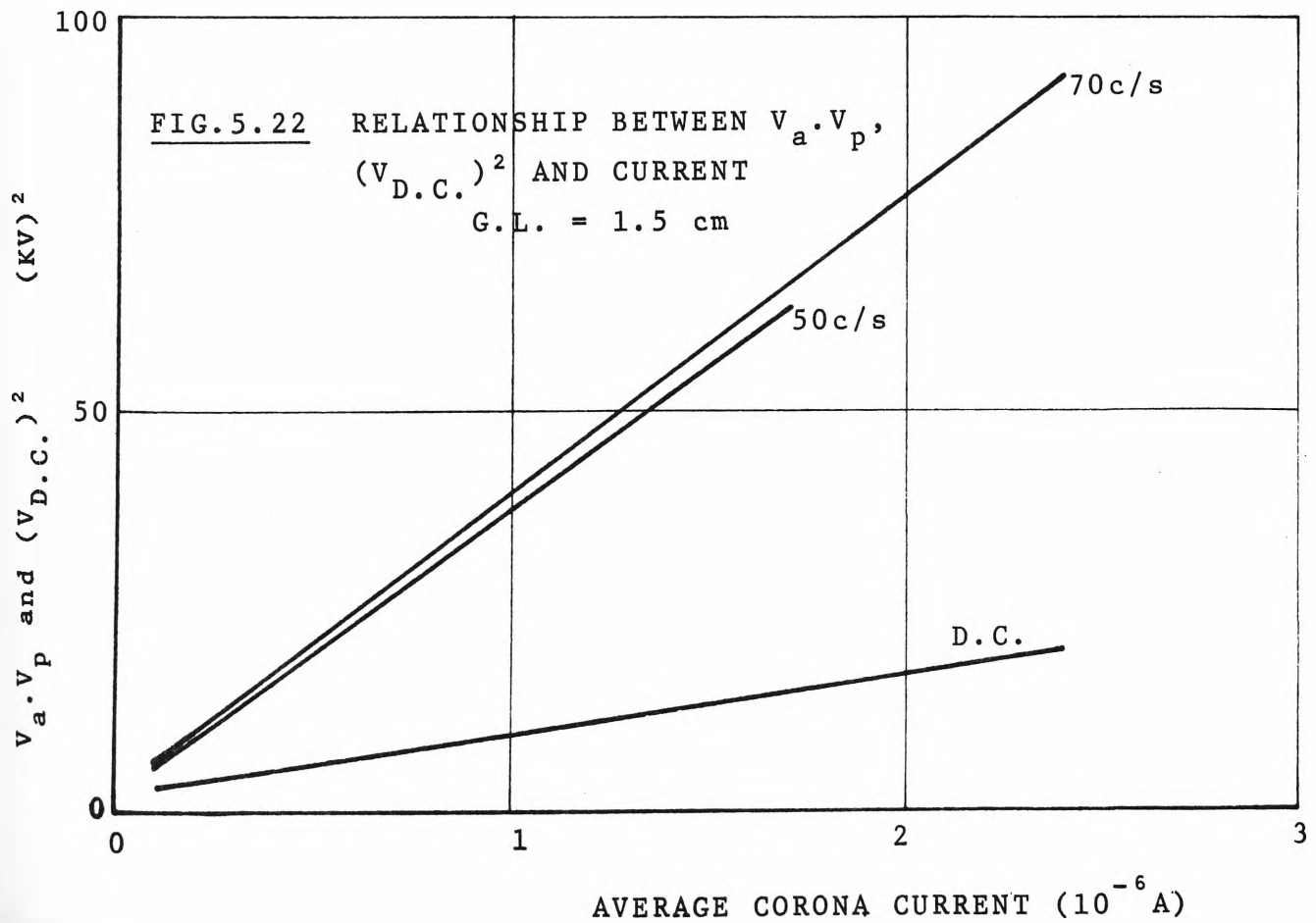
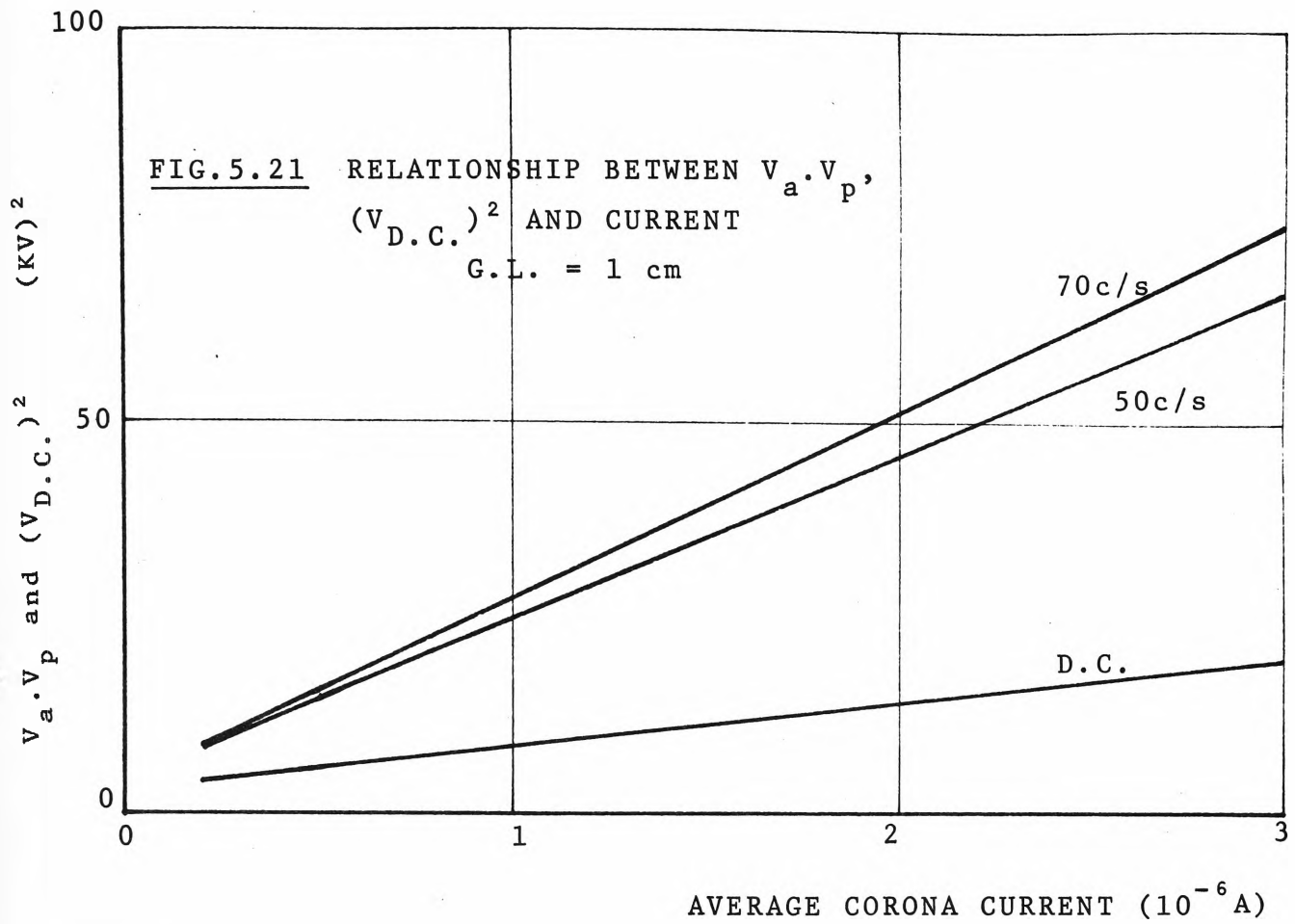
FIG. 5.20 CURRENT-VOLTAGE CHARACTERISTICS OF POINT
-TO-PLANE SYSTEM. G.L.=1.5 cm; P.R.=.045 cm

The allowable peak voltage is fixed by the value at which sparkover occurs and since this is higher where the voltage pulse has a low rise time and short duration, it is expected an optimum product of the average and peak voltages is possible with pulsed voltages. Fig.5.21 and 5.22 are the plots of this product against average corona current for both pulsed and D.C. voltages. They indicate that at a constant corona current, the product of V_{average} and V_{peak} is always higher than $(V_{\text{D.C.}})^2$. The corona power which is defined as the product of corona current and the effective voltage, is plotted against average voltage in Fig.5.23 and 5.24. They show at a constant voltage the maximum power attainable for pulsed voltage is higher than that for D.C. voltage.

5.3.3 Mathematical Model of a Corona System

5.3.3.1 Introduction

The relationship between the corona current and voltage of a corona system under the application of a smooth D.C. voltage has been well established, it is of a quadratic form in which the current is controlled by a space charge limited source which leads to a stable discharge regime. Although the current-voltage characteristics of a corona system under pulsed energisation has been measured by a few workers, [6], [15], [16] no attempt has been made to describe a mathematical model of the corona system behaviour under such conditions. The model is based on the equivalent circuit of the corona system at its steady state and the solution is obtained by a combination of graphical and numerical methods. This approach is proved to be a simple but useful tool to obtain reasonably accurate results.



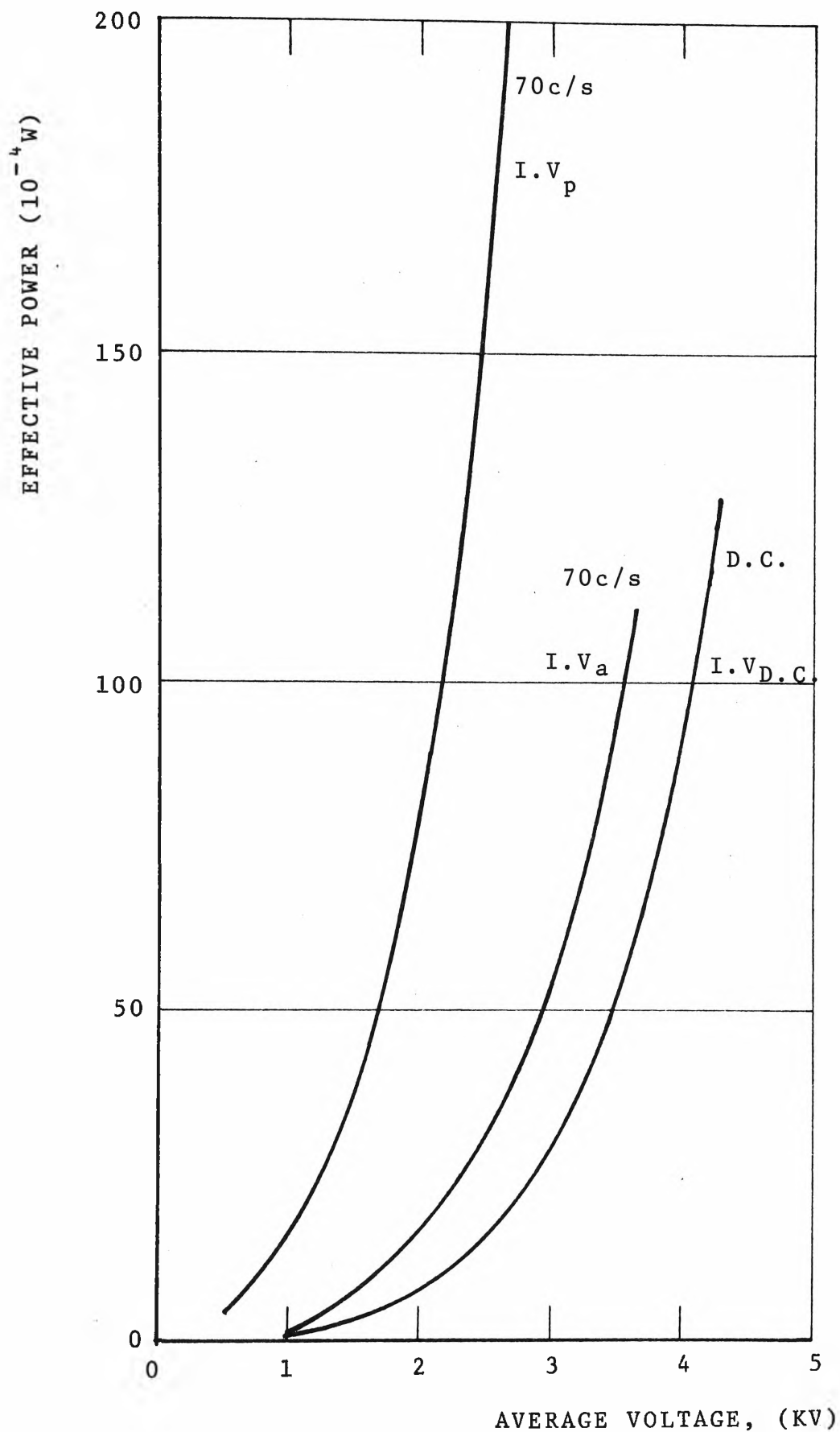


FIG. 5.23 RELATIONSHIP BETWEEN EFFECTIVE POWER AND AVERAGE VOLTAGE

G.L. = 1 cm

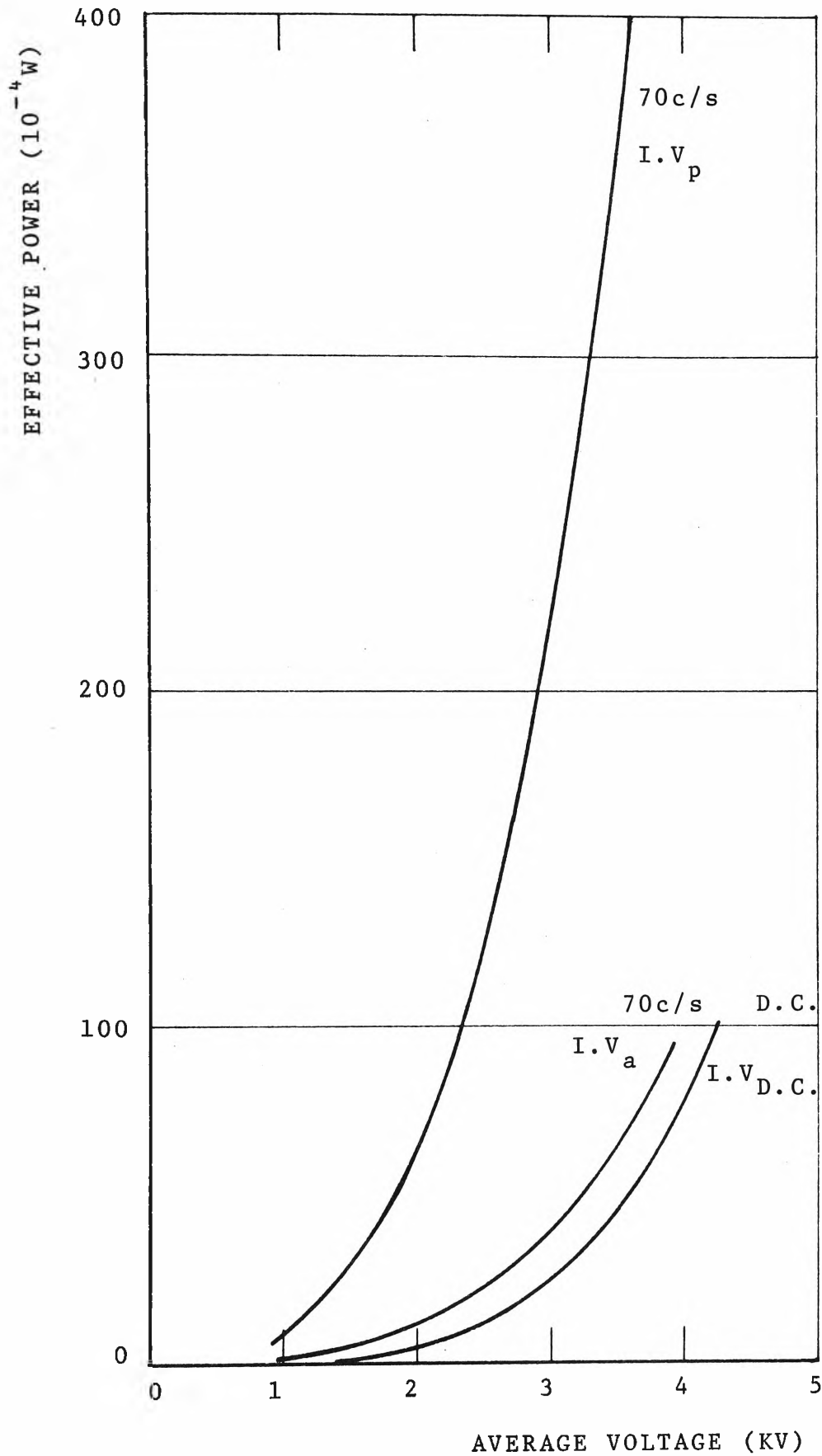


FIG. 5.24 RELATIONSHIP BETWEEN EFFECTIVE POWER AND AVERAGE VOLTAGE

G.L. = 1.5 cm

5.3.3.2 Equivalent Circuit of a Corona System

Under the stable and steady state condition, the formation and accumulation of the negative ions in the buffer region is equivalent to the charging of the region capacitor representing the buffer zone, and the transport of negative ions from the buffer region to the collecting plate is equivalent to the discharging process taking place through the equivalent resistance of the air space. The equivalent circuit of a corona system thus consists of a distributed capacitance C between the discharge electrode and the collecting plane, the effective non-linear resistance of the air gap connected in series with a back potential difference V_0 representing the corona onset voltage. The equivalent circuit is shown in Fig.5.25.

If an idealised case is considered where the applied voltage is rectangular and of regular frequency, then the shape of the voltage pulse between the electrode is as shown in Fig.5.26. During the period of the pulse, the distributed capacitance is charged to the peak value of the voltage. After the pulse, the capacitance discharges across the airgap. Its decay is a function of C and the value of the non-linear resistance R . Providing the period of the pulse is relatively short compared with the effective time constant, a voltage will normally be maintained across the electrodes for the period between pulses and corona current will continue to flow.

From the equivalent circuit, the following expressions for voltage and current can be obtained. A detailed description of the derivation is included in Appendix C.

$$V(t) = V_o + (V_p - V_o) \cdot \exp(-(t - t_o)/RC) \quad \text{for } t \geq t_o \quad (5.3)$$

$$i(t) = \frac{V_p - V_o}{R} \cdot \exp(-(t - t_o)/RC) \quad \text{for } t \geq t_o \quad (5.4)$$

and

$$i(t) = \frac{V_p - V_o}{R} \quad \text{for } 0 < t < t_o$$

The average current can be written:

$$\bar{I} = \frac{V_p - V_o}{R} \left(\frac{t_o}{T} \right) + \frac{C}{T} (V(t_o) - V(T)) \quad (5.5)$$

where

V_p is the peak value of the pulsed voltage

t_o is the pulse duration

T is the pulse period.

From the above equations, a current-voltage relationship could be readily obtained if the resistor R was a linear device.

The following method will be used to approximate the current-voltage characteristic by representing the non-linear resistor R by a piecewise-linear device.

5.3.3.3 Analysis of First Order Non-Linear Circuit

The piecewise-linear method is applied to solve the non-linear differential equation. It is a well-established method to obtain solution of non-linear network [95], and is briefly presented here.

At any time $t = t_o$, a piecewise-linear network must operate on some linear segment j of the characteristic curve as seen by the energy storage element. The operation will continue to stay on the same segment j until it reaches the breakpoint of this segment at some time $t = t_1$ (Fig.5.27).

During the time interval (t_o, t_1) , the non-linear resistor appears as a linear resistor to the energy storage element. Therefore, it can be replaced either by its Thevenin or Norton equivalent circuit as shown in Fig.5.28.

The following expressions can be obtained for the voltage and time t_1 within segment j

$$V_j(t) = V_{sj} + (V_j(t_o) - V_{sj}) \exp(-(t - t_o)/\tau_j) \quad \text{for } t \geq t_o$$

and

$$t_1 = t_o + \tau_j \ln \left[\frac{V_j(t_o) - V_{sj}}{V_j(t_1) - V_{sj}} \right]$$

where

$\tau_j = R_j C$: the time constant corresponding to the segment j of the network.

The same steps are repeated for all the other segments of the whole network. The pulse period T is then compared with various time intervals so that one can decide which segment must be used to find the average current in expression (5.5). The procedure can be summarised as follows:

- (i) Label the segments of the characteristic curve from 1 to n .
- (ii) Locate the pertinent segment j containing the initial state $V_j(t_o)$.
- (iii) Determine the intercept of the segment j (or its extension) and the voltage axis, this gives V_{sj} .
- (iv) With $V_j(t_o)$, V_{sj} , and τ_j known, sketch the exponential waveform and specify the corresponding equation $V_j(t)$ for $t \geq 0$.
- (v) If the value of $V_j(t)$ obtained in step (iv) stays within the interval of definition of segment j for all time $t \geq t_o$, then the complete solution consists

of this single exponential time function.

- (vi) If the value of $V_j(t)$ exceeds the interval of definition of segment j , then one must determine the time $t = t_1$ where $V_j(t)$ reaches the terminal state of segment j . The exponential solution is then valid only for $t_0 \leq t \leq t_1$.
- (vii) To find the continuation of the solution for $t \geq t_1$, determine the transition state by using the principle of conservation of charge.
- (viii) With the transition state obtained in step (vii) as the new initial state, repeat steps (ii) to (vii) as many times as necessary until the solution $V(t)$ is found for all times $t \geq t_0$.
- (ix) Compare the pulse period T with all times t_1 to determine which segment should be used to find $V(t = T)$.
- (x) Find the average current by using equation (5.5).

5.3.3.4 Comparison between Calculated and Measured

Results

The above method is applied to calculate the current-voltage characteristics of the wire-to-plane parallel electrode system used in section 5.2.2. The total capacitance which equals the sum of the stray capacitance, the distributed capacitance of the electrode system and the load capacitance is 50 pf. The D.C. characteristics of the corona system is reproduced in Fig.5.29, it is divided into five segments and the pertinent details of all the segments and the complete solutions for all the voltage levels varying from 5.5 kV to 16 kV are shown in Table 5.1

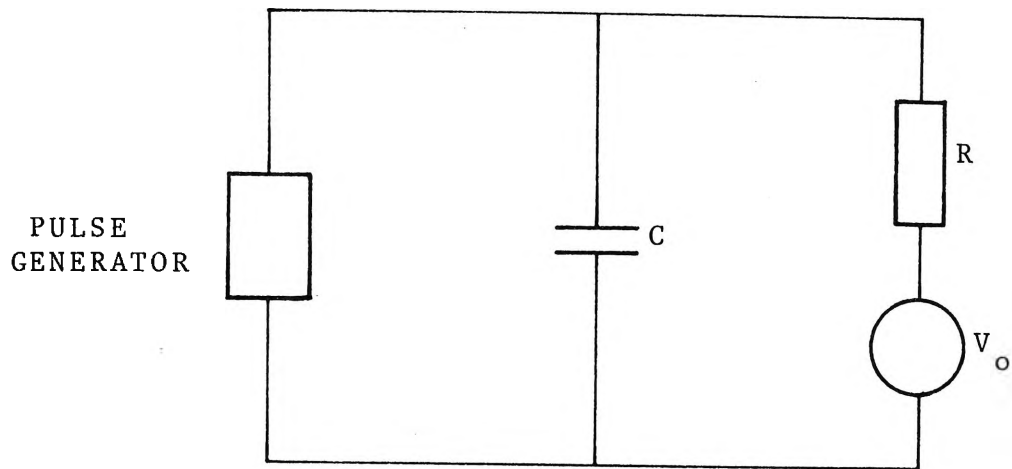


FIG. 5.25 EQUIVALENT CIRCUIT OF A CORONA SYSTEM

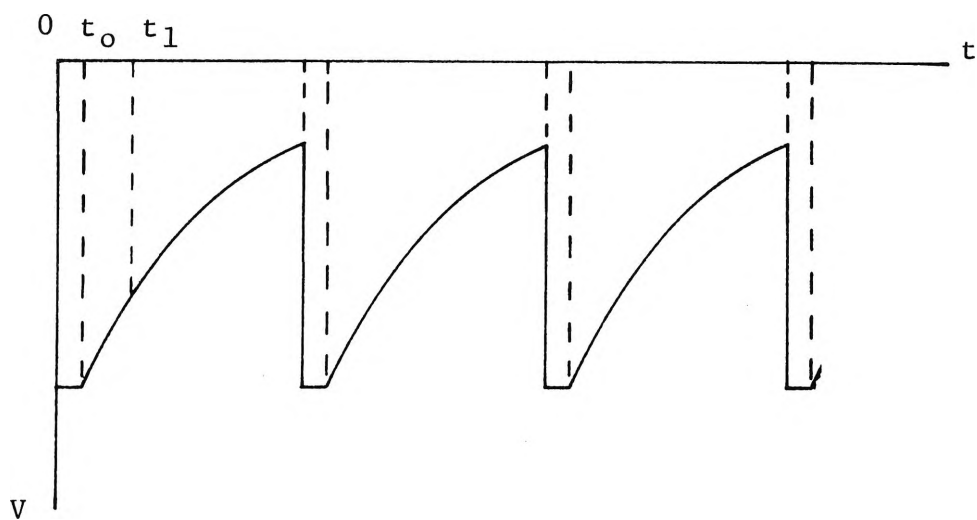


FIG. 5.26 WAVESHAPE OF APPLIED RECTANGULAR PULSED VOLTAGE

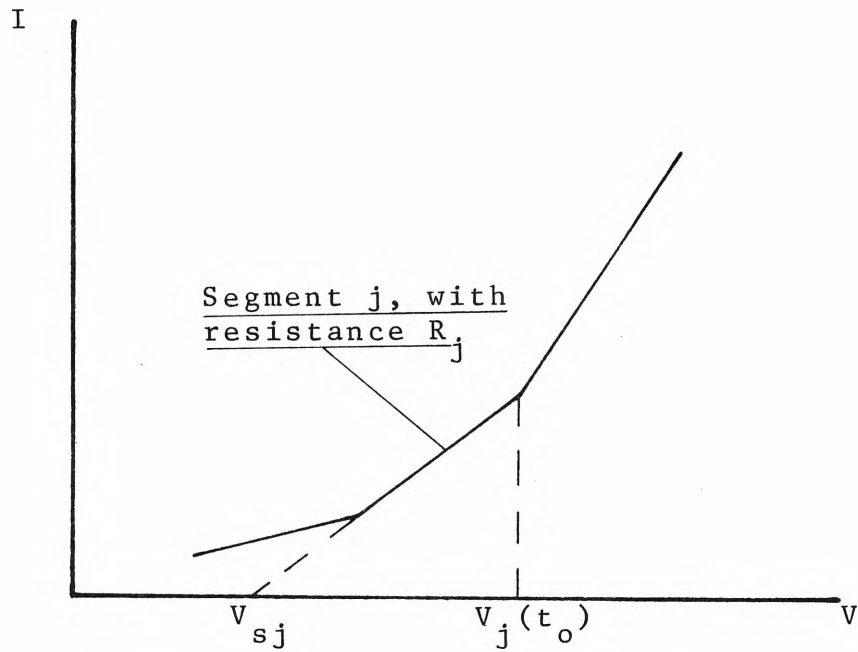


FIG. 5.27 CHARACTERISTIC CURVE AS APPROX-
IMATED BY PIECEWISE-LINEAR SEGMENTS

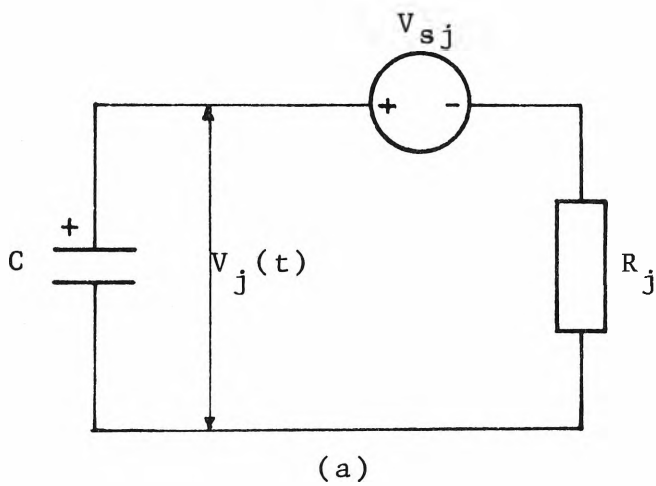
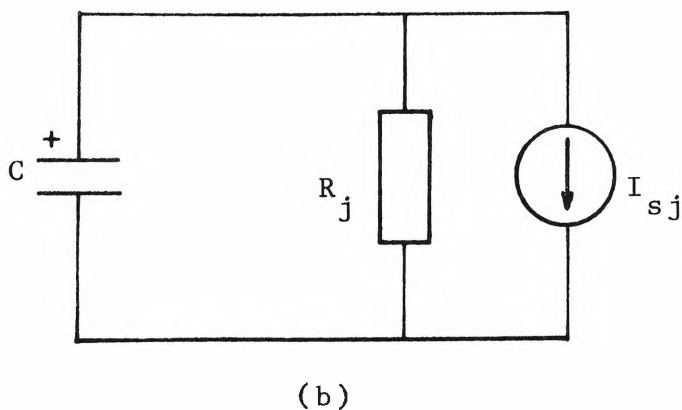


FIG. 5.28 EQUIVALENT CIRCUIT
OF THE NON-LINEAR DEVICE
WITHIN SEGMENT j

(a) THEVENIN EQUIVALENT
CIRCUIT

(b) NORTON EQUIVALENT
CIRCUIT



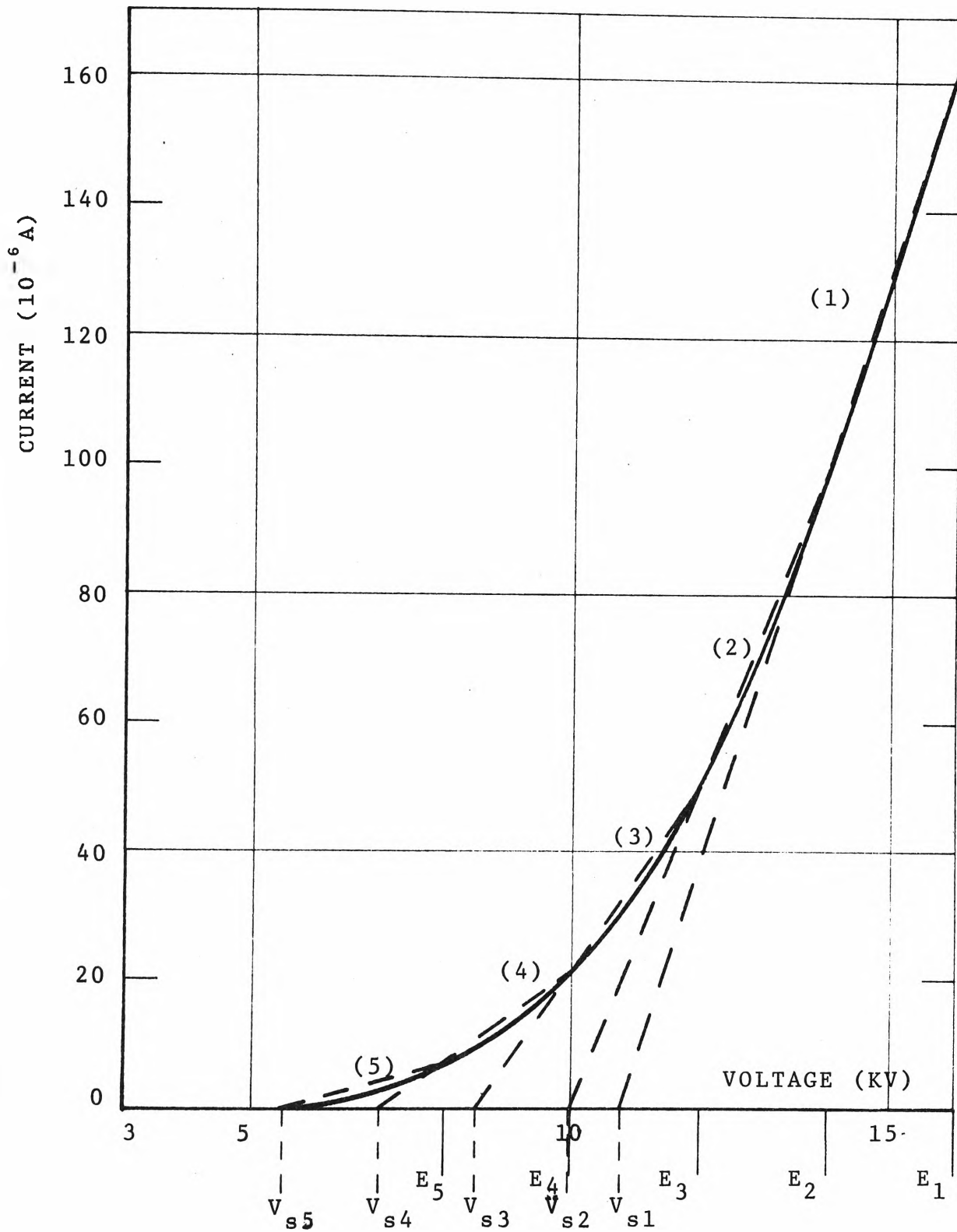


FIG.5.29 PIECEWISE LINEARISATION METHOD APPLIED TO CHARACTERISTIC SHOWN IN FIG.5.8.

Peak Voltage Range (KV)	V_{sj} (KV)	τ_j (sec)	Segment number
5.5-8	5.5	.017857	5
8-10	7	.007143	4
10-12	8.5	.0035	3
12-14	10	.0020	2
14-16	10.8	.001605	1

TABLE 5.1 SUMMARY OF VARIOUS PARAMETERS USED IN THE CALCULATION OF CURRENT-VOLTAGE CHARACTERISTICS WHEN THE ELECTRODE SYSTEM IS ENERGISED BY A PULSED VOLTAGE.

The calculated results are shown in Fig.5.30. They are consistent with the experimental results. The discrepancy will be minimised if the number of piecewise-linear segments is increased and the variation of the distributed capacitance with respect to the space charge condition is known. It has been reported that if the distributed capacitance of the electrode system is defined as the ratio of the charge available in the air space and the applied voltage then at steady state condition, the capacitance may triple its value at below corona onset when the applied voltage is larger than its onset value by 50 per cent [96].

The mathematical model has been used to predict fairly accurately the current-voltage characteristics of a coaxial cylindrical electrode system [97]. It also indicates the effects of the equivalent capacitance on the characteristics of the corona system energised by pulsed voltage of different pulse durations and duty ratios. As the frequency of the pulsed voltage increases, the average value of the voltage

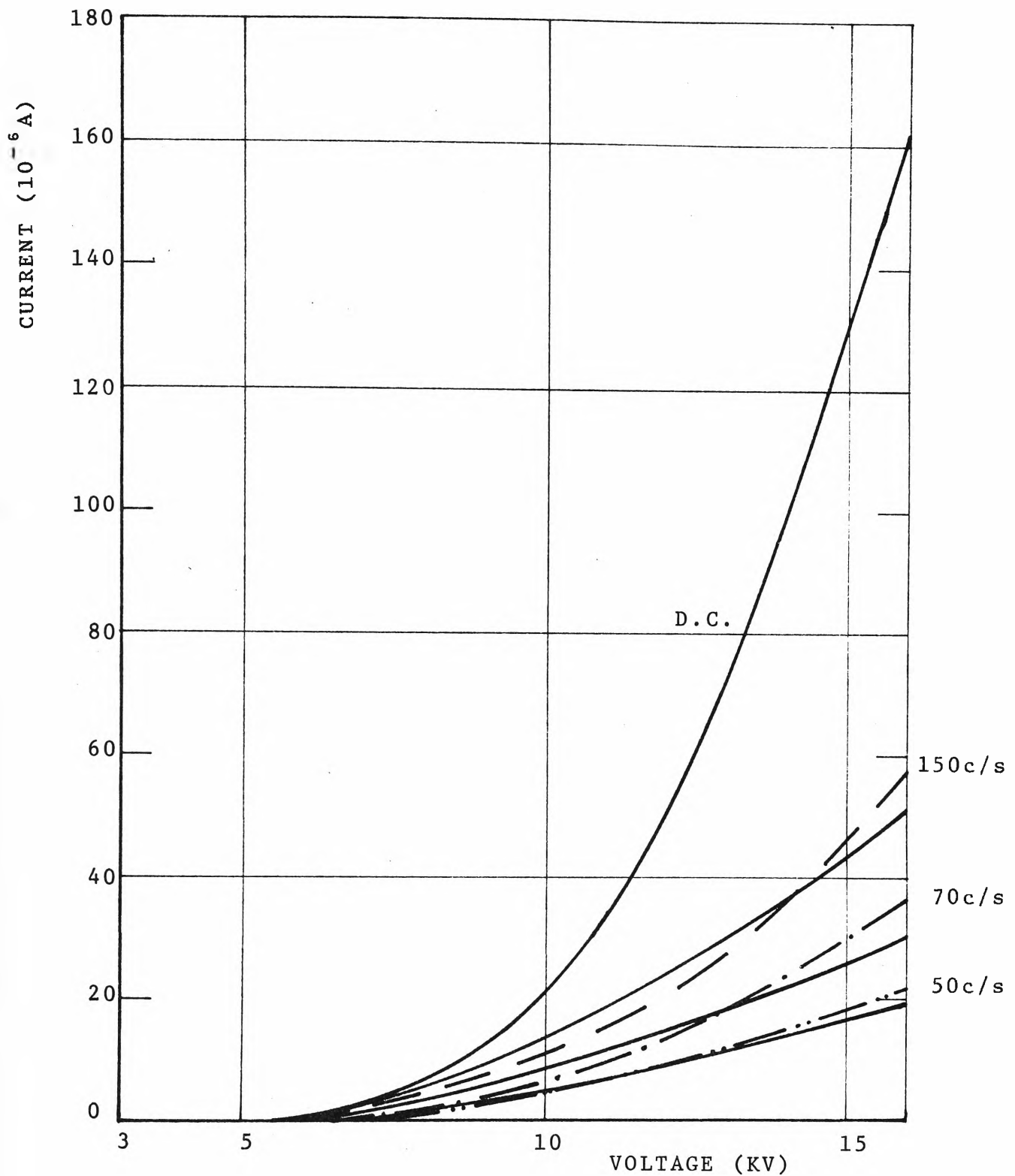


FIG.5.30 COMPARISON BETWEEN CALCULATED AND MEASURED RESULTS.

_____ CALCULATED
 - - - - - MEASURED AT 150c/s
 - . - . - " AT 70c/s
 - " AT 50c/s

increases since the fluctuation of the applied voltage between the electrodes is filtered out by the capacitor, consequently the average corona current flow between pulses will increase.

5.3.4 The Corona Wind

5.3.4.1 Introduction

The existence of corona wind has been known for a long time, the first quantitative analysis of the phenomenon was made by Chattock [98] at the end of the nineteenth century. He developed a relationship between the corona wind pressure and current for a plane-parallel electrode system. Löb used the same approach to extend Chattock's current-pressure relationship to other geometries in 1954 [99]. A few years later Harneys examined effects of the motion of gas stream on the electrical properties of the corona discharge [100]. A comprehensive analysis of the mechanism of the gas movement in the electric wind was considered by Robinson [55] in 1961. He offered an approximate theory which relates relevant electrical and aerodynamic quantities. He showed those relationships hold for an electrostatic blower, operating on the electric wind principle. His equations indicate a linear relationship between the corona wind velocity and the voltage, and the square root of corona current respectively. Using a similar approach, Loeb arrived at the same expressions [12]. In this part, a review of the theory is presented which will be referred to in the discussion of the experimental results.

5.3.4.2 Theory of Corona Wind

The electrode system considered in this analysis is a point-to-plane system with the plane having been perforated to resemble a mesh screen which permits the gas to flow through.

Consider a small volume of gas between the electrodes, the force acted on a unit volume of the gas is the product of the charge density ρ and the electric field \vec{E}

$$\vec{F} = \rho \vec{E}$$

The force per unit volume is equivalent to the gradient of the pressure i.e.

$$\nabla p = \rho \vec{E} \quad (5.6)$$

The current flows between the electrodes is the results of two simultaneous effects: the transport of charge by the gas stream and the movement of charge carrier under the action of the field. The first component is the gas velocity and the second component is the drift velocity of charge carrier which is predominant in the gas. The total velocity is then

$$v_t = v + v_d \approx v_d$$

The current density is the product of charge density and the velocity:

$$j = \rho(v + v_d) \approx \rho v_d \quad (5.7)$$

Elimination of ρ in equations (5.6) and (5.7) gives

$$\nabla p = \frac{j \vec{E}}{v_d} \quad (5.8)$$

Since the mobility of the ions is $k = v_d / \vec{E}$, equation (5.8) can be written as

$$\nabla p = \frac{j}{k} \quad (5.9)$$

Assuming that the axial component of the gradient of pressure predominates the flow of gas, equation (5.9) becomes

$$\frac{dp}{dx} = j/k$$

The pressure difference to maintain the corona wind between the electrodes is:

$$p = \int_0^d \frac{j}{k} dx = \frac{j d}{k} \quad (5.10)$$

The work done to move a mass of gas m through the gap length across an area A is thus:

$$W = p.A.d \quad (5.11)$$

Assume that this work is converted totally to the kinetic energy of the gas, it can be written:

$$W = K.E. = \frac{1}{2} m v^2$$

but $m = n.A.d$ where n is the density of the gas, hence

$$W = \frac{1}{2}(n.A.d)v^2 \quad (5.12)$$

Equate equation (5.11) to (5.12) and eliminate the common elements, one can obtain:

$$p = \frac{1}{2} n v^2 \quad (5.13)$$

Equations (5.10) and (5.13) give:

$$v = \left[\frac{2d}{A k n} \cdot i \right]^{\frac{1}{2}} \quad (5.14)$$

where the current density j has been replaced by i/A .

It has been established that in a nonsymmetrical electrode system, the relationship between the corona current and

the applied voltage is of the form:

$$i = K.V(V-V_o) \quad (5.15)$$

where K is an experimentally determined constant, V and V_o are the applied voltage and corona onset voltage respectively.

Substitute (5.15) into (5.14), and the wind velocity can be expressed as a function of the applied voltage

$$v = \left[\frac{2d}{A k n} \cdot K \right]^{\frac{1}{2}} \cdot [V(V-V_o)]^{\frac{1}{2}} \quad (5.16)$$

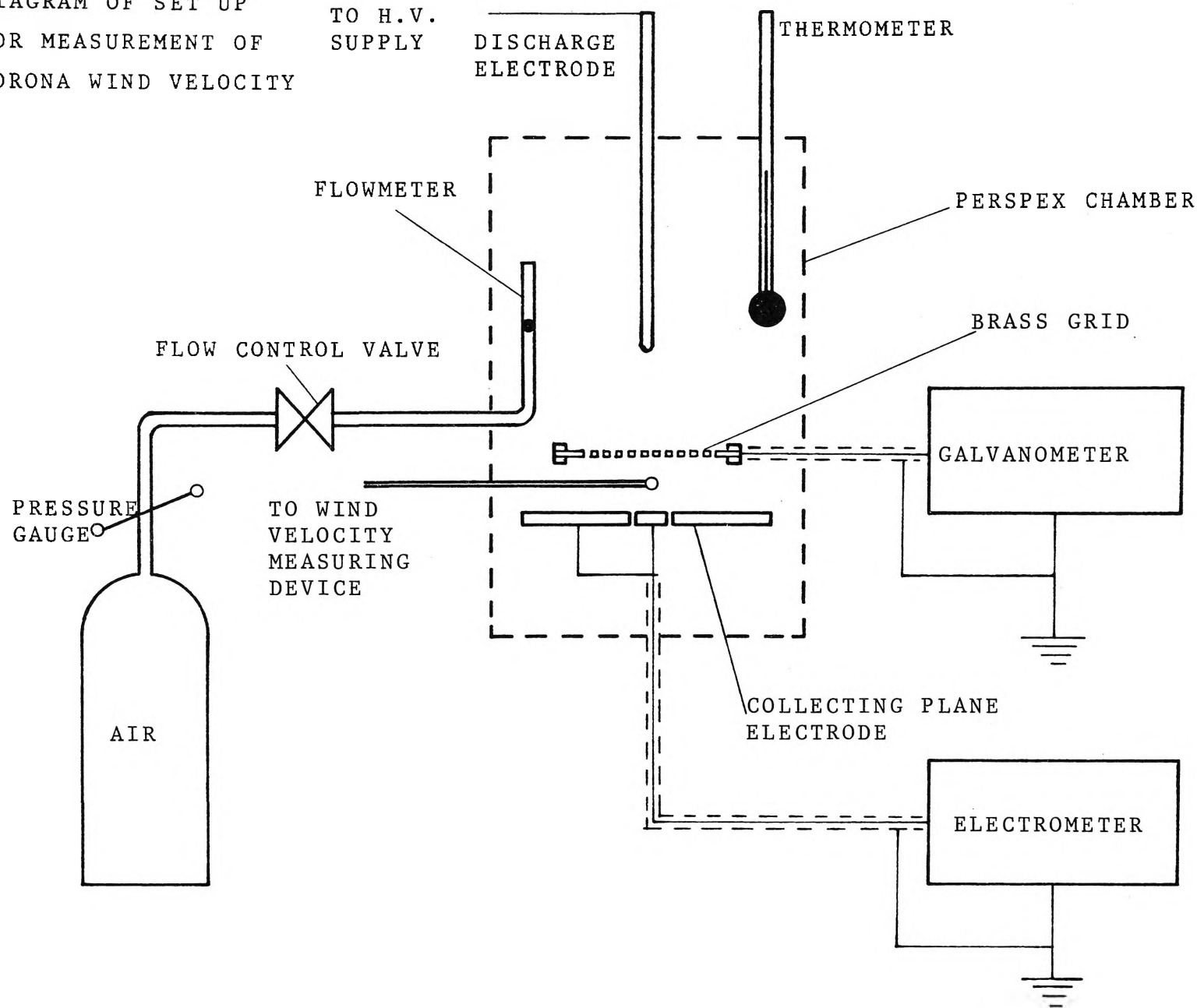
A linear relationship between the corona wind velocity and the voltage can be clearly observed in equation (5.16). It also indicates that the velocity is inversely proportional to the square root of the gap length at a given voltage because the effective collecting area A varies as the square of the distance from the cathode which acts as a source of disturbance .

5.3.4.3 Measurement Technique

The corona wind velocity is measured by means of the arrangement shown in Fig.5.31.

A few trial runs of the experiment indicate at corona onset and just above onset, the electrical wind, which results from the momentum given to the air molecule by impact of the ions and electrons as they move out from the high field regions, is not sufficiently strong to cause a significant change in the dissipation constant of the thermistor. The temperature drop of the thermistor is outperformed by the convection current produced by the heating effect in the thermistor, and the energy transfer in the inelastic impact between negative ions and the thermistor tip. At higher

FIG.5.31 DIAGRAM OF SET UP
FOR MEASUREMENT OF
CORONA WIND VELOCITY



voltage level, the deflection of the balanced bridge occurs proportionally to the applied voltage level. It then reaches a maximum and starts declining as the voltage is very high. This is the result of an increase in the negative ions density whose energy gain from the applied field is also greater under high applied voltage. The energy imparted to the thermistor tip and the frequency of impact are so large that the temperature drop due to corona wind is overtaken by temperature rise due to these factors. This phenomenon was observed when the thermistor was placed in the vicinity of the collecting plate. To overcome this problem a brass grid is used as a passive electrode collecting most of the negative ions. The measuring thermistor is placed underneath the grid and above the stainless-steel plate that is used to detect the amount of negative ions that get through. The flowmeter comprising a sapphire float and a control valve, is used for calibration and to bring the Wheatstone bridge back to the balance condition when the test effect is removed.

5.3.4.4 Results

The experimental values of the unbalanced voltage obtained at different voltages and currents are calibrated in terms of velocity of gas flow and plotted in Fig.5.32 and 5.33. Because of the limitation of the pulsed power supply and the difficulty of detecting the unbalanced voltage at very low corona current, the electric wind velocity is measured at two gap lengths 1. and 1.5 cm for pulsed voltage (Fig.5.32). With D.C. voltage, the sensitivity of

the measuring circuit is adequate to detect gas movement at gap length of up to 3 cm (Fig.5.33).

From Fig.5.33, the corona wind velocity is plotted against the square root of the current and shown in Fig.5.34. The relationship is linear for all gap lengths when the corona current varies from zero to 6 microamp. The deviation from a linear relationship may be caused by the heating effect that becomes prominent at high current, the obstruction of the gas flow due to the perforated collecting plane, the ineffective conversion of the electrical energy into the kinetic energy of the gas.

The variation of corona wind velocity with respect to gap length at constant corona current is plotted in Fig.5.35, the relationship is approximately hyperbolic: the velocity is inversely proportional to the square root of the distance. This result agrees with equation (5.14).

The characteristics of corona wind velocity and applied pulsed voltage at different frequencies are shown in Fig. 5.36 and 5.37 in which the electric wind velocity is plotted against the average and peak values of the pulsed voltage. The linear relationship that exists for both D.C. and pulsed voltages is consistent with equation (5.16), the derivation of which is based on the steady state of the corona discharge under D.C. energisation. The slope of the curves varies with respect to the frequency because of the dependence of the parameter K in equation (5.15) on the pulse frequency.

The variation of corona wind velocity with respect to the repetition rate of the pulsed voltage is shown in Fig. 5.38 and 5.39.

5.3.4.5 Discussion

(a) Variation of corona wind with respect to Gap Length

The linear regression technique is used to find the expression which describes the relationship between the corona wind velocity and the gap length. The relationship is found to fit the power curve best. The numerical results are summarised in Table 5.3 where r^2 is the coefficient of determination which indicates how closely the equation fits the experimental data, the closer r^2 is to 1, the better the fit.

The general form of the equation is:

$$v = A.d^B$$

where v : the corona wind velocity at a fixed
corona current

d : the gap length

A, B : constants which are found to fit the
curves best.

I [μA]	A [m/sec]	B	r^2
2	.43	-.48	.99
3	.53	-.49	.98
4	.58	-.48	.99
5	.63	-.48	1.00
10	.72	-.47	.99

TABLE 5.2 BEST FIT VALUES WHICH DESCRIBE THE RELATIONSHIP BETWEEN CORONA WIND VELOCITY AND GAP LENGTH AT VARIOUS CORONA CURRENTS.

The equation shows that the corona wind velocity is approximately inversely proportional to the square root of the distance at a constant corona current. This is concurrent with the relationship as expressed in equation (5.14)

(b) Effective area of Collector

The slope of the curves describing the relationship between corona wind velocity and the square root of corona current can be obtained from Fig.5.34, it is equal to the first term on the right hand side of equation (5.14). By using the mobility of negative ion in air and assuming the air is dry, the product kn is found equal to 2.87×10^{-4} Kg/V.sec.m, substitute this value into equation:

$$\text{slope} \equiv S = \left[\frac{2d}{A n k} \right]^{\frac{1}{2}}$$

the ratio d/A can be written

$$d/A = \frac{k n S^2}{2} \quad (5.17)$$

The effective area on the collecting plane can be represented by a circle having its centre coincident with the axis of the electrode system, it can be expressed as

$$A = \pi(Kd)^2$$

where K is the proportional factor, determined experimentally

d is the gap length

Equation (5.17) now becomes:

$$\frac{d}{\pi K^2 d^2} = \frac{k n S^2}{2}$$

which gives:

$$K = \left(\frac{2}{\pi k n S^2 d} \right)^{\frac{1}{2}} \quad (5.18)$$

The values of K are calculated for various gap lengths and are summarised in Table 5.3.

G.L. [cm]	S [m/sec.A ^{1/2}]	nk [K _g /V.sec.m]	K
1	283	2.87x10 ⁻⁴	1.66
1.5	225	"	1.71
2	205	"	1.62
2.5	188	"	1.58
3	165	"	1.65

TABLE 5.3 VALUES OF K WHICH DETERMINE EFFECTIVE COLLECTING AREAS FOR DIFFERENT GAP LENGTHS.

The average value of K obtained for the range of gap length used in this work is 1.7 which is fairly close to that obtained by monitoring the discharge pattern in the vicinity of the discharge point electrode (Appendix D). This indicates that the effective collecting area on the plane anode is directly proportional to the gap length between the electrodes. The closeness between the effective area of the electrical wind measurement and that of the corona current measurement (Appendix D) is predictable since the electrical wind is generated by the collisions between highly-energised charge carriers and gas molecules, consequently where the concentration of the charge carriers is sufficient, the turbulence created in the gas should be detectable.

A similar approach can be used to find the effective collecting area under pulsed energisation. By comparing Fig.5.32 with Fig.5.33 it can be seen that at a fixed average corona current, the electric wind moves faster than it does under D.C. energisation. Denoting the appropriate terms in equation (5.14) with subscript p for pulsed voltage, one gets

$$v_p = \left(\frac{2d}{A_p \cdot k_p \cdot n} \cdot i \right)^{\frac{1}{2}}$$

and

$$v = \left(\frac{2d}{A \cdot k \cdot n} \cdot i \right)^{\frac{1}{2}} \text{ for D.C. voltage.}$$

At a fixed current i, v_p is greater than v, this means that

$$A_p \cdot k_p < A \cdot k$$

for the other terms are the same under both voltages.

Since the mobility of negative ions is a function of the electric field, its value under a varying field poses a certain degree of uncertainty. However, assuming that at a fixed average current, the average field in the air space is the same for D.C. and pulsed voltages, the mobility of negative ions should presumably be the same i.e. $k_p = k$. The values of K determined for two gap lengths are 1.22 and 1.24 respectively, these are close to each other and smaller than that for D.C. voltage. The difference of the two values is 25 per cent of the D.C. value, which is reasonable for the assumed value of mobility.

(a) Relationship between Corona Wind Velocity and Voltage

The linear relationship that exists between the corona wind velocity and voltage has been described in equation (5.16) and it can be seen in Fig.5.36 and 5.37. The relative position of the characteristic lines for different pulsed voltage frequencies with respect to the D.C. characteristics is consistent with plots of corona current-voltage curves which have been presented in section 5.3.2. The dependence of the characteristics on frequency is evidently shown in those figures, as the frequency of the applied voltage is increased, the corona wind velocity increases with the peak value of voltage and the characteristics approach the D.C. line in the anti-clockwise direction, whereas the corona wind velocity reduces with the average value of voltage and the characteristics approach the D.C. line in the clockwise direction. This is predictable, since the number of collisions between energised ions and gas molecules is proportional to the number of ions generated, and the energy transferred between ions and gas molecules in the collision is proportional to the energy gained by the ions from the applied field. The number of ions created by the ionisation processes has been found to depend on the magnitude of the applied pulsed voltage and its repetition rate (Fig.5.8, 5.19,5.20,5.30). The energy gained by ions from the applied field can be interpreted as dependent on their drift velocity which, in turn, depends on the magnitude of the field.

The dependence of corona wind velocity on the frequency of the pulsed voltage can be described by an empirical expression, which is found to fit the curves shown in

Fig.5.38,5.39. It can be written:

$$v = A + B \cdot \ln (F)$$

where A, B : constants which are calculated to fit the experimental results best.

F : the repetition rate of the pulsed voltage.

The numerical results are summarised in Table 5.4 for two gap lengths.

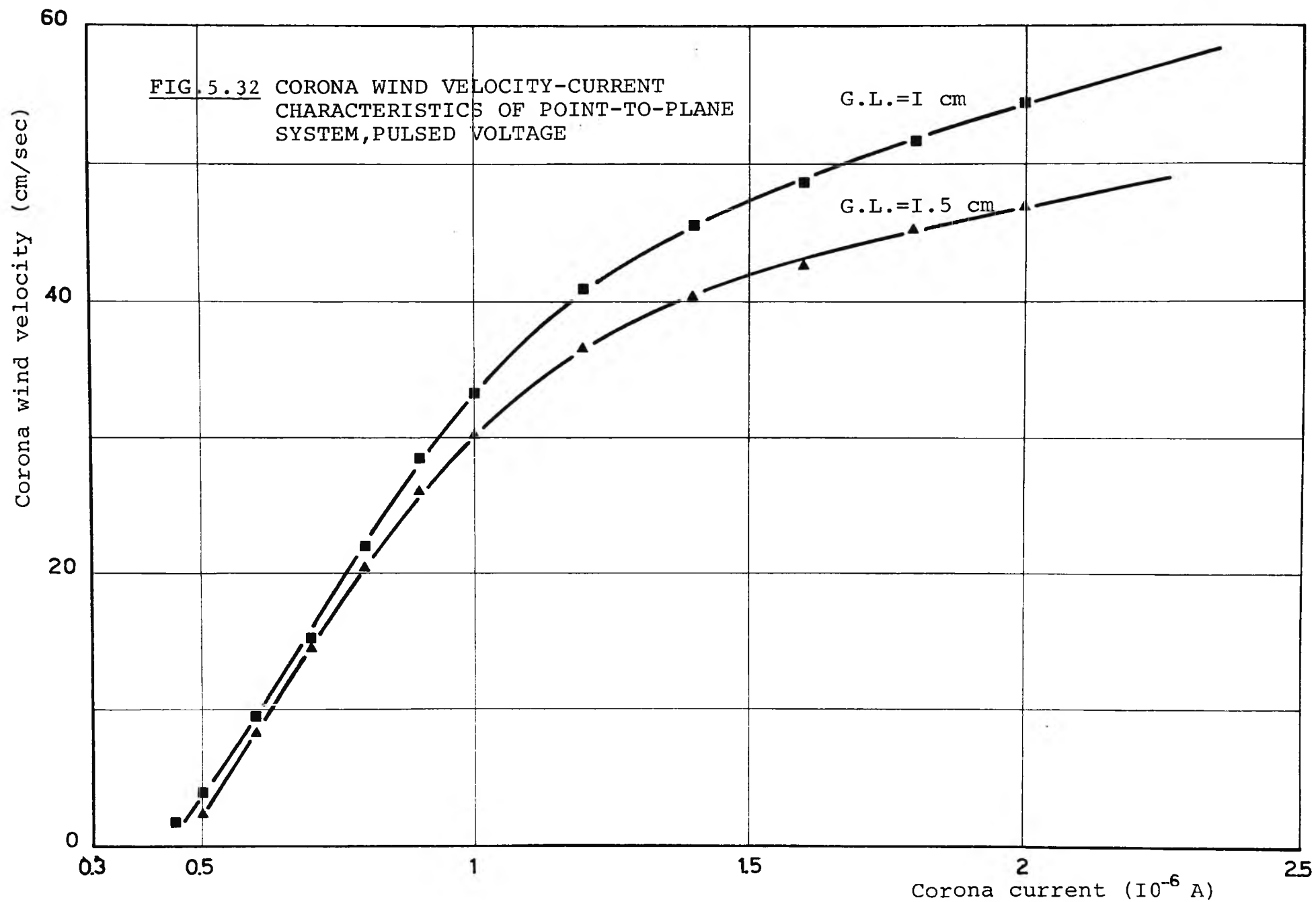
G.L. [cm]	V [KV]	A [m/sec]	B [m/sec]	r ²	B/V [m/sec.KV]
1	12	-1.12	.033	1.00	.028
	14	-1.26	.041	1.00	.029
	15	-1.39	.047	.99	.031
	16	-1.19	.044	.98	.027
1.5	15	-1.04	.032	.98	.021
	17	-1.04	.036	.98	.021
	19	-1.06	.039	.98	.021
	21	-1.06	.043	.98	.020

TABLE 5.4 VALUES OF CONSTANTS WHICH FIT THE CURVES IN FIG.5.38,5.39 BEST.

Since the constants A and B do not vary significantly with respect to the peak values of the pulsed voltage, a general form of equation can be used to express the corona wind velocity as a function of both the magnitude of the applied voltage and its frequency.

$$v = K_1 + K_2 \cdot V \cdot \ln (F)$$

where K₁, K₂ are the mean values of A and B/V respectively.



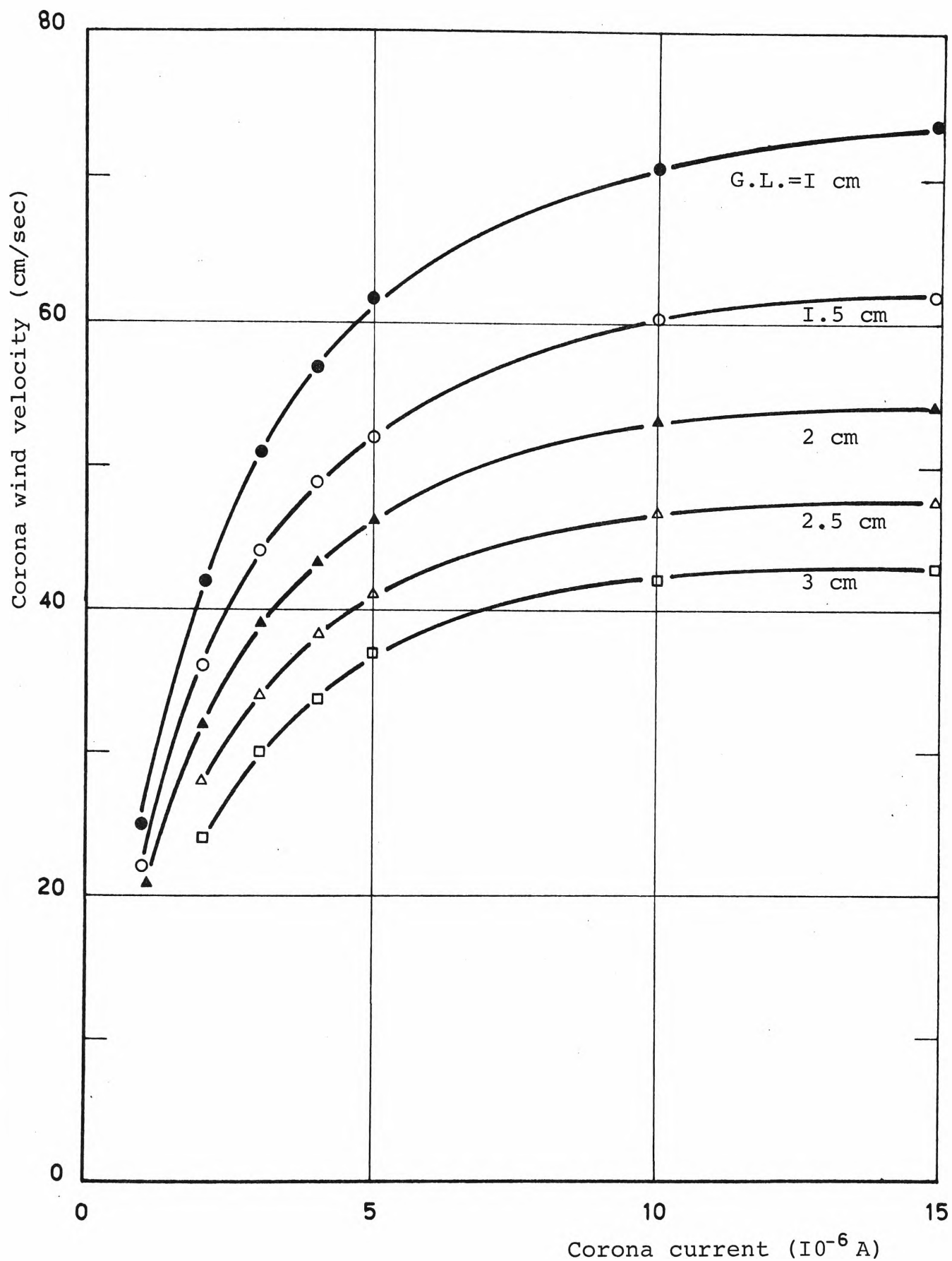


FIG.5.33 CORONA WIND VELOCITY-CURRENT CHARACTERISTICS
FOR D.C. VOLTAGE.

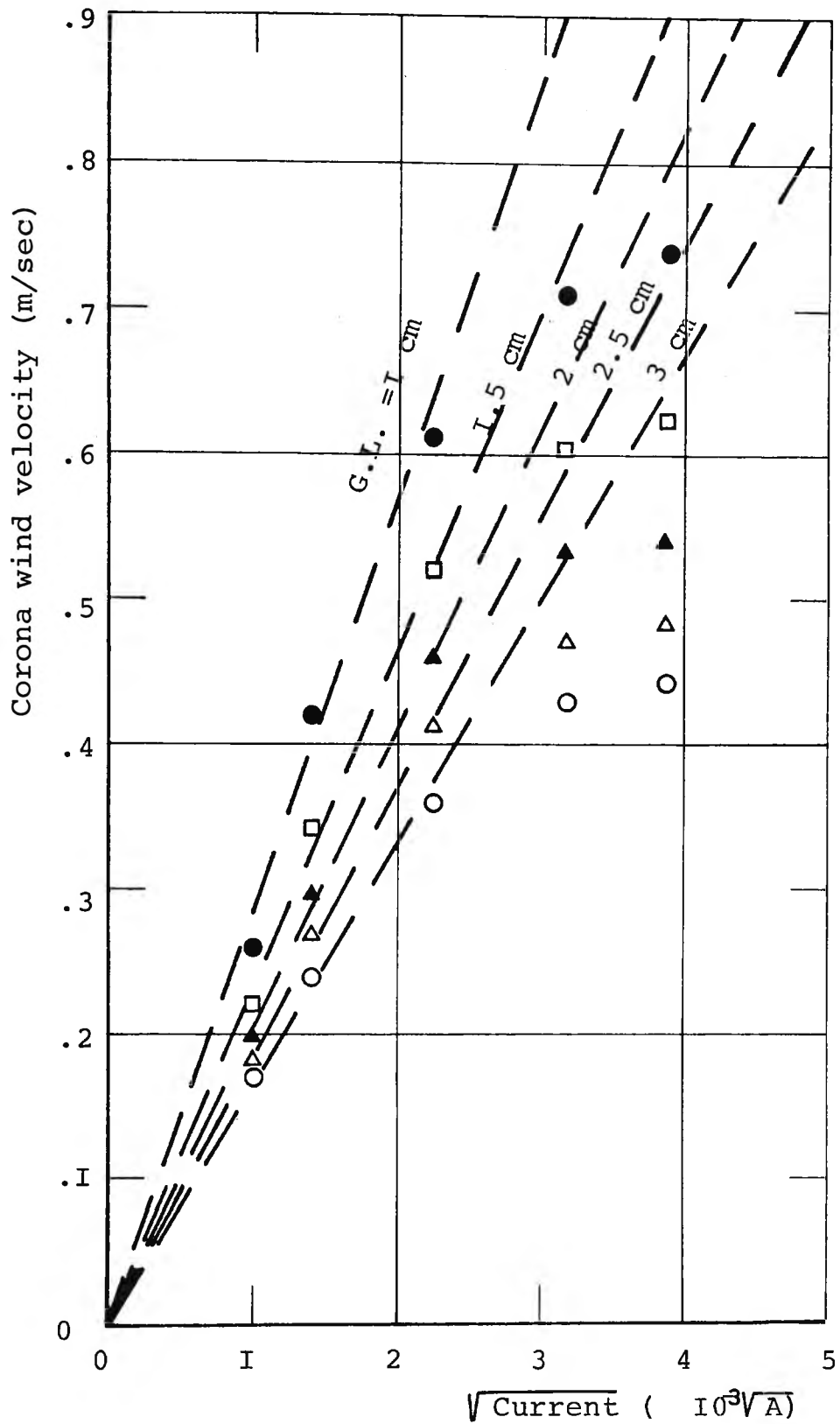


FIG.5.34 RELATIONSHIP BETWEEN CORONA WIND
VELOCITY AND SQUARE ROOT OF CURRENT

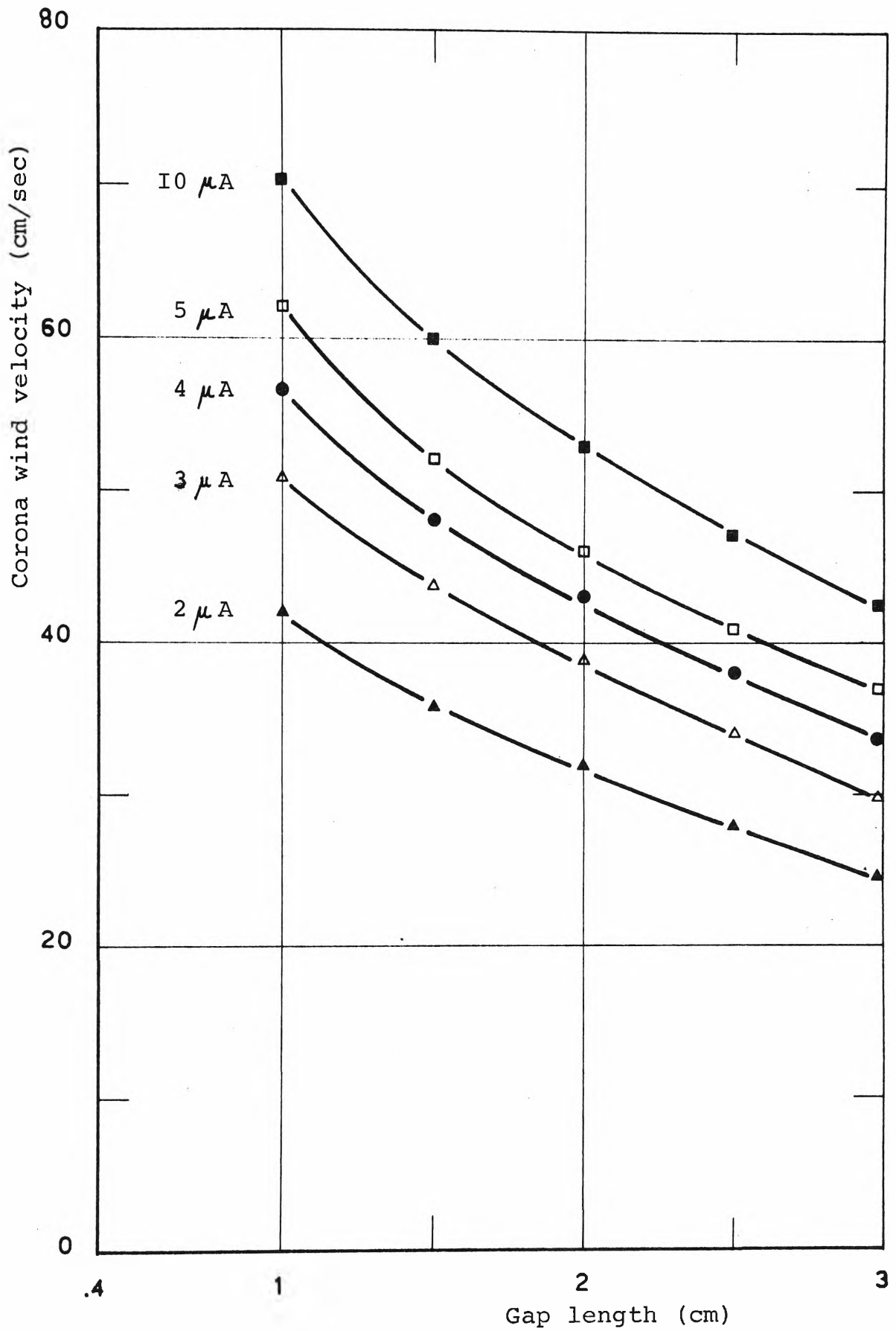


FIG.5.35 DEPENDENCE OF CORONA WIND VELOCITY ON GAP LENGTH.

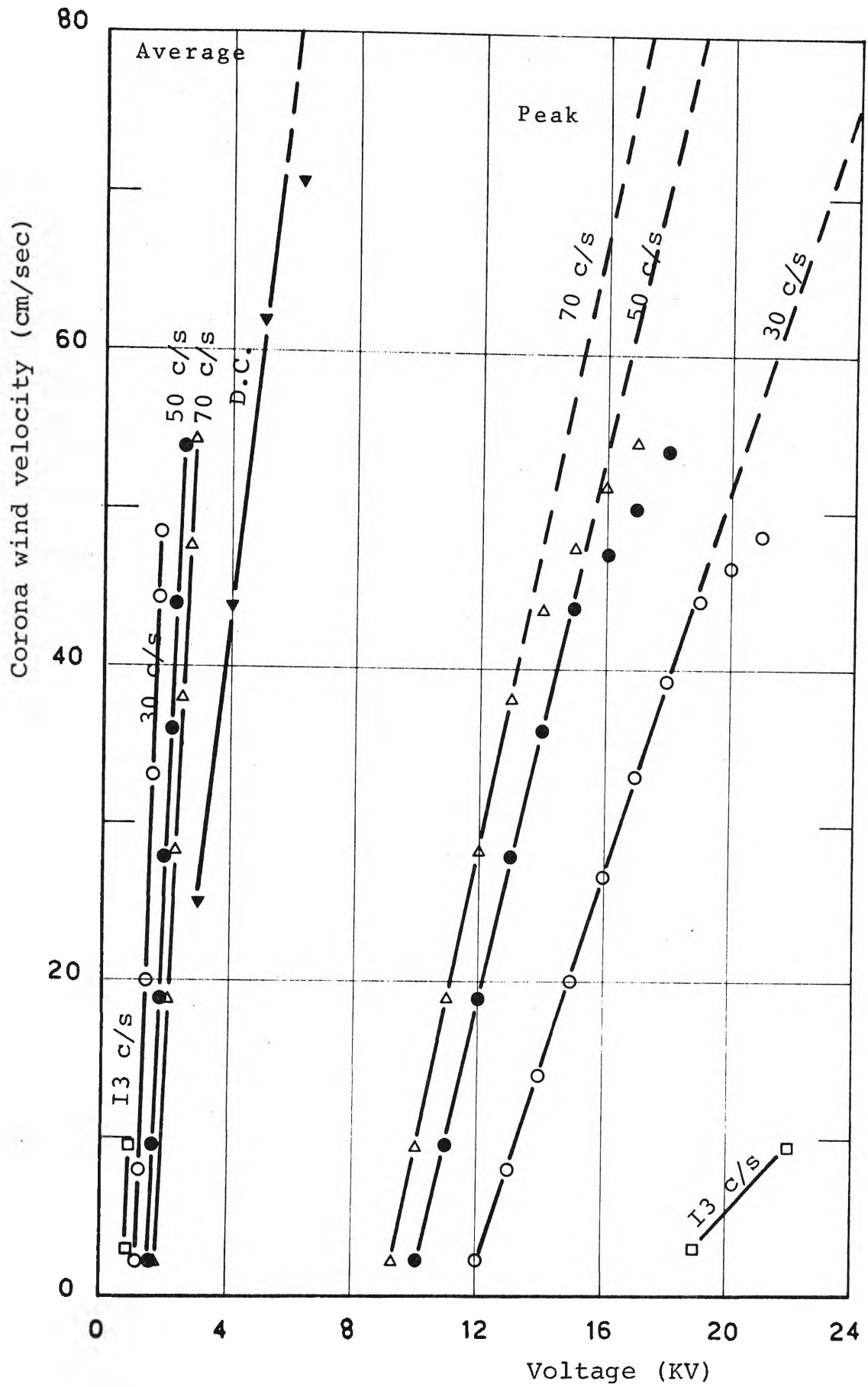


FIG.5.36 CORONA WIND VELOCITY-VOLTAGE CHARACTERISTICS.G.L.=1 cm

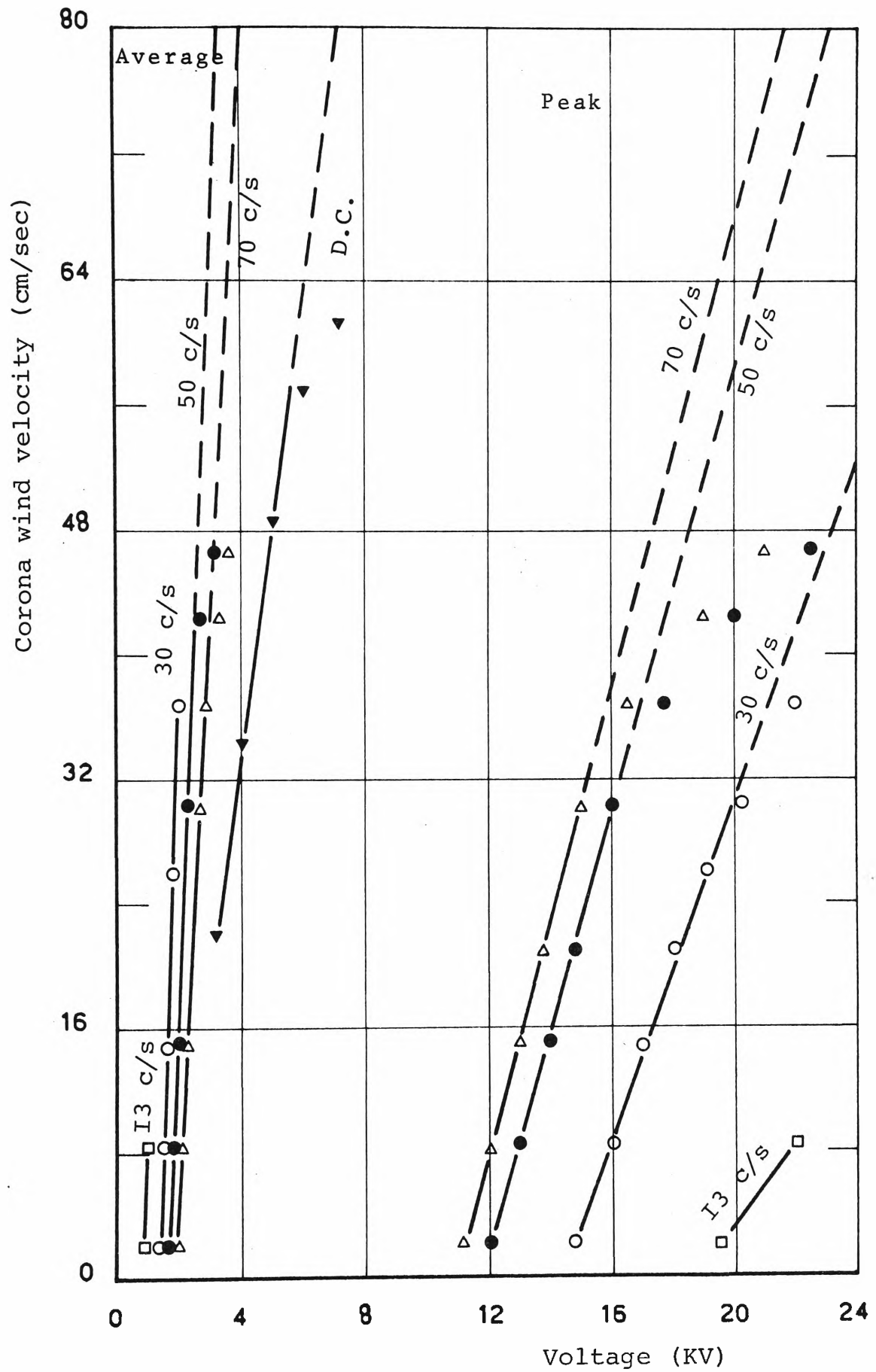


FIG. 5.37 CORONA WIND VELOCITY-VOLTAGE CHARACTERISTICS. G.L.=1.5 cm

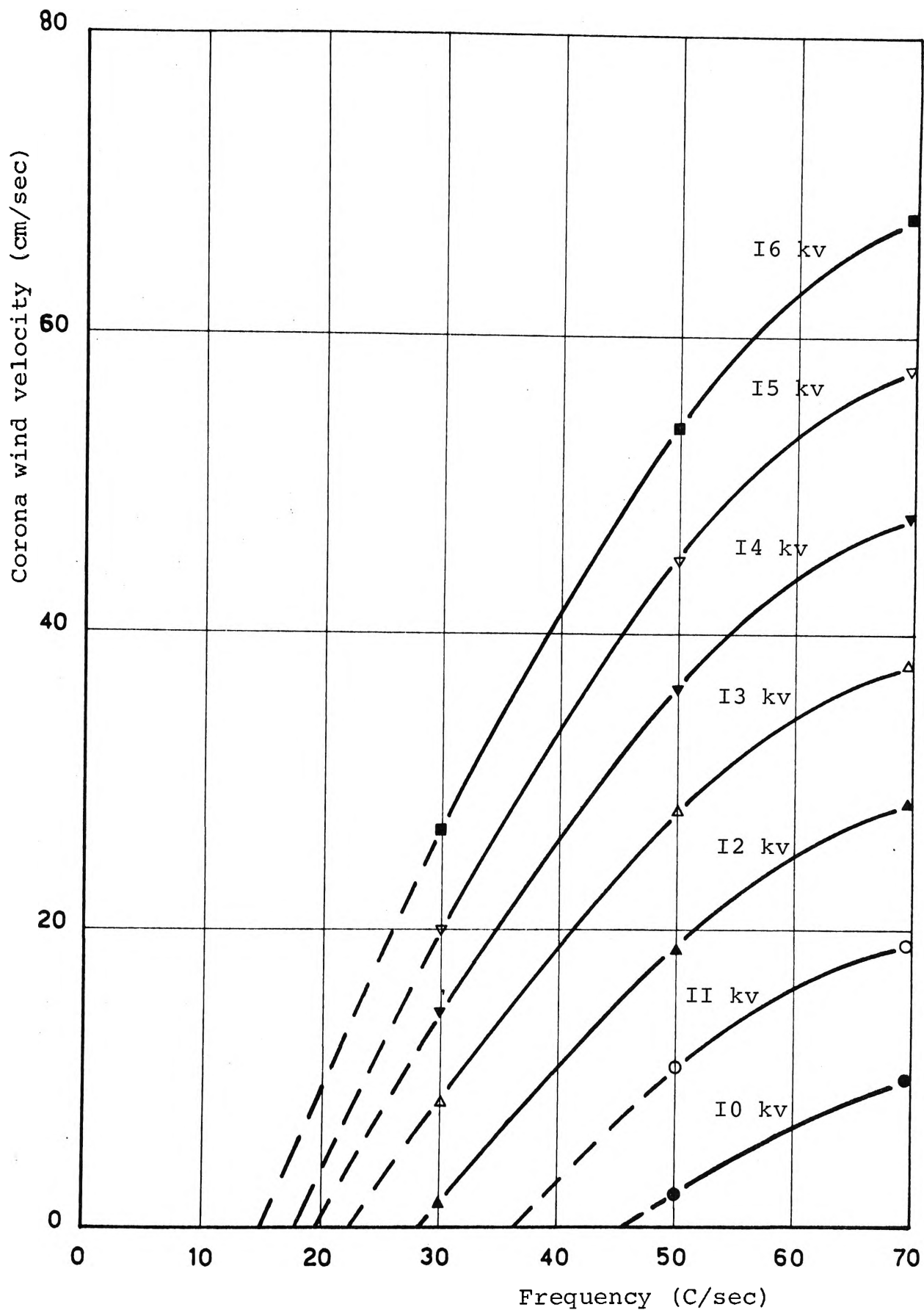


FIG.5.38 DEPENDENCE OF CORONA WIND VELOCITY ON
FREQUENCY OF APPLIED VOLTAGE.

G.L.= 1 cm

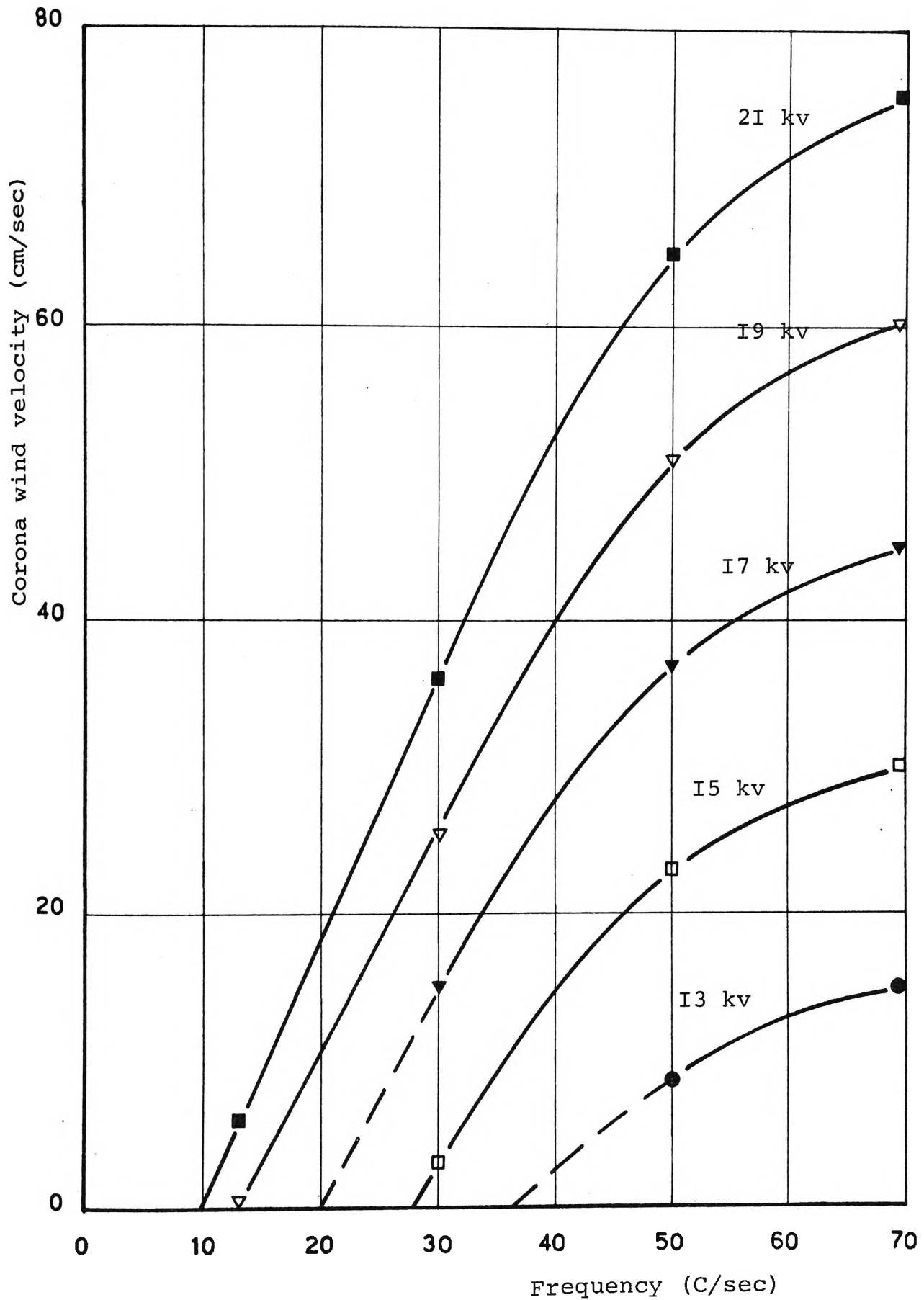


FIG.5.39 DEPENDENCE OF CORONA WIND VELOCITY ON
FREQUENCY OF APPLIED VOLTAGE.

G.L.= 1.5 cm

From Table 5.4, the following empirical expressions can be written:

$$v = -1.24 + .029 \cdot V \cdot \ln(F) \quad \text{for } G.L. = 1 \text{ cm}$$

and

$$v = -1.05 + .021 \cdot V \cdot \ln(F) \quad \text{for } G.L. = 1.5 \text{ cm}$$

5.4 Sparkover of Clean Electrode Systems

5.4.1 Introduction

Because the main advantage of using pulsed voltage to energise an electrostatic precipitator is a possible increase in the maximum peak voltage, it is of interest to investigate the sparkover mode of the electrode system. When an electrode system is contaminated, its characteristic, which is normally controlled by the ionisation process in the vicinity of the highly-stressed cathode, changes because of several factors such as the high resistivity of the contaminant, the breakdown of gas in the contaminant and its effect on the sparkover voltage of the contaminated electrode system. The reduction in sparkover voltage is more drastic under negative D.C. energisation than that under the application of negative pulsed voltage. In order to explain the change in sparkover voltage with pulsed excitation, it is necessary to investigate the sparkover of a clean electrode in the first instance. In this section the effects of the discharge process at one point electrode on those which take place at its neighbouring points are studied. The sparkover voltage of a multiple point-to-plane electrode system is compared with that of a point-to-plane system when the systems are energised by a negative D.C. voltage. This result then is

compared with that obtained with negative pulsed voltage.

5.4.2 Measurement of Sparkover Voltage

Three kinds of discharge electrode are used in this part to investigate the effect of one discharge point on the other and the sparkover mode of the corona system.

The discharge points are conically-capped cylinder electrodes having a radius of .05 cm and a tip angle of 30 degrees, they are arranged in a circular and linear pattern with their interelectrode separation varying from 2 cm down to practically zero cm, as shown in Fig.5.40. The collecting plane is made of stainless steel as it has been described previously.

The experiment was carried out at room temperature and atmospheric air with no correction of the air humidity. The electrode condition was checked after a series of five sparks and cleaned with methylated spirit. The applied voltage was increased at the rate of 10 kV per minute until the spark breakdown took place. The sparkover voltage at one gap length is the average of ten readings obtained without external irradiation source.

5.4.3 Results

Three basic modes of negative corona discharge were observed at different voltage levels. These are the Trichel pulse, the pulseless discharge and the sparkover.

The visual appearance of Trichel pulse corona discharge resembles a fan-like flare as described in Fig.5.41a. The waveshape and amplitude of the current pulse remains approximately constant as the voltage is increased, its frequency varies proportionally with the voltage. At higher potentials,

the outer edges of the fan spreads out to form a purple shower of discharge while the narrow central spike extends far out into the gap, the output current observed on the oscilloscope has a constant amplitude and the discharge is pulseless. This marks the beginning of a glow discharge which has been observed by several other investigators [12], [36]. Finally, the discharge reaches a limit when a spark-over takes place, just before this has happened, the central spike appears to contract slightly and then a bright filament originates from the anode plane to bridge the air gap. This observation by the author is similar to that described by Miyoshi [12] except for a lengthening of the central spike as mentioned by the latter. Throughout the voltage range, the negative streamers have not been observed. This is due to the fact that in short gap lengths the negative streamers and the sparkover occur almost simultaneously.

When the multiple-point electrode described in Fig.5.40c was used, similar modes of discharge were observed as for single point, except for the following interesting observation.

Throughout the voltage range, only point electrodes number 1,3,5 as described in Fig.5.42 had visible discharges. The purple envelope at point number 3 was compressed by its outer counterparts, resulting in slightly distorted discharge envelopes as shown in Fig.5.42. The central spike at point number 3 was fainter and shorter than the other two at points number 1 and 5. The bright filament which is also the positive streamer originating from the anode plane bridged the gap at point number 3 to yield a complete breakdown.

The same phenomenon was observed several times. The spark-over voltage is the same as that obtained for a single point electrode. The results are plotted against gap length in Fig.5.43 together with the curves obtained by Miyoshi [12] and Uhlmann [123] at atmospheric air. The agreement is reasonable good.

For the discharge electrodes shown in Fig.5.40b and 5.40a, bright discharges were observed at all the points, it appeared in this case the discharge at one point did not affect that at the other points, this is because of a rather long interelectrode distance existing between discharge points in comparison to the gap length.

The corona current is plotted as a function of the discharge point electrode potential for both single point and multiple point at different gap lengths as shown in Fig.5.44. The corona onset voltage of a multiple point is slightly higher than that of a single point. The current-voltage characteristics of the multiple point (dashed curves) all lie below those for single point from the onset of Trichel pulse until the transition to the glow discharge is reached. From this point onward, the slope of the characteristics for multiple point electrode is steeper than that of single point electrode characteristics.

5.4.4 Discussion

In a uniform field a positive streamer initiates a complete breakdown as soon as it arrives at the cathode. In highly nonuniform fields such as a negative point-to-plane gap with long gap length, just before sparkover, a streamer from the cathode is met at one third gap length from the

cathode by a positive streamer originating at the anode [102]. Similar phenomenon was observed and described by the author for shorter gap length with the exception that negative streamer has not been observed in this case. Because of the presence of a steady current component during the existence of this corona discharge mode, it can be considered as the extension of the pulseless discharge [36]. In the following, a qualitative explanation of the consistency of the bright filament bridging the gap at the middle discharge point electrode is offered. It is based on the well accepted illustration of the advancement of negative streamer which has been suggested by Raether [12] and independently by Loeb and Meek [25].

5.4.4.1 Effects of Streamer Branching on Sparkover Voltage

Using the Lichtenberg figure technique, Nasser [101] was able to show that under the application of a single voltage impulse, the streamer that emanates from the highly-stressed cathode propagates through the space charge free air gap and tends to split into different paths as a result of simultaneous avalanches. Under steady state condition, the advance of the streamer is hindered by the existence of the negative ion space charge, as a result, it has a more diffuse branching pattern.

In the prevalent experimental condition, when the gap space is still free of space charge, the ionisation process in the proximity of the highly-stressed cathode is determined mainly by the field distribution in the air gap. The

presence of extra discharge electrodes in the neighbourhood of one discharge point will cause the field distribution surrounding that point to alter due to the shielding effect exerted by the other points. From the theoretical study of corona discharge (Section 3.3.2), it has been found that the effective ionisation region which occupies a hemispherical volume has a radius equal to the radius of the discharge point, because of the repulsive force existing between electrons, the regions in the immediate surrounding of the discharge points number 2 and 4 in Fig.5.42 are completely ionisation free. This accounts for the bright discharges which occur only at point electrodes number 1,3 and 5.

When the avalanche starts from the highly-stressed cathode surface to build up an adequate electron density the electrons diverge outward from a high field to a lower field region (Fig.5.45a). The photons emitted and absorbed in the air may produce photoelectrons by the photoionisation process, which will move ahead to create a second generation of avalanche in advance of the primary avalanche (Fig.5.45b). If the external field is sufficient, the new avalanche will advance, and as it does so, its positive ion space charge will enhance the field between it and the head of the primary avalanche, this helps the primary avalanche to move further and eventually join the secondary generation of avalanche. In the meanwhile, the new photoelectrons will launch a new generation of avalanche ahead of the secondary avalanche and the streamer advances one more step into the gap (Fig.5.45c). The branching of the streamer as it advances through the gap space is due to simultaneous avalanches.

The negative space charge at an avalanche head with high electron mobilities and self-repulsion among the electrons causes the negative space charge to diffuse and dissipate radially instead of conserving it. The fast-moving electrons at the head of streamers repulse one another, this causes the negative streamer that originates from the central discharge electrode to have a smaller probability of branching in comparison with its outer counterparts. As a result, the energy of the central streamer is conserved as it advances through the gap, this in turn will make the electrostatic field at the streamer head relatively stronger than those at the outer electrode streamers. The photoelectrons produced by the central streamer will thus have a bigger chance of launching a positive streamer similar to that produced at point anode. This explains the consistency of the occurrence of positive streamer originating from the plane anode to join the negative streamer that emanates from the central point cathode (Fig.5.45d). The observation made by the author confirms the fact recognised by other workers that in nonsymmetrical gap the negative streamers do not play an important role in the breakdown mechanism, as the positive streamer usually predominates.

5.4.4.2 Dependence of Corona Current on the Condition of Cathode

The current-voltage relationship of the multiple-point electrode-to-plane system can be explained by using the quadratic expression derived by Herceg for a point-to-plane system.

By applying the conformal transformation into the hemispherically-capped cylinder-to-plane electrode, Herceg considered the discharge region in the gap as consisting of several flux tubes which can be transformed into prisms, he obtained the familiar quadratic relationship [40].

$$I = 9 \cdot \frac{C}{L^2} \cdot K \cdot V(V - V_0) \quad (5.17)$$

where

C : the space charge region capacitance

K : the mobility of negative ions in air

L : the gap length

V_0 : the corona onset voltage

Since the space charge capacitance C can be conveniently expressed as the ratio of the charge injected into the transport region and the voltage, it can be seen that for a multiple point electrode the number of charge injected into the transport region is proportional to the number of discharge points, consequently the corona current increases under such conditions.

5.4.4.3 Sparkover Voltage versus Gap Length

From the calculation of the corona onset voltage, it can be seen that this value depends little on the gap length as long as the gap length is considerably larger than the point radius. This is the result of nearly identical field intensity distribution in the ionisation and buffer regions for the same point radii. The physical significance of this is: the potential drop across the ionisation and buffer regions is approximately constant and the remainder of the potential difference is used to move the space charge across the gap.

By rearranging all the terms in equation (5.17) and approximating the field strength as (V/L) , it can be written:

$$\frac{I}{9C} \cdot L = K.E. (V - V_o) \quad (5.18)$$

Substitute K.E. by the drift velocity, v , of negative ions in equation (5.18) and one can obtain:

$$\left(\frac{I}{9Cv}\right) \cdot L = V - V_o \quad (5.19)$$

Because (I/v) is the charge density (in a one-dimensional model, this is equal to charge per unit length) in the transport region, it can be seen that when this density reaches a critical value, the space charge will enhance the field at the plane anode sufficiently to create a positive streamer from the anode plane and cause a sparkover. Define the value of (I/v) at sparkover as $(I/v)_c$ then the sparkover voltage can be approximately written from equation (5.19) as:

$$V_s = V_o + \frac{1}{9C} \left(\frac{I}{v}\right)_c \cdot L \quad (5.20)$$

This expression indicates a linear relationship between the breakdown voltage and the gap length within the range of experiment.

As for the multiple-point electrode system, the increase in corona current, I in the numerator of equation (5.20) is counterbalanced by the increase in the space charge region capacitance C in the denominator, this results in an approximately constant $(I/Cv)_c$ at spark breakdown, hence the independence of sparkover voltage on the condition of the cathode.

5.4.5 Sparkover Voltage with Pulsed Energisation

From the study of the discharge pattern along a wire electrode (Section 5.2.2), the corona current measurement (Sections 5.2.3 and 5.3.2), it has been shown that the space charge condition in an asymmetrical electrode system can be the same for both negative D.C. and pulsed voltages, the difference between the two voltages is that with pulsed voltage, a higher peak value is required to produce the same space charge condition as with D.C. voltage. This coupled with the independence of the sparkover voltage of a clean electrode system on whether the discharge cathode is a single point electrode or a multiple point one, suggest that the sparkover voltage will also be independent on the type of discharge electrode (single or multiple point type) when the system is energised by a pulsed voltage.

It is, therefore, only necessary to present the spark-over voltages which are measured when the point-to-plane system is excited by a negative pulsed voltage. The results are shown in Fig.5.43 for pulse repetition rate of 30 c/s. It is of interest to note that:

- (i) The linear relationship between sparkover voltage and gap length is also true for pulsed energisation.

This indicates that, at steady state, the space charge condition in the gap determines the sparkover voltage as suggested by equation (5.20).

- (ii) The sparkover voltage for pulsed energisation is higher than that for D.C. one at the same gap length. This is reasonable, since pulsed voltage requires a higher peak value to produce the same

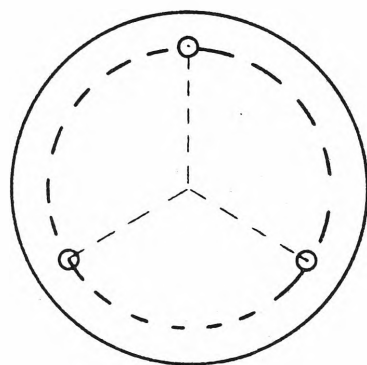
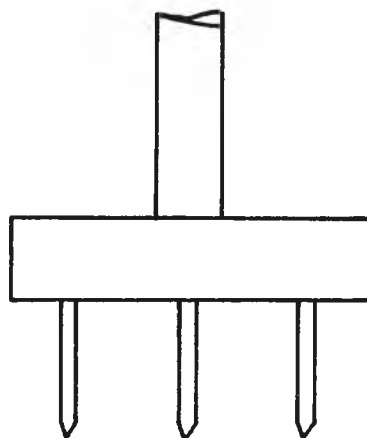
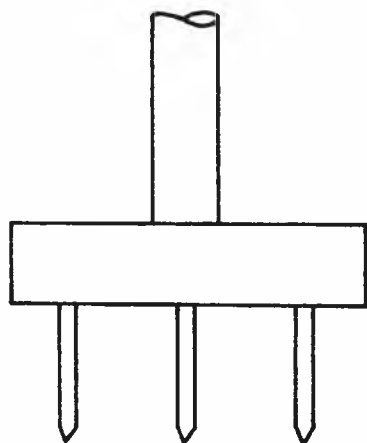
critical space charge condition, in which the charge density in the transport region is adequate to enhance the field at the plane anode sufficiently to generate a positive streamer.

5.5 Summary:

Some of the important characteristics of a corona system have been investigated. The similarity of the discharge patterns under pulsed and D.C. energisation for the condition studied in this work indicates that no significant difference exist in the discharge mechanism. The basic mode of negative corona discharge is the Trichel pulse, is evidently observed in both modes of energisation. Although the effects of positive and negative space charges on the ionisation process make the instantaneous characteristics of the Trichel pulse somewhat different from the D.C. counterpart, the mean characteristics do show the basic similarity. The consistency of the repetition rate of the corona current pulse and its amplitude at fixed voltage level is in line with the D.C. characteristics and moreover when the gross space charge in the air space is the same the average corona current and the discharge pattern are very similar. The linear relationship between the photon current and the corona current confirms that the number of photons emitted in a discharge in air is proportional to the number of ionising collisions. This connection provides a means to measure the corona current in terms of the intensity of the discharge where resolving the corona current from the total output current comprised of capacitor charging current and corona current is difficult. The similarity of the basic ionisation

process is also observed in less-popularly measured characteristics such as the electrical wind.

Since it is proved that the current distribution on the collecting plane has the same shape as the discharge pattern in the vicinity of the discharge electrode (Appendix D), the current distribution on the collecting plane would presumably have the same shape under pulsed and D.C. energisation. This coupled with the unimportant role of negative streamers in the spark discharge suggests that the increase in spark-over voltage of a clean electrode system under pulsed energisation is predominantly caused by the gross condition of space charge in the accumulation and transport regions of the air space.



(a)

(b)

(c)

FIG. 5.40 DIAGRAM OF MULTIPLE-POINT DISCHARGE ELECTRODES

(a)

(b)

(c)

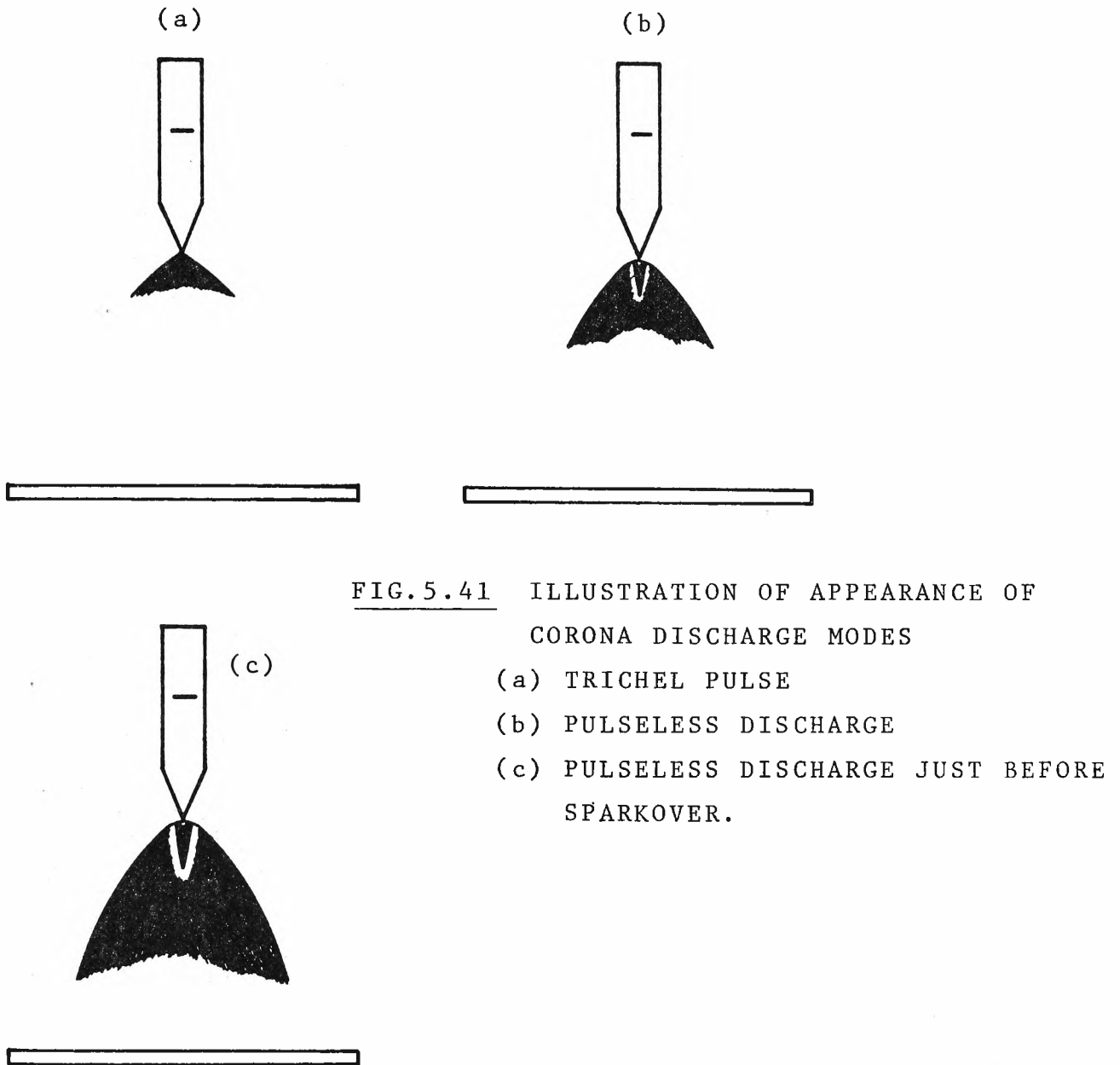
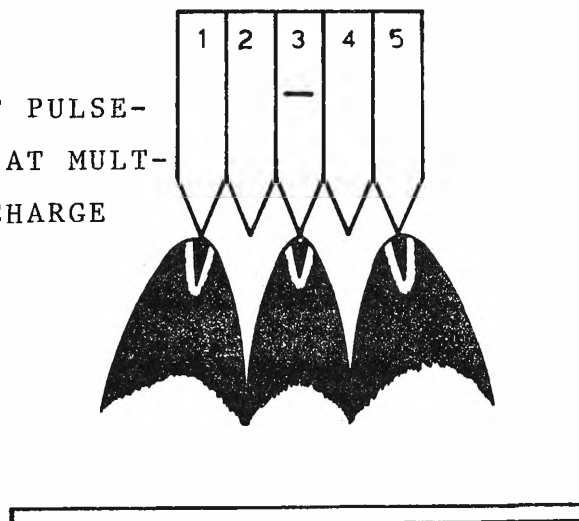


FIG. 5.42 ILLUSTRATION OF PULSELESS DISCHARGE AT MULTIPLE-POINT DISCHARGE ELECTRODE.



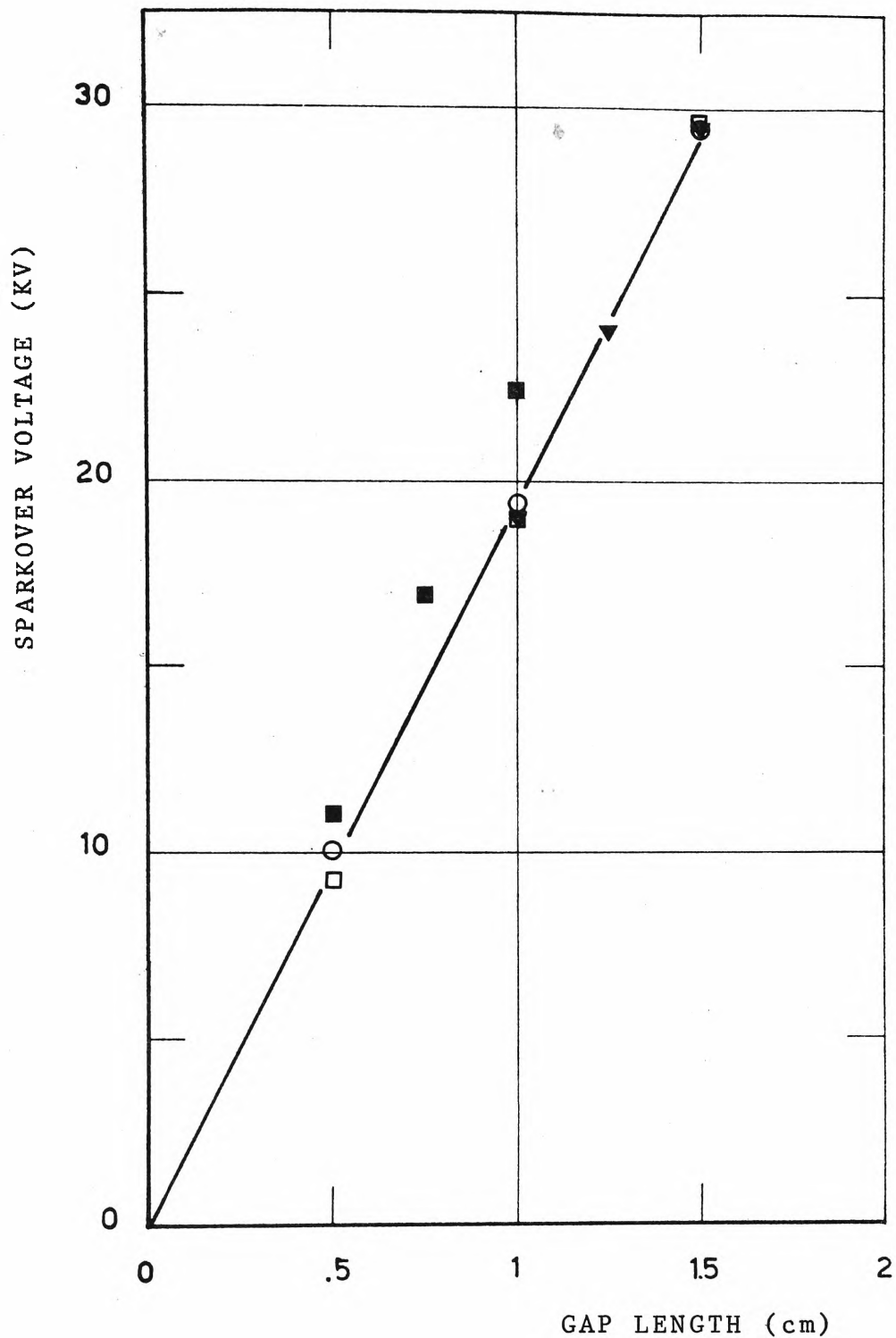


FIG. 5.43 SPARKOVER VOLTAGE VERSUS GAP LENGTH

- MIYOSHI'S RESULTS [12]
- UHLMANN'S RESULTS [123]
- ▼ MEASURED VALUES FOR SINGLE AND MULTIPLE POINT ELECTRODES (D.C.)
- MEASURED VALUES FOR SINGLE POINT ELECTRODE (PULSED VOLTAGE)

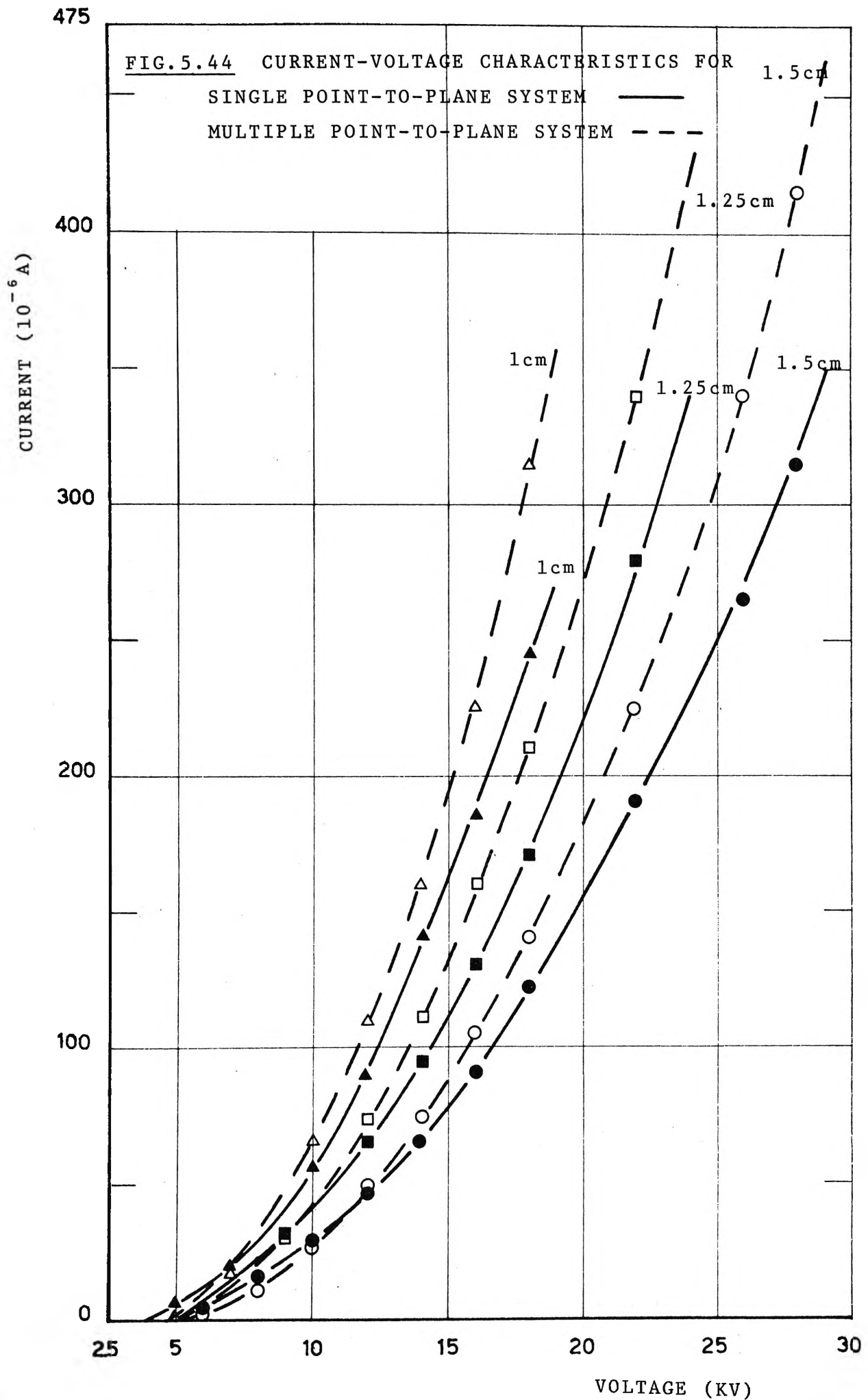


FIG.5.45 ILLUSTRATION OF THE ADVANCE OF NEGATIVE STREAMERS IN A MULTIPLE POINT-TO-PLANE SYSTEM LEADING TO THE FORMATION OF COMPLETE BREAKDOWN IN THE GAP SPACE

- (a) FORMATION OF PRIMARY AVALANCHE AND PHOTO-ELECTRONS
- (b) FORMATION OF SECOND GENERATION OF AVALANCHE TAKING PLACE AHEAD OF THE PRIMARY AVALANCHE WHILE IT IS MOVING TOWARD THE SECONDARY AVALANCHE
- (c) THE PRIMARY AND SECONDARY AVALANCHES JOINING TOGETHER WHILE THE NEW PHOTOELECTRONS PRODUCE A NEW GENERATION OF AVALANCHES
- (d) THE NEGATIVE STREAMERS APPROACHING THE PLANE ANODE AND INDUCE THE FORMATION OF POSITIVE STREAMER WHICH IS MOST LIKELY TO JOIN THE CENTRAL NEGATIVE STREAMER TO CAUSE A SPARK-OVER.

○	:	PHOTONS
○	:	PHOTONS PRODUCE PHOTOELECTRONS
+	:	POSITIVE IONS
-	:	ELECTRONS

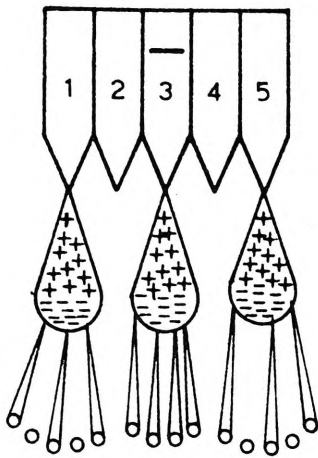


FIG. 5.45(a)

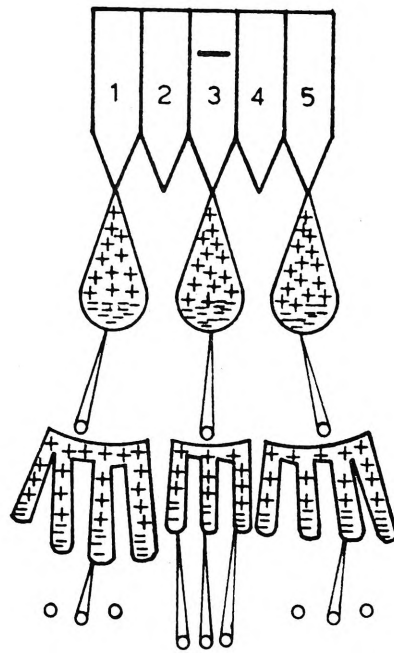


FIG. 5.45(b)

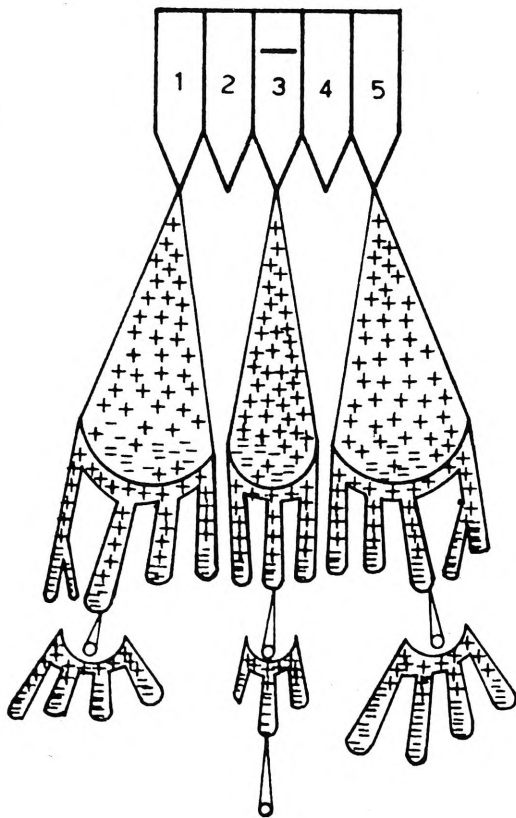


FIG. 5.45(c)

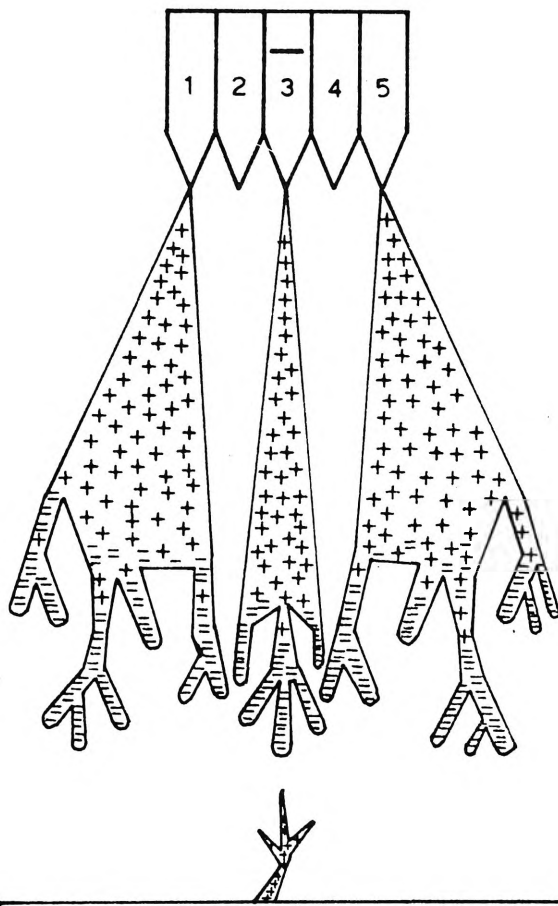


FIG. 5.45(d)

CHAPTER 6: CHARACTERISTICS OF CORONA SYSTEM-
CONTAMINATED COLLECTING ELECTRODE.

6.1 Introduction

In this chapter, the contaminated condition of an electrostatic precipitator is investigated and simulated by placing a layer of insulating material on the surface of the plane anode. The characteristics of the contaminated system are investigated with particular attention given to the ionisation process that takes place in the low field strength region and its effects on the overall electrical characteristics.

In order to explain the change of sparkover voltage with pulsed voltage energisation, it is necessary to describe in much greater detail, than has been done in the past, the formation of back corona. Since the whole process is very complex, it is convenient to do this by describing each step of its formation. Hence this chapter will discuss:

- (i) The build up of voltage across the layer of contaminant. The distribution of the voltage indicates that in a negative point-to-plane system, the central part of the contaminant is more likely to undergo a breakdown which, depending on the voltage level, may trigger a sparkover.
- (ii) The conduction of current through the contaminant. Because of the constriction of current flow through the contact areas between adjacent particles, high field is set up in the air voids which are present in the contaminant. This phenomenon results in an increase in the effective contact areas and may

trigger local gas discharge to occur in the contaminant.

- (iii) The gas discharge that takes place in the contaminant is investigated by analysing a theoretical model whereby the field in the air voids is determined and compared with the breakdown field strength in air. The discharge causes the perforation to take place in the contaminant and with the presence of the discharge, the distribution of the surface potential is altered in such a manner that more negative ions will contribute to the maintaining of the discharge.
- (iv) An analytical study of the potential distribution is presented to confirm the significant role played by the surface potential gradient in the vicinity of back discharge channel. This gradient helps to maintain a stable back discharge in the contaminant and at higher applied voltage tends to enhance the development of the back discharge into space streamers.
- (v) A mechanism of the formation of back corona discharge is proposed, whereby all important features discussed in previous parts are combined to lead to a qualitative interpretation of this phenomenon.
- (vi) Effects of back corona on sparkover of the contaminated electrode system are investigated and the dependence of sparkover voltage on the contaminant thickness is summarised in a semi-empirical expression. The reason for the difference of sparkover

voltage under pulsed excitation with that under D.C. energisation is hypothesised by extending the above mechanism and comparing the results with those obtained by other workers. Experiments are also used to demonstrate some important points.

(vii) Finally, the application of the technical evidences and fundamental processes to industrial situation is discussed.

6.2 A Survey on the Subject

The collection of particles by means of an electrostatic precipitator becomes difficult when the collecting plate is covered with a layer of high-resistivity particles. The corona current, as it flows through the layer of particles, induces a potential drop across the layer. When this reaches a threshold level, it causes local breakdown in the layer, which may trigger a complete sparkover across the electrodes. This phenomenon, commonly known as back corona, was observed by Wolcott [105] in 1918 and about 30 years later by Pauthenier et al [106]. The deleterious effects of this kind of secondary discharge on the collection efficiency are described in books by White [1], Rose and Wood [2] and Robinson [3]. The back discharge emits ions of polarity opposite to that of the primary discharge and causes an increase in corona current and a drop in sparkover voltage.

The increase in corona current was investigated by Laurent [107]. He used a point-to-plane system and covered the passive electrode with a layer of mica perforated to simulate the porosity in a layer of dust. His results show a gradual increase in corona current after the onset of back

corona. He assumed that the mica in the proximity of the hole behaves like a capacitor which discharges when the charging voltage provided by primary ions reaches the breakdown value of gas in the hole.

The drop in sparkover voltage as a result of surface conditions of the passive electrode in D.C. corona was studied by Penney and Craig [108],[109]. They observed a local discharge consisting of repetitive current pulses which originate from a fixed location on the passive anode and frequently tend to increase in magnitude until sparkover occurs. This kind of discharge was called "Flare discharge". They also hypothesised that an imperfect insulating coating on the anode and a source of ionisation, current pulses followed by sparkover can occur if the average voltage gradient is of the order of 5 kV/cm. Recently, work done by Masuda [65] on the same kind of discharge using photomultiplier technique provides results which support some early observations by Penney and Craig.

In depth investigation of the conduction mechanisms in a layer of high-resistivity particles (borosilicate and silica glass) has been carried out by McLean [110], who has explained the increase in current is due to transfer of electrons across the air gap between adjacent particles, caused by the Schottky emission mechanism. Herceg [40] has studied the modes of corona discharge in clean and contaminated corona system energised by positive and negative steady voltages. Their works contribute to the understanding of the manner in which electrical conduction takes place in layers of precipitated fly-ash and offer a possible solution to the

suppression of back corona e.g. by A.C. energisation [8] whereby the frequency and D.C. offset of a square-wave power supply can be controlled.

6.3 Voltage Distribution across the layer of Contaminant

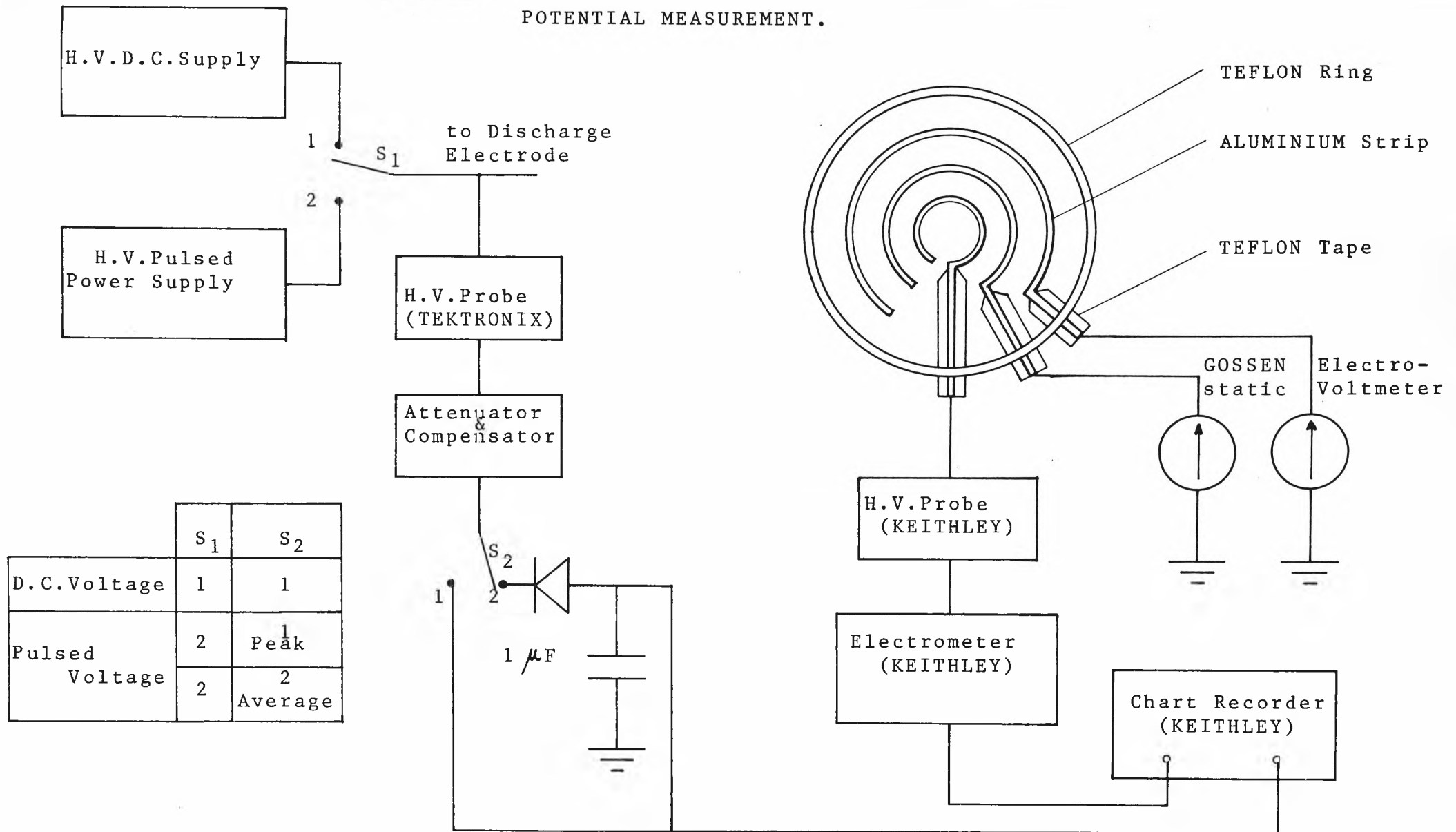
6.3.1 Introduction

In a contaminated corona system, the presence of a layer of high-resistivity contaminant on the collecting plane affects the transport of charge carriers in the air gap to the collector. It has been observed by many workers [40], [65], [66] that the distribution of current on the clean collector is characterised by high-current density at the centre and low density at the outer part of the plane. When the resistivity of the contaminant is low (10^9 ohm-cm), the current distribution on the plate is nearly identical with that obtained for a clean plate [1]. When the resistivity is high (10^{12} ohm-cm) the distribution curve shows a marked redistribution of the current. This phenomenon, according to White [1], is due to the high dust resistance, which causes most of the corona current to flow to the edge. In this section, a qualitative discussion of the redistribution of the charge carriers on the surface of the contaminant is presented. The discussion is based on the observed distribution of potential across the contaminant layer.

6.3.2 Measurement of Surface Potential

The surface potential of the contamination versus the steady state D.C., average and peak pulsed voltage characteristics can be measured and plotted simultaneously with the arrangement shown in Fig.6.1. Due to the symmetrical nature of the point-to-plane configuration in the radial direction,

FIG.6.1 SCHEMATIC DIAGRAM OF SET-UP FOR SURFACE
POTENTIAL MEASUREMENT.



no angular variation in the potential in the plane surface of the contamination is anticipated around the point of projection of the point electrode. The surface potential probe was made in the form of a circular ring with an assembly of several concentric rings, used to monitor the potential variation throughout the surface of the contamination. The rings were made of aluminium foil which has been carefully smoothen out in order to reduce its thickness ($16\mu\text{m}$) and increase its adhesivity to the contamination surface.

The width of the rings is 1 mm, a compromise between the minimum detectable variation of the surface potential and the ease of practical handling of the probe. To reduce the possible error caused by the interference of one ring over the potential measured by the next ring, the straight part of each probe is carefully insulated with Teflon tape as illustrated in the diagram. The rings are located at the same distance from one to another, and are glued to the contamination surface by silicon grease. The periphery of the contamination was firmly pressed onto the collecting plane electrode by a Teflon ring used as a weight and to limit the surface area of the contamination exposed to corona discharge. For comparison purpose, the Teflon ring was also used in measuring the current-voltage characteristics of the clean electrode system. The introduction of the surface potential probe assembly into the contaminated corona system did not contribute significant error in the overall characteristics. This was checked by obtaining the measurements for the contaminated corona system with and

without the probe assembly under similar laboratory conditions, the difference in the two cases was less than 5%. The probe assembly that has been described is suitable for studying the potential distribution on the surface and inside the contamination.

The total resistance of the surface potential probe and the high voltage measuring equipment should be compatible with the bulk resistance of the contaminant to minimise any possible disturbance to the characteristics of the composite corona system. The surface potential can be plotted against the applied voltage by using a high voltage probe (Keithley 6130A) in conjunction with an electrometer (Keithley 610B). The 10^{12} ohm input resistance of the electrometer high voltage probe is adequate for this measurement. The potential distribution over the surface of the contaminant can be measured simultaneously but discreetly by means of electrostatic voltmeters (Gossen) that have an input resistance of 10^{13} ohms.

6.3.3 Results and Discussion

The surface potential was measured when the contaminated corona system was energised by D.C. and pulsed voltages. The results are shown in Fig.6.2 and 6.3 respectively for D.C. and pulsed voltage at 30 c/s. Similar patterns were observed for different-thickness and frequencies, and are not shown here. The surface potential distribution follows the same shape for both D.C. and pulsed voltages. At the same surface potential the peak value of the pulsed voltage is much higher than the D.C. voltage. This behaviour is concurrent with the corona current-voltage characteristics

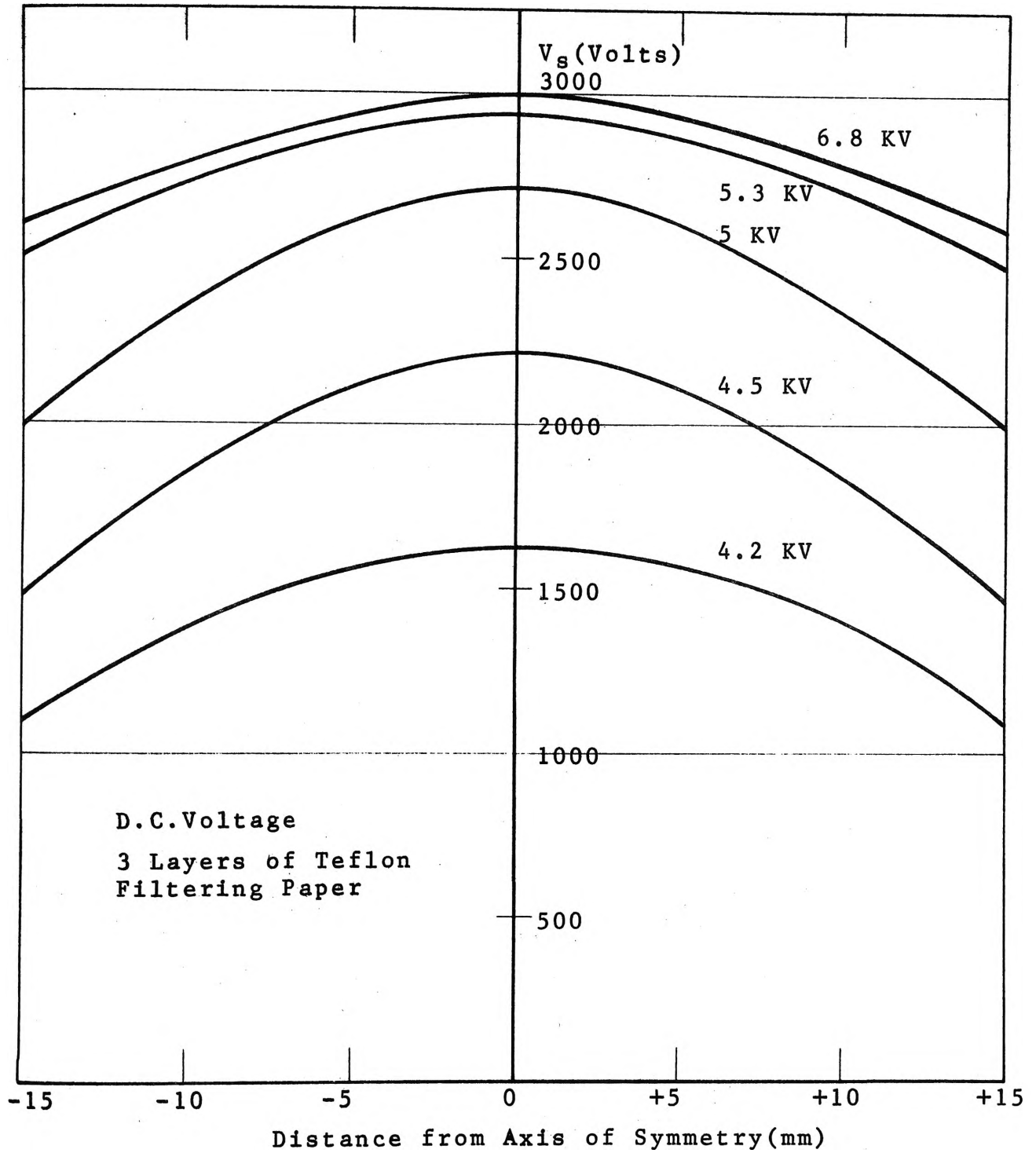


FIG.6.2 SURFACE POTENTIAL DISTRIBUTION FOR D.C. VOLTAGE. CONTAMINANT THICKNESS = 375 μ m.

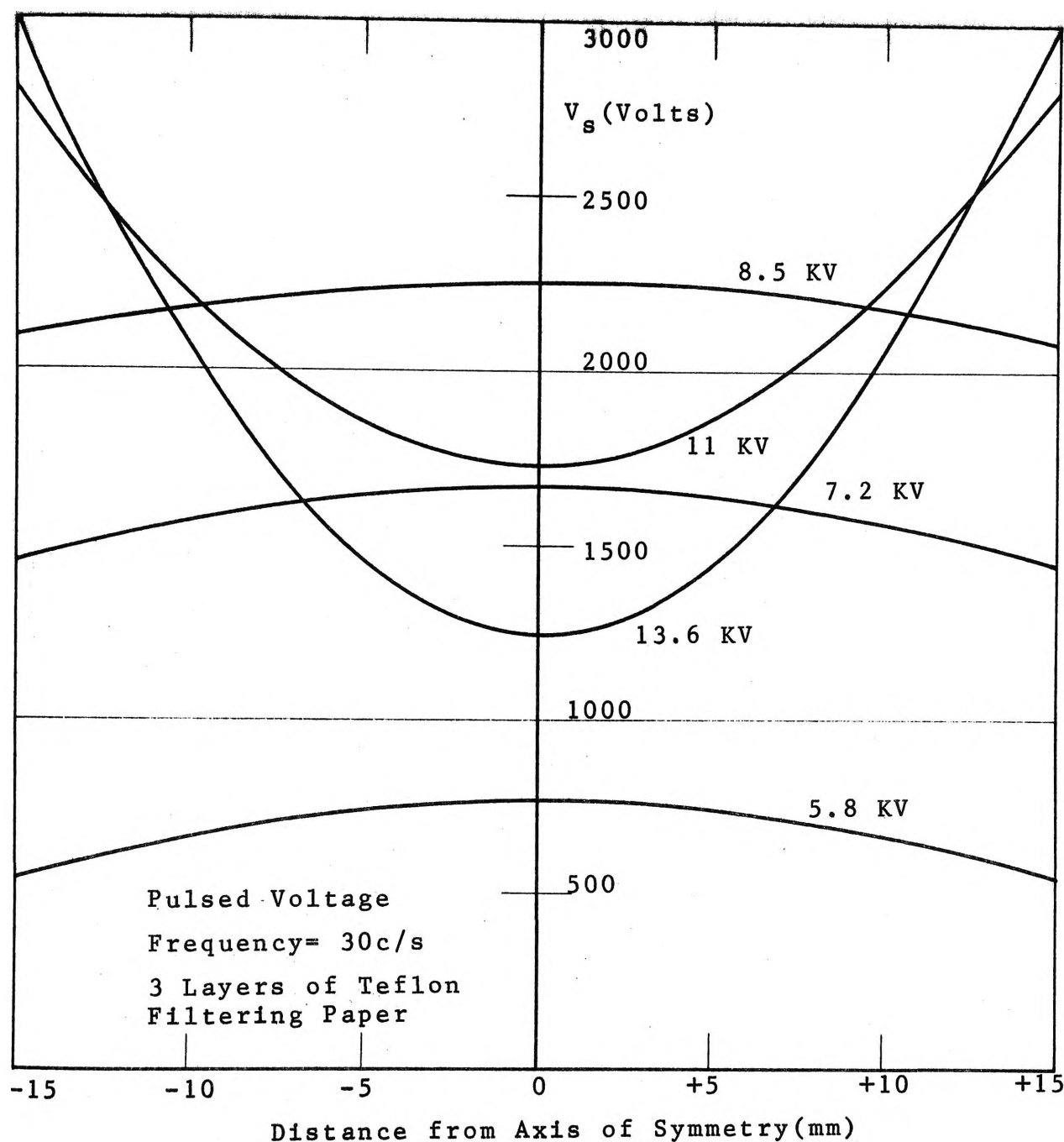


FIG.6.3 SURFACE POTENTIAL DISTRIBUTION FOR PULSED VOLTAGE. CONTAMINANT THICKNESS = $375\mu\text{m}$, REPETITION RATE = 30c/s (Peak Voltage is shown beside each curve).

obtained previously for the clean electrode system.

From the linear distribution of potential in the contaminant with respect to its thickness which is shown in Fig.6.4, it is reasonable to assume that most of the negative ions accumulate on the surface of the contaminant. The ions tend to form a surface charge layer rather than space charge inside the contaminant. The surface charge is thus proportional to the potential across the layer of contaminant, and consequently has the same distribution as the potential. It can be seen in Fig.6.2 that the distribution of the potential (and the charge) resembles a Normal Distribution curve which can be written as:

$$q(r) = \frac{q_0}{\pi r_e^2} \exp\left(-\frac{r^2}{r_e^2}\right) \quad (6.1)$$

where $q(r)$ is the surface charge density at distance r from the centre of the contaminant layer, q_0 is the total charge that remains on the layer surface and r_e is the mean radius of an area over which the charge carriers disperse.

Since the potential is proportional to charge, from equation (6.1) the following equation can be written:

$$\frac{V_1}{V_2} = \exp\left(\frac{r_2^2 - r_1^2}{r_e^2}\right) \quad (6.2)$$

where V_1 , V_2 are potential across the layer at radii r_1 and r_2 respectively.

The mean radius, r_e , is thus:

$$r_e = \sqrt{\frac{r_2^2 - r_1^2}{\ln(V_1/V_2)}} \quad (6.3)$$

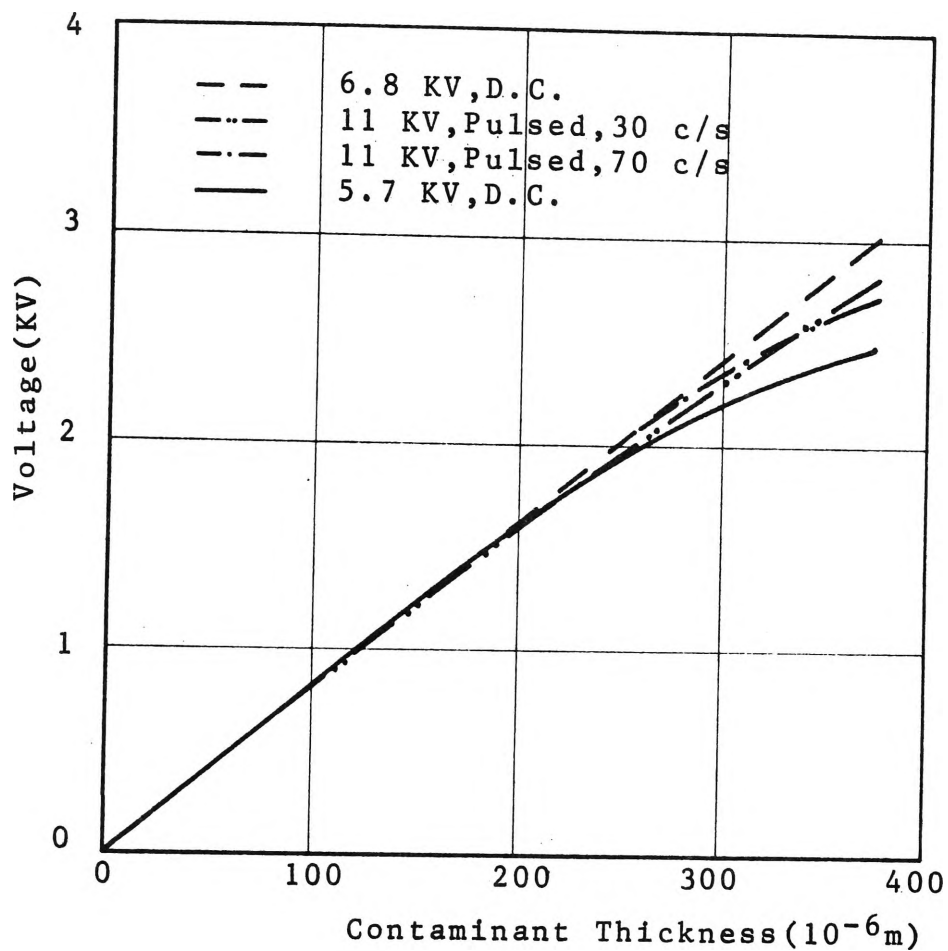


FIG.6.4 DISTRIBUTION OF VOLTAGE AS A FUNCTION OF CONTAMINANT THICKNESS. (Peak value is shown for Pulsed Voltage).

Substituting the values obtained from Fig.6.3 into equations (6.2) and (6.3), one gets

$$r_e = 23 \text{ mm}$$

$$q_o = 160 \times 10^{-9} \text{ Coul.}$$

for $r_1=7.5 \text{ mm}$, $r_2=15 \text{ mm}$, $V_1=1500 \text{ volts}$ and $V_2=1100 \text{ volts}$ at applied voltage of 4.2 kV .

The shape of the potential distribution is caused by the following factors:

- (i) The injection of charge carriers onto the contaminant layer. The negative ions which are created in the buffer region of the air space tend to follow the field lines to the collecting plane. Along the axis of the electrode system, the field strength is highest and consequently there are much more ionisation activities and accumulation of negative ions in the central part of the air gap than the outer space. The negative ions on arrival at the surface of the contaminant would undergo a diffusion process along the radial direction. However, because the mobility of negative ions at room temperature is low, it can be shown that the diffusion radius is negligible e.g. the transit time of negative ions between electrodes is in the order of milliseconds (Chapter 3), the diffusion coefficient, D of negative ions at room temperature can be estimated as equal to $.043 \text{ cm}^2/\text{sec}$, assuming the diffusion to take place along the radial direction, the mean diffusion radius can be found equal to $r_e = \sqrt{4Dt} = .01 \text{ cm}$.

- (ii) The build up of potential across the layer of contaminant tends to oppose further accumulation of the negative ions on the surface. The repulsive force between charge carriers on the surface and the on-coming negative ions is proportional to the surface charge density. This means that the repulsion in the central part of the contaminant is more vigorous than that at the outer one since the charge density is highest in the centre of the contaminant layer. The repulsion activities cause negative ions to spread out over a large area on the layer and result in a distribution curve which has a fairly broad hump in the middle.
- (iii) The broadening of the distribution curve is also caused by the non-linear relationship between the voltage across the contaminant and the current. The resistivity of the central part of the layer is much less than that of the outer part due to larger density of charge carriers present in the centre. The build up of voltage is, at first, linearly dependent on the current density on the plate, and the voltage in the central part of the layer is higher than that at the edge. When the current has reached the non-linear region of the current-voltage characteristics, the voltage in the central part increases somewhat slower, but is still higher than the voltage at the edge of the contaminant layer.

6.4 Conduction of Current in the Contaminant

6.4.1 Introduction

The build up of potential across the contaminant indicates that the contaminant layer acts like a leaky capacitor, the potential of which depends on the average amount of charge injected and dielectric resistance. The equivalent capacitor tends to smooth out any fluctuation due to the pulsating nature of the pulsed voltage. From the constancy of the surface potential at a given applied voltage, it is permissible to assume that the conduction of current through the contaminant, exposed to the injection of charge carriers on one side and adheres to the collecting plane on the other side, is the same under both D.C. and pulsed energisation. In this section, the conduction current is plotted against applied voltage when the contaminant is placed between plane parallel electrodes. This technique is suitable to investigate the flow of current under steady state condition i.e. the input charge carrier, at any moment, is equal to the carriers removed. The conduction mechanism is discussed by considering the common properties of different contamination materials. The contaminant is modelled as comprising of spherical volumes of homogeneous structure that are compacted in a simple cubic array. This model represents closely the realistic structure of a layer of fly-ash which practically has the spherical form, and only the equivalent structure of amorphous, inhomogeneous insulating materials such as Teflon filtering papers, writing paper..etc. Attention is given to the conduction through a thin layer of the spherical surface. This mode of conduction is more

predominant at room temperature and induces high electric field in the air voids between adjacent volumes due to the constriction of current that flows through the contact area.

6.4.2 Measurement of Conduction Current

The current conduction mechanism in a contaminant is investigated by using equipotential parallel surfaces. The contaminant is the same kind of Teflon filtering paper as used in the surface potential measurement. It is placed between two parallel electrodes as described in Fig.6.5. The bottom electrode has a guard ring around its central part through which the current is measured. The teflon disc is much larger than the central probe to avoid edge effect. The guard ring is earthed through the shielding part of a coaxial-cable connecting the central probe to the electrometer, 610B.

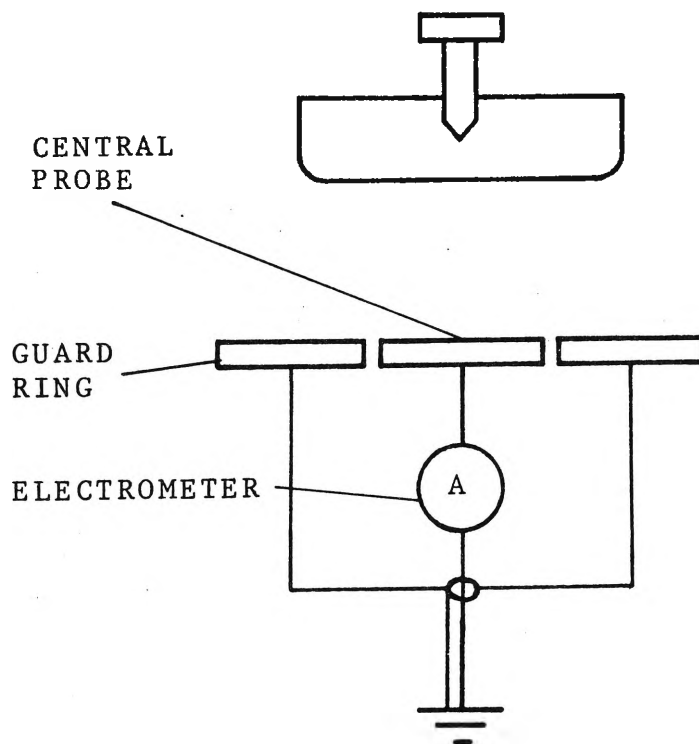


FIG.6.5 PLANE PARALLEL ELECTRODES USED TO
STUDY THE CONDUCTION OF CURRENT
THROUGH THE CONTAMINANT.

A steady voltage is applied to the top electrode. At a certain voltage level the current was observed to have its highest value when the voltage was changed and gradually decreased to a constant value, this was then recorded. The experiment was carried out at room temperature and atmospheric pressure.

6.4.3 Results and Discussion

The current-voltage characteristics are shown in Fig.6.6 for two thicknesses and voltages up to near the breakdown values. The current is a function of the voltage and its exponent. This relationship also holds for paper and precipitated fly-ash at normal temperature. It is therefore suitable to propose a mechanism of the current conduction in several substances such as Teflon filtering paper, fly-ash which are commonly used to simulate the contaminated condition in a corona system.

The current conduction through borosilicate and silica glass (the major constituencies of precipitated fly-ash) has been investigated by McLean [110], who has explained the deviation from linearity of the current-voltage relationship is due to the Schottky emission taking place in the vicinity of contact areas between insulator particles.

By formulating the common properties of different materials (fly-ash, paper, Teflon filtering paper) such as the amorphous nature and the inhomogeneous structure of those materials, Herceg [40] assumed that the insulating substances behave like semi-conductors. He obtained an expression which includes currents due to volume conduction and the Schottky emission.

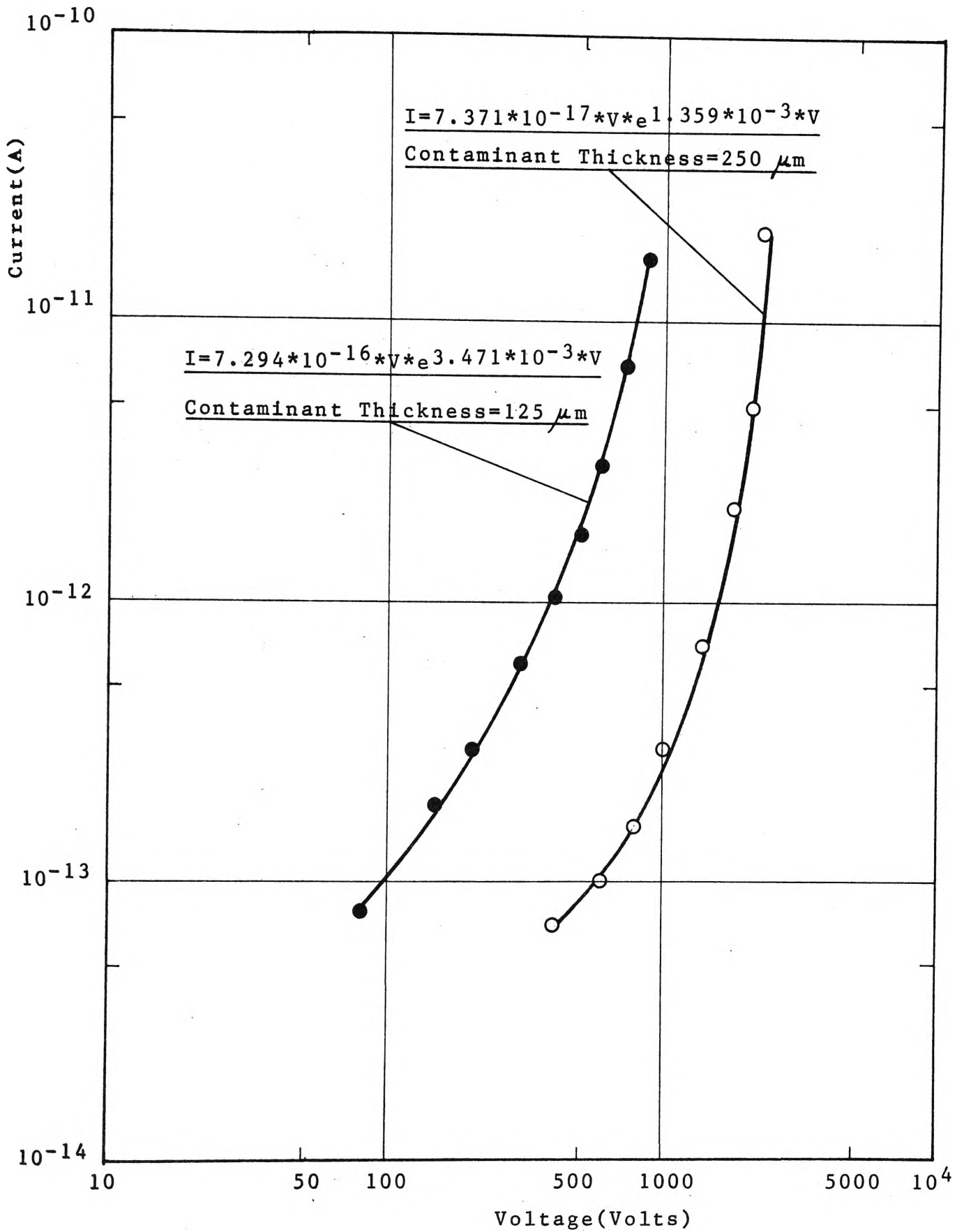


FIG. 6.6 CURRENT-VOLTAGE CHARACTERISTIC OF TEFLON
FILTERING PAPER USED AS CONTAMINANT.

The interpretation of the conduction mechanism uses a similar equivalent structure for different contamination materials as proposed by Herceg. The model is developed further by considering the contaminant as comprising of homogeneous volumes having spherical shape. These volumes are compacted in a simple cubic array to form a layer of contaminant. The conduction of current through the layer of contaminant is due to two modes: the surface conduction and volume conduction. An expression is obtained in which the conduction through a thin surface layer is considered more significant than the conduction through the bulk volume of contaminant. This is justifiable since it has been suggested by McLean [111] that at low temperature, the effective resistivity of a layer of insulating particles approaches the surface resistivity.

The amorphous structure of the contaminant can be considered as consisting of solid and pores which are separated from each other and it can be represented by a lumped one-dimensional model as shown in Fig.6.7. The model is applicable for both particulate or fibrous contaminant layer placed between two plane parallel electrodes.

Two solid, homogeneous volumes of contaminant are pressed together by a force, the effective contact area can be divided by two parts, A and B.

The current that flows through the contact area A is comprised of two components: one is due to the conduction through the volume of the homogeneous region and the other component is due to the conduction through a thin layer on the surface of the solid region.

6.4.3.1 Volume Conduction Current

The current component due to conduction through the homogeneous volume of contaminant is obtained by finding the constriction resistance of the contact area and the average voltage across this region.

The calculation of the constriction resistance of contacts between two surfaces has been investigated and summarised in books by Jones [112], Windred [113], and Holm [114]. A good survey and evaluation of various approaches has been done by McLean [110] in his investigation of current conduction through borosilicate and silica glasses. The following expression is Holm's equation.

Holm [114] developed an expression for the effective resistance of point contacts between parallel plates in his work on metallic contacts. He generalised the expression by assuming an elliptic point of contact with the semi-axes α and β .

The constriction resistance from the plane of contact to one equi-potential surface can be expressed as:

$$R_{\mu} = \frac{\rho_v}{4\pi} \int_0^{\mu} \frac{d\mu}{\sqrt{(\alpha^2 + \mu)(\beta^2 + \mu)\mu}}$$

where ρ_v is the volume resistivity of the material, $\sqrt{\mu}$ is the height of the equi-potential surface which is a semi-ellipsoid, its axis in the X and Y directions are $\sqrt{\alpha^2 + \mu}$ and $\sqrt{\beta^2 + \mu}$ respectively, Fig.6.8.

If the contact area is circular instead of elliptic, $\alpha = \beta = a$, then:

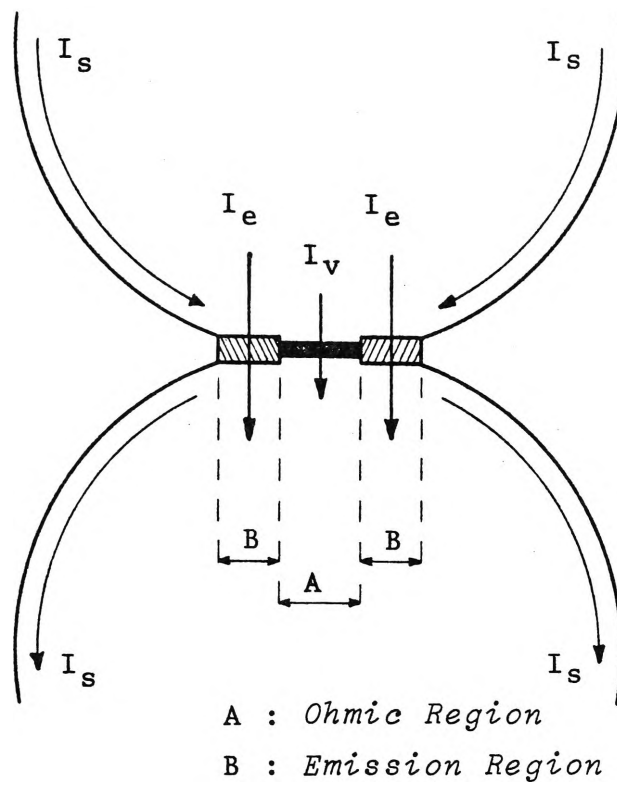


FIG. 6.7 ILLUSTRATION OF VARIOUS MODES OF THE CONDUCTION OF CURRENT THROUGH TWO ADJACENT PARTICLES.

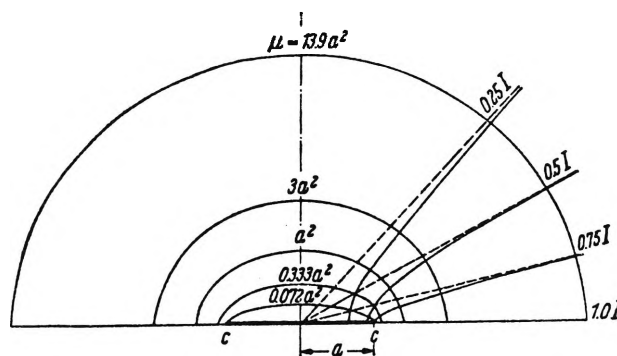


FIG. 6.8 LINES OF CURRENT FLOW AND EQUIPOTENTIAL SURFACES. [114]

$$R_{\mu} = \frac{\rho_v}{2\pi a} \tan^{-1} \sqrt{\frac{\mu}{a}}$$

The total constriction resistance of the contact is determined when μ approaches ∞ .

$$R = \frac{\rho_v}{4a}$$

This equation gives the effective resistance of the contact between a particle and a flat metal surface. The constriction resistance of the metal electrode is assumed to be negligible compared to that of the particle.

The total contact resistance between two particles due to volume conduction is written:

$$R = \frac{\rho_v}{2a} \quad (6.4)$$

Because of the constriction of current flow in the region of the contact points and the magnitude of the resistivity, very high electric fields are generated in the particle itself and across the air gap between adjacent surfaces.

In the above model, it is further assumed that the homogeneous volumes are packed to form a simple cubic array. This arrangement illustrates an ideal mode of packing of contaminant which is in particulate form (fly-ash), and an equivalent structure for amorphous contaminant (paper, Teflon filtering paper). The layer of contaminant is assumed to be subjected to a constant voltage gradient of E_{ave} , the voltage across each particle is given by:

$$V_p = E_{ave} \cdot 2S$$

where S is the radius of the particles or the homogeneous volumes. Or,

$$V_p = \frac{V}{L} \cdot 2S \quad (6.5)$$

where V is the applied voltage across the layer of contaminant of thickness L .

The current component due to conduction through the homogeneous region of the contaminant can be written:

$$I_v = \frac{V_p}{R} = \frac{2a}{\rho_v} \cdot \frac{V}{L} \cdot 2S$$

$$I_v = \frac{4a}{\rho_v} \cdot \frac{V}{L} \cdot S \quad (6.6)$$

This equation is derived on the assumption that this mode of current conduction does not cause significant change in the conduction of current through a thin film on the surfaces of particles.

6.4.3.2 Surface Conduction Current

The component of current due to conduction through a thin layer of the surfaces of particles is found by determining the total surface resistance from the point of contact. The derivation will be described in section 6.5.2, it can be shown that:

$$R = \frac{\rho_s}{2\pi} \ln \left[\frac{\tan \pi/4}{\tan \theta_o/2} \right]$$

or

$$R = - \frac{\rho_s}{2\pi} \ln(\tan \theta_o/2) = \frac{\rho_s}{2\pi} \ln(\cot \theta_o/2)$$

This equation gives the surface resistance between the contact plane and the great circle on the surface of the particle. It can be approximated by :

$$R \approx \frac{\rho_s}{2\pi} \ln(2S/a), \quad \text{since } \theta_o \text{ is small.}$$

By using the expression (6.5), the current can be written:

$$I_s = \frac{2\pi}{\rho_s} \cdot \frac{V}{L} \cdot S \cdot \frac{1}{\ln(2S/a)} \quad (6.7)$$

By superimposing the two current components, an expression for the total current flowing through the contact area A can be obtained:

$$\begin{aligned} I_T &= I_v + I_s \\ &= \frac{4a}{\rho_v} \cdot \frac{V}{L} \cdot S + \frac{2\pi}{\rho_s} \cdot \frac{V}{L} \cdot S \cdot \frac{1}{\ln(2S/a)} \end{aligned} \quad (6.8)$$

For a simple cubic array, the total current that flows over a unit area can be expressed as a product of the current through each contact area and the total number of contact area per unit area of the contaminant.

$$\begin{aligned} J_1 &= I_T \cdot N_p \\ J_1 &= \frac{a}{\rho_v} \cdot \frac{V}{L} \cdot \frac{1}{S} + \frac{\pi}{2\rho_s} \cdot \frac{V}{L} \cdot \frac{1}{S} \cdot \frac{1}{\ln(2S/a)} \end{aligned} \quad (6.9)$$

where $N_p = 1/4S^2$ is the number of parallel paths per unit area of contaminant.

From the resistivity-temperature characteristics obtained for a sample of fly-ash within the temperature range of 120-240°C, McLean [111] suggested that at low temperatures the effective resistivity approaches the effective surface resistivity because it (the effective surface resistivity) is much smaller than the effective volume resistivity. Since the effective surface resistivity is proportional to the surface resistivity by a factor determining the mode of packing of the layer, in equation (6.9) J_1 approaches the

second term on the right hand side i.e.

$$J_1 \approx \frac{\pi}{2\rho_s} \cdot \frac{V}{L} \cdot \frac{1}{S} \cdot \frac{1}{\ln(2S/a)} \quad (6.10)$$

This expression is plausible because of the presence of traces of moisture being absorbed by the contaminant at room temperature.

6.4.3.3 Current Due to Schottky Emission

It can be seen from expression (6.10) that the current density is a linear function of the applied electric field. However from the current-voltage characteristics, the deviation from linearity of the curve at high electric fields indicates the presence of a source for the increase in current. Because of the constriction of current flow in the region of the contact and the high value of the surface resistivity, very high electric fields are created across the air gap between adjacent particles. This field lowers the potential barriers and causes electrons to jump across the air gap. The emission current has been discussed by McLean [110] who found the evidence of the Schottky emission within the region B. This current is dependent on the ohmic current that flows through the contact area. An expression for the emission current has been derived by Tassicker et al. [115] by assuming the contaminant (fly-ash) at high temperature to behave like intrinsic semi-conductor, they found the current that flows by the alteration of the potential barrier under the application of an electric field. Their expression was found to fit the characteristics obtained for fly-ash within the temperature range 143°C-220°C. Because of different experimental conditions prevalent in this work, the express-

ion may not be applicable.

The results obtained by the author are found to agree with those measured by McLean [110], and they satisfy the functional form

$$J = k_1 \cdot V \cdot \exp(k_2 V)$$

where J is the total current comprised of the ohmic current through the contact areas and the emission current, k_1, k_2 are constants determined empirically.

An expression for the emission current can thus be obtained semi-empirically:

$$J_e = k_1 \cdot V \cdot \exp(k_2 V) - \frac{\pi}{2\rho_s} \cdot \frac{V}{L} \cdot \frac{1}{S} \cdot \frac{1}{\ln(2S/a)}$$

From the experimental results, the total current can be written:

$$I = 7.3 \times 10^{-16} \cdot V \cdot \exp(3.5 \times 10^{-3} V)$$

and

$$I = 7.4 \times 10^{-17} \cdot V \cdot \exp(1.3 \times 10^{-3} V)$$

for thicknesses of 125 μ m and 250 μ m respectively.

This indicates at high electric fields the electron emission across adjacent particles or homogeneous regions is predominant, the contribution of the surface conduction is small compared to the transfer of electrons. This transfer may vary with separation between surfaces of particles, and the net effect is equivalent to an increase in the effective contact areas between particles. However, at distance further out from the contact region where the separation is a hundred or more times the mean free path of air molecules the jumping electrons may gain sufficient energy from the generated field

in the air gap to produce ionising collision. Experimental measurement of the sparking voltage in air at gap length from $10\mu\text{m}$ up to $100\mu\text{m}$ has been carried out by Ahmed [116] between metal electrodes coupled with observation made by Böning [117] that Paschen's law also holds for breakdown in air voids in dielectrics suggests that local breakdown may be initiated by the generated field whenever the Paschen's value is satisfied.

6.5 Electrical Breakdown in Contaminant

6.5.1 Introduction

The constriction of current flow through the contact area between adjacent particles induces a very high electric field in the air voids of the contaminant layer. Depending on the distance from the contact plane, the separation between particles may be sufficient to permit collision between highly energised electrons and neutral air molecules. In this section, the electric field in the air voids between adjacent particles is calculated and compared with the breakdown field strength in air, which is determined by Paschen's law. The theoretical model is used to propose that the perforation of a layer of high-resistivity contaminant is triggered by the local gas discharge which takes place inside the contaminant. This model is an expansion of the previous one (Section 6.4.3) in which the conduction through a thin surface layer of the particle is considered and the contaminant is placed between plane parallel electrodes. This model is also applicable in the case where one side of the contaminant is exposed to the ionised gas produced by the discharge electrode and one side is in contact with the passive

anode. The difference is due to the distribution of potential on the surface of the contaminant, the central part of which is more likely to undergo a breakdown than the outer region. When breakdown takes place in the contaminant, the layer is perforated at several locations which are clearly visible in the contaminant. The formation of back corona and its effects on the distribution of potential is discussed as a preliminary step to an analytical model which is used to predict the distribution (Section 6.6). The critical resistivity of the contaminant is discussed by applying Gauss's law at the boundary of ionised gas and contaminant. The values of resistivity found in this work are agreeable with the commonly accepted values.

6.5.2 Contaminant between Plane Parallel Electrodes

6.5.2.1 Calculation of Field between Adjacent Particles

In this part the electric field strength in the air voids between homogeneous volumes of contaminant is calculated by finding the surface resistance from the great circle to the contact surface as shown in Fig.6.9. The potential at any point along the surface can be expressed in terms of the average field strength across the contaminant and the local field strength is then found by dividing the potential by the separation distance. The derivation can be described as follows:

Consider an annular ring located at position corresponding to angle θ at the centre of the spherical volume, the surface resistance as the current traverses a distance dl can be written:

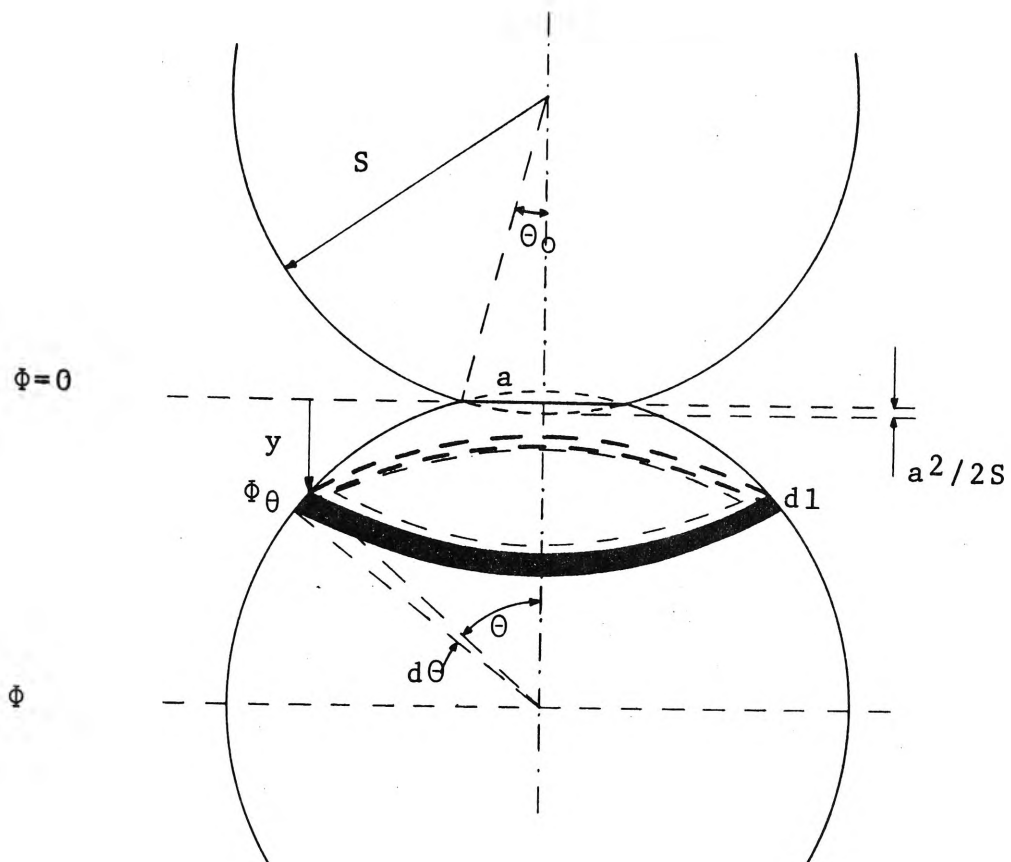


FIG. 6.9 ARRANGEMENT OF TWO IDEALISED PARTICLES (OR SOLID AND HOMOGENEOUS VOLUMES OF AMORPHOUS, INHOMOGENEOUS CONTAMINANT) IN CONTACT.

$$dR = \rho \frac{dl}{dt}$$

where

$$dl = S \cdot d\theta$$

$$dt = 2\pi S \sin\theta$$

then:

$$dR = \frac{\rho}{2\pi} \csc\theta \cdot d\theta$$

The surface resistance measured from the contact surface to the angle θ is:

$$R_{\theta} = \int_{\theta_o}^{\theta} \frac{\rho}{2\pi} \csc\theta d\theta$$

or

$$R_{\theta} = \frac{\rho}{2\pi} \ln\left\{\frac{\tan\theta/2}{\tan\theta_o/2}\right\}$$

The surface resistance measured from the contact surface to the great circle is:

$$R = \frac{\rho}{2\pi} \ln\left\{\frac{\tan\pi/4}{\tan\theta_o/2}\right\}$$

The potential at the angle θ on the surface of the homogeneous sphere is:

$$\begin{aligned} \Phi_{\theta} &= \Phi \cdot \frac{R_{\theta}}{R} \\ \Phi_{\theta} &= -\Phi \cdot \frac{\ln\left\{\frac{\tan\theta/2}{\tan\theta_o/2}\right\}}{\ln(\tan\theta_o/2)} \end{aligned}$$

where the potential at the contact plane is assumed to be zero and Φ is the potential at the great circle. This can be expressed in terms of the voltage applied across the contaminant and its thickness.

$$\Phi = \bar{E} \cdot S$$

$$\Phi = \frac{V}{L} \cdot S$$

The potential Φ_θ is thus:

$$\Phi_\theta = -\frac{V}{L} \cdot S \cdot \frac{\ln\left\{\frac{\tan\theta/2}{\tan\theta_o/2}\right\}}{\ln(\tan\theta_o/2)} \quad (6.11)$$

The separation distance between any point on the surface of the sphere and the contact plane can be expressed as,

$$y = S(1-\cos\theta) - \frac{a^2}{2S}$$

$$y = \frac{2S^2(1-\cos\theta) - a^2}{2S}$$

where a is the radius of the contact area and $a^2/2S$ is the squashing distance due to the deformation of two spherical volumes being pressed together [110].

The electric field strength at any angle θ is thus:

$$E_\theta = -\frac{\Phi_\theta}{y}$$

$$E_\theta = \frac{V}{L} \cdot \frac{2S^2}{(2S^2(1-\cos\theta) - a^2)} \cdot \frac{\ln\left\{\frac{\tan\theta/2}{\tan\theta_o/2}\right\}}{\ln(\tan\theta_o/2)} \quad (6.12)$$

It can be seen that the electric field strength in the air void is a function of the applied field strength across the contaminant, the sizes of the homogeneous volume and the contact area. This value is compared with the breakdown field strength of air at atmospheric pressure by using Paschen's law which can be written as [118],

Field strength:

$$E_s = \frac{Bp}{\ln\left\{\frac{Apd}{\ln(1/\gamma)}\right\}} \quad (6.13)$$

Voltage:

$$V_s = \frac{Bpd}{\ln\left\{\frac{Apd}{\ln(1/\gamma)}\right\}} \quad (6.14)$$

where

d : the distance between two parallel electrodes

p : pressure

A, B : constants which relate the Townsend's coefficient of ionisation collision to the ratio E/p

γ can be determined by using sparkover voltage measured in air. From data which has been published up-to-date by various workers [118],[119], those obtained by Schumann is selected in this work due to its clarity. From equation (6.13), the minimum distance at which sparkover can take place at atmospheric pressure is determined by the minimum product of pressure and the distance. This value is found approximately equal to $9\mu\text{m}$ which is about a hundred times the mean free path of air molecules at normal pressure. This distance is perhaps sufficient for free electron(s) to produce ionisation by colliding with air molecules in the pores. For shorter distance electrons could jump across the gap without collision with air molecules as proposed by McLean [110].

Equations (6.12) and (6.13) are computed by means of a digital computer for particulate sizes of $100\mu\text{m}$ - $400\mu\text{m}$ and contact radius of $1\mu\text{m}$. The computation process starts by calculating E_0 at the minimum separation distance in terms of the potential, V_s at the great circle. E_0 is then compared with E_s to determine whether ionisation can take place at this potential. If E_0 is greater than or equal to E_s , the potential marks the onset of local gas discharge. The separation distance is then increased and the computation cycle is repeated until the condition for ionisation to

occur along the great circle is found, the potential at this limit is the breakdown voltage of the contaminant.

The calculated results are summarised in Table 6.1.

Radius of Particulate (μm)	Radius of Contact Area (μm)	Conditions for the onset of local gas Discharge		Conditions for breakdown across the contaminant	
		E_s (KV/CM)	V_s (Volts)	E_s (KV/CM)	V_s (Volts)
100	1	577	730	96	960
200	1	577	758	77.5	1550
300	1	577	772	69.6	2088
400	1	576	780	64.9	2596

TABLE 6.1 CALCULATED FIELD STRENGTHS AND VOLTAGES AT THE ONSET OF LOCAL GAS DISCHARGE AND THE ELECTRIC BREAKDOWN OF CONTAMINANT.

It can be seen that the potential at the great circle does not vary as much at the onset of local gas discharge as it does at the electrical breakdown of the contaminant with respect to the particulate size.

The calculated results indicate that if the potential across a layer of particulate is sufficient to cause a breakdown along the great circle of the particle then ionisation can take place in the vicinity of the contact area before complete breakdown is observed across the contaminant.

6.5.2.2 Limitation of the Model

The model is applicable for imperfect dielectric, i.e. dielectric which has holes or voids in its mechanical structure or in particular, a layer of particulates. It is not suitable for perfect dielectric in which intrinsic

breakdown can take place when electrons in the dielectric gain enough energy from the applied field to cross the forbidden energy gap from the valence band to the conduction band [120]. The electric field strength required for this kind of breakdown is in excess of 10^6 V/cm.

The high field strength is induced by the conduction of current along a thin layer of the surface of particle, the condition existing along the surface of particle will be somewhat dissimilar to two parallel metal conductors. The correct value of γ suffers a certain degree of uncertainty in the case of metal electrodes because γ is a function of E/p . This point is illustrated by Fig.6.10 in which the breakdown field strength is plotted against the gap length. Curve number 1 is a direct reproduction from data obtained by Schumann [118], which can be expressed in the form of equation (6.14). Curve number 2 is obtained from Sillars's book and curve number 3 is obtained by expressing the data of curve 2 in the form of equation (6.14). These three curves diverge from one another at small gap lengths but converge at greater lengths.

6.5.3 Contaminant on the Collecting Electrode

6.5.3.1 Formation of Back Corona Channels

For the reasons discussed in section 6.3, the contaminant placed on the collecting electrode of the corona system, will have a surface potential distribution resembling the Normal Distribution curve. The potential in the central part of the layer of contaminant is somewhat higher than that in the outer region. Neglecting the defects in the mechanical structure of the contaminant, this means that the

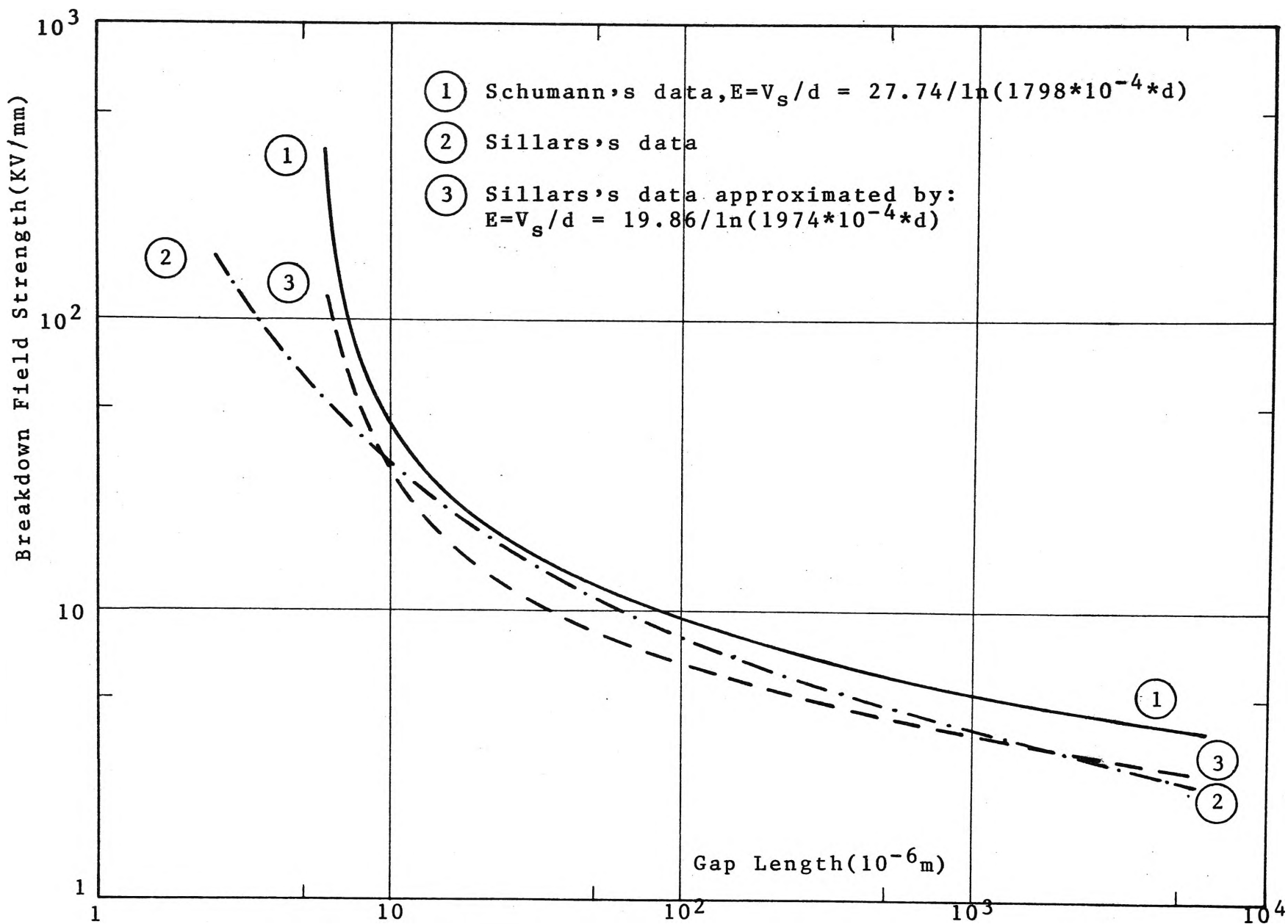


FIG.6.10 RELATIONSHIP BETWEEN BREAKDOWN FIELD STRENGTH AND GAP LENGTH OF UNIFORM GAP.

central part will be easier to undergo a breakdown than its outer counterpart. The process of forming back corona channels can be described in the following steps.

- (i) The constriction of current flow through the contact areas between adjacent particles or homogeneous volumes of contaminant induces high electric field in the air voids that exist in the contaminant. When this induced field is sufficiently strong, it accelerates the free electrons that are the major charge carriers to undergo ionising collisions with neutral air molecules in the voids. This small breakdown marks the onset of a gas discharge which is also known as back corona in the air voids within the contaminant.
- (ii) When the voltage build up across the layer of contaminant is increased by a few hundred volts from the onset value for back corona, the discharge becomes so vigorous that it propagates right through the layer and forms substantial channels (or perforations) in the contaminant. In the case of filtering paper, these holes are easily visible. The potential measured on the surface of the layer is close to the breakdown values obtained when the contaminant layer is placed between plane parallel electrodes i.e. approximately equal to the Paschen's values. The results are shown in Fig.6.11 for D.C. and pulsed voltages.
- (iii) Once the back corona channels are created and if the applied voltage is maintained at such level

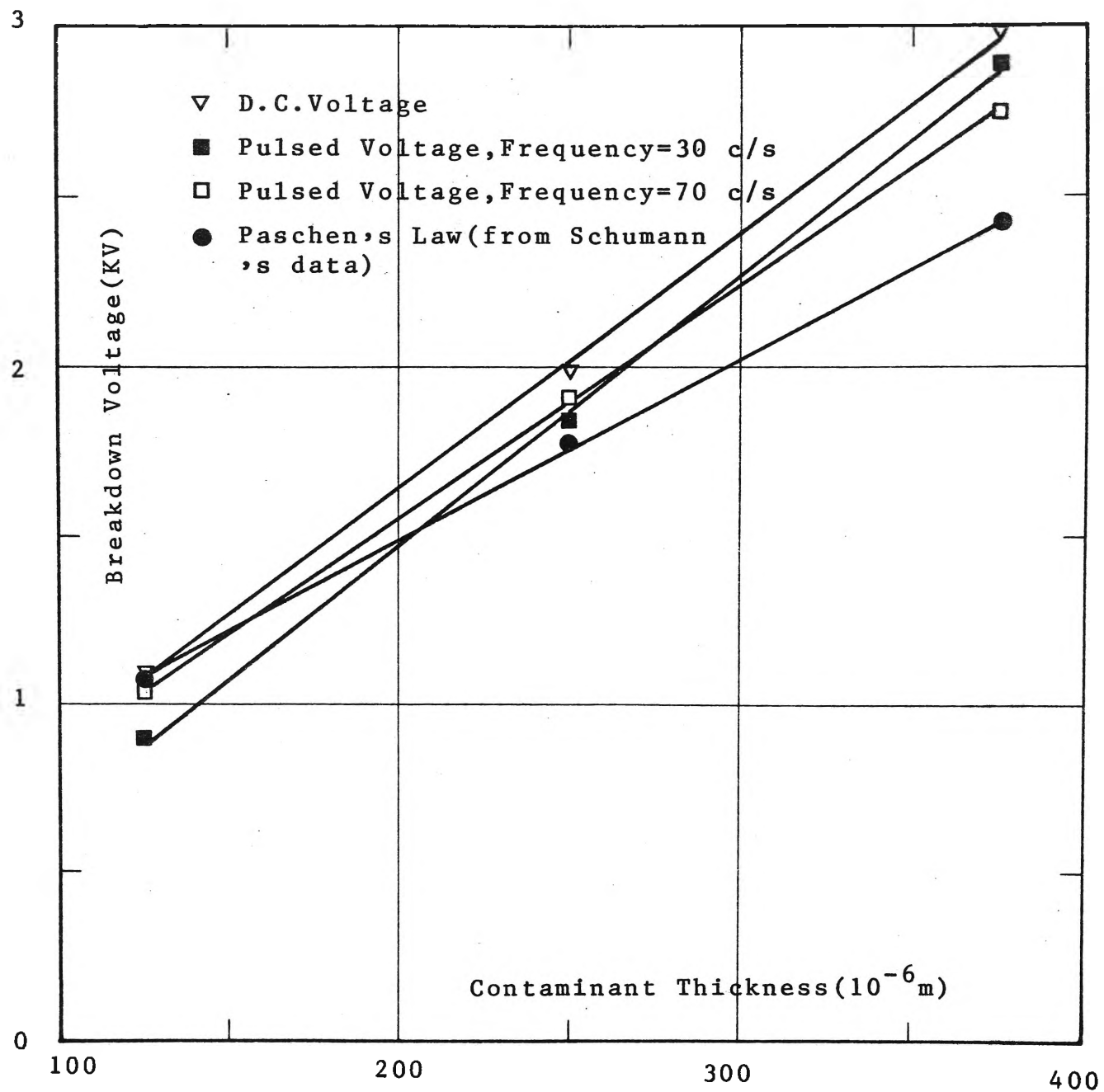


FIG. 6.11 RELATIONSHIP BETWEEN BREAKDOWN VOLTAGE AND
CONTAMINANT THICKNESS.

that the voltage build up across the layer reaches the same value as that in (ii), the back corona in the channels is maintained by:

- (a) the flow of negative ions from the highly-stressed cathode.
- (b) the electric field set up in the contaminant by the leakage current through the layer.

The mechanism and the conditions in which the back discharge is maintained, will be discussed in section 6.7.

6.5.3.2 Effects of Back Corona on Potential across the Contaminant

When back corona channels are formed and with the presence of back corona, the potential in the neighbourhood of the channels drops below the Paschen's values. This is caused by the plasma-like air path formed in the channels with positive ions moving to the upper surface of the layer and free electrons being collected by the anode. The potential is partly diminished by the partial neutralisation of negative ions injected from the remote discharge electrode, which takes place inside the channels and in the vicinity of the channels. In a layer of contaminant, the simultaneous presence of several back corona channels suggests the alteration of potential distribution on the surface of the layer, but at the same time tends to obscure the true distribution of potential around each channel. Nevertheless, a general dip in the distribution curve is expected in the central part of the layer since this is where back corona is most likely to occur. This is confirmed in Fig.6.3 for pulsed voltage at peak values of 11kV and

13.6 kV respectively.

6.5.4 The Critical Resistivity

The building-up of the surface potential stops when the potential reaches the breakdown level of the contaminant. The relationship between the breakdown field strength and the equivalent resistivity of the contaminant can be obtained by applying the Gauss's law at the boundary of gas and contaminant.

The accumulation of negative charge carriers on the surface of the contaminant tends to form a layer of surface charge of negligible thickness.

Considering a small area on the surface of the contaminant as shown in Fig.6.12, because of the difference in the dielectric constant of gas and contaminant, an electric flux density leaving the contaminant can be expressed as:

$$D_g - D_d = \sigma \quad (6.15)$$

where D_g and D_d are electric flux density vectors in gas and the contaminant respectively, σ is the surface charge density.

The average current that flows in the gaseous medium can be written:

$$j_g = knE_g$$

and the average current that flows through the contaminant is given:

$$j_d = \frac{E_d}{\rho_d}$$

where k is the mobility of gas, n is its density, ρ_d is the equivalent resistivity of the contaminant.

Applying the continuity of current flow at the boundary gives:

$$j = j_g = j_d$$

or

$$j = \frac{E_d}{\rho_d} = knE_g \quad (6.16)$$

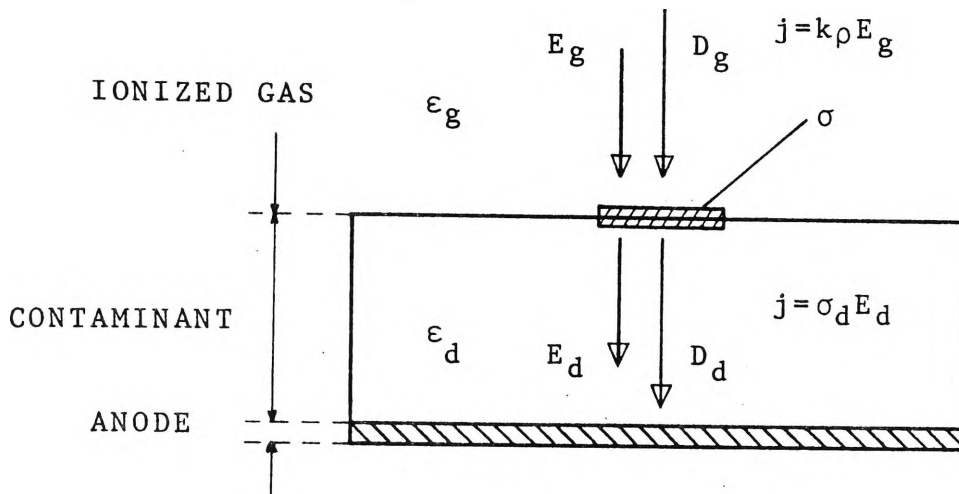


FIG. 6.12 ELECTRIC FLUX DENSITIES, AND FIELDS AT THE IONISED GAS-TO-CONTAMINANT BOUNDARY IN A CONTAMINATED CORONA SYSTEM.

Substituting the electric field strengths into equation (6.15) gives

$$\epsilon_g E_g - \epsilon_d E_d = \sigma$$

which can be written by using equation (6.16)

$$\sigma = \left[\frac{\epsilon_g}{kn} - \epsilon_d \rho_d \right] knE_g \quad (6.17)$$

The contaminant breakdown at the location of observation when the surface charge is shunted to ground, this means that the surface charge density at this location is approaching zero i.e. $\sigma \rightarrow 0$.

Equation (6.17) then gives:

$$(\rho_d)_c = \frac{\epsilon_g}{\epsilon_d} \cdot \frac{1}{kn}$$

or

$$(\rho_d)_c = \frac{\epsilon_g}{\epsilon_d} \cdot \frac{E_g}{j} \quad (6.18)$$

Equation (6.18) implicitly means that the critical resistivity of the contaminant can be found by measuring the electric field in the gas in the proximity of the breakdown spot and the current density. It can also be used as a justification of the application of Gauss's law at the boundary of gas and contaminant in a contaminated corona system, since by substituting $\epsilon_g E_g / \epsilon_d$ by E_d (a direct consequence of equation (6.17) when σ is equal to zero), equation (6.18) becomes $\rho_d = E_d / j$, which can be obtained by the definition of resistivity.

On the other hand, if the critical resistivity is known then the electric field in the vicinity of the contaminant where back corona occurs can be found.

Since $1/kn$ is equivalent to the resistivity of the ionised gas, the physical significance of this is that the electrical breakdown takes place in the contaminant when the time constant of the ionised gas, ϵ_g / kn equals to that of the contaminant, $\epsilon_d \rho_d$, as it has been recognised by Cooperman [3], [121].

Because of the non-linear relationship between the current density and the electric field at high surface potential level, equation (6.18) would only give an approximate of the critical resistivity. It is dependent on the current density detected just before breakdown occurs and

this value can vary over a fairly large range over the collecting electrode.

By combining various parameters obtained from the current-voltage characteristics (Fig.6.13 and 6.14), the breakdown voltage-thickness curves (Fig.6.11) and the surface potential-applied voltage curves (Fig.6.21 and 6.22), the critical resistivity can be found for D.C. and pulsed voltages. The results are summarised in Table 6.2 for two thicknesses.

It is apparent that the average corona current detected before the onset of back corona is larger for thicker layer of contaminant, however this does not imply that a contaminated corona system can tolerate more current when the contaminant is thick than it does when the layer is thin. From the current-voltage characteristics, it can be seen that as soon as back corona takes place the current increases very rapidly and leads to a complete sparkover with a thick layer of contaminant.

The critical resistivity calculated from equation (6.18) is higher for pulsed voltage than for D.C. voltage. This means that for a contaminant, D.C. energisation is more easily able to produce back corona than pulsed energisation. This advantage of pulsed voltage over D.C. voltage is complementary to the fact that a contaminated corona system undergoes a complete sparkover at higher level with pulsed voltage than with a D.C. one.

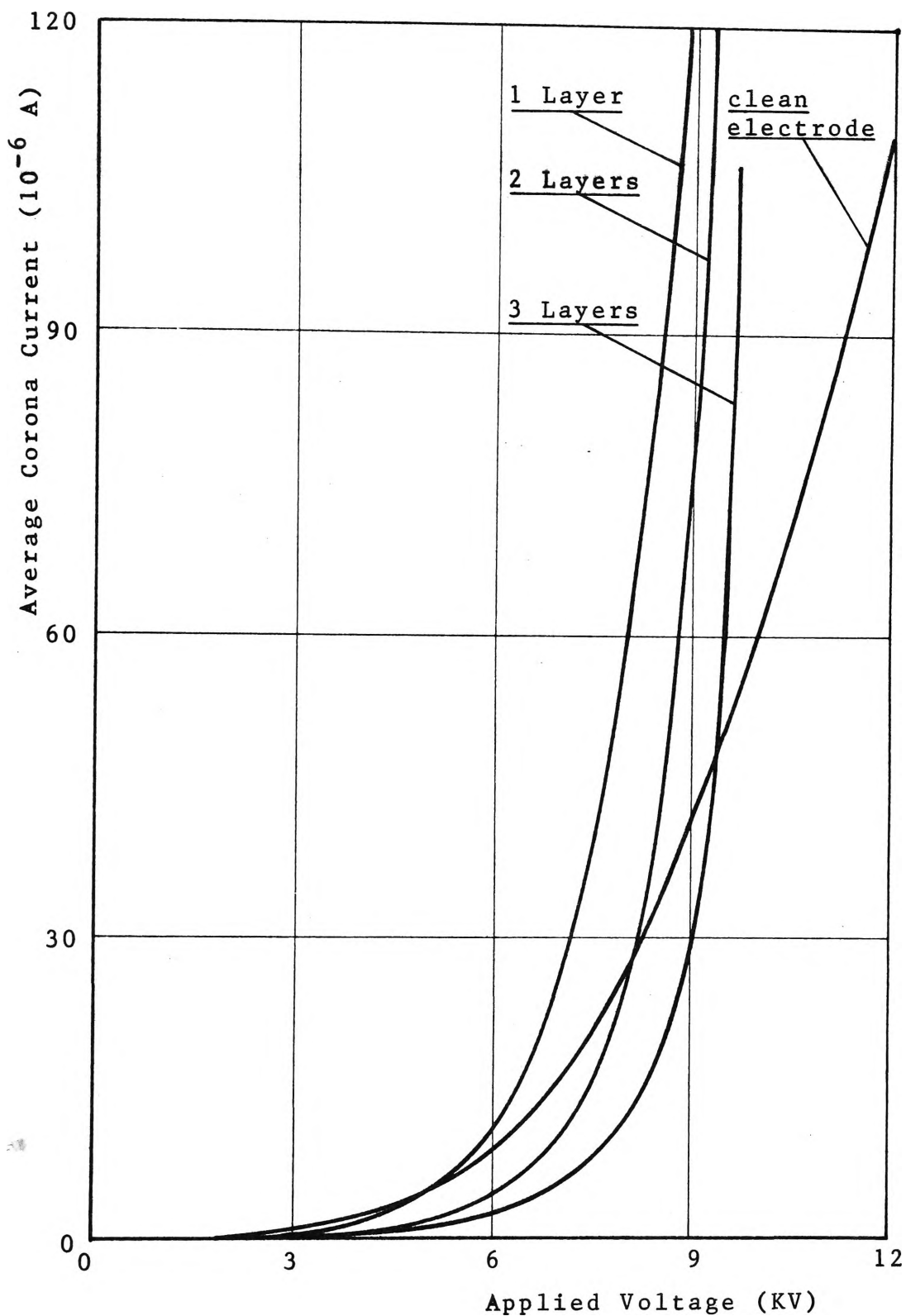


FIG.6.13 AVERAGE CORONA CURRENT-VOLTAGE CHARACTERISTICS OF CONTAMINATED CORONA SYSTEM.
D.C. VOLTAGE.

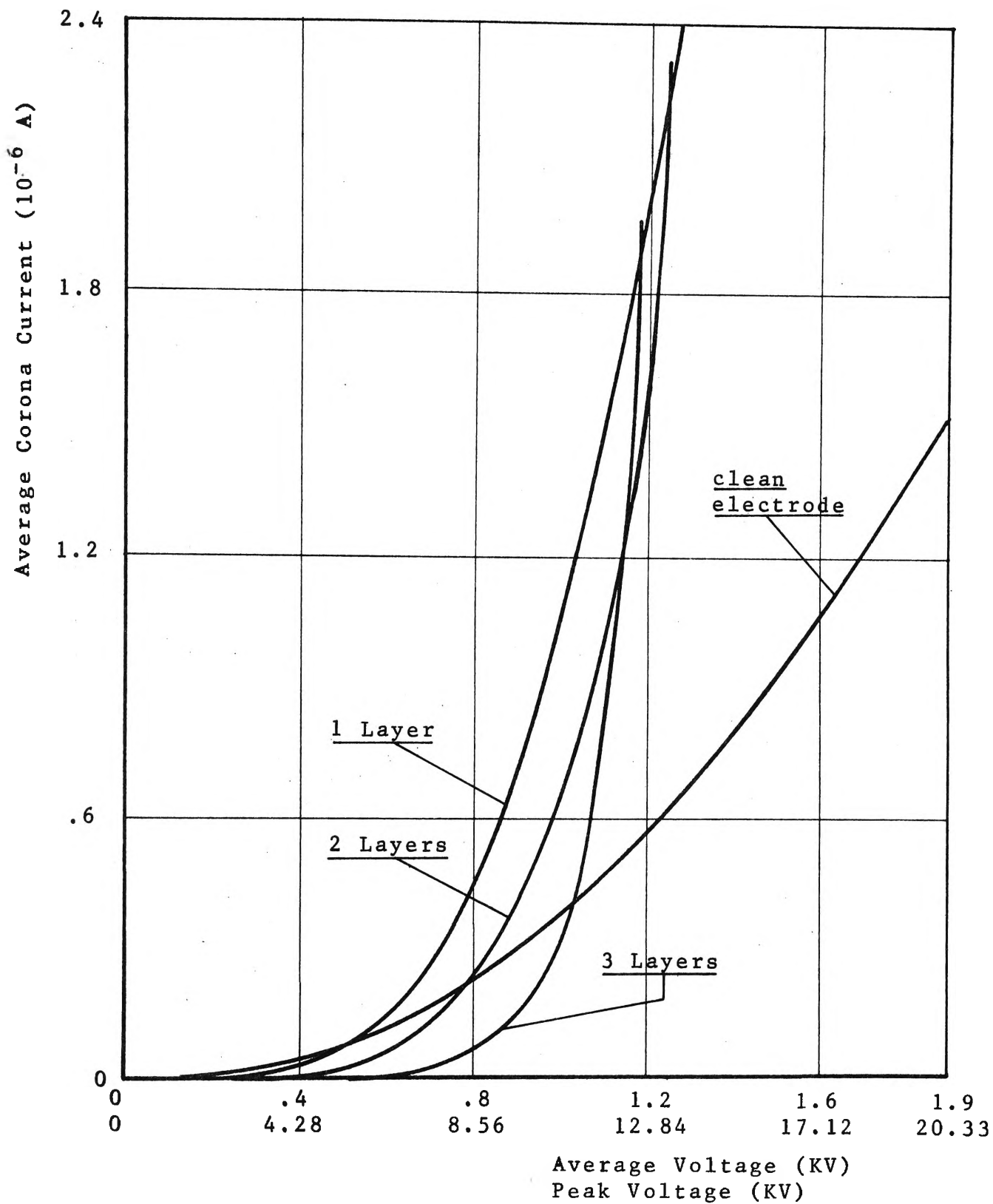


FIG.6.14 AVERAGE CORONA CURRENT-VOLTAGE CHARACTERISTICS OF CONTAMINATED CORONA SYSTEM. PULSED VOLTAGE, REPETITION RATE = 30c/s.

Contaminant Thickness	Breakdown Voltage		Breakdown Current		Critical Resistivity	
	D.C.	30c/s	D.C.	30c/s	D.C.	30c/s
125×10^{-4}	1100	900	6	.8	2.9×10^{10}	1.8×10^{11}
375×10^{-4}	3000	2900	8	2	2×10^{10}	7.7×10^{10}
cm	Volts		Micro Amperes		Ohm-cm	

TABLE 6.2 CRITICAL RESISTIVITIES AS MEASURED FOR D.C. AND PULSED VOLTAGES.

6.6 Distribution of Surface Potential when Back

Corona is present

6.6.1 Introduction

With the presence of back corona channels in the layer of contaminant, the field distribution in the gas space is altered as it is illustrated diagrammatically in Fig.6.15. The negative ions generated from the discharge electrode follow two possible flux lines which terminate on the passive anode, one flux tube terminates at the openings of back corona channels and the other is formed by the surface of contaminant exposing to the gas space and the volume of contaminant.

As discussed in the previous section, the conduction of current through the contaminant sets up an electric field across the contaminant, the maximum field strength of which is determined by Paschen's law. When this value is attained, the electrical breakdown that takes place in the contaminant is initiated by the ionising collisions of electrons in the

air space of back corona channels. The ionisation in the contaminant produces ion pairs in the channels with positive ions emerging from the contaminant and electrons being removed by the grounded anode. The positive ions partially neutralise the oncoming primary negative ions inside the channels and attract the negative ions that have already been present in the vicinity of the back corona channels. This neutralisation results in a lowering of the potential in the neighbourhood of the channels. In this section, the alteration of surface potential distribution under this condition is analysed.

6.6.2 Analytical Study of Surface Potential Distribution

In an actual layer of contaminant, back corona may take place simultaneously at different locations, the simultaneous presence of several back discharge spots results in a slight dip of the potential distribution curve as discussed in section 6.5.3. In order to make the analysis of the potential distribution, under such condition, mathematically feasible, a rather idealised model is used. All the back corona channels are lumped together to form an equivalent channel and it is placed coaxially with the symmetrical axis of the electrode system. The arrangement is illustrated in Fig.6.16 in which the solid homogeneous part of the contaminant is represented by an insulator and the back corona channels are simulated by a perforation which is punctured through the insulator. The conduction of current through the bulk of the insulator is assumed as negligible in comparison to that over a thin layer of the surface of the insulator.

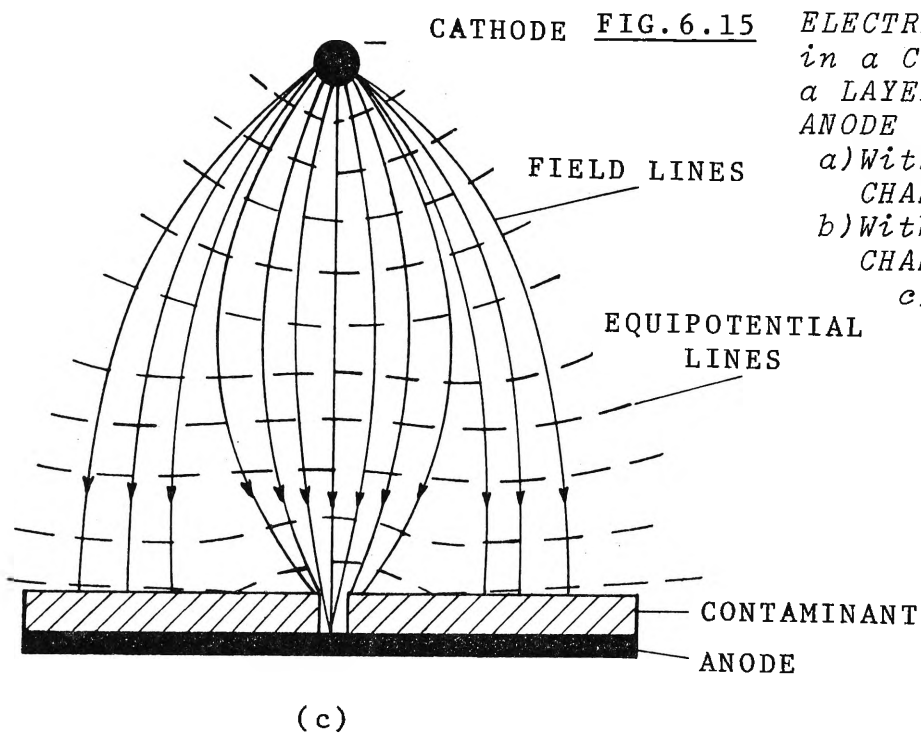
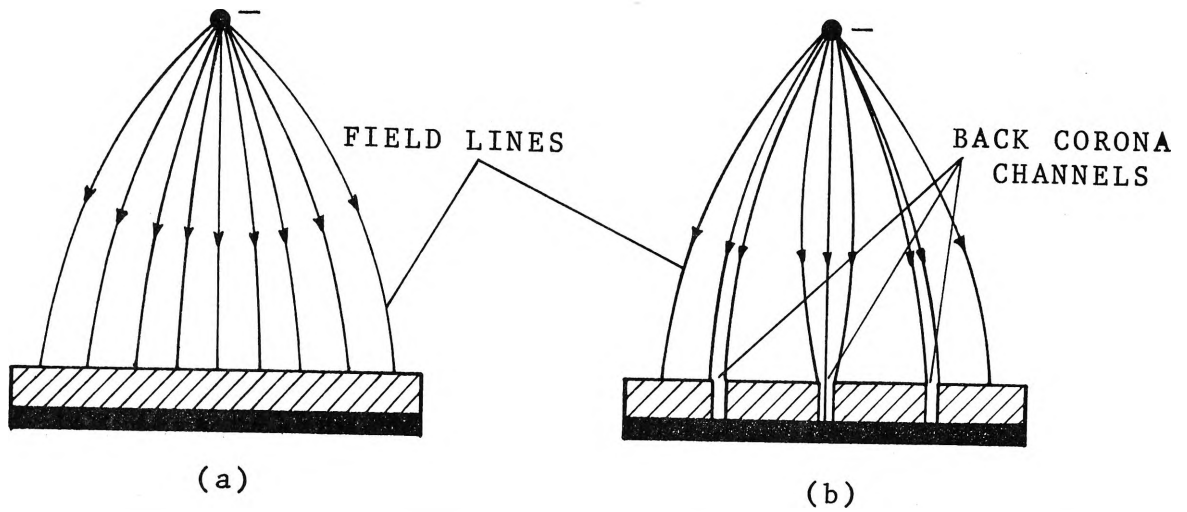


FIG. 6.15

ELECTRIC FIELD LINES
in a CORONA SYSTEM with
a LAYER of CONTAMINANT on
ANODE

a) Without BACK CORONA
CHANNELS

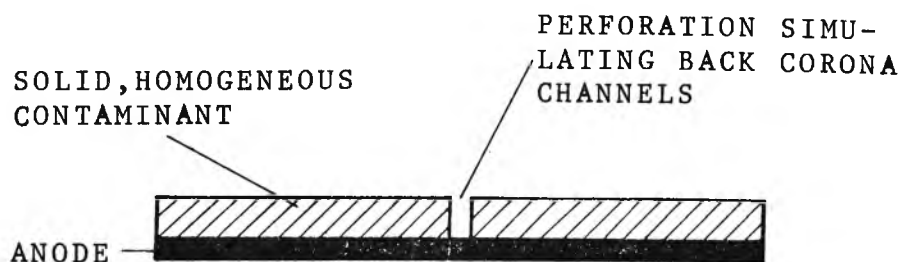
b) With BACK CORONA
CHANNELS

c) Equivalent diagram
to case (b)

FIG. 6.16 MODEL simulating
MECHANICAL STRUCTURE of
CONTAMINANT with BACK CORONA
CHANNELS



HIGHLY STRESSED
CATHODE



In the new, distorted configuration of the electric field distribution in the gas space, it can reasonably be assumed that the distribution of current density follow the functional expression:

$$J(r) = \frac{2J_0}{r_1^2} \cdot r \cdot e^{-r^2/r_1^2}$$

where J_0 is the total current measured from the collecting plane, r_1 is the radius of the layer of contaminant.

Because of the finite dimension of the layer, the current is comprised of two components; one flows over the central part of the layer toward the back corona channel and the other flows toward the outer edge of the contaminant surface. This results in a surface potential distribution having a maximum in the vicinity of the back corona channel and lower values at the edges.

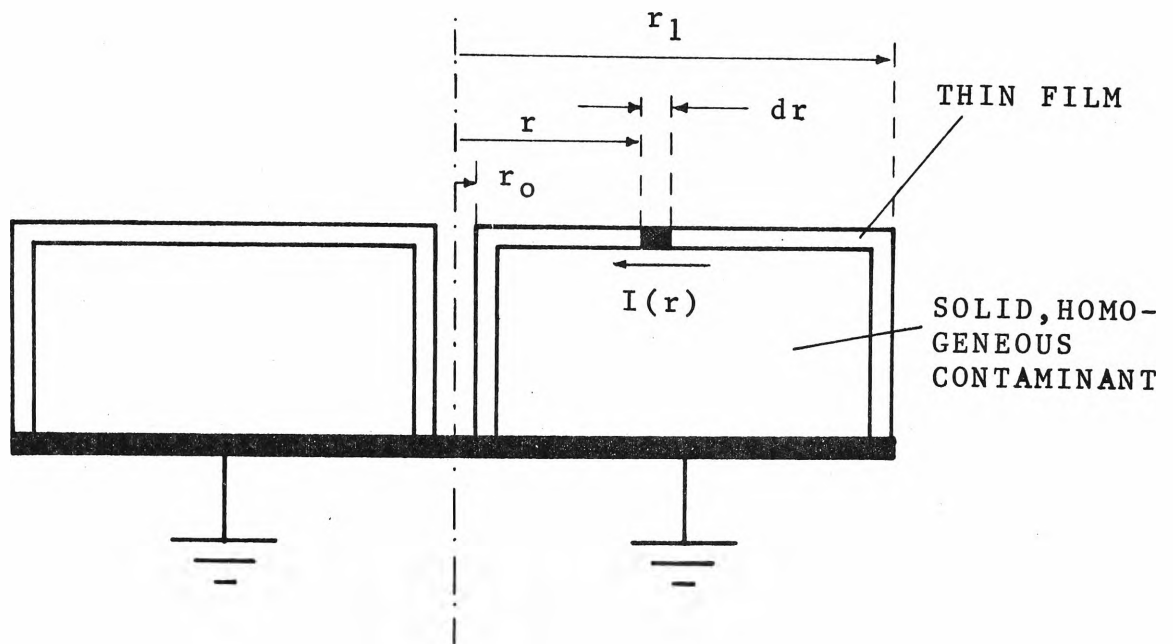
Since the main interest of this analysis is in the surface potential distribution, it can be safely assumed that the corona current which flows freely in the air space of back corona channel is negligible and likewise for the current which flows through the volume of the contaminant.

The mechanical structure of the layer of contaminant can be represented by its equivalent circuit as shown in Fig.6.17 where the surface resistance can be expressed as:

$$R_s(r) = \frac{R}{2\pi} \ln(r/r_o) \quad (6.19)$$

where R is the surface resistivity of the contaminant.

Considering an infinitesimal length dr located at a distance r from the centre of the back corona channel, a potential difference, dV due to a difference in surface



(a) EQUIVALENT CIRCUIT OF CONTAMINANT

(b) SKETCH OF SURFACE POTENTIAL vs RADIAL DISTANCE

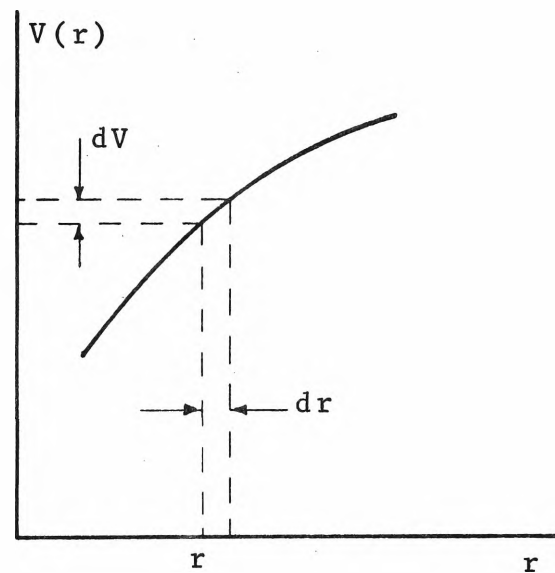


FIG. 6.17 EQUIVALENT STRUCTURE OF CONTAMINANT WITH BACK CORONA CHANNELS AND GENERAL SHAPE OF THE VOLTAGE DISTRIBUTION.

resistance dR_s can be written:

$$dV(r) = I(r) \cdot \frac{dR_s(r)}{dr} \cdot dr$$

which is identical to:

$$\frac{dV(r)}{dr} = I(r) \cdot \frac{dR_s(r)}{dr}$$

Differentiate this expression with respect to r , and one gets:

$$\frac{d^2V(r)}{dr^2} = \frac{dI(r)}{dr} \cdot \frac{dR_s(r)}{dr} + I(r) \cdot \frac{d^2R_s(r)}{dr^2}$$

which can be written after $dI(r)$ is substituted by $J(r) \cdot dr$ and $I(r)$ by dV/dR , and the subscript s is removed for the sake of convenience

$$\frac{d^2V}{dr^2} = J(r) \cdot \frac{dR(r)}{dr} + \frac{dV}{dR} \cdot \frac{d^2R}{dr^2}$$

or

$$\frac{d^2V}{dr^2} = J(r) \cdot \frac{dR}{dr} + \frac{dV/dr}{dR/dr} \cdot \frac{d^2R}{dr^2}$$

alternatively:

$$\frac{d^2V}{dr^2} - \left(\frac{d^2R}{dr^2} / \frac{dR}{dr} \right) \frac{dV}{dr} = J(r) \cdot \frac{dR}{dr} \quad (6.20)$$

Equation (6.20) can be written after the first and second derivatives of R are found from equation (6.19)

$$\frac{d^2V}{dr^2} + \frac{1}{r} \cdot \frac{dV}{dr} = J(r) \cdot \frac{R}{2\pi r}$$

or

$$\frac{d^2V}{dr^2} + \frac{1}{r} \cdot \frac{dV}{dr} = \frac{2J_o}{r_1^2} \cdot r \cdot e^{-r^2/r_1^2} \cdot \frac{R}{2\pi r}$$

$$\frac{d^2V}{dr^2} + \frac{1}{r} \cdot \frac{dV}{dr} = \frac{2J_o R}{2\pi r_1^2} \cdot e^{-r^2/r_1^2} \quad (6.21)$$

where R is the surface resistivity.

Equation (6.21) can be written as:

$$\frac{du}{dr} + \frac{1}{r} \cdot u = \frac{2J_o R}{2\pi r_1^2} \cdot e^{-r^2/r_1^2} \quad (6.22)$$

where $u = dV/dr$

The solution of equation (6.22) can be found by multiplying both sides by the integrating factor $e^{\ln(r)}$

$$u = - \frac{RJ_o}{2\pi r} \cdot e^{-r^2/r_1^2} + \frac{C_1}{r}$$

or

$$\frac{dV}{dr} = - \frac{RJ_o}{2\pi r} \cdot e^{-r^2/r_1^2} + \frac{C_1}{r} \quad (6.23)$$

where C_1 is the constant determined by the boundary condition. The surface potential can be found by integrating the above expression with respect to r .

$$V = - \frac{RJ_o}{2\pi} \int_{r_o}^r \frac{1}{r} \cdot e^{-r^2/r_1^2} dr + C_1 \ln(r/r_o) + C_2$$

Since the integrand is not definite, the potential cannot be expressed in a convenient form, however it can be plotted by integrating its gradient numerically.

The distance at which the potential is maximum is determined by equating equation (6.23) to zero:

$$r_m^2 = r_1^2 \ln(RJ_o/2\pi C_1)$$

or

$$r_m = r_1 \sqrt{\ln(RJ_o/2\pi C_1)}$$

Since r_m should be a real value, C_1 should satisfy:

$$C_1 < \frac{RJ_o}{2\pi}$$

Expression (6.23) is plotted by substituting some typical values of all the terms in (6.23) such as:

$$R = 10^{11} \text{ ohms}$$

$$J_o = 10^{-6} \text{ Amp.}$$

$$r_o = .025 \text{ cm}$$

$$r_l = 100 r_o = 2.5 \text{ cm}$$

$$\text{and } r_m = 30 r_o = .75 \text{ cm}$$

The result is shown in Fig.6.18 together with its integration. The surface potential curve has a maximum in the neighbourhood of the channel and gradually decreases to smaller values at the periphery of the channel and at the edge of the contaminant layer. This shape of the surface potential distribution affects the field pattern in the air gap so as to direct the oncoming negative ions generated by the discharge cathode into the back corona channel. In the vicinity of the channel, the magnitude of the field component parallel to the layer drops very rapidly with distance, but is sufficiently high to induce local ionisation along the edge of the channel.

The analytical model suffers a limitation because of the approximate nature of some pertinent parameters. The distribution of current density may not follow exactly the assumed functional form (this function is known as the Rayleigh's distribution function, defining the probability of one event to fall within certain limits in a cylindrical co-ordinate system). The effects of the applied electric field and the space charge field of negative ions have been neglected. Nevertheless, the model predicts qualitatively the distribut-

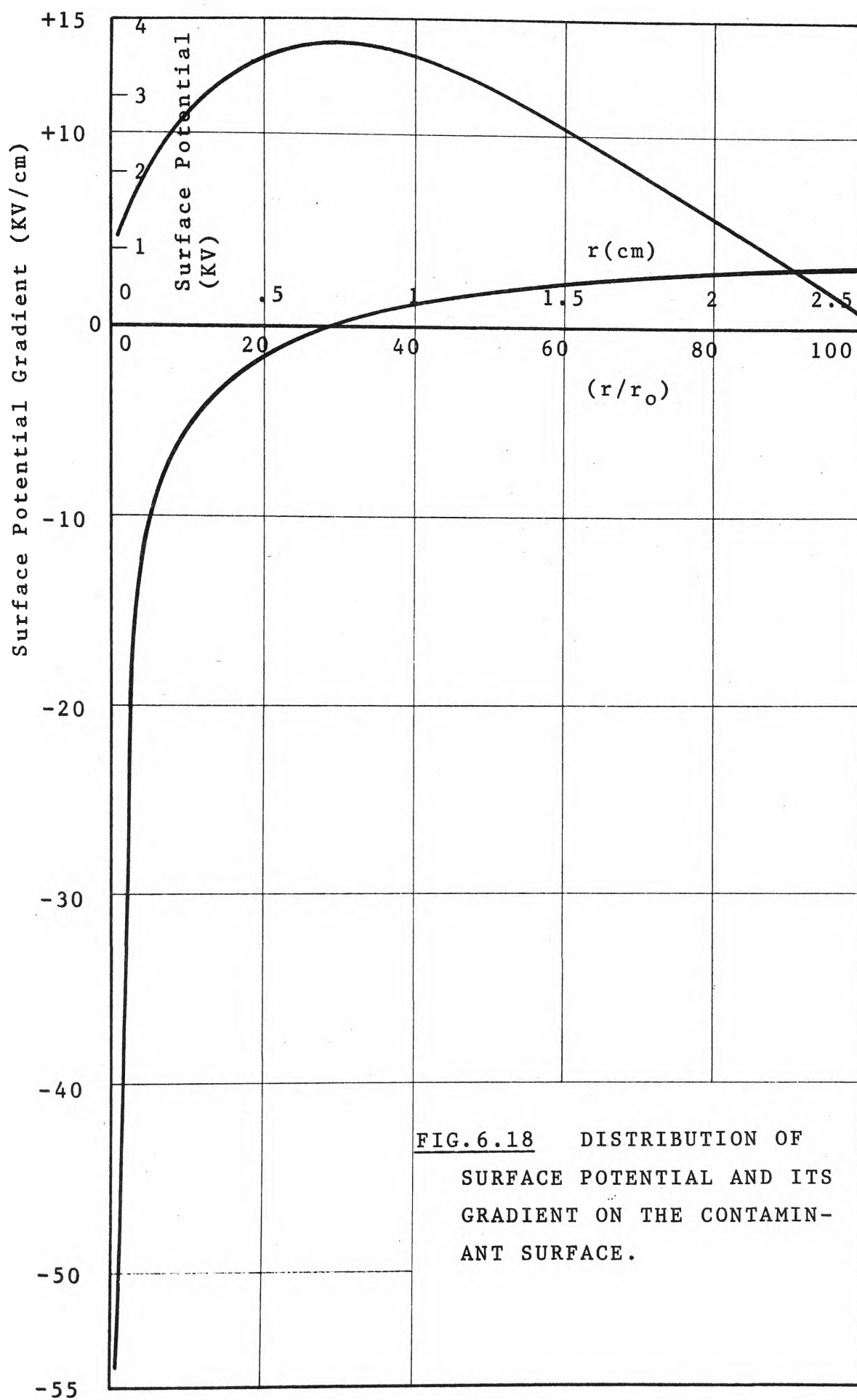


FIG.6.18 DISTRIBUTION OF
SURFACE POTENTIAL AND ITS
GRADIENT ON THE CONTAMIN-
ANT SURFACE.

ion of surface potential on the surface of the contaminant when back corona takes place in the channel.

Up to this stage, it can be postulated that the presence of high surface potential gradient in the vicinity of back corona channel facilitates the development of a stable discharge in the back corona channel. When the field strength in the air space between the contaminant and the point cathode is sufficient, the discharge propagates through the air space to form a complete sparkover. The formation of the stable back discharge and the drop in sparkover voltage will be discussed in sections 6.7 and 6.8 respectively.

6.6.3 Comparison between Estimated and Measured Potentials

The surface potential distribution is measured when a layer of mica (300 μ m thick and diameter of 5 cm) which is perforated to simulate the equivalent structure described in Fig.6.16 is used. The diameter of the perforation is 0.7 mm. The surface potential probes are similar to those used before (section 6.3). The results are shown in Fig.6.19 and 6.20 for D.C. and pulsed voltages. The distribution curves are similar to those obtained for Teflon filtering papers (Figs.6.2 and 6.3) before the onset of back corona. When back corona takes place in the perforation, the surface potentials detected by two innermost probes indicate a sharp drop, while those measured at locations further out remain unaffected (curves at 6.2kV and at 9.2kV for D.C. and pulsed voltages respectively). The potential gradients measured between the first two probes (of radii 1.5 mm and 5 mm) are estimated to be 2.2 kV/cm (Fig.6.19) and 2.5 kV/cm (Fig.6.20), which are in the same order of magnitude to that

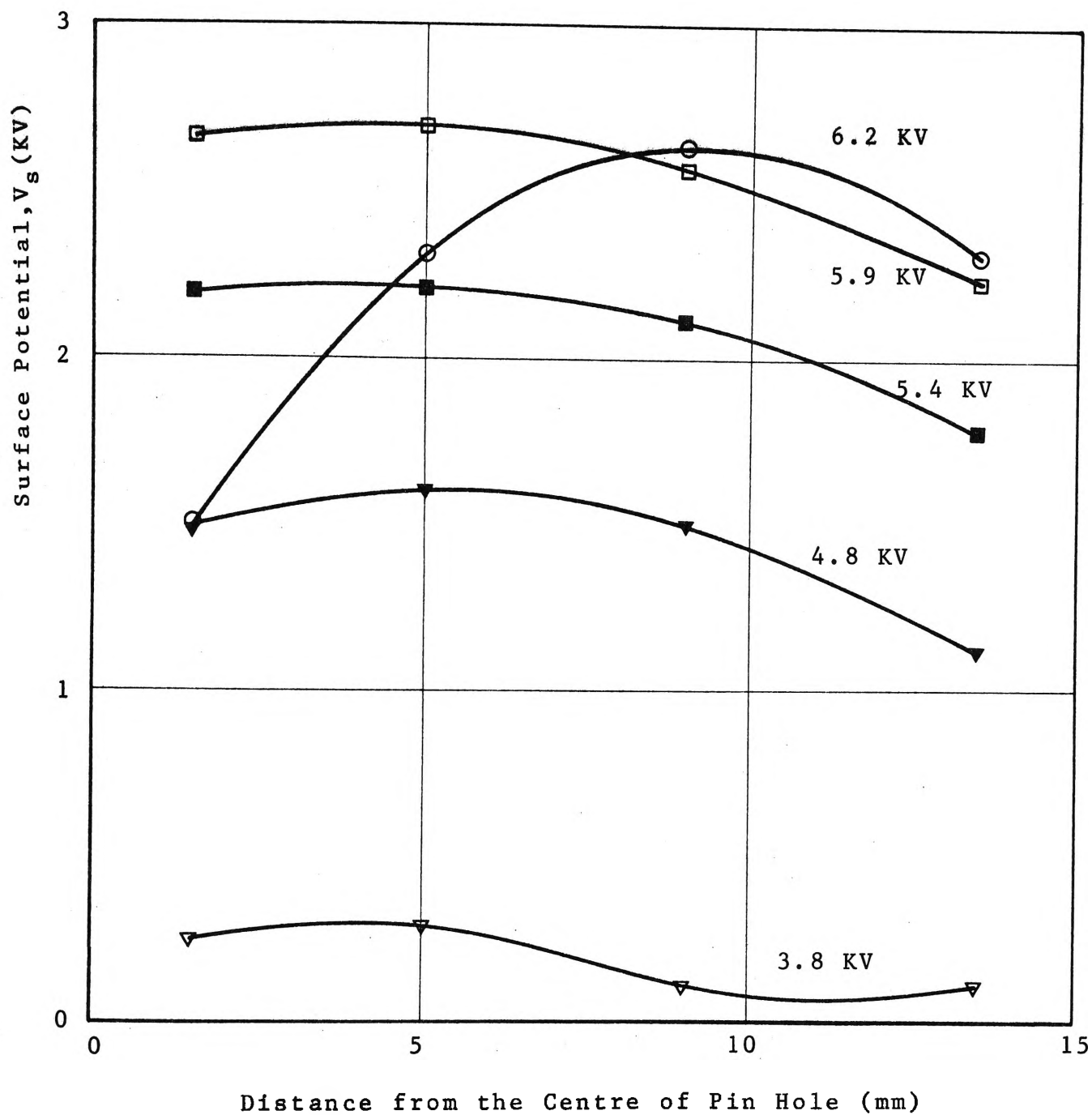


FIG.6.19 DISTRIBUTION OF SURFACE POTENTIAL ON THE CONTAMINANT SURFACE. D.C. VOLTAGE. PERFORATED MICA AS CONTAMINANT.

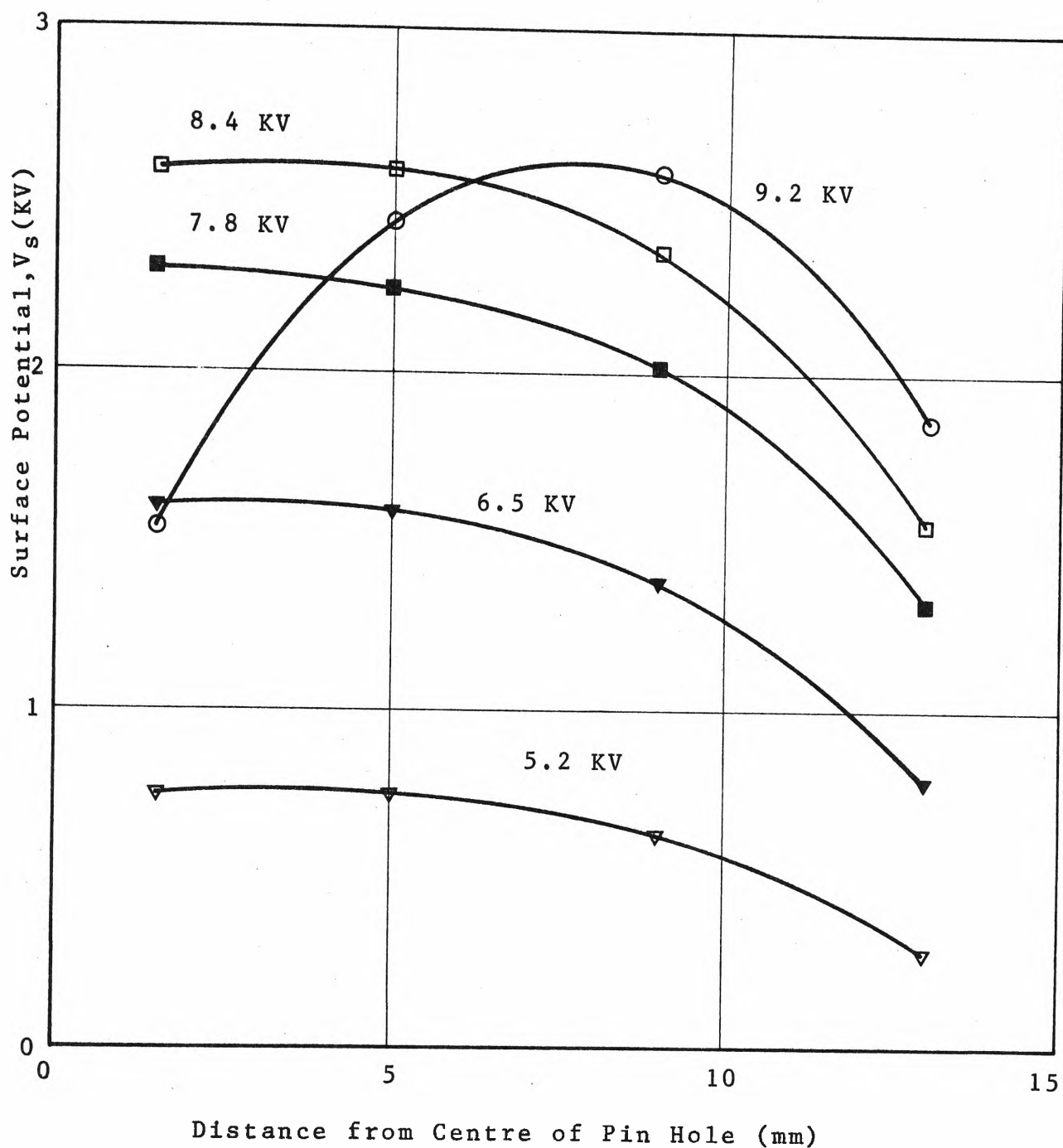


FIG.6.20 DISTRIBUTION OF SURFACE POTENTIAL ON THE CONTAMINANT SURFACE. PULSED VOLTAGE. REPETITION RATE = 30c/s. PERFORATED MICA AS CONTAMINANT. PEAK VOLTAGE IS SHOWN BESIDE EACH CURVE.

calculated at $r = 3\text{mm}$, $E = 4.2 \text{ kV/cm}$ (Fig.6.18).

6.7 A Proposed Mechanism of the Formation of Back Corona

In this section, a mechanism of the formation of back corona is proposed by combining important features discussed previously. It has been pointed out earlier, the experimental conditions investigated in this work are simplified to exclude possible mutual effects of one factor over the other. Simplification, in many scientific investigations, is usually considered as a rule rather than an exception. The technical evidences and fundamental processes presented in this proposed model are also applicable to an industrial situation.

6.7.1 The Build up of Voltage across the Contaminant

The presence of a layer of high-resistivity contaminant on the collecting plane anode of an electrode system affects the transport of negative ions between electrodes. The accumulation of negative ions on the surface of contaminant stops when the charge carriers input equals to the removed one. Assuming that the carriers form a surface charge layer that stays on the surface of contaminant, the voltage build up across the layer of contaminant is then proportional to the total amount of charge on the surface. The voltage was measured for various contaminant thicknesses and the results are shown in Fig.6.21, 6.22 for D.C. and pulsed voltages. It is seen that the surface potential reaches the same value for both D.C. and pulsed voltages at the same thickness. The build up of surface potential is proportional to the repetition rate and it requires a higher peak value with pulsed excitation than with D.C. excitation to attain the

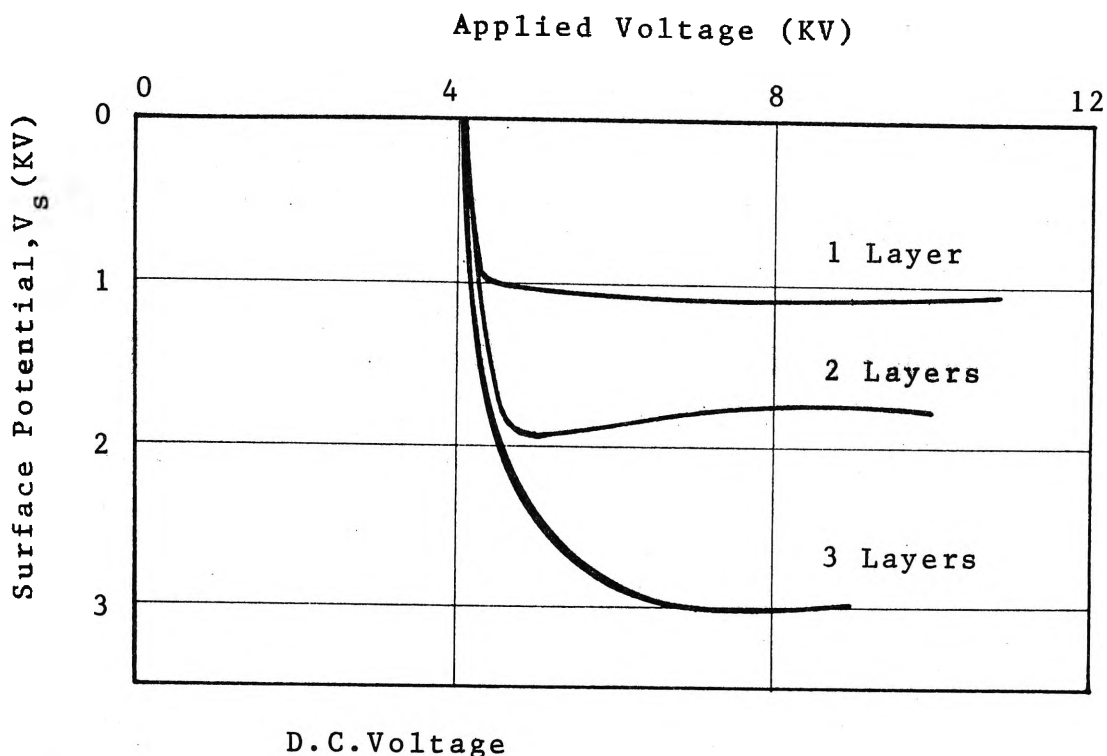
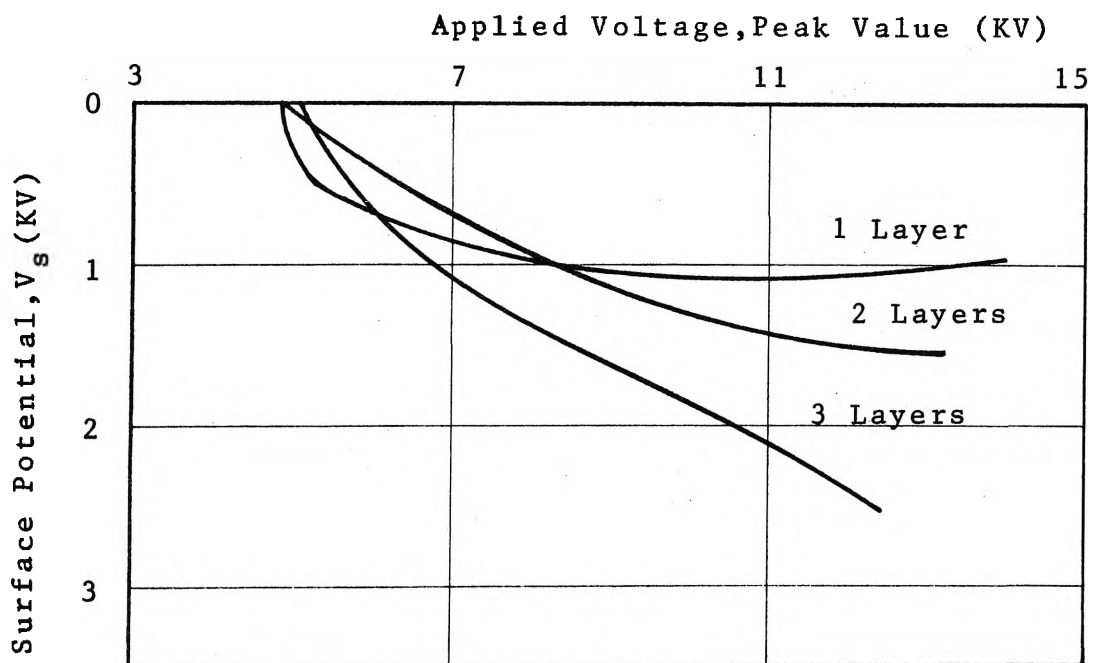
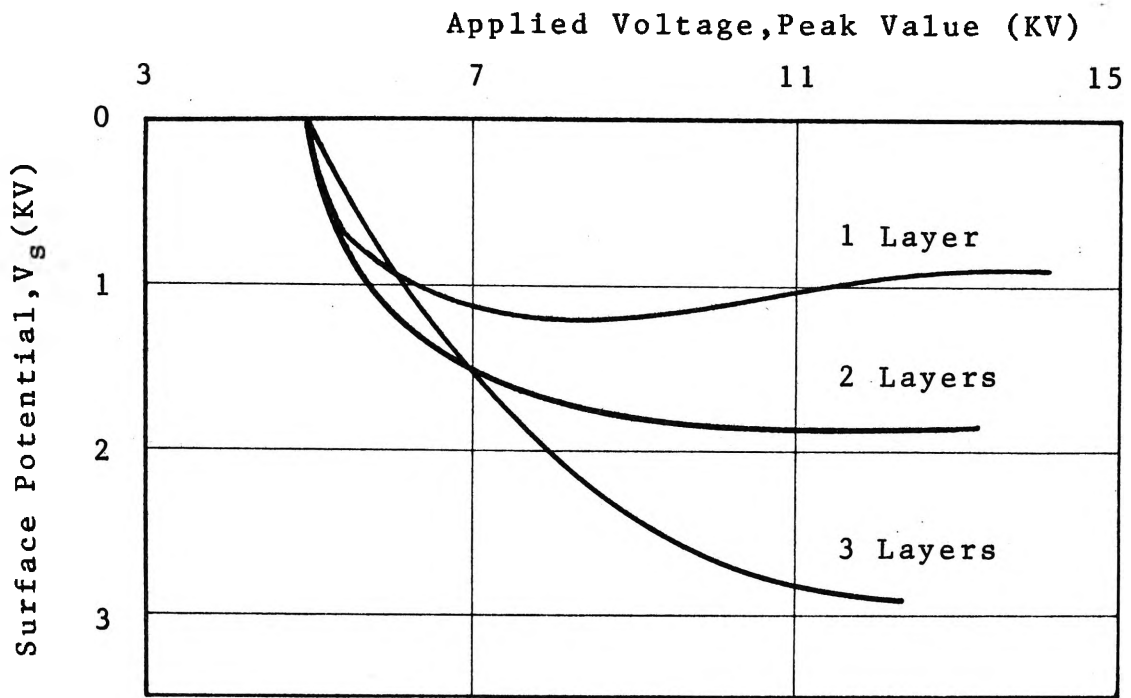


FIG.6.21 RELATIONSHIP BETWEEN SURFACE POTENTIAL OF THE CONTAMINANT AND APPLIED VOLTAGE. D.C. VOLTAGE.



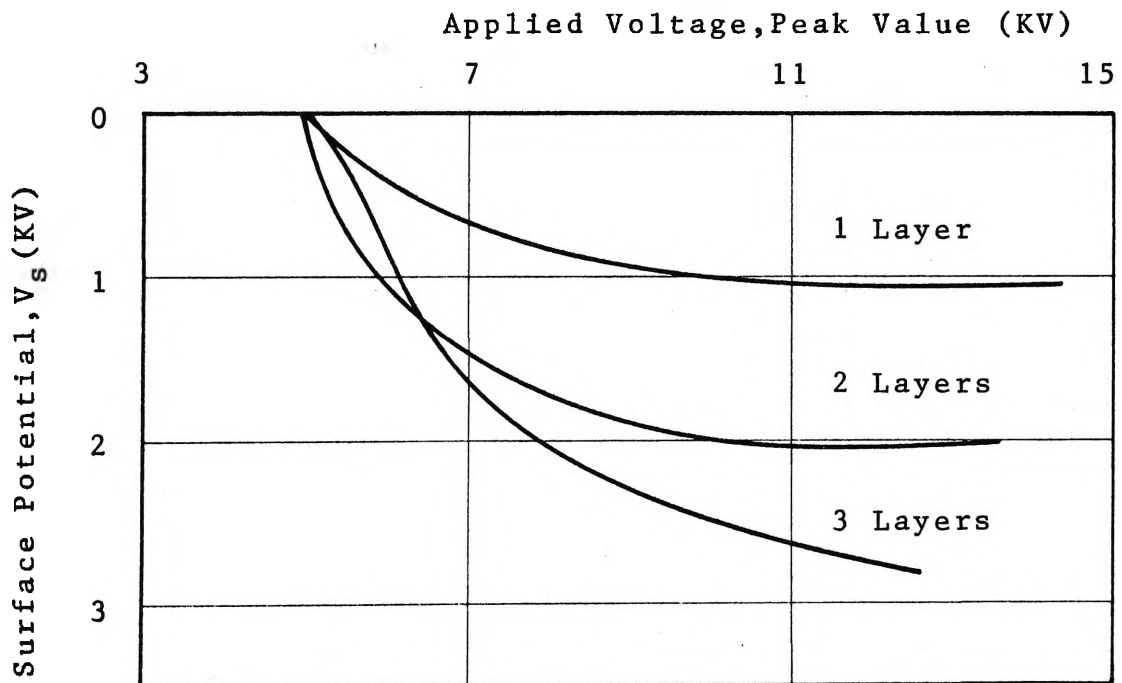
(a) Pulsed Voltage, Frequency = 13 c/s

FIG.6.22.a RELATIONSHIP BETWEEN SURFACE POTENTIAL OF THE CONTAMINANT AND APPLIED VOLTAGE. PULSED VOLTAGE.



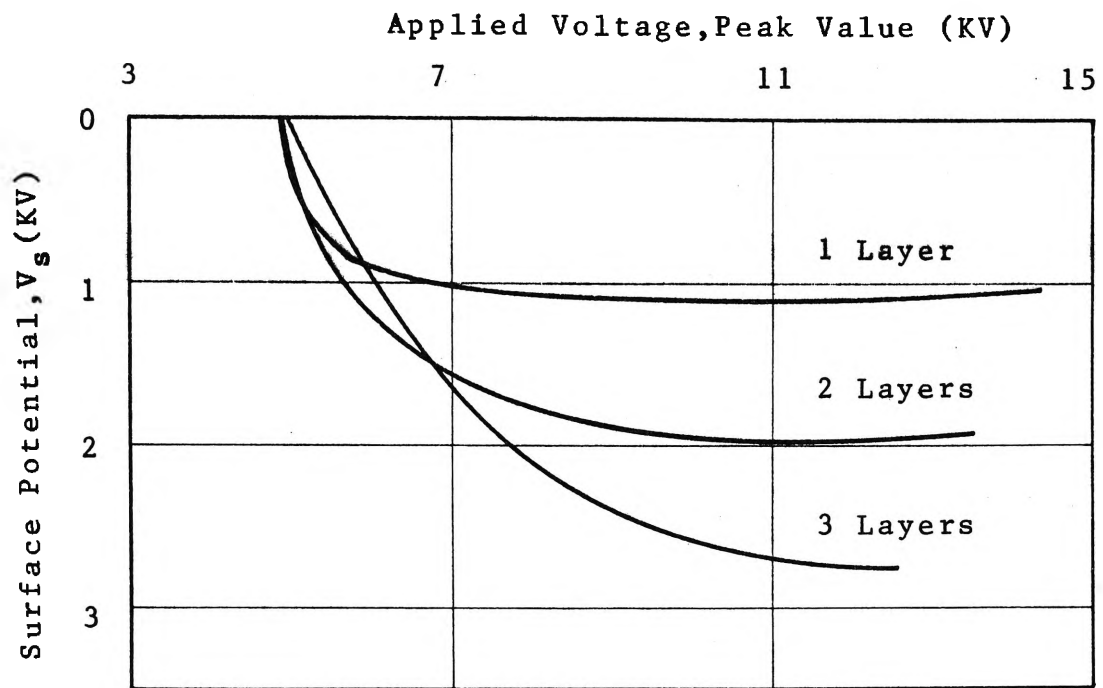
(b) Frequency = 30 c/s

FIG. 6.22.b.



(c) Frequency = 50 c/s

FIG. 6.22.c.



(d) Frequency= 70 c/s

FIG.6.22.d.

same constant magnitude. This is predictable because from the previous chapter, the same average corona current requires a higher amplitude with pulsed voltage than it does with steady voltage, and at higher frequencies, the average charge carriers injected into the contaminant is larger. The constancy of the surface potential at a given applied voltage confirms that the leakage time constant of the contaminant is so high that the fluctuation of the voltage is not noticeable.

The surface potential versus applied voltage curves also indicate a marked difference in the charging up of the contaminant when its surface potential has not reached the breakdown level. The curves for D.C. voltage (Fig.6.21) show a steep linear region and the saturation voltage is attained when the applied voltage is a few kilovolts above the corona onset voltage. On the contrary, the curves for pulsed voltage possess a linear region which spreads over a larger voltage range and this range appears to be inversely proportional to the repetition rate of the pulsed voltage. This is concurrent with the injection of charge carriers into the contaminant.

Since the equivalent resistance of the contaminant is a function of the electric field across the layer of contaminant, the build up of the surface potential is approximately a linear function of the current when the resistance depends very little on the field strength (this corresponds to the conduction of current through the contact area between adjacent particles or homogeneous volumes of contaminant). When the field strength is sufficiently high as a result of

an increase in applied voltage, which causes the injection of charge to increase, the resistance drops significantly because of the dominance of the Schottky emission current. Consequently, the build up of potential across the layer increases very slowly with respect to applied voltage. Finally, the saturation (or maximum) voltage across the contaminant is reached when the electric field in the air gap between adjacent particles is sufficient to initiate a breakdown in the contaminant.

6.7.2 The Perforation of Contaminant Layer

The breakdown voltages are shown in Fig.6.11 together with the Paschen's values for different thicknesses. The electrical breakdown causes perforation to take place in the contaminant. Because of the low resistance of the plasma-like state of the air path (inside the channel), it is justifiable to assume that at the moment of breakdown, the surface of contaminant at the breakdown spot is shunted to ground. This action causes the surface charge at the same spot to be removed, and the potential is very close to ground level. This process, however, is not observable from the experimental results because the surface potential probes are not located at the same breakdown spot and with the continual injection of charge carriers from the discharge cathode, the surface charge is replenished almost instantly. The critical resistivity, determined by applying Gauss's law at the boundary of the ionised gas and the contaminant, is agreeable with commonly accepted values. The physical significance of this phenomenon can be summed up as follows. The breakdown that takes place in the air voids, which are

present in the contaminant, produces positive ions and electrons in a similar manner to the Townsend's type of breakdown. The electrons, because of their high mobility move to the anode plane by conduction through thin surface layer of particles and by jumping across the air gap between adjacent particles. The positive ions which have lower mobility, probably emerge from the upper surface of the contaminant layer in a similar way as electrons do. At the spot where positive ions reach the surface, they neutralise the negative ions that accumulate at the same location, the neutralisation results in a zero net charge density.

6.7.3 The Formation of Stable Discharge

When back corona channels are formed in the contaminant and if the applied voltage is maintained so that the potential build up across the contaminant layer reaches the same value as above, the breakdown of air in the channels is caused by free electrons (which either exist naturally in air due to cosmic radiation or come from negative ions by electron-detachment). These electrons gain energy from the field set up in the channels and collide with neutral gas molecules in the channels. Electrons which are produced by ionising collisions move to anode and get neutralised. Positive ions reach the top side of the contaminant layer and neutralise negative ions which accumulate in the vicinity of the openings. The neutralisation of negative charge on the surface results in a drop in potential in the neighbourhood of the channels and alters the potential distribution. Consequently, the field line distribution in the air space between discharge cathode and contaminant is distorted in

such a manner that more negative ions are directed toward the channels. The surface potential distribution, with its maximum close to the channel, tends to drive most of the negative ions to the centre of the channel and confine the back discharge within a limited area surrounding the channel. In the experiment with a layer of perforated mica being used as contaminant the stable back discharge was observed in the channel when the potential across the layer reached the maximum value. It appeared as a reddish-purple glow and the potential dropped at the moment the discharge occurred. Further increase in applied voltage resulted in a further drop in surface potential while the discharge became more vigorous, its intensity increased and was more purple.

6.8 Sparkover of the Contaminated Corona System

6.8.1 Introduction

The stable discharge which takes place in a contaminated corona system could develop into space streamers and cause a complete sparkover if the applied field is sufficiently high. In this section, effects of back discharge on sparkover of the contaminated electrode system is investigated and the dependence of sparkover voltage on the contaminant thickness is expressed in a semi-empirical equation which is obtained by modifying the expression for breakdown of air in uniform gap. Explanation for the increase in sparkover voltage with negative pulsed voltage over that obtained with D.C. excitation is proposed by applying the mechanism of back corona formation and comparing the results with those measured by other workers. Experiments are used to demonstrate important features which are included in the

interpretation.

6.8.2 Effects of Contaminant on Sparkover Voltage

6.8.2.1 Negative D.C. Energisation

In a contaminated electrode system, the presence of back corona in the contaminant marks the transition from unipolar corona discharge to a bipolar one. The point-to-plane system behaves similarly to a point-to-point system with the second point electrode being played by the contaminated passive anode. The simultaneous presence of both the axial component of the electric field in the contaminant (section 6.5) and the radial component due to the distribution of surface potential surrounding the back corona channel (section 6.6) transforms the back corona channel into the equivalent point electrode. The resultant field in the proximity of the back corona channel under this condition is sufficiently high (> 30 kV/cm) to accelerate free electrons and causes ionising collisions with neutral gas molecules. The free electrons are produced by detachment of negative ions or present in air because of cosmic radiation. The collisions result in a local gas discharge similar to that which occurs in the neighbourhood of a positively-stressed point-electrode. An increase in applied voltage under this condition causes an increase in voltage across the air space and little change in the surface potential of the contaminant. When the voltage in the air space is sufficiently high the local ionisations existing at the two electrodes approach each other and eventually bridge the air gap to form a sparkover [19].

Up to this stage, the drop in sparkover voltage of a

contaminated point-to-plane electrode system energised by a negative D.C. voltage can be explained as follows:

- (i) The point-to-plane system behaves like a point-to-point system with ionisation taking place in the proximity of the low potential point electrode. This gas discharge is similar to that which occurs at a highly stressed positive point electrode. This equivalent state is tested by measuring the sparkover voltage of a clean point-to-point electrode of the same gap length as that of the contaminated point-to-plane system. The results are reasonably close to each other within the statistical uncertainty, which is less than 10 per cent for both cases.
- (ii) The surface potential gradient that is present in the vicinity of the back corona channel enhances the propagation of positive streamers through the air space.

The significant role of the surface potential gradient is demonstrated in the following experiment.

An annular disc of aluminium foil is adhered on the surface of a perforated layer of mica. Its centre is coincident with the centre of the perforation and its inner diameter can be varied from the diameter of the perforation to ten times larger. Its outer diameter is constant and smaller than the diameter of the mica layer. The dimensions of the arrangement are as follows: $2r_0 = .7$ mm, $2r_1 = 47$ mm, $2r_2 = 34$ mm, r_2 is the outer radius of the aluminium

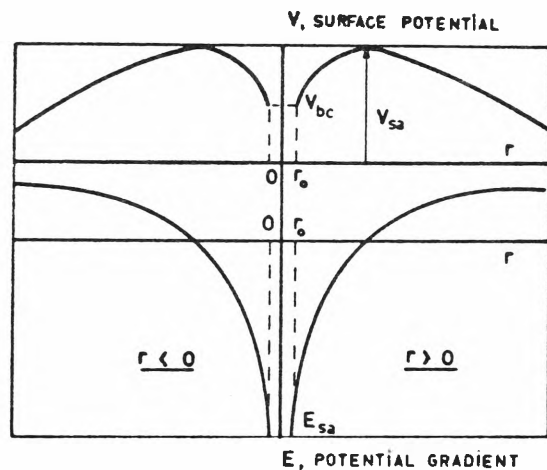
disc. By this means, the exposed part of the mica layer can be controlled and its surface potential gradient can be varied since the aluminium disc represents an equi-potential surface. The experiment is used to illustrate at least qualitatively the relative variance of the sparkover voltage with respect to the variation of the surface potential gradient in the vicinity of the perforation (simulating the back corona channel).

The results are summarised in Table 6.3 and the modes of the spark discharge, the surface potential and its gradient are illustrated diagrammatically in Fig.6.23.

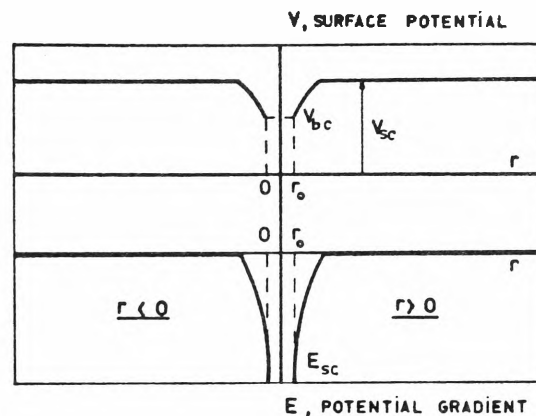
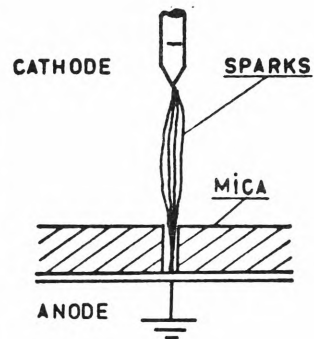
Condition of Contaminant Surface as illustrated in Fig.6.23	a	b	c	d
Inner radius of Metalised part, r	$r_a = \infty$	$r_b = 10r_o$	$r_c = 3r_o$	$r_d = r_o$
Sparkover Voltage, V_T	$V_{Ta} \approx$	$V_{Tb} <$	$V_{Tc} <$	V_{Td}
Surface Potential, V_s	$V_{sa} \approx$	$V_{sb} >$	$V_{sc} >$	$V_{sd} = V_{bc}$
Surface Potential Gradient, E_s	$E_{sa} \approx$	$E_{sb} >$	$E_{sc} >$	$E_{sd} = 0$

TABLE 6.3 SUMMARY OF THE SPARKOVER VOLTAGE, THE SURFACE POTENTIAL AND ITS GRADIENT OF A CONTAMINATED SYSTEM FOR VARIOUS CONDITIONS OF THE CONTAMINANT SURFACE.

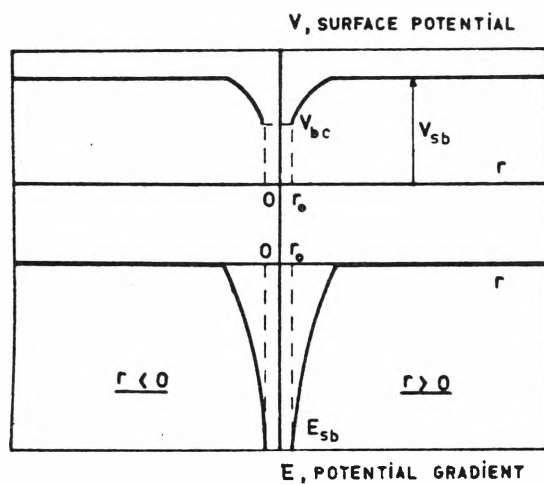
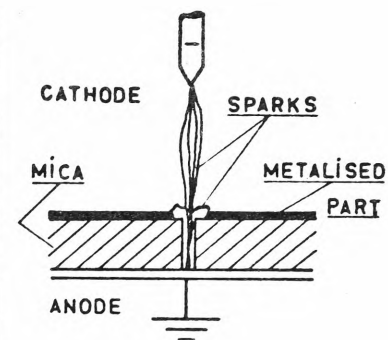
FIG.6.23 ILLUSTRATION OF THE SURFACE POTENTIAL, ITS GRADIENT AND THE SPARKING BETWEEN ELECTRODES FOR DIFFERENT CONDITIONS OF CONTAMINANT SURFACE.



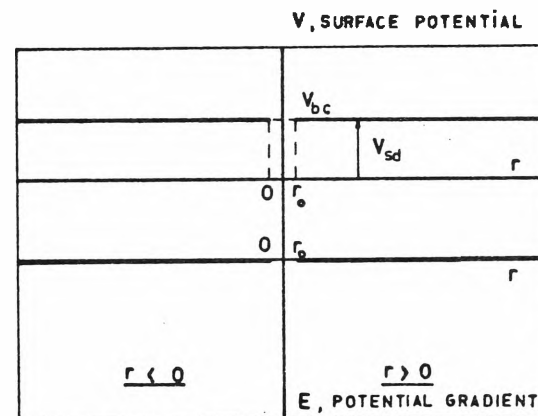
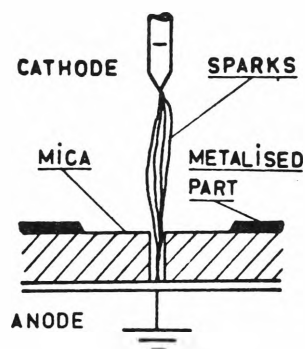
(a)



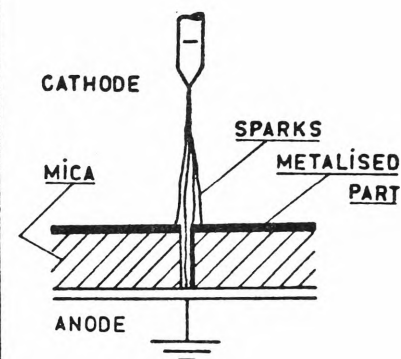
(c)



(b)



(d)



It can be seen that when the inner diameter of the aluminium disc is ten times the diameter of the hole, the spark discharge takes place only between the main electrodes and the sparkover voltage is close to that measured without the aluminium disc. This is understandable because from the calculation of the surface potential distribution (section 6.6), the potential gradient drops quickly with distance from the centre of the hole and the presence of the aluminium disc would cause only a minor change of the surface potential. The potential gradient is close to that without the disc (c.f. Fig.6.23a and 6.23b). As the inner diameter of the aluminium disc is three times the diameter of the hole, the spark discharge occurs between the disc, the passive anode and the highly-stressed point cathode. The sparkover voltage is higher than the above value (Fig.6.23c) but still smaller than that measured with aluminium disc covering the whole mica layer except the perforation (Fig.6.23d). The sparkover voltage in case d is somewhat smaller than that of a clean point-to-plane system. This is presumably due to a slight reduction of the length of the air space and the surface resistance of the inner wall of the perforation.

6.8.2.2 Negative Pulsed Energisation

The sparkover voltage of a contaminated corona system is also lower than that obtained with a clean system energised by a pulsed voltage. The difference between the negative

pulsed sparkover voltage and the D.C. value is caused by the following factors:

- (i) Pulsed voltage energisation requires a higher peak value to charge up the contaminant to the breakdown level (section 6.7.1) so that the condition (i) for D.C. voltage is satisfied.
- (ii) The sparkover voltage of a point-to-point system under pulsed energisation is higher than that under steady negative voltage. This point is confirmed by experimental results obtained for both D.C. and pulsed voltage at the same gap length and also by measurements of Waidmann [12] for a point-to-point system of different gap length.

In a symmetrical, non-uniform gap like the point-to-point system, ions of opposite signs (negative ions from cathode and positive ions from anode) tend to attract each other and come into the neighbourhood of the electrodes. This results in an alleviation of the quenching property of the ions on their electrode of origin and a plasma-like space charge in the middle of the gap. At the cathode, Trichel pulse discharge transits into pulseless (or negative glow) discharge, while at the anode the presence of negative ions - being partly generated by the local ionisation and partly coming from the cathode - facilitates the formation of a sheath terminating the positive streamers and forms the Hermstein glow. Steady corona discharges set in at cathode and anode.

At high voltage level, the neutral state of the space charge in the mid-gap may become unstable and lead to a complete sparkover. The difference between D.C. and pulsed sparkover voltage is caused by the average amount of charge carriers created and injected into the air space. Because of the short duration of the voltage pulse, it requires the pulsed voltage to have a higher magnitude to produce the same amount of space charge than it does to the D.C. voltage.

6.8.3 Dependence of Sparkover Voltage on Contaminant

Thickness

The sparkover voltage of the contaminated corona system was measured for three thicknesses of Teflon filtering paper used as a contaminant. The measurement of sparkover voltage suffers a certain degree of uncertainty because of the sporadic nature of back corona discharge. Under steady state energisation, the D.C. power supply was stripped simultaneously with the occurrence of a complete spark, whereas the pulsed power supply can tolerate several sparks, it can recover after each spark and its output remains unaffected. The degree of uncertainty with pulsed voltage is somewhat higher than that with D.C. voltage because the mode of sparking can vary from one spark per several voltage pulses to one spark per each pulse. However, the general trend for both D.C. and pulsed voltages is that within the range of thickness (125-375 μm), the sparkover voltage decreases as the thickness of the contaminant increases. The voltage drop with D.C. voltage is smaller than that with

pulsed voltage.

It was arbitrarily selected that the sparkover voltage under pulsed energisation was the value at which the first spark was observed irrespective of the time lapse from the moment the voltage was applied until the spark occurred. The results are shown in Fig.6.24 with each value as the mean of ten readings.

From the experimental results, the sparkover voltage can be conveniently expressed as a function of the contaminant thickness. The equation is obtained by modifying the well-known expression for breakdown of air in uniform gap [122]:

$$V = 24.22 \left(\frac{293P}{760T} \right) d + 6.08 \sqrt{\left(\frac{293P}{760T} \right) d}$$

The usual value of d is replaced by a (constant $\times d$). This constant which is dependent on the contaminant thickness, is found by applying the least square method into the experimental curve of sparkover voltage versus contaminant thickness of a point-to-plane electrode system. It can be written:

$$V = 24.6[-2.4t+.33]d + 6.08\sqrt{1.01[-2.4t+.33]d} \quad (6.24)$$

for D.C. voltage

and:

$$V = 24.6[-2.9t+.46]d + 6.08\sqrt{1.01[-2.9t+.46]d} \quad (6.25)$$

for pulsed voltage

where V is the sparkover voltage in [KV] (peak value for pulsed voltage), t is the contaminant thickness in [cm], and d is the gap length in [cm], the pressure and temperature are atmospheric pressure and 67°F (17.2°C).

Alternatively, expressions (6.24) and (6.25) can be written as:

$$V_{D.C.} = 24.22 \left(\frac{293P}{760T} \right) (-2.4t + .33)d + 6.08 \sqrt{\left(\frac{293P}{760T} \right) (-2.4t + .33)d}$$

and

$$V_p = 24.22 \left(\frac{293P}{760T} \right) (-2.9t + .46)d + 6.08 \sqrt{\left(\frac{293P}{760T} \right) (-2.9t + .46)d}$$

where P is the gas pressure measured in [Torr.] and T is the gas temperature measured in [$^{\circ}$ K].

The estimated values obtained with expressions (6.24) and (6.25) are plotted in Fig.6.24 (the broken curves).

Since the onset voltage of back corona is proportional to the contaminant thickness, and the sparkover voltage of the contaminated system is inversely proportional to the contaminant thickness, it can be seen that smaller voltage across the air space is required to facilitate the propagation of positive streamers. It thus appears that the contaminated corona system can tolerate more current flow and higher sparkover voltage at small thicknesses. This is complementary to the ease of the formation of back corona at small thicknesses. For larger thicknesses, as soon as the contaminant undergoes a breakdown the positive streamers emanating from the back corona channels will propagate across the air gap to link with the cathode and causes a complete sparkover. This phenomenon may be explained with the following factors:

- (i) The generation of positive ions in the back corona channel and its vicinity transforms the passive plane anode into a point electrode with the rest of the contaminant acting like a wall. The confinement of

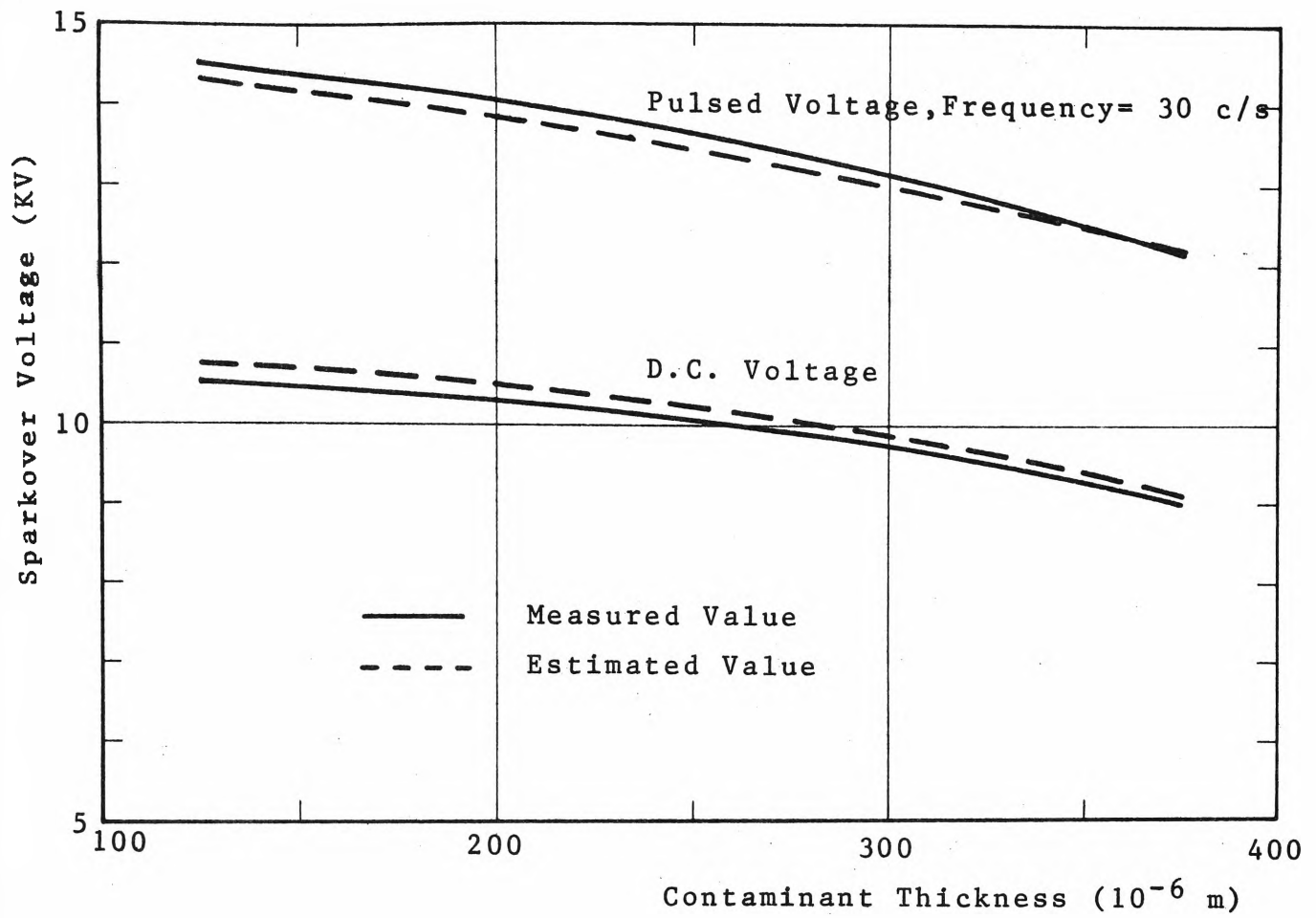
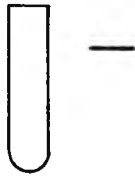


FIG.6.24 RELATIONSHIP BETWEEN SPARKOVER VOLTAGE AND CONTAMINANT THICKNESS FOR D.C. AND PULSED VOLTAGES.

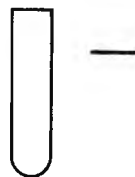
positive ions within this wall of contaminant tends to conserve the energy at the head of positive streamers. The degree of conservation of energy is proportional to the contaminant thickness. As a result, positive streamers created in a thicker layer of contaminant are more readily able to propagate into the air space than those generated in a thinner layer. This point is demonstrated by using a point-to-point electrode system with the grounded electrode being covered with a Teflon sleeve. The sparkover voltage is observed lower as the point electrode submerges in the sleeve than that measured when the tip of point electrode protrudes from the Teflon sleeve. The results are illustrated diagrammatically in Fig.6.25.

- (ii) The back corona discharge appears to be more stable and spread over a larger area with a thin layer of contaminant and constrict within the back corona channel with a thick layer.
- (iii) The minimum voltage in the air space is approximately equal to 5 kV, dividing this value by the gap length of 1 cm gives an average field intensity of 5 kV/cm which incidentally is also the value observed by Penney and Craig [109] with the contaminated corona system of longer gap length.

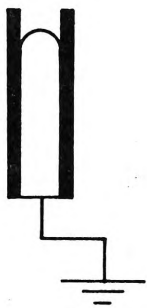
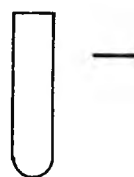
(1)



(2)



(3)



$$V_{s1} < V_{s2} \approx V_{s3}$$

FIG. 6.25 SPARKOVER VOLTAGE OF A POINT-TO-POINT ELECTRODE SYSTEM AS AFFECTED BY THE CONTAMINATION CONDITION AT THE GROUNDED POINT.

6.9 Summary

Characteristics of a contaminated corona system have been investigated with interests being focussed on the formation of back corona and sparkover. Although a laboratory model was used under normal temperature and pressure, the technical evidence can also be applied to the industrial situation.

In an electrostatic precipitator, the electrical conduction of a layer of particles (dust) is attributed to both surface and volume properties of the particles. Surface conduction is usually predominant in dust particles at low temperature because of the absorption of moisture which is present naturally in most industrial gases. As the electric field across the layer increases, the constriction of the current flow through the contact areas of adjacent particles, generates high field and causes electrons to jump across the air space. This results in an increase of the effective contact area and current. When the generated field is sufficiently high, ionising collision may take place in the air space between adjacent particles and initiate a complete breakdown across the dust layer. This marks the onset of back corona. Pulsed voltage requires a higher peak value than D.C. voltage to charge up the dust layer to breakdown level.

Back corona causes the alteration of the surface potential distribution in the vicinity of the back corona channels. The presence of sufficiently high surface potential gradient tends to enhance the local ionisation and facilitate the propagation of positive streamers through the

air gap. In a dust layer of non-uniform thickness, the thinner part is more ready to undergo back corona discharge and subsequently attracts more negative ions toward the channels and results in a marked increase in current and a drop in sparkover voltage. Whereas if back corona happened in the thicker part of the layer, it would likely cause the positive streamers to bridge the gap and reduce the spark-over voltage even further.

The simultaneous presence of the field components in the dust layer and along its surface (in the vicinity of the back corona channels) transforms the channel into a point electrode. In this equivalent system, the participation of ions of opposite signs in the neighbourhood of the electrodes causes pulseless glow discharge to take place at the cathode (negative glow) and on the surface of the dust layer (Hermstein's glow). The neutralisation of space charges of opposite polarities results in a plasma-like space charge in the mid-gap. At high potential, the plasma may become unstable and lead to a complete sparkover. The stable state of the plasma is disrupted at a threshold level, this level is higher under pulsed energisation than that under a D.C. voltage.

REFERENCES

- [1] WHITE, H.J. - "Industrial Electrostatic Precipitation"
ADDISON WESLEY, 1963.
- [2] ROSE, H.E. and WOOD, A.J. - "An Introduction to Electrostatic Precipitation in Theory and Practice"
CONSTABLE and CO., LONDON, 1966.
- [3] ROBINSON, M. - "Electrostatic Precipitation" - Air Pollution Control (edited by W. STRAUSS) - WILEY-INTERSCIENCE 1971.
- [4] WHITE, H.J. - "A Pulse Method for Supplying High Voltage Power for Electrostatic Precipitator"
Trans.A.I.E.E., Vol.71, Pt.1, pp.326-329.
- [5] THOMAS, J.B. and WILLIAMS, T.R. - "Pulsed Corona Discharges", in Gas Discharges and the Electrical Supply Industry. Ed. FOREST, J.S., BUTTERWORTH, LONDON, 1962.
- [6] KOSCHANY, E.M. - "The Operation of an Electrostatic Precipitator with Pulsed Voltages".
Staub-Reinholt-Luft, 1969, Vol.27, No.4, pp.5-8.
- [7] LAU, H. - "A.C. Electrostatic Precipitator" Staub-Reinholt-Luft, 1969, Vol.29, No.8, pp.10-13.
- [8] HERCEG, Z. and HUEY, R.M. - "Model for Corona Modes in Point-to-Plane Device with Coated Electrodes".
Proc.IEE, 1973, Vol.120, No.3, pp.394-399.
- [9] COOPERMAN, P. - "Positive Polarity Operation of Electrical Precipitators", Trans.I.E.E.E., 1964, Vol.83, No.75, pp.792-794.
- [10] COOPERMAN, P. - "Positive Polarity Precipitation Revisited", Publication of the Symposium on The Changing Technology of Electrostatic Precipitation, 1974.
- [11] HALL, H.J. - "Trends in Electrical Energisation of Electrostatic Precipitators". Proc. of E.S.P. Symp, Feb.1971, Birmingham, Alabama.
- [12] LOEB, L.B. - "Electrical Coronas - Their Basic Physical Mechanism", 1965, UNI. OF CALIFORNIA PRESS.
- [13] HALL, H.J. - "Notes on Impulse Corona Studies in Air"
Physical Reviews, New York, N.Y., Vol.72, 1947, p.185.

- [14] MOORE, D.B. and ENGLISH, W.N., - "Point-to-Plane Impulse Corona", J. of Appl. Phys., New York, N.Y., Vol.20, 1949. pp.370-375.
- [15] THOMAS, J.B. and WILLIAMS, T.R. and SUZUKI, T. - "Power Relationships and Temperature Dependence in the D.C. Corona Field". Trans.A.I.E.E., Vol.79(I), 1960, pp.1-4.
- [16] THOMAS, J.B. and WILLIAMS, T.R. - "Current-Voltage Relationships in Negative Pulsed Corona". Trans. A.I.E.E., Vol.79(I), 1960, pp.136-139.
- [17] SOUTHERN RESEARCH INSTITUTE - "Dust Resistivity and Precipitator Performance". A Quarterly report to Environmental Protection Agency. Research Triangle Park, North Carolina.
- [18] BROWN, S.C. - "Basic Data of Plasma Physics", Cambridge Massachusetts. M.I.T. Press.
- [19] NASSER, E. - "Fundamentals of Gaseous Ionisation and Plasma Electronics". New York, N.Y., JOHN WILEY and SON INC., 1971.
- [20] SCHUMANN, W.O. - "Elektrische Durchbruchfeldstärke von Gasen". Berlin. Germany - SPRINGER-VERLAG, 1923.
- [21] HUTTON, J.G. - "Determination of Corona Starting Voltages for Non-uniform Fields in Air" Trans.A.I.E.E., Vol.66, pp.1674-1680, 1947.
- [22] VER PLANCK, D.W. - "Calculation of Initial Breakdown Voltages in Air", Trans.A.I.E.E., Vol.60, pp.99-104, 1941.
- [23] MEEK, J.M. = Physical Review 57 (1940), p.722.
- [24] RAETHER.H. - Arch. Elektrotech. 34 (1940), p.49.
- [25] LOEB, L.B. and MEEK, J.M. - "The Mechanism of the Electric Spark", STANFORD UNIVERSITY PRESS, 1941.
- [26] RAETHER, H. - Z. Phys. 117 (1941), 394, 524.
- [27] LOEB, L.B. and WIJSMAN, R.A. - Journal of Appl. Phys. 19 (1948), 797.
- [28] PETROPOULOS, G.M. - Phys.Rev. 78 (1950), 250.
- [29] LÜTHI, J.E. - Dissertation ETH-Zürich (From Ref.[30]).
- [30] MASUDA, S. - Research on Electrostatic Precipitation 1975 - Masuda Laboratory - Department of Electrical Engineering - University of Tokyo.

- [31] R.C.A. Manual for Photomultiplier Tubes.
- [32] LOEB, L.B. - Phys. Rev. 73, 798 (1948).
- [33] LOEB, L.B. - Phys. Rev. 74, 2 (1948).
- [34] HEIZSLER, M. = "Analysis of Streamer Propagation in Atmospheric Air". Ph.D. dissertation. IOWA STATE UNIVERSITY, 1971.
- [35] WOBODITSCH, W. - "Die Charakteristiken von technischen Funkerstrecken mit stark inhomogenen Feld". Wiss. Z, Tech. Hoch., Dresden, 8, 861, (1959).
- [36] GIAO, T.N. and JORDAN, J.B. - "Modes of Corona Discharges in Air". Trans. I.E.E.E. PAS.87, 1207 (1968).
- [37] BEATTIE, J.E. and CROSS, J.D. - "Hermstein Glow Corona in a Quasi-Uniform Field". Third Int. Conf. on GAS DISCHARGES - LONDON, 1974, p.279.
- [38] NASSER, E. and LOEB, L.B. - "Impulse Streamer Branching from Lichtenberg Figure Studies". J. of Appl. Phys., 34, 3340, 1963.
- [39] AKAZAKI, M. and TSUNYASU, I. - "Breakdown Mechanisms of the Positive Point-to-plane Gap in Air under Impulse Voltages". Third Int. Conf. on GAS DISCHARGE, LONDON 1974, p.220.
- [40] HERCEG, Z. - "Electrical Characteristics of Contaminated Corona System". Ph.D. Dissertation, UNI. OF N.S.W., 1970.
- [41] LOEB, L.B., PARKER, J.H., DODD, E.E. and ENGLISH, W.N. "The Choice of Suitable gap forms for the study of corona breakdown and the field along the axis of a hemispherically capped cylindrical point-to-plane gap". Rev.Sci. Instr., Vol.21, pp.42-47, 1950.
- [42] ABOU-SEADA, M.S. and NASSER. E. - "Digital Computer Calculation of the Electric Potential and Field of a Rod Gap". Proc.I.E.E.E., Vol.56, No.5, May 1968, pp.813-820.
- [43] GUCK, R.W. - Die negative Koronaentladung in der Spitze-Platte-Funkenstrecke", Müller, Karlsruhe, 1955.
- [44] SMITH, P.V. - "Spatial Distribution of Temperature and Related Quantities in N₂,...UHF Plasma Torch". Ph.D. Dissertation, UNI. OF N.S.W., 1968.

- [45] SHARPE, J. - Electronic Technology, Jun.-Jul. (1961).
- [46] LEMKE, E. - "Der durchschlagsmechanismns von luftfunkenstrecken bei schaltspannungen". Wiss. Zeitschr. der TU. DRESDEN 17. pp.105-115.
- [47] ACKER, E.E. and PENNEY, G.W. - "Some Experimental Observations of the propagation of streamers in Low Field Regions of an Asymmetrical Gap." J. of App. Phys.40. pp.2397-2400.
- [48] HUDSON, G.G. and LOEB, L.B. - Streamer Mechanism and Main stroke in the Filamentary Spark Breakdown in Air as revealed by Photomultipliers and Fast Oscilloscopic Techniques". Phys. Rev. 123, pp.29-43.
- [49] MIYOSHI, Y. and HOSOKAWA, T. - "Pre-Corona Discharge in Air". Int. Conf. on GAS DISCHARGES - LONDON 1970, pp.26-30.
- [50] ZENTNER, R. - Abhandlungen des Instituts fur Hochspannungs-technik und electrische Analgen, Karlsruhe. Germany. UNI. OF KARLSRUHE, No.14.
- [51] NASSER, E. and HEISZLER, M. - "The Propagation of Streamers in Air". Third Int. Conf. on GAS DISCHARGES, 1974, pp.178-181.
- [52] HUDSON, R. - "Infrared System Engineering". JOHN WILEY and SON. Inc., 1969.
- [53] CHATTOCK, A.P. and TYNDALL, A.M. - Phil. Mag. 19, p.543, 1909.
- [54] RATNER, S. - Phil. Magn., 32, p.442, 1916.
- [55] ROBINSON, M. - "Movement of Air in the Electric Wind of the Corona Discharge" - A.I.E.E. Trans. on Communications and Electronics. Part I, May, 1961, pp.143-150.
- [56] LE NY, R., LE NY, A.M. and BOULLLOUD, A. - "Positive Point-to-Plane Corona Discharge: new observations on Hermstein's Glow". Third Int. Conf. on GAS DISCHARGES - LONDON. Sept. 1974. pp.306-310.
- [57] BECKER, J.A., GREEN, C.B. and PEARSON, G.L. - "Properties and Uses of Thermistors - Thermally Sensitive Resistors". Bell System Technical Journal, 1947. pp.170-212.

- [58] UDO, T. - "Sparkover Characteristics of Large Gap Spaces and Long Insulator Streings". I.E.E.E. Trans. on Power Apparatus and System 83(5), 1964, pp.471-483.
- [59] BOYLETT, F.D.A., EDWARDS, H.G.J. and WILLIAMS, B.G. "Variation of Breakdown Voltage of a Positive-point/Plane gap with Applied Voltage Waveshape". NATURE, Sept. 4, 1965, pp.1085-1086.
- [60] ABDULLAH, M. and KUFFEL, E. - "Development of Spark Discharge in Non-uniform Field gaps under Impulse Voltage", Proc.I.E.E., Vol.112, No.5, May 1965, pp.1018-1024.
- [61] HUGHES, R.C. and ROBERTS, W.J. - "Application of Flashover Characteristics of Air Gaps to Insulation Co-ordination". Proc.I.E.E., Vol.112, No.1, 1965, p.198.
- [62] UDO, T. - "Switching Surge and Impulse Sparkover Characteristics of Large Gap Spacings and Long Insulator". Trans. I.E.E.E., PAS-84, No.4, 1965, P.304.
- [63] AMIN, M.R. - "Fast Time Analysis of Intermittent Point-to-Plane Corona in Air.III. The Negative Point Trichel Pulse Corona", J. of Appl. Phys., Vol.25, No.5, May 1954.
- [64] McLEAN, K.J. and THANH, L.C. - "Effect of Pulsating Negative Voltage on the Corona Discharge of a Wire Electrode", Third. Int. Conf. on GAS DISCHARGE - LONDON, 1974, pp.298-301.
- [65] MASUDA, S. - "Recent Progress in Electrostatic Precipitation", Inst. Phys. Conf. Ser. No. 27, 1975, Ch.3.
- [66] TASSICKER, O.J. - "Aspects of Forces on Charged Particles in Electrostatic Precipitators", Ph.D. thesis, UNIV. OF N.S.W., 1972.
- [67] TRICHEL, G.W. - "The Mechanism of the Negative Point-to-Plane Corona near onset". Phys. Rev. 54, (1938), p.1078.
- [68] EL-DEBEIKY, S. and KHALIFA, M. - "Calculating the Corona Pulse Characteristics and its Radio Interference". I.E.E.E. Trans. P.A.S, Vol.PAS-90, No.1, 1971, pp.165-179.

- [69] SOUTHWELL, R.V. - "Relaxation Methods in Theoretical Physics", Vol.1 and 2, OXFORD UNIVERSITY PRESS 1952, 1956.
- [70] KUNZ, K.S. - "Numerical Analysis", MCGRAW HILL, 1957.
- [71] GALLOWAY, R.H., RYAN, H.McL, and SCOTT, M.F. - "Calculation of Electric Fields by Digital Computers" Proc.IEE, 114 (1967), pp.824-9.
- [72] BINNS, K.J. and LAWRENSON, P.J. - "Analysis and Computation of Electric Field and Magnetic Field Problems". PERGAMON PRESS - Oxford 1963, 1973.
- [73] HAMMOND, P. - "Electric and Magnetic Images", Proc.IEE, May 1960, pp.306-313.
- [74] SARMA, M.P. and JANISCHEWSKYJ, W. - "Electrostatic Field of a System of Parallel Cylindrical Conductors" Trans.IEEE, pt.3, 88 (1969), pp.1069-1079.
- [75] SINGER, H., STEINBIGLER, H. and WEISS, P. - "A Charge Simulation Method for the Calculation of High Voltage Fields", Trans. IEEE, PAS.93, No.5, 1974, pp.1660-8.
- [76] ABOU-SEADA, M.S. and NASSER, E. - "Digital Computer Calculation of the Electric Potential and Field of a Rod Gap". Proc.IEEE, Vol.56, No.5, 1968, pp.813-820.
- [77] ABOU-SEADA, M.S. and NASSER, E. - "Digital Computer Calculation of the Potential and its Gradients of a Twin Cylindrical Conductors". Trans.IEEE, pt.3, 88 (1969), pp.1802-1814.
- [78] PEEK, F.W. - "Dielectric Phenomena in High-Voltage Engineering", MCGRAW-HILL, 1929.
- [79] WHITEHEAD, J.B. - "High-Voltage Corona" in "International Critical Tables", MCGRAW-HILL, 1929.
- [80] STOCKMEYER, W. - "Koronaverluste bei höher Gleichspannung, Wiss. Verofl. SIEMENS, 1934, 13, (2), p.27.
- [81] GARY, C.H., HUTZLER, B.P. and SCHMITT, J.P. - "Peek's Law Generalisation; Application to Various Field Configurations". 72549-4 IEEE-PES Summer Meeting 1972.

- [82] ZAENGL, W.S. and NYFFENEGGER, H.U. - "Critical Field Strength for Cylindrical Conductors in Air: An extension of Peek's Formula" Third Int. Conf. on GAS DISCHARGES - LONDON, 1974, pp.302-305.
- [83] ALEKSANDROV, G.N. - "Physical Conditions for the production of a D.C. corona discharge in smooth Conductors". Soviet Phys. Tech. Phys., 1957, pp.2554-2565.
- [84] KAPZOW, N.A. - "Elektrische Vorgänge in Gasen und im Vakuum", VEB Deutscher Verlag der Wissenschaften, Berlin, 1955.
- [85] SARMA, M.P. and JANISCHEWSKYJ, W. - "D.C. corona on Smooth Conductors in Air - Steady State Analysis of the Ionisation Layer". Proc.IEE, Vol.116, No.1, Jan.1969 pp.161-166.
- [86] KHALIFA, M., ABDEL-SALAM, M., and ABOU-SEADA, M. - "Calculation of Negative Corona Onset Voltages". IEEE Power Engineering Society Winter Meeting N.Y. Jan 16, 1973.
- [87] JOHNSON, G.W. - "Ionisation Currents in Divergent Fields in Hydrogen and Air". Phys. Rev.73, 284 (1948).
- [88] HARRISON, M.A. and GEBALLE, R. - "Simultaneous Measurement of Ionisation and Attachment Coefficients" Phys. Rev. 1953, 91, pp.1-7.
- [89] MASCH, K. - "Über Elektronenionisierung von Stickstoff und Luft bei geringen und hohen Drucken". Arch. Elektrotek, 1932, 26, pp.587-596.
- [90] SANDERS, F.H. - "Measurement of the Townsend Coefficient for ionisation by Collision". Phys. Rev., 1933 44, pp.1020-1024.
- [91] LOEB, L.B. - "Basic Processes in Gaseous Electronics" UNIV. OF CALIFORNIA, 1955.
- [92] FLETCHER, R.C. - "Impulse Breakdown in the 10^{-9} -sec. Range of Air at Atmospheric Pressure". Phys. Rev. Vol.76, No.10, 1949, pp.1501-1511.
- [93] HEINTZ, V.W. - "Untersuchung des Hochfrequenten Spektrums periodischer Entladungen" - Zeitschrift für angewandte Physik - Vol.11, No.2, 1959, pp.51-59.

- [94] ENGLISH, W.N. and LOEB, L.B. -
J. of App. Phys. 20, 707, (1949)
- [95] CHUA, L.O. - "Introduction to Nonlinear Network
Theory", MCGRAW-HILL BOOK COMPANY.
- [96] PENNEY, G.W. - Discussion on the paper by THOMAS, J.B.
et al. AIEE Trans. Communication and Electronics.
pt. 1, Vol.80, 1961, p.319.
- [97] THANH, L.C. and McLEAN, K.J. - "Some Consequences of
using Pulsed Voltages to Energise Electrostatic
Precipitators". Proc. of symposium on The Changing
Technology of Electrostatic Precipitation - The
Inst. of Fuel - Nov. 1974, ADELAIDE.
- [98] CHATTOCK, A.P. - "On the velocity and mass of ions
in the electric wind in air". Phil. Mag. 48,
1899, pp.401-420.
- [99] LÖB, E.- Archiv. der Elektrischen Übertragung, Berlin,
Germany, Vol.8, 1954, pp.85-90.
- [100] HARNEY, D.J. - "An aerodynamic study of the electric
wind" M.S. Thesis CALIFORNIA INSTITUTE OF
TECHNOLOGY, 1957.
- [101] NASSER, E. and SHAH, R. - "Analysis of Streamer
branching in atmospheric air". Int. Conf. on
Phenomena in Ionised Gases. Bucharest Conf. Proc.
9:271.
- [102] ALLIBONE, T.E. and MEEK, J.M. - Proc. Roy. Soc.
(LONDON) A166, 97 (1938), A169, 246 (1938).
- [103] RAETHER, H. - "Electron Avalanches and Breakdown in
Gases", London, BUTTERWORTH, 1964.
- [104] LEGLER, W. - Z. Phys., 143, 173 (1955).
- [105] WOLCOTT, E.R. - In discussion on p.272 of ESCHHOLZ,
O.H., Electrical Precipitation, Trans.A.I.M.E.,
1918, 60, 243-79.
- [106] PAUTHENIER, M., DEMON, L. et LAURENT, E. - "La Contre-
Emission secondaire dans les filtres électriques".
Comptes rendus des Séances de l'Académie des Sciences,
20, MAI 1946, CCXXII pp.1219-20.

- [107] LAURENT, M.E. - "La Contre Emission Secondaire dans les Dispositifs de Précipitation Electrique des Poussières et à travers les Surfaces Poreuses". Revue Générale d'électricité Vol.LVII, No.3, pp.114-116.
- [108] PENNEY, G.W., CRAIG, S.E. - "Sparkover as Influenced by Surface Conditions in D.C. corona"., Trans. A.I.E.E., May (1960), Vol.79, pp.112-118.
- [109] PENNEY, G.W., CRAIG, S.E. - "Pulse Discharges Preceeding Sparkover at Low Voltage Gradients", Trans.A.I.E.E., May (1961), Vol.80, pp.156-162.
- [110] McLEAN, K.J. - "Electrical Conduction in High Resistivity Particulate Solids". Ph.D. dissertation, UNIV. OF N.S.W., Wollongong, 1969.
- [111] McLEAN, K.J. - "Factors Affecting the Resistivity of a Particulate Layer in Electrostatic Precipitators".
- [112] JONES, F.L. - "The Physics of Electrical Contacts" Great Britain, OXFORD UNIV. PRESS, 1957.
- [113] WINDRED, G. - "Electrical Contacts", London, MacMILLAN, 1940.
- [114] HOLM, R. - "Electric Contact Handbook". Stockholm, Hugo Gebers Forlag, 3rd Ed., 1958.
- [115] TASSICKER, O.J., HERCEG, Z. and McLEAN, K.J. - "Mechanism of Current Conduction through Precipitated Fly-Ash", Bulletin No.10, UNIV. OF N.S.W. 1966.
- [116] AHMED, S.U. - "Sparking in Air for Gap Lengths of Ten to One Hundred Microns", Thesis, UNIV. OF N.S.W. 1969.
- [117] BÖNING, W.- "Luftgehalt und Luftspaltverteilung geschichteter Dielektrika (I)". Archiv für Electrotechnik, Vol.48, 1963, pp.7.22 (from Ref.[40].
- [118] COBINE, J.D. - "Gaseous Conductors - Theory and Engineering Applications", DOVER, 1958.
- [119] SILLARS, R.W. - "Electrical Insulating Materials".
- [120] KUFFEL, E. and ABDULLAH, M. - "High Voltage Engineering, PERGAMON PRESS, 1966.

- [121] COOPERMAN, P. - Private Communication.
- [122] BRUCE, F.M. - "Calibration of Uniform Field Spark Gap
for High Voltage Measurements at Power Frequencies"
J. of I.E.E., 100, 145 (1953).
- [123] MEEK, J.M. and CRAGGS, J.D. - "Electrical Breakdown
of Gases". OXFORD, 1953.

APPENDIX A - Flow Diagram for Computing the Corona
Current Waveshape.

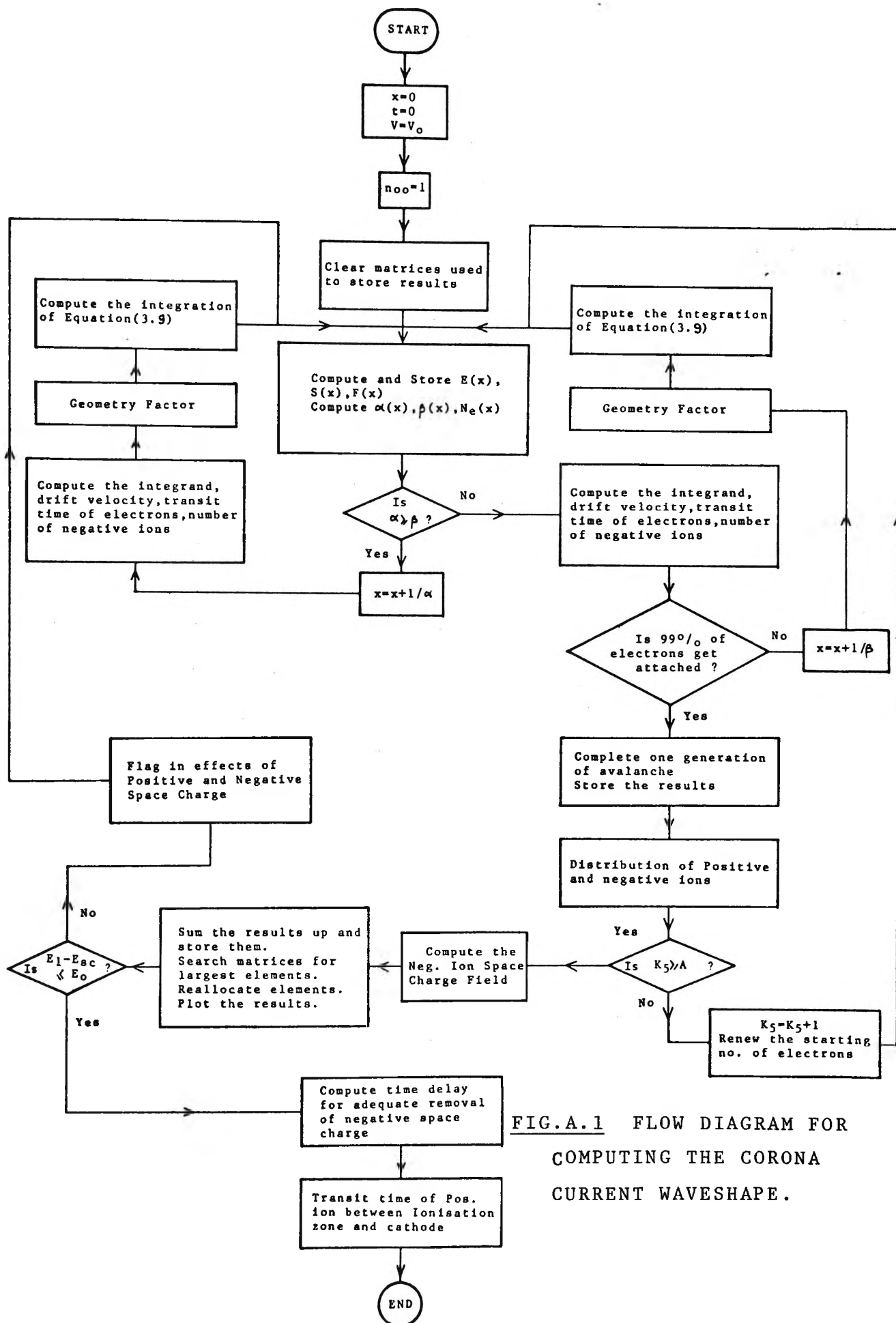


FIG.A.1 FLOW DIAGRAM FOR
COMPUTING THE CORONA
CURRENT WAVESHAPE.

APPENDIX B - Frequency of the Pulsed Power Supply and the
Waveshape of the Voltage Pulse.

The power supply described in Fig.4.10 can be used to generate voltage pulse of different rise times and frequencies. The rise time of the voltage pulse is controlled by resistance R_1 which is in series with the discharge wire and capacitance C_1 . Since the repetition rate of the pulsed voltage increases as the amplitude of the voltage pulse increases, the following method is used to determine the dependence of the characteristics of the corona system on the pulse frequency.

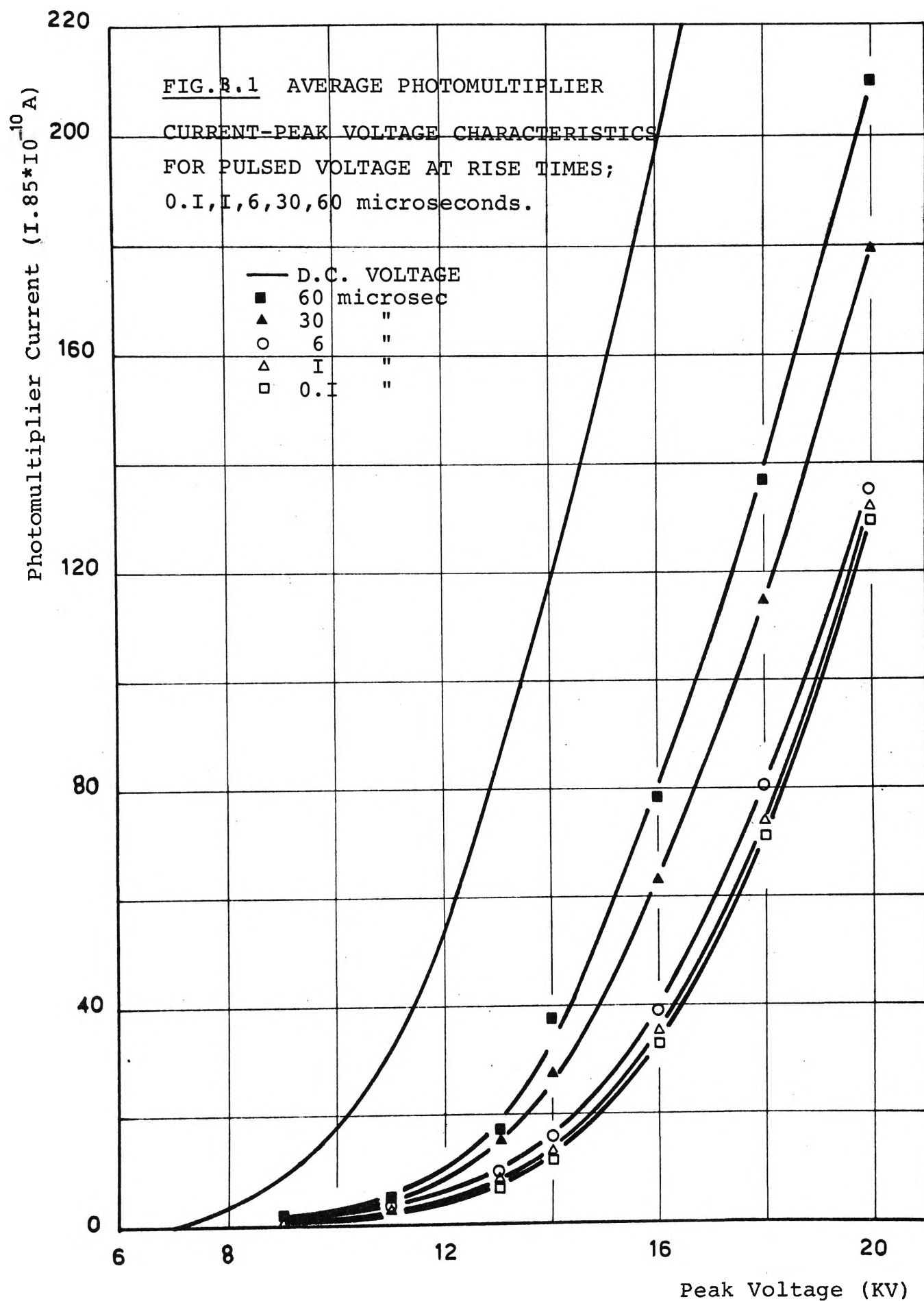
From the set of records similar to those shown in Fig.5.3 and the oscilloscopic records of the voltage pulses, the spatial average current from the photomultiplier is plotted against the average and peak values of the voltage as shown in Fig.B.1 and B.2. Similarly the average corona current measured electrically is plotted against the average and peak values of the voltage for several rise times and is shown in Fig.B.3 and B.4. It can be seen that the average current-average voltage characteristics obtained with both optical and electrical methods depend little on the rise time of the voltage pulses. This is understandable as under steady state conditions a difference of the rise time by one order of magnitude would hardly affect the distribution of negative ion space charge.

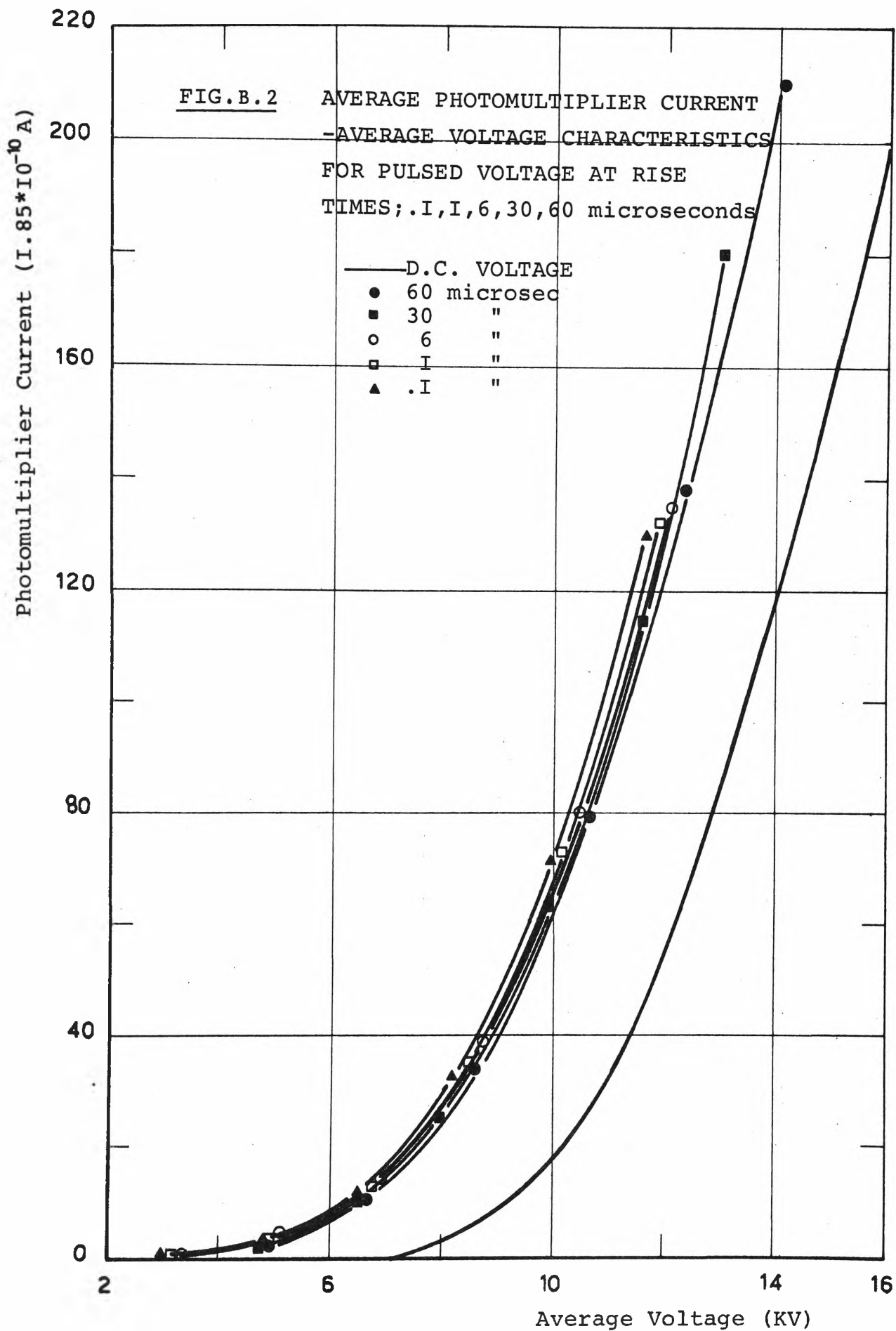
The pulse repetition rate of the power supply is plotted against the peak value of pulsed voltage for different rise times in Fig.B.5. It indicates the variation of pulse frequency with respect to rise time at a certain voltage level

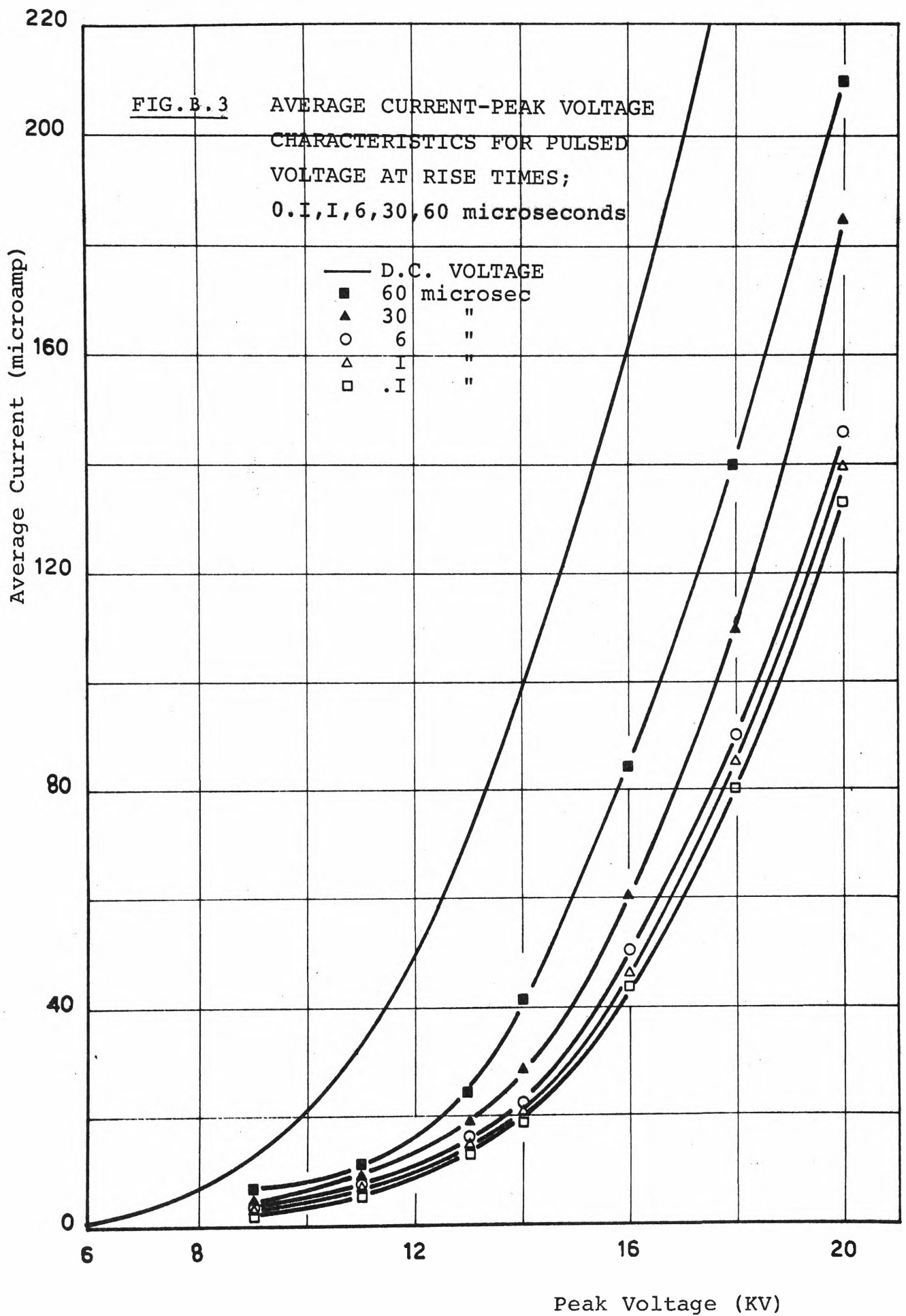
and the readiness of the spark gap to be triggered at high rise time. This is because at high rise time, the sphere connected to the output of the D.C. power supply requires a higher voltage to undergo the first spark, this means the spark gap under such condition is more over-volted than when the rise time is short. As a result, in the subsequent sparks electrons are more readily available.

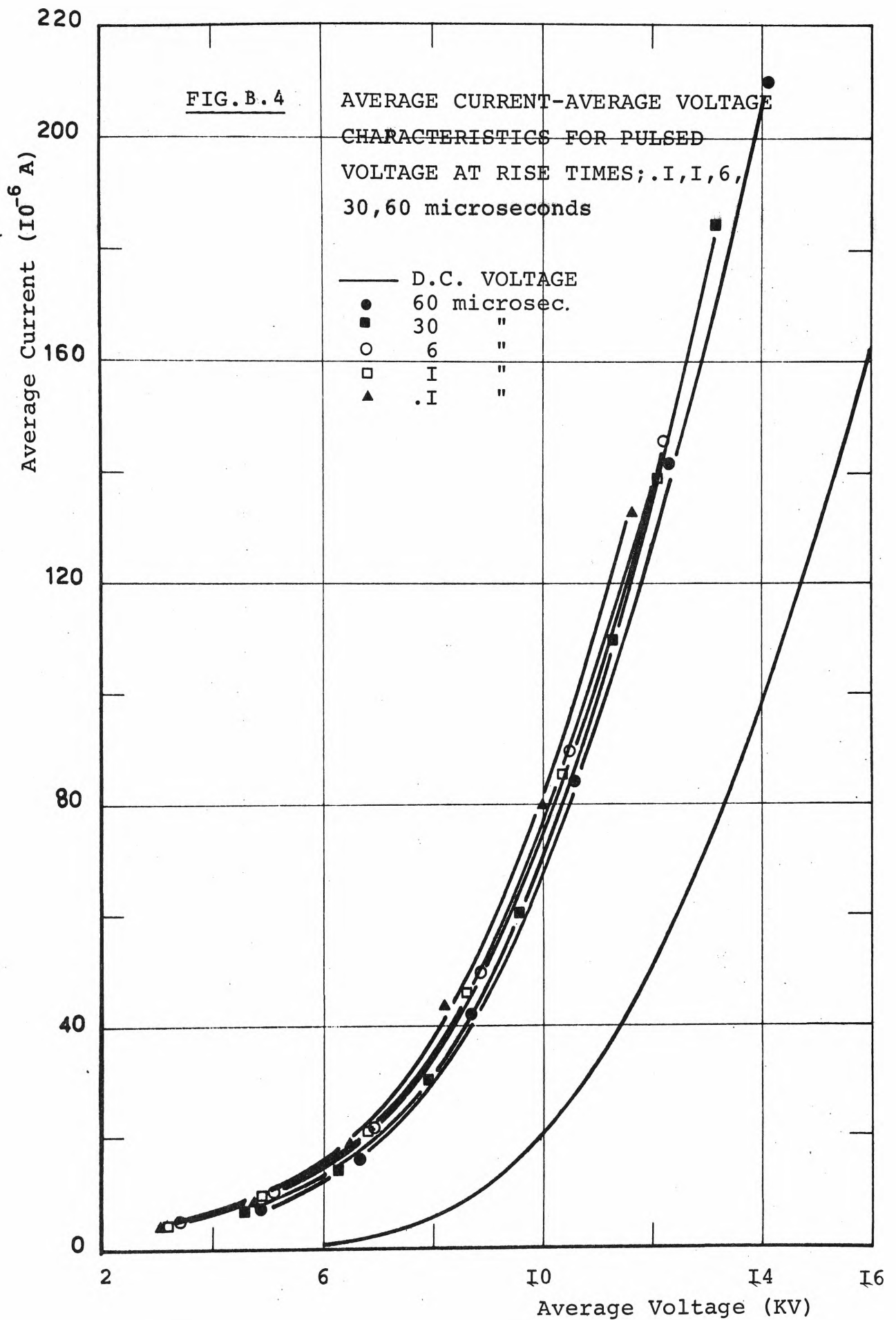
The average value of the pulsed voltage is plotted against its peak value in Fig.B.6. The upward shifting of the relationship as the rise time increases is consistent with the increase in the pulse frequency as it has been discussed. The broken lines are drawn by finding the intersection points of constant frequency lines with the frequency-peak voltage curves in Fig.B.5. The dependence of the current-voltage characteristics on the pulse frequency is then determined by interpolating the results shown in Fig.B.5, B.6 together with those in Fig.B.1, B.2, B.3 and B.4. They are plotted in Fig.5.8 and 5.7.

The typical waveshapes of the voltage pulses which are generated by the two power supplies as described in Fig.4.10 and 4.11 are reproduced in Fig.B.7, B.8 and B.9 respectively.









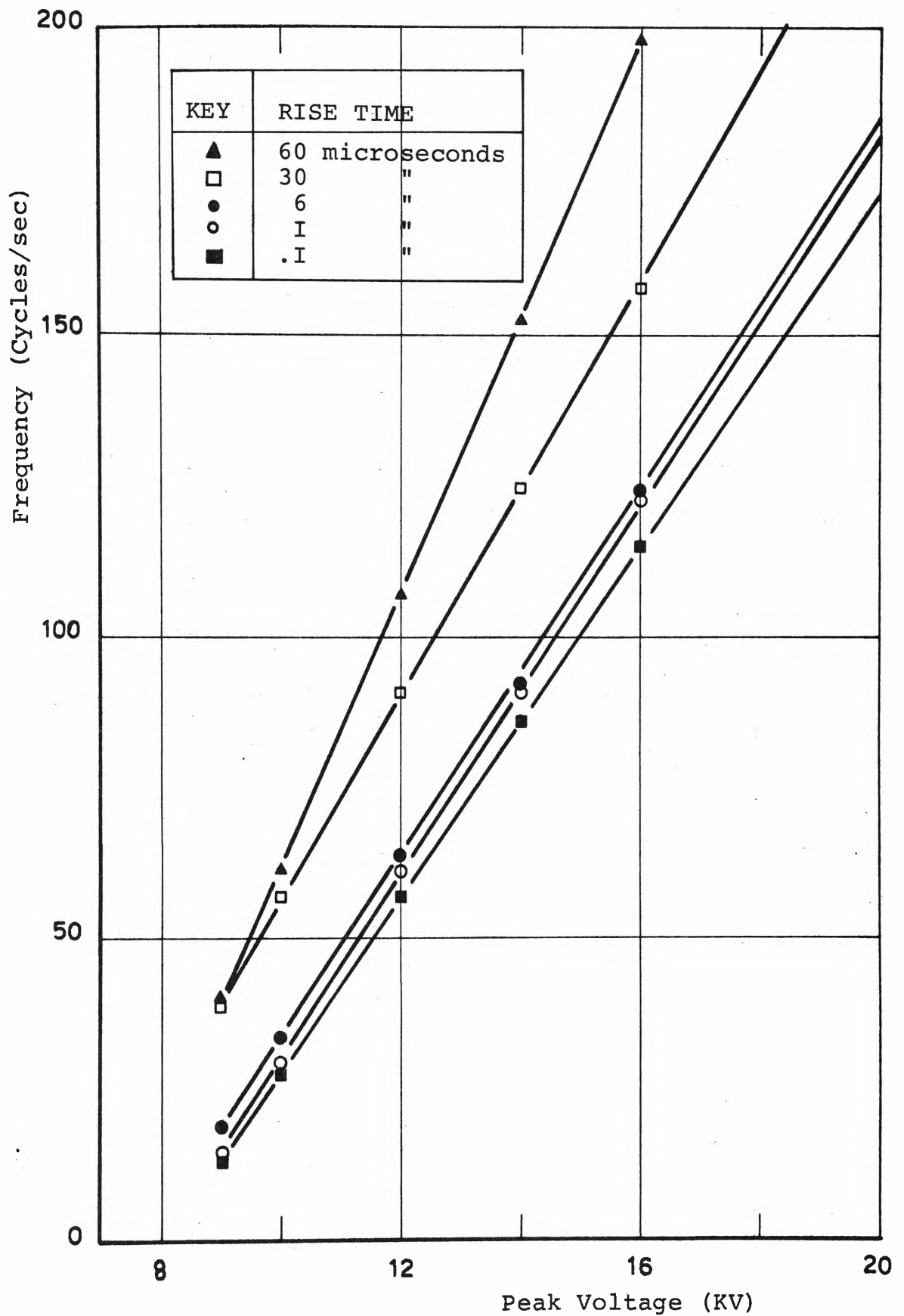


FIG. B.5 FREQUENCY-PEAK VOLTAGE RELATIONSHIPS
FOR PULSED POWER SUPPLY AT RISE
TIMES; .1, 1, 6, 30, 60 microseconds.

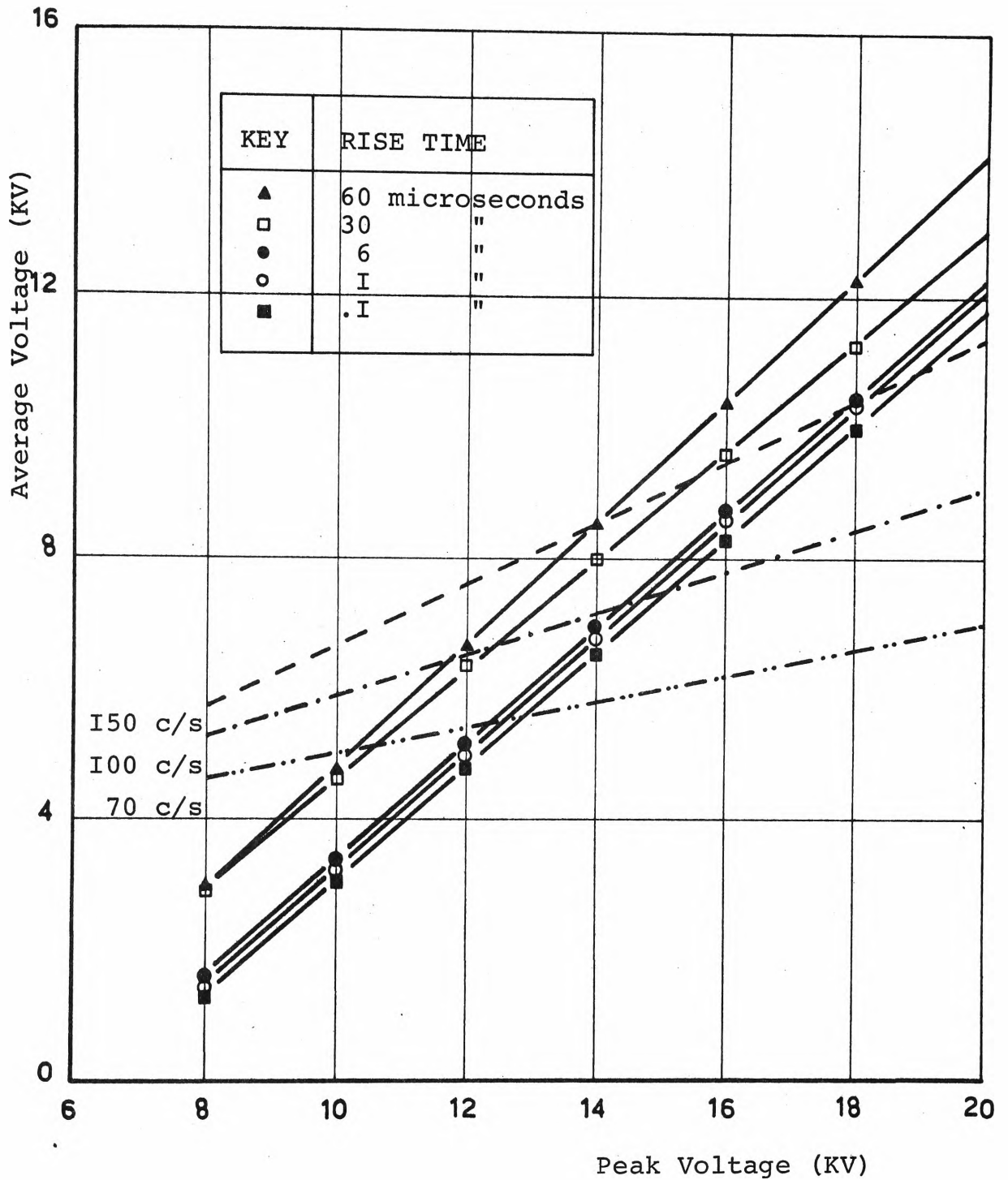


FIG. B. 6

AVERAGE VOLTAGE-PEAK VOLTAGE RELATIONSHIPS
 FOR PULSED POWER SUPPLY AT RISE TIMES; .1, 1,
 6, 30, 60 microseconds, and FREQUENCIES; 70, 100,
 150 cycles/sec.

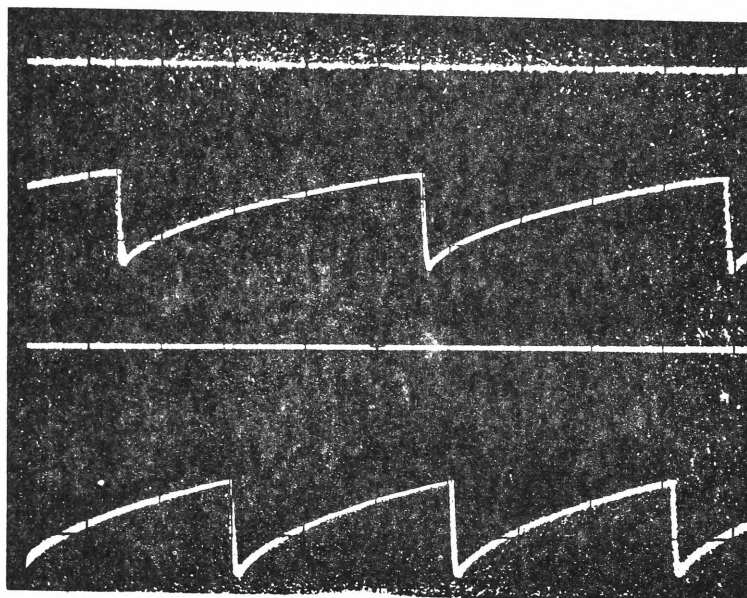


FIG.B.7 WAVESHAPE OF VOLTAGE PULSE GENERATED BY
POWER SUPPLY (FIG.4.10)
TIME CONSTANT = $30\mu\text{sec}$
VER. = 5KV/CM , HOR. = 2msec/cm
TOP TRACE, $V_p = 14\text{KV}$, BOTTOM TRACE, $V_p = 16\text{KV}$

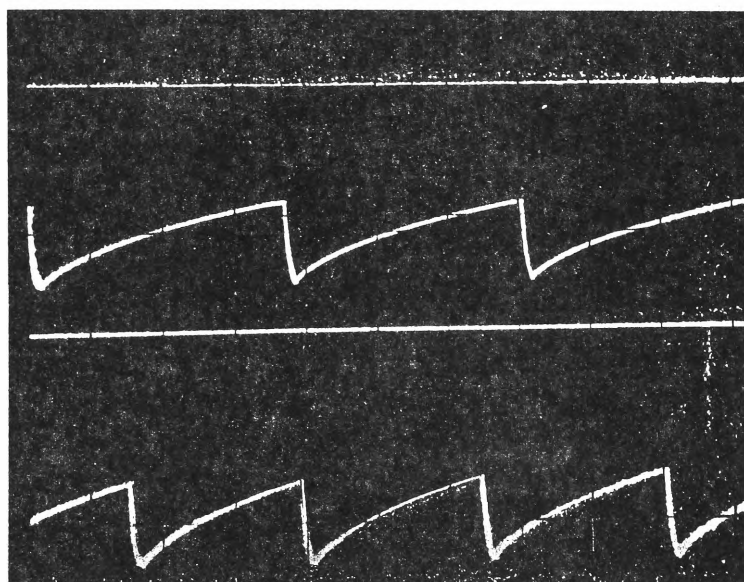


FIG.B.8 WAVESHAPE OF VOLTAGE PULSE GENERATED BY
POWER SUPPLY (FIG.4.10)
TIME CONSTANT = $60\mu\text{sec}$
VER = 5KV/CM , HOR. = 2msec/cm
TOP TRACE, $V_p = 14\text{KV}$, BOTTOM TRACE, $V_p = 16\text{KV}$

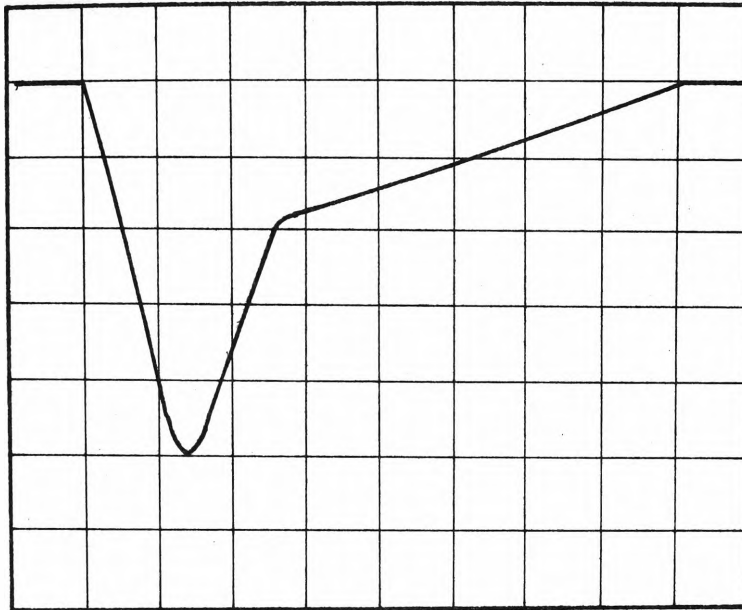


FIG. B. 9 WAVESHAPE OF VOLTAGE PULSE GENERATED
BY POWER SUPPLY (FIG. 4.11)
VER = 2KV/CM, HOR. = .2msec/cm.

APPENDIX C - Derivation of Equations (5.3) and (5.4)

The derivation of the voltage and current when the corona system is energised by a pulsed voltage can be described in four steps. The equivalent circuit of a corona system as shown in Fig.5.25 is redrawn in Fig.C.1 where switches S_t and S_c are included to describe the charging of the equivalent capacitor and the discharging through the non-linear resistor.

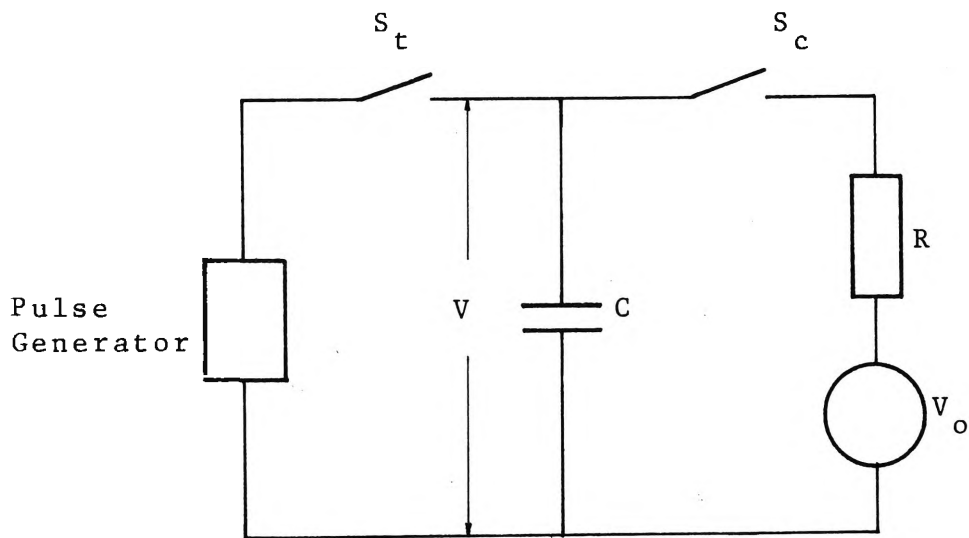


FIG.C.1 EQUIVALENT CIRCUIT OF A CORONA SYSTEM

(i) S_t closed, S_c opened

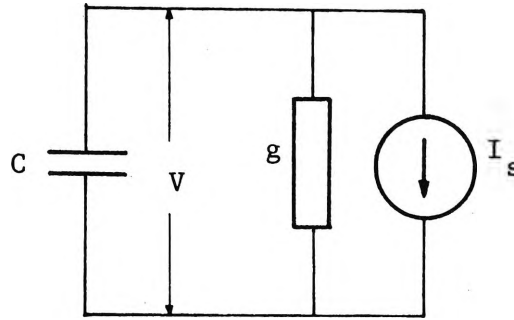
The voltage V across the capacitor C is built up immediately to its peak value V_p . Switch S_c is opened when $V < V_o$.

(ii) S_t closed, S_c closed

S_c is closed when $V \geq V_o$ and the air gap starts conducting, $V = V_p$ for the time interval $0 \leq t \leq t_o$ where t_o is the voltage pulse duration.

(iii) S_t opened, S_c closed

At $t_o < t \leq T$, switch S_t is opened and the voltage V starts decaying because capacitor C discharges through the equivalent, non-linear resistor R . The equivalent circuit thus becomes:



where $g = 1/R$, $I_s = V_o/R$

The Kirchoff's current law gives:

$$g.V(t) + C.\frac{dV(t)}{dt} = I_s \quad (C.1)$$

The Laplace's transform of equation (C.1) gives:

$$gV(p) + C(pV(p) - V(t_o)) = \frac{I_s}{p}$$

where $V(p)$ is the Laplace's transform of $V(t)$

$V(t_o)$ is equal to V_p

$$\text{or } V(p) = \frac{C.V_p}{g+pC} + \frac{I_s}{p(g+pC)}$$

$$V(p) = \frac{C.V_p}{g+pC} + \frac{I_s}{g} \cdot \frac{1}{p} - \frac{I_s.C}{g(g+p.C)} \quad (C.2)$$

The inverse of Laplace's transform of equation (C.2) gives:

$$V(t) = V_p \cdot \exp(-(t-t_o)/RC) + \frac{I_s}{g} - \frac{I_s}{g} \cdot \exp(-(t-t_o)/RC)$$

$$V(t) = \frac{I_s}{g} + (V_p - \frac{I_s}{g}) \cdot \exp(-(t-t_o)/RC)$$

or

$$V(t) = V_o + (V_p - V_o) \cdot \exp(-(t - t_o)/RC) \quad (5.3)$$

$$\text{for } t \geq t_o.$$

The corona current or load current can be found by using the following relationship:

$$i_c = -i$$

where i_c is the capacitor current and i is the load current.

From

$$i(t) = -C \frac{dV(t)}{dt}$$

the corona current can be written as:

$$i(t) = \frac{V_p - V_o}{R} \cdot \exp(-(t - t_o)/RC) \quad (5.4)$$

$$\text{for } t \geq t_o.$$

(iv) S_t opened, S_c opened

S_c is opened when $V(t) < V_o$. Depending on the equivalent time constant of the corona system, the voltage $V(t)$ drops to a certain level when the next voltage pulse comes at $t = T$, where T is the pulse period.

APPENDIX D - Relationship between the Discharge Pattern
and the Current Distribution

Because the ionisation taking place in the vicinity of the discharge electrode gives rise to the accumulation and transport of negative ion space charge to the collecting plane, it is of interest to see whether the distribution of the current on the collector relate to the radiation pattern in the proximity of the cathode.

A point-to-plane electrode system is used. The results obtained by scanning the optical system which is focussed on the vicinity of the cathode (corresponding to the positive column in the discharge region) over a distance along which the discharge intensity is detectable, is compared with the current distribution on the collecting plane of similar electrode system obtained by other workers.

The discharge electrode is a hemispherically-capped steel cylinder having a diameter of .04 cm and the gap length is 1 cm long. The discharge pattern obtained when the system is energised by D.C. voltage as detected by the optical system is shown in Fig.D.1 for two voltage levels. The distribution curves of the radiation intensity show perfect symmetry of the ionisation process taking place in the proximity of the point electrode.

For comparison purpose, the curves in Fig.D.1 are normalised with respect to the maximum discharge intensity in the ordinate scaling and the gap length in the abscissa scaling, the results are plotted in Fig.D.2. The shape of the normalised distribution curves is very similar to those

for current distribution on the collecting anode plane obtained by Masuda [30] and Tassicker [66]. Masuda's results are reproduced in Fig.D.3. The slight difference of the author's results with those in Fig.D.3 is probably caused by point electrode of different radius being used. For a larger point electrode, the field in the neighbourhood of the electrode diminishes slowly with distance. This causes the ionisation process to take place over a wider area on the electrode surface and consequently the distribution curve decreases less rapidly in the proximity of the discharge cathode.

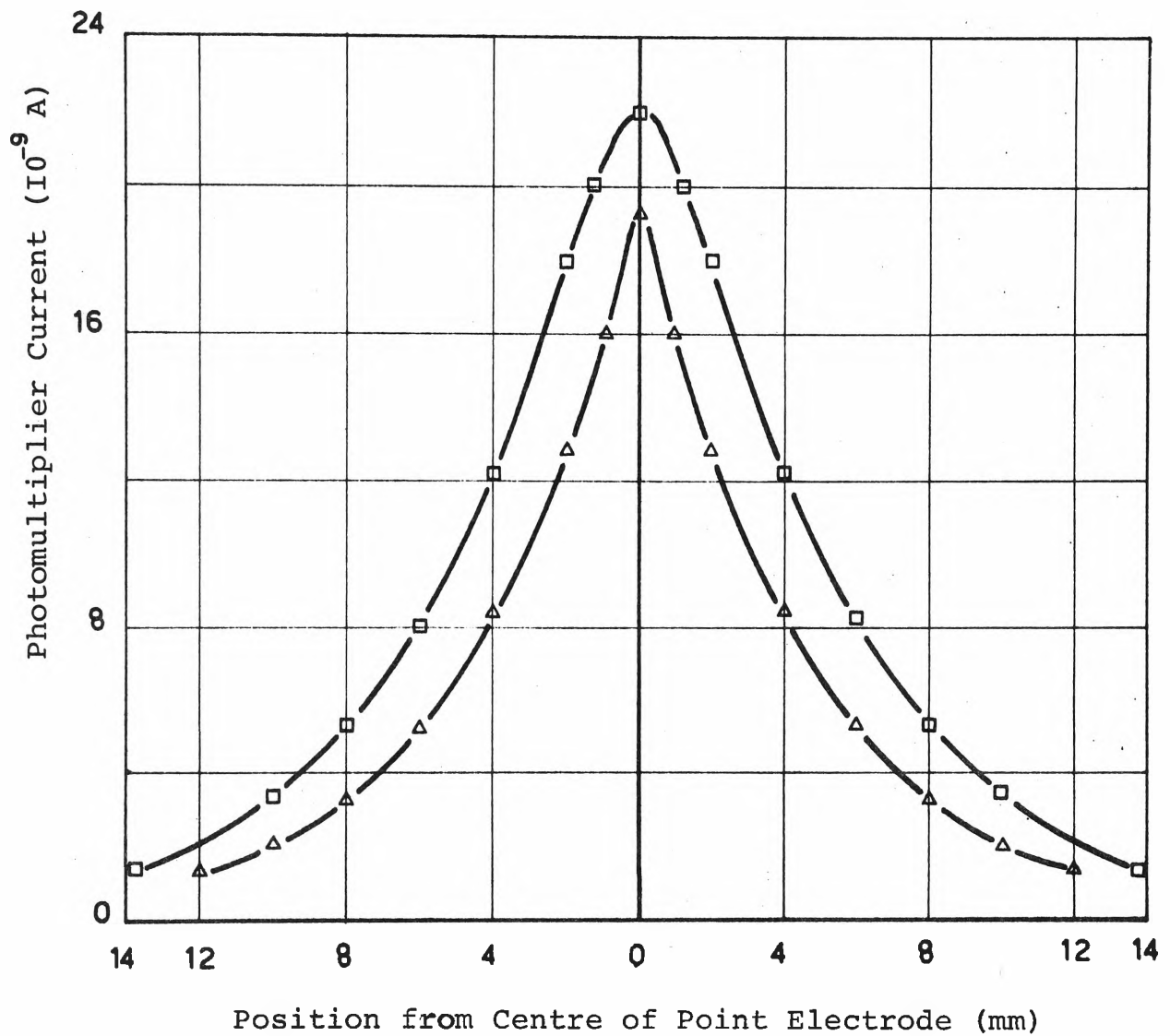


FIG.D.1

DISCHARGE PATTERN AROUND POINT ELECTRODE.

Δ $V = -11$ kv , $I = 55$ microamp.

\square $V = -12$ kv , $I = 72$ microamp.

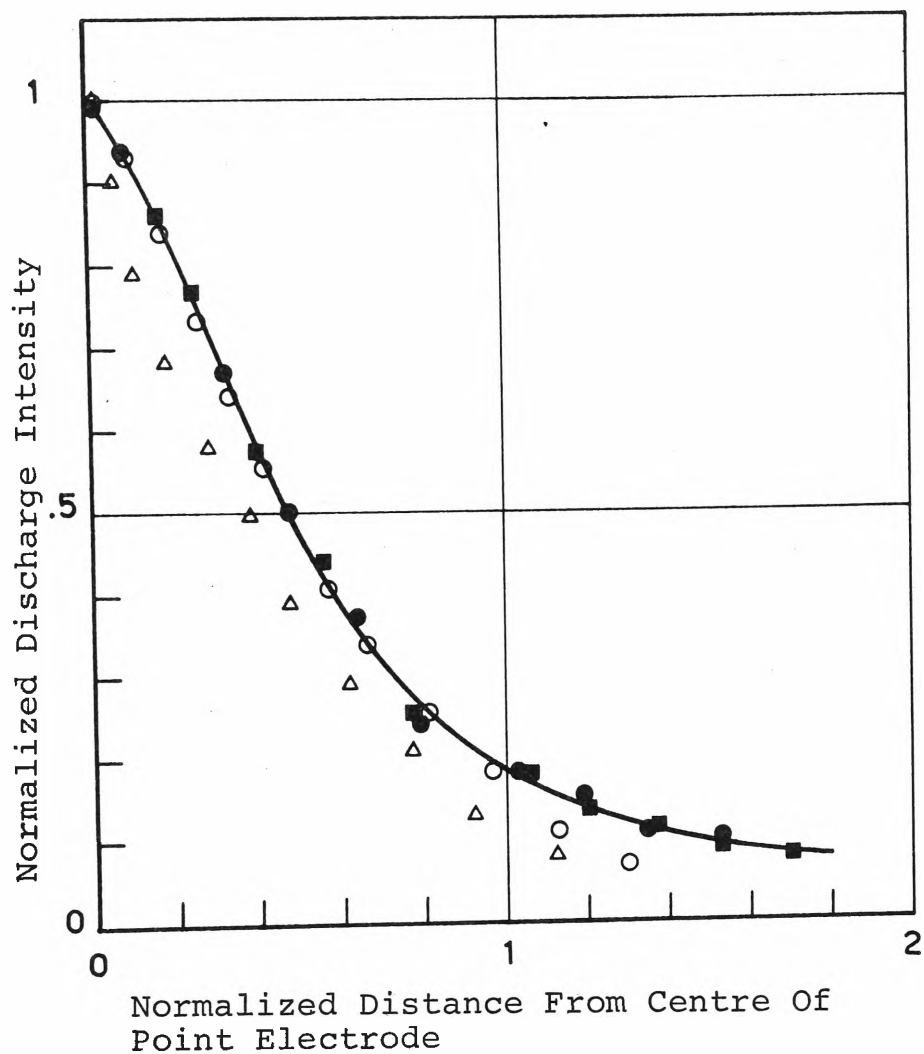
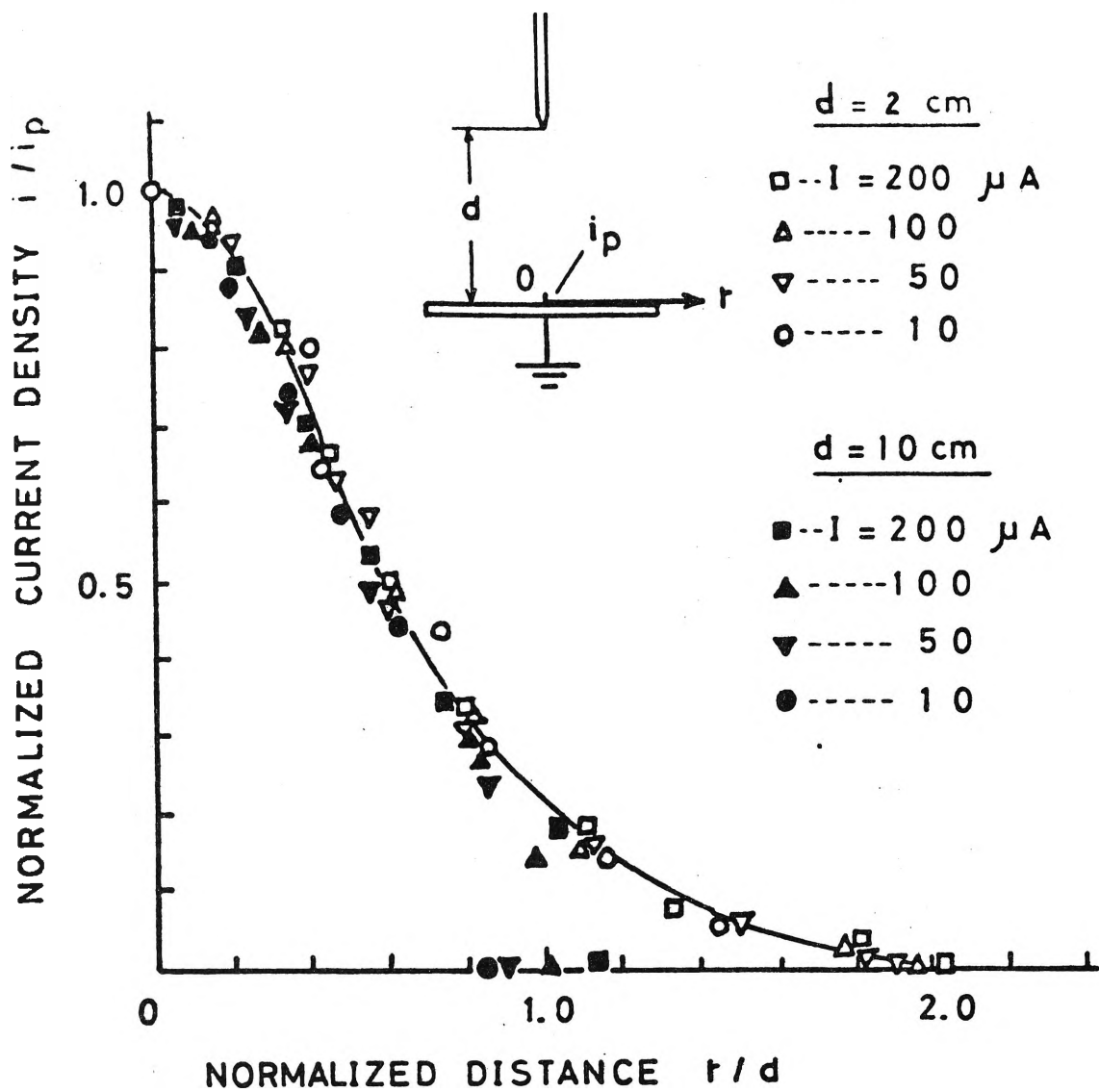


FIG.D.2

NORMALIZED DISCHARGE INTENSITY
VS NORMALIZED DISTANCE.PLOT
OBTAINED FROM FIG.D.1 AND RESULTS
MEASURED AT -13 kV, 88 μ A AND
-14 kV, 106 μ A.



NORMALIZED CURRENT DENSITY ON PLATE ELECTRODE i/i_p
VS NORMALISED DISTANCE r/d .

FIG.D.3 MASUDA'S RESULTS OBTAINED BY ELECTRICAL
METHOD [30].

